Supramolecular Engineering of Functional 2D Bi-Component Networks

CARLOS-ANDRES PALMA

Universtité de Strasbourg

STRASBOURG • FRANCE
2010

To friends and accomplices, past, present and future - and to all of those, whom, opposed to our instinct of survival, continue to fight for utopia.

Contents

Statement of Trust and Acknowledgments

The author declares that, except when noted, all the reported data, figures, equations and schemes are his own. The experimental conception of the work have been made jointly with Prof. Bonifazi and Prof. Samori. When explicit material from collaborators have been used it has been stated clearly below. An special original contribution to the work is acknowledged to **Dr. Jonas Björk** and **Dr. Felix Hanke**, who performed density functional theory from jointly conceived research in Chapters 2 and 4. Note that Chapter 1 consists exclusively from state of the art examples in the literature. Also in the Methods Chapter, most equations are taken from literature unless when noted. In the **Appendix**, Prof. Lackinger's theory and **Figure 8-7** and **Figure 8-8** are taken from the literature. The X-ray figures in the right hand side of **Figure 3-14**, **Figure 3-9** and **Figure 6-18** have been taken from the literature. All data reported correspond to a minimum of doubly reproducible experiments and error bars are given as the standard deviation of three or more data sets.

Contributions from Collaborators. Dr. Anna Llanes-Pallas, Joceline Zeitouny, Dr. Yuri Avlasevi and Laura Magini synthesized the molecules used in this study. Dr. Jonas Björk and Dr. Felix Hanke are responsible for **Figure 2-13**, **Figure 2-14**, **Figure 4-11b** and **Figure 4-17**. They are also responsible for the original contributions of **Equation 2-20** and **Table 4-3**. Dr. Halim Belbakra performed the experiment which was jointly designed in **Figure 4-5** and independently designed in **Figure 6-3b** and **Figure 6-4b**. Dr. Luc Piot is responsible for the images in **Figure 3-1**, **Figure 4-2** and **Figure 4-3**. Dr. Marco Cecchini provided the scripts for calculating free energy in Chapter 2 and the conception of the "blocks" simulations in Chapter 5. Massimo Bonini obtained the images in **Figure 6-3** and **Figure 4-13a**. Artur Ciesielski obtained **Figure 2-18a** and formatted the images in **Figure 1-5** and **Figure 1-6**. Salah Bessibes helped obtaining the IR spectra in **Figure 2-10**, **Figure 2-11** and **Figure 2-12**. Dr. Marco Cecchini, Dr. Massimo Bonini, Prof. Davide Bonifazi, Prof. Mats Person and Prof. Paolo Samori provided advice and contributed extensively to the text, which consists mostly on published work.

Special acknowledgment is given to **Prof. Paolo Samori** which coordinated the present work. This work would not have been possible without financial support from the EU project **Marie-Curie RTN PRAIRIES** (MRTN-CT-2006-035810) the **Université de Strasbourg** and the HPC resources of CCRT/CINES/**IDRIS** under the allocation 2009 (075114) made by GENCI (Grand Equipement National de Calcul Intensif).

Foreword

On hermeneutics, self-assembly and analogics

The present work endevours to predict the properties of a thermodynamic ensemble by embedding molecules with information, and as such it naturally ventures into the realm of hermeneutics. In this regard, information and prediction seem ill descriptors of the previous context, since *information* is a manmade concept for *predicting* future and past events. In classical determinisim (Karplus and Porter 1970), where the basic ansatz is that atoms are the basic constituents of matter and as such their understanding will provide accurate prediction of materials' functions, these predictions can be made with help of statistical thermodynamics, where two types of metaphysical scales of information and lack thereof are fundamental variables: energy and entropy. Energy[1] and Entropy are two scaling variables that have been proposed *ad-hoc* by many (Campbell 1973) in the early 19th century and have been embedded in the works of authors as Gibbs, Boltzmann, Maxwell (McQuarrie 1997), to produce the well known atemporal thermal quantity functions called free energies. The minimization of the free energy function for every basic constituent of the material (degrees of freedom) under the ergodic hypothesis (atemporal equilibrium) constitutes the best analytical prediction of its position or *state*.

In the following chapters experimental techniques and classical determinism (Karplus and Porter 1970) are used to try and extract qualitative rules for the construction of (2D) bi-component architectures. The so-formed architecture is referred to as "self-assembled" as its formation is ruled by the information stored in the components which undergo recognition events under well-defined experimental conditions, without the need of external perturbations, leading to complex structures. In other words, given a system composed of n elements of A, B and C, the $(n-x)$ elements of A and $(n-y)$ B will dispose in space in a time t to give an architecture characterized by an order parameter φ encompassing an average composition $<(n-x)$ in A and $(n-y)$ in B$>$, where x and y are averages substractors. Through out the text a simplified notation for the case of two-dimentional assembly of such architecture is given as AB_{ad}, where the subscript denotes adsorption onto an interface. Note that under dynamic conditions there will exist a *C* element which acts only as a mediator, e.g. a solvent. The act of using quantitative rules for predicting self-assembly is encompassed here in the neologism of *Supramolecular Engineering.* In other words, *a priori* knowledge

---

[1] Note that a Hamiltonian alone can "predict" the future in classical mechanics, yet it needs the knowledge of *states* (which in turn requires knowledge of their existence in time) for sub-atomic particles and thermodynamic ensembles. This gives evidence that there is a fundamental difference in what we can *count* and what we cannot, what is distinguishable and not, what we know and we do not, which in most cases bears energy and power units.

(pre-programming and prediction) of the order parameter and average composition of the A, B architecture is one goal of *Supramolecular Engineering*, the second being to generalize the design of functional A and B components for achieving the mentioned purpose. The previous is much analogous to *de novo* design in the farmaceutical industry.

Our work follows a practical approach to the field of *Supramolecular Engineering.* In this respect, it does not introduce concepts nor diagrams which may be widely available on existing texts. It rather presents a pragmatic (and sometimes historical) discussion of the techniques used, which is helpful in the actual performing of the experiments.

Chapter 1 introduces the state of the art in *Supramolecular Self-Assembly* in 2D
Chapter 2 introduces methods for studying self-assembly in 2D
Chapter 3 puts forward the chemical principles behind 2D self-assembly
Chapter 4 proves the pre-programming of self-assembly but not its prediction
Chapter 5 shows simulation as a first step towards *Supramolecular Engineering*
Chapter 6 introduces function and perspectives towards *Device Self-Assembly*
Page 207 compiles the chemical structures of the molecules used, much helpful during the reading of this work.

Finally, the epilogue of *Supramolecular Engineering* would be the full description of the state function $f(T,P,\varphi)$ in free energy space, i.e. a hypersurface to describe the intensive and extensive variables where the architecture is formed such as temperature (T) pressure (P) and order parameter (φ), to ultimately form *a priori* phase diagrams. Nonetheless, even when this milestone is reached, it would mainly conceal the ontological *science of prediction* or more accurately *information theory* [2]. As such, it is the author's duty to disclaim the tyranny in the logical machinery put forward by modern science, regardless of its mathematical beauty, not only because the intricate nature of free energy function is by itself obscure but it is also separated from spoken and written syntax, much like in Wittgenstein absolutistic logic[3]. It is this non-contextual everyday use of apophantics in science which led Heidegger to state much appropriately *Wissenschaft denkt nicht*[4].

We expect that in the future, besides the technocratic advantages of bottom-up synthesis of devices with atomic precision i.e. *Device Self-Assembly*, accurate analogical operations may be extracted from visionary thermodynamical ensemble driven machinery. Ultimately, such computers, which sole input are a distribution of events in time and naturally evolve to interpret information, will succeed in reconciliating hermeneutics and technology.

---

[2] Not to be confused with the theory of information, by Shannon, C. E. and W. Weaver (1963). The Mathematical Theory of Communication, Board of Trustees of the University of Illinois.

[3] Wittgenstein, L. (1921) Tractatus Logico-Philosophicus Ann. der Naturphilosophie, 14, pgs. 185

[4] Heidegger, M. (1984) Was heißt Denken? Tübingen: Niemeyer, pgs.4.

1 Introduction

1.1 2D Self-Assembly

Supramolecular *engineering* comprises the design, synthesis and self-assembly of well-defined molecular modules into tailor-made architectures. The incorporation of functional units in these molecular modules makes it possible to provide a pre-programmed function to the overall architecture, thus paving the way towards its technological application (Lehn 1990).For this purpose, the last decade has witnessed an increasing interest towards the 3D engineering of supramolecular materials (Braga, Grepioni et al. 1998; Yaghi, O'Keeffe et al. 2003; Hosseini 2005; Palmer, Velichko et al. 2007; Mann 2009). The colossal task of achieving full control over self-assembled systems however, is the ongoing endeavour of the supramolecular scientists and to date only few systems may be pre-programmed to undergo controlled self-assembly in 3D (Winfree, Liu et al. 1998). In contrast, 2D interfaces provide a simplified platform for supramolecular and crystal engineering, and the field has known an exciting growth (Palermo and Samorì 2007; Bonifazi, Mohnani et al. 2009; Elemans, Lei et al. 2009; Lackinger and Heckl 2009). These early attempts of 2D crystal engineering are exemplified in the pre-programmed molecular (self-) organization at surfaces and interfaces, a realm that holds *per se* a great potential for the generation of novel 2D nanoscale devices (Joachim, Gimzewski et al. 2000) or devices with custom-made properties, such as charge injection (Hamadani, Corley et al. 2006), transport (Reed, Zhou et al. 1997; Metzger 2008) and storage(Arico, Bruce et al. 2005).

Self-assembly at room temperature and atmospheric pressure is highly appealing, especially when working at the solid-liquid interface: in fact, thanks to the possibility of operating under equilibrium conditions and to mimic phenomena occurring in Nature, it represents a privileged playground where functional molecular systems can be elaborated. At such interface the self-assembly may be thermodynamically driven, making it possible to lay the foundation for 2D pre-programmed self-assembly (Kampschulte, Werblowsky et al. 2008; Palma, Bjork et al. 2009). In fact *supramolecular engineering* relies on the prediction of the thermodynamic state occupied by the grand majority of molecules at a given time in a free-energy *hypersurface*, i.e. the prediction of the exact architecture resulting from the molecular self-assembly.When a system reaches equilibrium conditions, its state is the result of the difference in free energy between all possible configurations. Unfortunately, we will learn in Chapter 2 that the computation of free energy differences is still a major research challenge (Meirovitch 2007), limiting *supramolecular engineering* to a semi-quantitative approach, which we here refer to as pre-programming self-assembly.

We will see in Chapter 4 that the pre-programming approach takes into account only enthalpic contributions to predict short-range self-assembly (Silly, Weber et al. 2008; Palma, Bonini et al. 2009; Palma, Bjork et al. 2009). In this semi-quantitative approach, the prediction of the most probable 2D pattern relies naturally on the differences in potential energies (including both intermolecular and adsorption energies) per unit area between probable polymorphs.(Palma, Bjork et al. 2009). Minimization of the potential energy per unit area translates into polymorphs being dependent on compensation of adsorption energies by intermolecular energies. Moreover, because of current challenges in obtaining accurate adsorption energies (Chapter 2), one can make a system independent of adsorption energies by working in excess surface area, i.e. (sub-)monolayer regimes, were only intermolecular energies per molecule are considered (Palma, Bonini et al. 2008; Palma, Bjork et al. 2009). An a priori knowledge of intermolecular interaction energies is thus of paramount importance, being the base for qualitative *supramolecular engineering*. As such, qualitative supramolecular *engineering* at surfaces relies in the deep understanding of non-covalent interactions, such as *van der Waals*, *hydrogen-bond* and *metallo-ligand*.

In this Chapter, we will glance over current literature enrolling the previous intermolecular interactions in the self-assembly of prototype functionalities, *enroute* towards fully integrated functional supramolecular architectures. In the first section (1.1.1), we begin by exploring systems engineered exclusively through van der Waals (vdW) interactions, introducing adsorption at interfaces. We then expose recent examples in 2D crystal engineering using alkyl chain interdigitation as the main building strategy. Further on we give an introduction on strategies employed in some vdW systems for bottom-up self-assembly, as well as the electronic and logic characterization of some prototype systems. In the second section (1.1.2) we focus mainly on systems engineered with the help of hydrogen-bonds and the influence on multiple hydrogen-bonds on the supramolecular entities.

1.1.1 Through vdW Interactions

Adsorption and van der Waals interactions: In 1873 Johannes Diderik Van der Waals (vdW) hypothesized the existence of intermolecular forces to formulate his equation of state for molecular gases(van der Waals 1920). Van der Waals forces come into play at first instance in the adsorption of molecules on atomically flat surfaces. Atomically flat surfaces which are commonly used for experiments at the solid-liquid interface include highly oriented pyrolytic graphite (HOPG), Au(111) and MoS_2, because of their ease of cleaning, stability in air, and their inert character. However, to properly understand the nature of molecular physisorption one must first consider the interaction of molecules with the surfaces. For instance, as we will discover in Chapter 2, the theoretical values of heat of adsorption of benzene on HOPG may vary between -8.6 to -11.1 kcal/mol for some popular density functional theory and force field calculations (Björk, Hanke et al. 2009) as compared to the experimentally determined values of -11.5±6 kcal/mol from thermal desorption experiments (Zacharia, Ulbricht et al. 2004). Interestingly, alkanes have been reported to have a stronger adsorption on HOPG if compared to aromatics having the same number of carbon atoms. For the sake of example, hexane has a desorption barrier of ~-17 kcal/mol on HOPG(Gellman and Paserba 2002) and slightly lower, ~-13 kcal/mol, on Au(111) (Wetterer, Lavrich et al. 1998). In analogy to large aromatic compounds (Kastler, Pisula et al. 2005), these apparent large exothermic changes are heavily countered by endothermic de-solvation phenomena, such that the choice of the solvent heavily influences the overall exothermic adsorption process. Moreover, even in the absence of a solvent to weaken adsorption energies, diffusion at surfaces is fast (~mm/s) (Zhdanov 1991) and hopping events from adsorption sites occur in the picosecond timescale (Barth 2007).

From the above diffusion rates, it follows that formation of crystals as opposed to that of amorphous phases at the solid-liquid interface relies not only on *strong* intermolecular interactions, but most importantly on the *directional* nature of such interactions. In Chapter 5 we will also give insight to the critical role played by the diffusion constant and reversivility in the self-assembly of extended architectures.

Order in van der Waals interactions: alkyl chain interdigitation. When dealing with neutral atoms or molecules, vdW forces have their origin on *London dispersion forces* (Margenau 1939; Israelachvili 1992), which arise from the attraction of the instantaneous dipoles generated by atomic electron clouds. Exploiting *London's dispersion* forces, stabilization of the 2D self-assembly has been achieved by equipping the molecules of interest with long aliphatic chains; in this way the interdigitation of alkyl chains belonging to adjacent molecules made it possible to form crystalline patterns (Rabe and Buchholz 1991). This occurs through the entrapping of an alkyl chain in-between two adjacent ones with an approximate energy of interaction of ~0.7 kcal/mol per methylene unit.(Samorì, Fechtenkötter et al. 2001) This value is markedly lower than the energy of adsorption on HOPG, which is ca. four times larger, as normalized per methylene unit(Yin, Wang et al. 2001; Gellman and Paserba 2002). Such an interdigitation between alkyl chains features a *pseudo-directionality* because the interdigitation approach rests on a fairly preferential sorption of the rod-like alkyl chains along the six identical main crystallographic lattice directions of HOPG (the non-redundant directions having Miller-Bravais indices of. As a result, the physisorption is not characterized by a surface commensurability with

HOPG *per se,* although the sorption of the methylene hydrogens into the centres of the graphite rings would be preferred (Rabe and Buchholz 1991; Ilan, Florio et al. 2008). Charra and co-workers (Bleger, Kreher et al. 2007) have recently made use of this approach to steer the orientation of phenyl-vinylenes on HOPG (**Figure 1-1a**), a versatile approach that can result in patterning of all five 2D Bravais lattices.

Very recently De Feyter and co-workers (Adisoejoso, Tahara et al. 2009) (**Figure 1-1b**) have further employed this strategy to realize the first example of a four-components 2D crystal. It has been also possible to observe one of the smallest aromatic molecules, i.e. an unsubstituted triphenylene (yellow arrows), immobilized in a 2D crystal. It is worth noting that neither triphenylene nor coronene can be visualized when deposited from solutions on HOPG as single components, because their high diffusion at room temperature, due to the absence of stabilizing lateral interactions with adjacent molecules. Such result confirms the importance of lateral interactions in forming a 2D crystal at room temperature. **Figure 1-1c** shows an example of the same strategy employed for the encapsulation of a triangular polyaromatic molecule (Lei, Tahara et al. 2008). Despite the huge adsorption energy which polyaromatics may exhibit, disorder is always evident in the pores, which measure 4.7 nm edge-to-edge, with a record 7.0 nm edge-to-edge when using longer alkyl chains ($C_{30}H_{61}$) (Tahara, Lei et al. 2008).

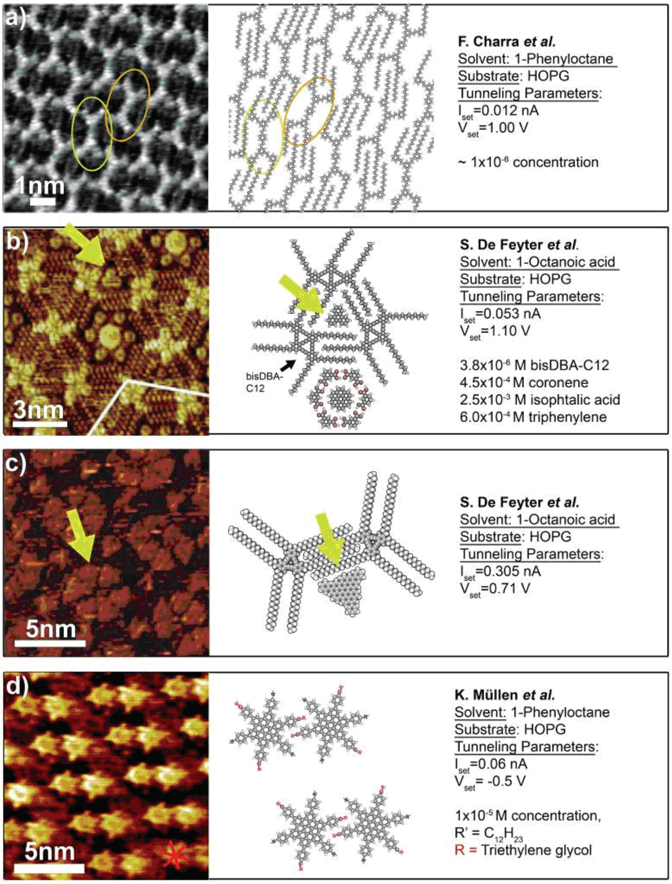

Figure 1-1
STM images and related packing models showing as well as experimental relevant parameters of (a-c) 2D Crystal engineering through alkyl chain interdigitation and (d) bottom layer structure of discotic liquid crystals.

De Feyter and co-workers also demonstrated that the interdigitation approach is not flawless (Lei, Tahara et al. 2008). Given the amount of conformational freedom of alkyl chains, almost all patterns relying on alkyl-chain interdigitation are affected by polymorphism. Nevertheless, interdigitation represents an elegant strategy to decorate thus nanopattern surfaces.

From 2D to 3D architectures: there is plenty of room at the top! Once accurate 2D positioning is mastered, the controlled placement of objects in the third dimension may be envisaged. A fundamental question arises concerning all different intermolecular interactions that can be exploited for 3D control: is there a minimum boundary in the magnitude of a force needed for effective bottom-up self-assembly?

Liquid crystals are the proof that very weak interactions are sufficient to create complex 3D architectures (De Gennes and Prost 1993). By using liquid-crystal forming molecules such as alkyl substituted hexa-*peri*-benzocoronene derivatives it was possible to visualize by STM supramolecular architectures featuring a high degree of order extended even to the third dimension in the region near to the surface (Samorì, Fechtenkötter et al. 2001). Similar result has been also obtained on bi-component assemblies of an electron donor and acceptor systems.(Samorì, Severin et al. 2002) **Figure 1-1d** reports an STM image of a complex C-3 symmetric hexa-*peri*-benzocoronene (Feng, Pisula et al. 2009). In the bulk, this molecular module forms columnar phase dictated by the π-π stacking (Grimme 2008; Björk, Hanke et al. 2009; Mativetsky, Kastler et al. 2009), with an inter-planar distance of 0.35 nm. Despite of its attractiveness for charge transport (Feng, Marcon et al. 2009; Mativetsky, Kastler et al. 2009), π-π stacking is not the most controlled strategy towards bottom-up construction, as it is poorly directional and features modest selectivity.

Recently, Charra and co-workers have shown that nano-pillars consisting of [2.2]paracyclophanes can be consistently positioned onto the 2D platforms, thus forming highly crystalline 3D patterning (**Figure 1-2a**) (Bleger, Kreher et al. 2008). Visualization of such covalently linked double-decker molecules extending into the third dimension was pioneered by Rabe and co-workers on HBC double-deckers (Watson, Jäckel et al. 2004). This strategy was later applied with double-deckers made from phtalocyanines complexes (Gomez-Segura, Diez-Perez et al. 2006; Klymchenko, Sleven et al. 2006; Takami, Arnold et al. 2006). These complex modules have been chosen since phtalocyanines are known to feature long-range order in 2D monolayers (Qiu, Wang et al. 2000), which can be then used as playground to control the position of such 3D architectures. For instance, Weiss and co-workers (Takami, Arnold et al. 2006) have visualized the formation of highly ordered double-decker phtalocyanines in equilibrium with single phtalocyanines (**Figure 1-2b**). Another sophisticated and versatile approach to access the third dimension was shown by Herges and co-workers (Baisch, Raffa et al. 2009). Making use of triazatriangulenium ionic platforms, they introduced a variety of functional units, such as aryl or azobenzene substituents, that extend perpendicularly to the surface into the third dimension (**Figure 1-2c**). A similar approach can be pursued by using metallo-ligand interactions. Feringa and co-workers(Visser, Katsonis et al. 2009) gave recently a proof-of-principle on how metallo-organic interactions can be extended into the third dimension, which may serve for bottom-up 3D construction (Yaghi, O'Keeffe et al. 2003; Shekhah, Wang et al. 2009), by complexation of pyridines onto a self-assembled layer of zinc porphyrins. Beyond equilibrium conditions, non-equilibrium organization such as layer-by-layer assembly (Decher 1997) can also be used in conjunction with van der Waals interactions to control the 3D structure of architectures. In 2004 Fichou and co-workers demonstrated that alkyl chains can be, in a first step, self-assembled at the solid-liquid interface and subsequently used to self-assemble alkyl substituted hexa-*peri*-benzocoronene (HBC) in an epitaxial fashion (**Figure 1-2d**) (Piot, Marchenko et al. 2005). Alkyl substituted HBCs are highly symmetric aromatic discs which have been extensively studied by Rabe and co-workers (Stabel, Herwig et al. 1995; Ito, Wehmeier et al. 2000; Samorì, Fechtenkötter et al. 2001; Samorì, Severin et al. 2002). This strategy can be further refined by taking advantage of the formation of charge-transfer complexes (Samorì, Fechtenkötter et al. 2001; May and Kühn 2004; Samorì, Yin et al. 2004) (see later in this chapter). The control of 2D assembly represents the first step towards the tailoring of 3D architectures for a wide range of applications, e.g. from charge and gas storage (Yaghi, O'Keeffe et al. 2003) to optoelectronics (Liscio, De Luca et al. 2008).

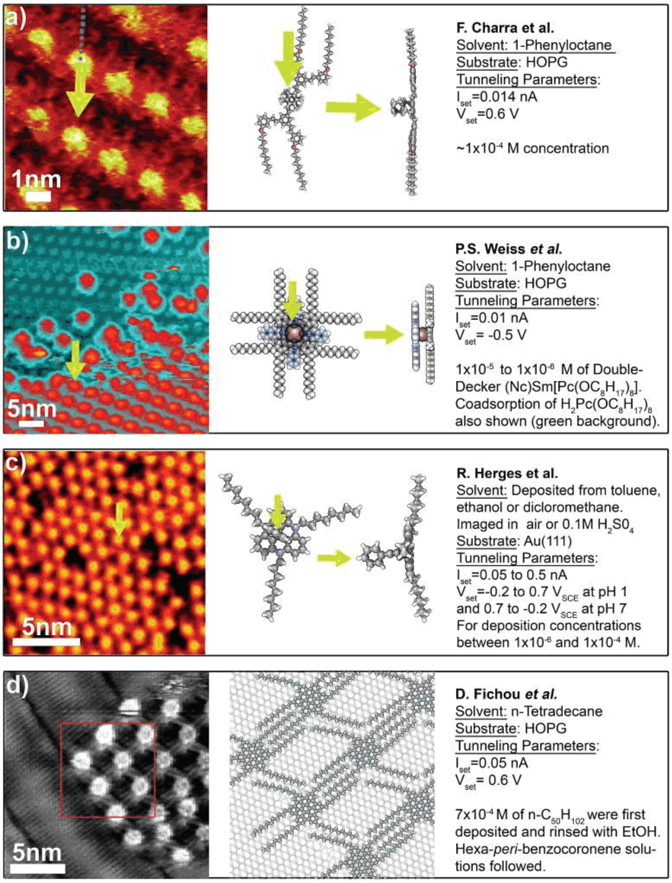

F. Charra et al.
Solvent: 1-Phenyloctane
Substrate: HOPG
Tunneling Parameters:
I_{set}=0.014 nA
V_{set}=0.6 V

~1x10^{-4} M concentration

P.S. Weiss *et al.*
Solvent: 1-Phenyloctane
Substrate: HOPG
Tunneling Parameters:
I_{set}=0.01 nA
V_{set}= -0.5 V

1x10^{-5} to 1x10^{-6} M of Double-Decker (Nc)Sm[Pc($OC_8H_{17})_8$]. Coadsorption of $H_2Pc(OC_8H_{17})_8$ also shown (green background).

R. Herges et al.
Solvent: Deposited from toluene, ethanol or dicloromethane. Imaged in air or 0.1M H_2SO_4
Substrate: Au(111)
Tunneling Parameters:
I_{set}=0.05 to 0.5 nA
V_{set}=-0.2 to 0.7 V_{SCE} at pH 1 and 0.7 to -0.2 V_{SCE} at pH 7
For deposition concentrations between 1x10^{-6} and 1x10^{-4} M.

D. Fichou *et al.*
Solvent: n-Tetradecane
Substrate: HOPG
Tunneling Parameters:
I_{set}=0.05 nA
V_{set}= 0.6 V

7x10^{-4} M of n-$C_{50}H_{102}$ were first deposited and rinsed with EtOH. Hexa-*peri*-benzocoronene solutions followed.

Figure 1-2
STM images and related packing models showing as well as experimental relevant parameters of (a-c) Three-dimensional architectures at interfaces and (d) a two-layered assembly of polyaromatics on top of hydrocarbons.

The era of organic electronics: Rectifiers and Switches. The beginning of the organic electronics era was marked by the studies on electrical conductivity and luminescence in polymers over 30 years ago(Chiang, Fincher et al. 1977) and it has bloomed into full maturity during the last few decades. The discovery of carbon nanotubes less than 20 years ago(Iijima 1991) and the dawn of graphene(Geim and Novoselov 2007) have definitely consolidated the importance of organic electronics. Because of these reasons, the interest on the electronic properties of low-dimensional materials is now ubiquitous. In this regard, low-dimensional graphenes (Samorì, Simpson et al. 2002) like graphene nanoribbons are novel architectures that present important electronic properties (Son, Cohen et al. 2006). Towards this goal, Müllen and co-workers (Yang, Dou et al. 2008) have successfully produced and imaged long (~10 nm) ribbons at the HOPG interface (**Figure 1-3a**, solubilizing groups are not shown). Accessing such “1D” electronically-active objects by synthetic methods opens interesting perspectives in supramolecular electronics.

In (semi-)conducting systems, I/V curves or current-voltage characteristics are a common tool for qualitative understanding of electronic transport (Datta, Tian et al. 1997). For example, **Figure 1-3b** exhibits an STM image of a HBC-based architecture in which coronene di-imide acceptor has been co-deposited (Jackel, Watson et al. 2006). The exact location of the acceptor in the assembly can be revealed by the electron acceptor nature of di-imides. The figure displays the scanning tunneling spectroscopy (STS) I/V characteristics exhibiting clear asymmetric behaviour, which can be analyzed considering *orbital mediated tunneling* (OTS) or, more in general, *resonant tunnelling* (Hipps and Scudiero 2005; Hipps and Vij 2006). When the substrate (being HOPG with a work function of ~4.7 eV or gold with a work function of ~5.1 eV (CRC Handbook 2007) is positively biased, electrons from the Platinum/Iridium (Pt/Ir) tip (having a work function ~ 5.7 eV (Hipps and Vij 2006)) will flow to the sample assisted by the orbital aligned between the electrodes, which is normally the Lowest Unoccupied Molecular Orbital (LUMO) of an *acceptor* molecule (whose electron affinity varies normally between 1-3 eV (2007)). This results in a higher current at positive sample biases for the coronene di-imide (red curve) than from the bright cores (black curve), proving that indeed coronene di-imide is located between the diagonals of the bright-cores.

The general host-guest complexation is a common strategy in the supramolecular chemist’s toolbox. Host-guest interactions are encompassed behind a broader definition of fundamental interactions, arising from the 1890 seminal Lock-and-Key paper by Emil Fischer’s (Kunz 2002). In this context, De Feyter and co-workers showed that supramolecular recognition can occur at a surface between a macrocycle and a charged guest, a tropylium ion (Tahara, Lei et al. 2008) (**Figure 1-3c**). In molecular electronics, host-guest interaction might be mediated by the formation of charge-transfer complexes (May and Kühn 2004) and is of special importance for designing charge-separation (Wasielewski 2006), energy-harvesting (Balaban 2005) and rectifying devices

(Mujica, Kemp et al. 1996). For instance, complexation of the well-known donor-acceptor thiophene and fullerene (C_{60}) pair (Smilowitz, Sariciftci et al. 1993) has been characterized at the solid-liquid interface by Freyland and co-workers (Pan, Cheng et al. 2006). By using a macrocycle decorated with di-thiophene units, C_{60} can undergo preferential adsorption onto the dithiophene "host" sites (in **Figure 1-3d** the macrocycle ordered monolayer is only shown, while the illustration shows where C_{60} is adsorbed after deposition).

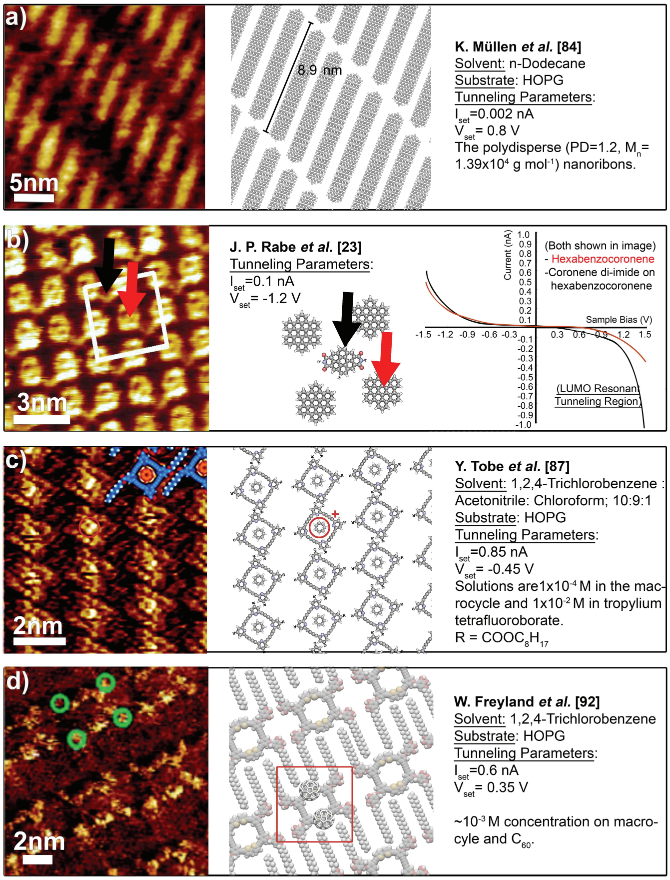

Figure 1-3
STM images and related packing models showing as well as experimental relevant parameters of (a) Nano graphene ribbons at interfaces and (b),(c),(d) host-guest interactions at interfaces.

By using a similar approach on oligo-thiophene macrocycle building blocks, Bäuerle and co-workers(Mena-Osteritz and Bäuerle 2006) went one step further into the electronic characterization of the complex formation. Figure 4a shows two STS curves, before and after adsorption of the C_{60} onto the macrocycle, giving evidence of the formation of the complex (**Figure 1-4a**). Moreover, Lee and co-workers(Yang, Chang et al. 2007) have recently shown that, when using pentacene as the electron donor and depositing C_{60} on top of it, a marked rectifying behaviour is observed. No apparent contribution of the LUMO of C_{60} to the resonant tunneling at positive sample biases is present (**Figure 1-4b**, the STM image shows only the first pentacene layer). It is expected that such kind of architectures will become more and more routinely during the next few years, following the prototype rectifier described by Aviram-Ratner (Aviram and Ratner 1974) for the creation of 2D molecular diodes (Dorogi, Gomez et al. 1995; Mujica, Kemp et al. 1996; Joachim, Gimzewski et al. 2000; Metzger 2008). Moreover, two-layered architectures are of special interest to the field of nanomechanical transistors (NMT)(Joachim, Gimzewski et al. 1998), where switching of a molecular transistor may be accomplished by mechanical compression of C_{60} using the STM tip apex.

To date, one prototype molecular transistor at the solid-liquid interface has been reported by Rabe and co-workers (Jäckel, Watson et al. 2004). In a first step, a molecular dyad(Tchebotareva, Yin et al. 2003; Samorì, Yin et al. 2004; Surin and Samorì 2007; Mativetsky, Kastler et al. 2009) consisting in HBC decorated with anthraquinone substituents is used to pattern a surface. When an electron donor (9,10-dimethoxyanthracene) is added to the supernatant solution, a domain where the electron donor forms a complex with anthraquinone appears, corresponding to the STM image in **Figure 1-4c**. When STS is performed directly on top of the HBC in both domains, a significant difference is observed in the domains where the 9,10-dimethoxyanthracene was co-adsorbed, which exactly corresponds to the newly induced surface dipoles.

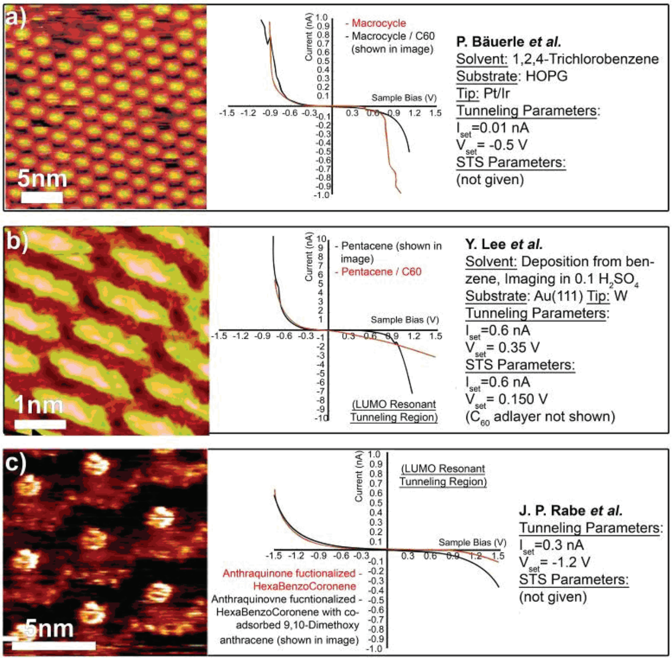

Figure 1-4
STM images and related packing models showing patterns of (a) a thiophene-containing macrocycle where C_{60} has been added (b) a pentacene monolayer (c) an HBC-Anthraquinone based prototype molecular transistor

1.1.2 Through Hydrogen Bonds

A widely employed non-covalent interaction in supramolecular chemistry is hydrogen-bond. This interaction type is unique: it offers a high level of control over the molecular self-assembly process, since it combines reversibility, directionality, specificity and cooperativity (Brunsveld, Folmer et al. 2001; Sherrington and Taskinen 2001; Greef and Meijer 2008; Ciesielski, Schaeffer et al. 2009).

H-bonding interactions benefit among all from a wide range on interaction energies, depending on the number and position of consecutive strong hydrogen-bond donor (D) and acceptors (A) moieties. Jeffrey (Jeffrey 1997) reported that the energy per single A---D pair in the solution quantified by typical methods like NMR or UV-Vis amounts to 1.0 - 1.4 kcal/mol per hydrogen-bond. In the case of three parallel H-bonds in ADA---DAD pairs, *ab initio* calculated interaction energies can rise to 18 kcal/mol (Palma, Bjork et al. 2009) and up to 26 kcal/mol in DDD-AAA pairs (Murray and Zimmerman 1992; Djurdjevic, Leigh et al. 2007). For four consecutive H-bonds, AADD---DDAA (i.e. a tetra-hapto moiety) in ureidopyrimidone dimers (Söntjens, Sijbesma et al. 2000;

Lukin and Leszczynski 2002), the association energy gives a record value of 47 kcal/mol.

In particular, the association of H-bond molecules bearing complementary recognition groups is the most straightforward pathway for pre-programming network self-assembly of extended architectures (Fouquey, Lehn et al. 1990; Lehn 1995), both in solution and in the solid state (Fan, Vicent et al. 1994; Macdonald and Whitesides 1994; Subramanian and Zaworotko 1994). In the solid liquid interface however, the formation of extended self-assembled architectures has been widely limited to monocomponent self-assembly, with few examples on the formation of bi-component extended architectures.

Monocomponent Self-Assembly of extended 2D H-bond architectures. While there is a rich plethora of self-recognition H-bond moieties, ranging from lactams (Mourran, Ziener et al. 2006) to quadruple bonds (Gesquiere, Jonkheijm et al. 2004), the hydrogen-bonding among two adjacent carboxylic acids is the most widely used di-hapto H-bond type for pre-programming 2D networks (Lackinger and Heckl 2009). Many groups (Lackinger, Griessl et al. 2004; MacLeod, Ivasenko et al. 2007; Blunt, Russell et al. 2008) have reported systems relying on such a di-hapto recognition at the solid-solution interface. Among them, Lackinger and co-workers (Lackinger, Griessl et al. 2004) showed the formation of linear polymer arrays by the deposition of an isophthalic acid (1,3-benzene-dicarboxylic acid) solution in heptanoic acid onto HOPG surface (**Figure 1-5a)**. Interestingly, out of the same simple principle a wild diversity of extended architectures can be unveiled, going through quasicrystals (**Figure 1-5b)**, “flower” crystals (**Figure 1-5c)** and crystalline networks (**Figure 1-5d)**.

In quasicrystals, Beton and co-workers (Blunt, Russell et al. 2008) have shown that terphenyl-3,5,3’,5’-tetracarboxylic acids (TPTC) arrange without translational symmetry but featuring a hexagonal superstructure (**Figure 1-5b**). The star-shaped structures (highlighted in the square) represent one among five possible arrangements of TPTC molecules. The previous is a clear example of supramolecular polymorphism. Polymorphism may arise in carboxylic acids also from the possibility of trimerization of carboxylic acids on surfaces. For instance, pure trimesic acid regions based on trimerization of the carboxyl moieties may form two polymorphs: the chicken-wire and the “flower” structure (**Figure 1-5c**). Furthermore, the “flower” phase may host ‘guest’ C_{60} molecules within their pores whereas the TMA/alcohol bicomponent network does not offer any stable adsorption site for the C_{60} molecules (MacLeod, Ivasenko et al. 2007).

Interestingly, the selectivity of one polymorph among others may be modulated by the choice of the solvent. Lackinger and co-workers described this phenomenon in the 2D pattern formation of 1,3,5-benzenetribenzoic acid (BTB)(Kampschulte, Lackinger et al. 2006). Depending on the ability of the solvent to hydrogen-bond the solute molecules, either an oblique or a hexagonal lattice for BTB was observed, with the former structure exhibiting rectangular pores and the latter exhibiting hexagonal pores (**Figure 1-5d,e).**

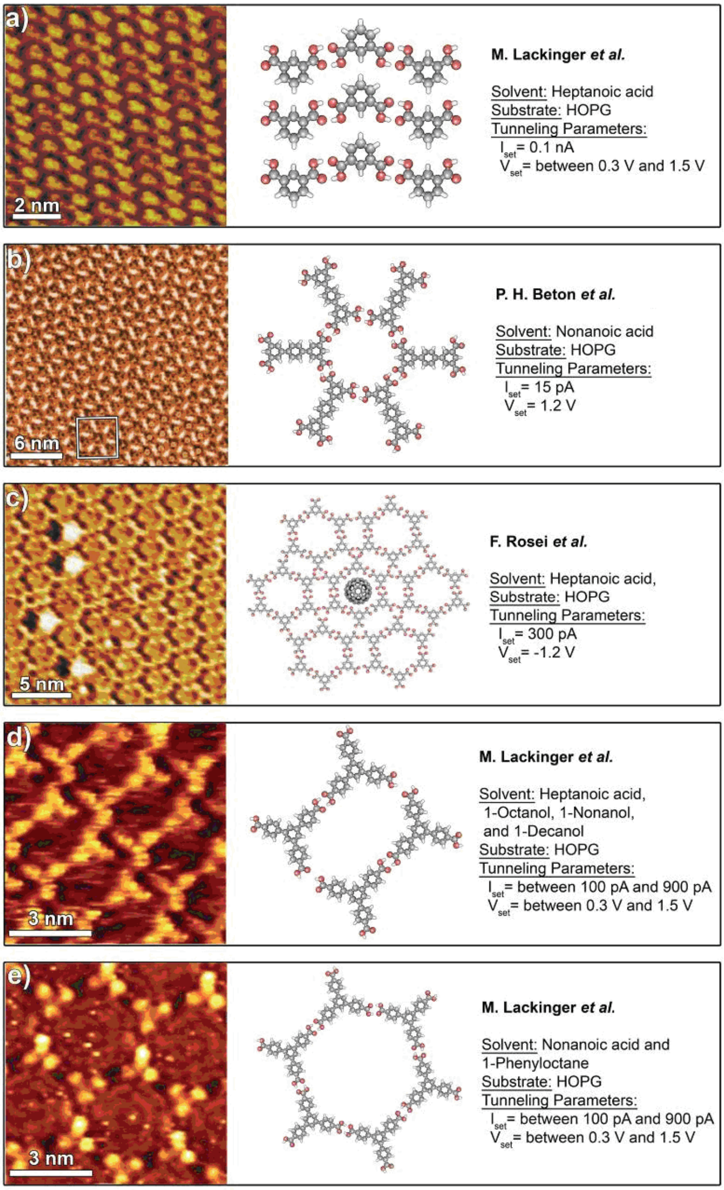

Figure 1-5

STM images and related packing models showing patterns and parameters of (a) orto-phtalic acid (b) a tetra-carboxylic acid moiety (c) trimesic acid (d) one polymorph of a tri-carboxylic acid derivative and (e) a second polymorph of the previous derivative.

Bi-component Self-Assembly of extended 2D H-bond architectures. The present work focusing in the formation of bi-component architectures, it is of key importance to understand the state of the art in bi-component self-assembly. Astonishingly, to our best knowledge, only two reports describe bi-component networks formed at the solid-liquid interface. The bi-component network of 1,3,5-tris(4-pyridyl)-2,4,6-triazine (TPT) and trimesic acid (TMA) with a 6-fold symmetry has been described by Lackinger *et al.*(Kampschulte, Werblowsky et al. 2008). **Figure 1-6a** depict a STM image where the single TPT molecules appear as a triangle with a central depression and pores are readily evidenced featuring screeches which might stem from a transient adsorption of guests (either TMA, TPT, or heptanoic acid molecules). The second example in **Figure 1-6b** originates from the assembly of melamine and PTCDI in dimethyloformamide allowing for the formation of a bi-component supramolecular network (Madueno, Raisanen et al. 2008). While such templating approach was demonstrated in the seminal work by Beton and coworkers under UHV conditions (Theobald, Oxtoby et al. 2003), its feasibility under ambient conditions for technological applications has not been yet reported.

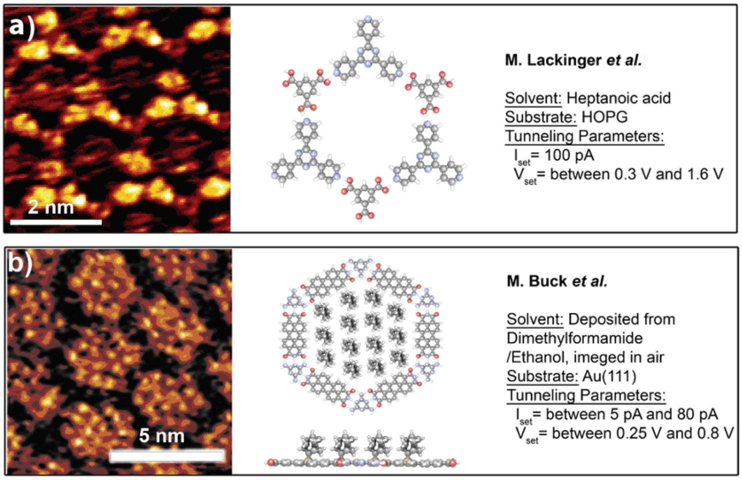

M. Lackinger *et al.*

Solvent: Heptanoic acid
Substrate: HOPG
Tunneling Parameters:
I_{set}= 100 pA
V_{set}= between 0.3 V and 1.6 V

M. Buck *et al.*

Solvent: Deposited from Dimethylformamide /Ethanol, imeged in air
Substrate: Au(111)
Tunneling Parameters:
I_{set}= between 5 pA and 80 pA
V_{set}= between 0.25 V and 0.8 V

Figure 1-6

STM images and related packing models showing patterns and parameters of (a) a trimesic acid plus pyridine-like bi-component system and (b) a melamine plus perylene tetracarboxylic di-imide porous network.

To date, no examples of tri-component H-bond architectures have been given in the literature at solid-liquid interfaces, nonetheless (Madueno, Raisanen et al. 2008) have used the aforementioned strategy to successfully template a variety of host molecules. Upon addition of adamantine thiol on top of melamine/PTCDI network, the generation of hybrid chemisorbed /physisorbed structures was achieved, which at the same time constitutes the highest resolution chemical lithographic method ever reported. While the last system maybe considered one of the few examples of tri-component self-assemblies in the literature, we have showes that De Feyter and co-workers reported a tetra-component architecture held by vdW interactions (Adisoejoso, Tahara et al. 2009).

In summary we have evidenced the ongoing effort in the literature to control intermolecular forces in order to create multi-component self-assembled architectures. Such investigations represent the first steps in the new field of Supramolecular Engineering, notions of which we will introduce in the following Chapters.

2 Methods

Theoretical and experimental methods are the fundamental tools in the assembly of extended architectures at surfaces. In the first row stand the techniques which allow extracting order parameters at the (supra)molecular level, thus correlating the phase structure with intra and intermolecular geometries. In two dimensions, and more precisely on conducting solid interfaces, this tool is undeniably the scanning tunneling microscope (STM). In order to provide unambiguous structural information, the STM must be imperatively complemented with a theoretical technique so that accurate correlation of the molecule's geometry may be mapped into the current or height feedback space outputted by the STM. Such limitations make density functional theory (DFT) and molecular dynamics (MD) mandatory complementary techniques for such spatial architectonic investigation. At the same time, diffraction and photophysical measurements may give additional quantitative information about intermolecular geometries. However their technological adaptation *in situ* to the solid-liquid interface, in both sensitivity and robustness, is yet to be optimized. On the other hand, supramolecular engineering relies in the prediction of the final structure from initial disposition of molecules in a state. Assuming classical determinism, molecular dynamics is the only candidate for the task. Within our century's technological limitations, the description of full systems by molecular dynamics relies in parameterization of Newton's equations of motion. Such parametrization may only be obtained from high-quality ab-initio data or thermochemical data. Again, in the view of the technological dependence of the previous, thermochemical methods constitute an important tool for supramolecular engineering. Moreover, Supramolecular Engineering being a new field of research, new methods must be adapted to work in dynamic environments (solid-liquid interfaces) where both design and self-assembly of the supramolecular architecture may be monitored.

In the following chapter we will briefly establish the ground of Scanning Tunneling Microscopy (STM), Density Functional Theory (DFT), Molecular Dynamics (MD) and Isothermal Calorimetry (ITC) and also show practical examples on new methodology for the characterization of Supramolecular Architectures in Supramolecular Engineering.

2.1 Tunneling Microscopy (STM)

The need for exploring ordered architectures at the molecular scale has made Scanning Tunneling Microscope (STM) (Binnig, Rohrer et al. 1982) a widely employed, though extremely powerful tool to study supramolecular assemblies at interfaces with a sub-molecular resolution (Cyr, Venkataraman et al. 1996; Elemans and De Feyter 2009; Yang and Wang 2009). Moreover, as previously introduced, STM investigations may provide electronic and thus chemical (Piot, Bonifazi et al. 2007) insights on the sub-nm scale.

Theory. The working principle of STM is the tunnelling of electrons from a sharp scanning tip to a substrate **Figure 2-1**.

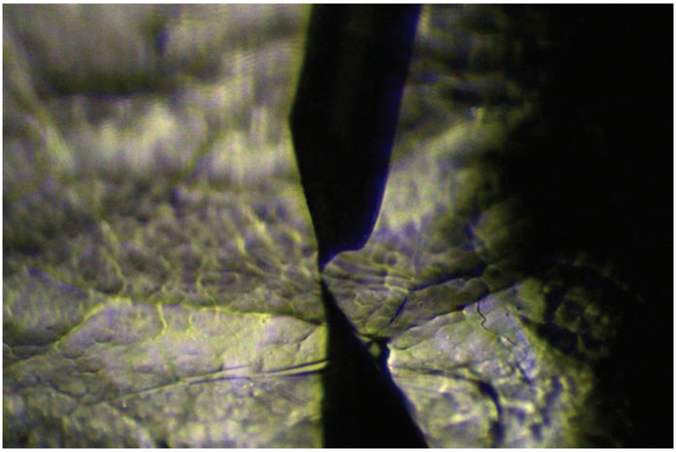

Figure 2-1
A mechanically cut Pt/It (80:20) Goodfellow STM wire (0.250mm in diameter) at a few micrometers from a highly oriented pyrollitic graphite HOPG *ZYH Material Quartz* substrate. This setup is used through out the present work.

Electron tunnelling as termed by Schottky (Merzbacher 2002) is above all an empirical observation. In the early 1900's Hobbs, Kinsley, Earhart among others (Millikan and Eyring 1926) carried out experiments which proved that electrons could be pulled out of cold metals through intense electric fields. In 1926 Millikan and Eyring (Millikan and Eyring 1926) established the first relation of the current from tunnelling electrons with the field strength;

$$I = C_0 \exp\left(-\frac{a}{F} \right)$$

Equation 2-1

where C and a are constants and F is the electric field strength. Note that by strong fields, Millikan meant 1-7(x10^6 V/m) at ~1 cm apart electrodes, a field that is now considered small when compared to the fields in tunnelling microscopy, ~ 10^8 V/m (i.e. 0.1V at 1nm separation). Latter Nordheim and Fowler put forward a quantum mechanical formulation to explain this phenomenon (Fowler and Nordheim 1928). For sake of standard notation, we introduce at this point Nicol, Shapiro and Smith (Nicol, Shapiro et al. 1960) parameterization of electron tunneling;

$$I = a\int \rho_2(E-eV)\rho_1(E)dE$$

Equation 2-2

where a is a constant ρ_2(E-eV) is the density of states of one electrode up to a voltage (V) and ρ_1(E) is the density of states of the other up to an energy E. That same year, Bardeen interpreted rather obscurely the experimental results of Nicol et al. by comparing **Equation 2-2** with a Fermi's Golden Rule-like expression;

$$I = \frac{2\pi}{\hbar}\left|M\right|^2 \rho_f$$

Equation 2-3

where M is the transition matrix element and ρ_f is the final density of states. Today, the interpretation of **Equation 2-2** and **Equation 2-3,** for instance by Lang (Lang 1986), gives the generalized form of uni-dimentional tunneling, combining **Equation 2-2** and **Equation 2-3**;

$$I = \int T(E)\rho_2(E-eV)\rho_1(E)dE$$

Equation 2-4

where we have set *T(E),* the transmission probability, equal to the modulus square of the matrix element. In this convenient form, the transition element can be calculated through any desired formalism, for instance the WKB formalism (Bransden and Joachain 2000) which accounting for the shape and height of the tunnelling barrier gives;

$$T(E) = \exp\left(-2\int_{x_2}^{x_1}\left(\frac{2m(V(x)-E)}{\hbar^2}\right)^{1/2} dx\right)$$

Equation 2-5

where *m* is the mass of the electron, and in the case of a metal, E is the Fermi level E = E_F = V(x) – W; where W is the work function of the metal, for equal electrodes. In the case of a triangular barrier, the original Nordheim and Fowler 1928 result can be recovered. When the barrier's potential shape is squared (constant) V(x)=V_0 (i.e. the potential of electrons in vacuum) the quantity in the inner parenthesis is named the decay length in vacuum kappa (κ). As we can see, both previous equations have a curious relation with the length of the barrier, x_2-x_1 (also dissimulated in the constant *a* of **Equation 2-1**). It was not until the seminal introduction of the STM work by Binnig, Rohrer, 1982 that this distance dependence, *z*, finally became evident in experiment,

$$I = C_0 \exp\left(-\alpha z\right)$$

Equation 2-6

Notice that in this equation "α" is exactly equal to (κ/2) if there is a vacuum gap in between, whereas it can be renamed as molecular attenuation factor $-\beta$ when the gap is filled by a scattering material such as a molecule (Fan, Yang et al. 2002). Shortly thereafter, Tersoff and Hamman (Tersoff and Hamann 1985) gave an analytical expression for the puzzling STM lateral resolution;

$$I = 32\pi^3\hbar^{-1}e^2V_tW^2D_{tip}(E_F)R^2\kappa^{-4}e^{2\kappa R} \times \sum_v \left|\psi_v(\vec{r_0})\right|^2 \delta(E_v - E_F)$$

Equation 2-7

where V_t is the applied bias, *W* is the work function, $D_{tip}(E_F)$ is the density of states of the tip at the Fermi energy E_F, κ is the decay length in vacuum, R is the radius of curvature of the tip, ψ_v are the wavefunctions of the substrate at the position of the centre of curvature of the tip r_0 , and E_v is the ground state energy (in absence of tunnelling) of the substrate. Note that the summation term is the only term dependent on the molecular nature, since it is exactly equal to the local density of states (LDOS) of the substrate, which in the case of adsorbed molecules is the system composed by molecule+substrate. However, such a raw approximation only holds for equilibrium conditions, i.e. the result comes out following Bardeen's assumptions and assuming low biases ~10mV. Nowadays, tunnelling is better regarded in terms the scattering theory of transport, following the 1952 development of Landauer (Landauer, 1952);

$$I = \frac{2e}{h}\int_{-\infty}^{+\infty} dE\ T_{qp}(E)f_p(E) - T_{pq}(E)f_q(E)$$

Equation 2-8

where *T* are transmission elements from the electrode *p* to *d* and vice versa, but now in the form of a matrix to account for multiple energy channels and not one-dimensional like the previous cases. The respective Fermi functions at each electrode $f_q(E)$ and $f_q(E)$ will be populated up to an energy once a bias is applied. However such an approach is not as popular in the literature due to its increased complexity (Datta, Tian et al. 1997; Joachim and Ratner 2005; Joachim and Ratner 2005).

Technical details. Because the tunnelling current is proportional to the amplitude of the molecular states of the molecule+substrate system within an energy range close to the energy of the upper valence orbitals (Tersoff and Hamann 1985), the STM contrast output in the so called “constant (tip) height” mode will appear higher amongst valence electron-rich aromatic molecules than valence electron-poor aliphatic groups. There is however some obscurity surrounding the previous statement of “constant height” mode. In fact it sounds very hard to believe that an atomically sharp tip may be allowed to scan thousands of points during ~100nm scans at a constant separation from the surface without an effective feedback system. In practice it is the “feedback image” and not a “constant height” image the real output, which tries to follow an iso-current countour. The “constant height” image is in fact the feedback complementary image, more correctly called, the “current error” image, since we will see in equation **Equation 2-9** that is the quantity measured in order for the feedback to respond. When the current error image tends to zero the feedback image is a true “constant current” image, i.e. the piezo reacts immediately to the changes of current to follow an iso-current path, so that we follow exactly the contour of one electronic state or orbital, allowing the imaging of molecular orbitals. Such an ideal image may be obtained in some ideal condition cases and under very slow scanning (Pascual, Gomez-Herrero et al. 2000). At the solid-liquid interface however, and in most STM equipment, the “current error” image is very different from zero since the electronics cannot adapt instantly to the changes in current. Moreover the feedback image responds dominantly not to the current error, but by the response of the *current integral* which is the time average of the difference between the instantaneous current (*I*) and the current set point (I_t) i.e. and average current error. The first term of the analogical **Equation 2-9** for an APE Research STM (page 50 of SPM Control System Program, Version 6.4.1 Rev2/2009), shows the current integral, along with a second term which is proportional to the current error;

$$Z = G\int_{t_2}^{t_1} \left(I - I_t\right)dt + P\left(I - I_t\right)$$

Equation 2-9

where *Z* is the response of the piezo in volts, *G* is a tunable parameter called the integral gain and *P* the proportional gain. In addition, the feedback system in the

STM equipment used through out the present work, a Veeco multimode with a Nanoscope III controller, works through a logarithmic feedback, such that,

$$Z = G\int_{t_2}^{t_1} \log\left(I - I_t\right)dt + P\log\left(I - I_t\right)$$

Equation 2-10

Note that such **Equation 2-10** was inferred from the Veeco Multimode Manual rev B, so that it should be used with caution (multiple attempts to contact Veeco personnel failed in order to verify **Equation 2-10**). Such a logarithmic feedback translates into big oscillations of the tip so that the images in this work barely resemble a true “constant current” image.

Conditions. STM imaging can be in principle performed in almost any solvent, as long as Faradaic and capacitive currents are minimized. This can be achieved by insulating the STM tip through the use of coatings or by using low-dielectric media, allowing to work in the picoampere regime. Some of the most common solvents used when picoamperes currents are sought are 1,2,4-trichlorobenzene (TCB), heptanoic acid, 1-phenyloctane, n-tetradecane and 1-octanol, with relative dielectric constants near 2.5 (2007). On the other hand, when working in aqueous or in other high-dielectric media, it is common to use a reference electrode and an insulated tip. This setup is usually termed an Electrochemical STM (ECSTM, not to be confused with SECM, Scanning Electrochemical Microscopy) (Wiesendanger, Guntherodt et al. 1992; Itaya 1998).

2.1.1 Scanning Differential Tunneling Microscopy (SDTM)

It was readily introduced that semi-quantitative measurements on the electronic structure of the molecules can be obtained by means of Scanning Tunneling Spectroscopy (STS), a mode which consists of obtaining characteristic instant current/ bias voltage curves (I/V), so probing the elastic tunnelling changes associated with the surface/molecule local density of states (LDOS) (Samorì and Rabe 2002; Hipps and Scudiero 2005; Hipps and Vij 2006). This method was successfully employed to investigate on isolated molecules various phenomena such as charge-transfer, (Jäckel, Perera et al. 2008) rectification (Joachim, Gimzewski et al. 2000; Jäckel, Wang et al. 2004) and switching (Jäckel, Watson et al. 2004). Nonetheless, the analysis of STS remains semi-quantitative because it can vary enormously from measure to measure and is very sensitive to tip height. One alternative is to obtain the Differential Tunneling Spectra, which is the derivative of the current with respect to the voltage, dI/dV. Such a technique gives quantitative information when performed in ideal conditions which implies low temperatures and vacuum conditions (Grobis, Khoo et al. 2005; Grobis, Wachowiak et al. 2005). However, at the solid-liquid interface, it does not offer significant advantage, since the drift of the tip and the changing conditions in a solvent would not offer any advantage over STS. An alternative is what we term Scanning Differential Tunneling Microscopy (SDTM), which would allow obtaining full images at specific "positions" (corresponding to the dI/dV amplitude at an specific bias) of the current derivative curve dI/dV. Besides the reproducible information, the interpreration of the derivative of the current is important since it is related, in the weak coupling regime, i.e. the Tersoff-Hamman approximation and the WKB approximations, to the molecular density of states, derivating **Equation 2-7**;

$$\frac{dI(V,r)}{dV} \cong \rho(r,E)$$

Equation 2-11

This offers a tremendous advantage since in an image, quantitative information on the molecular orbitals can be obtained. We remark however that **Equation 2-11** is an approximation that no longer holds in the case of strong coupling where a more developed expression must be obtained through other formalisms.

Although in theory, the derivative of the current seems a naïve numerical quantity to obtain, in practice it is extremely difficult and full of caveats. Numerical derivation of a I/V characteristic is nearly imposible without means of reducing the noise from point to point, and fitting of the curve will cause losing of quantitative features. Indeed, what follows is an effort to shed light into obtaining dI/dV curves, which should be taken as an experimental procedure in progress. The first thing we need to tackle is the noise problem. This can be done through a lock-in amplifier or in other words an instrument including a *phase sensitive detector* (PSD). A PSD not only detects small voltage signals (V_{sig}) but does it in a way where we can directly obtain a signal that approximates closely and analogic dI/dV signal. Consider the lock-in amplifier Standford instruments SR810. When we apply reference AC signal, V_{ref} sin(wt+ θ_{ref}) and use it to "lock" (by means of wave multiplication) its frequency to that of a signal of interest V_{sig} sin(wt+ θ_{sig}) we obtain a PSD output voltage;

$$V_{PSD} = \frac{1}{2} V_{sig} V_{ref} \cos(\theta_{sig} - \theta_{ref})$$

Equation 2-12

where V_{PSD} is a DC output signal, V_{ref} is the amplitude of a reference AC signal created internally by the lock-in at a frequency of interest, V_{sig} is the amplitude of our signal of interest at the reference frequency and θs are their respective phases (the equation is taken from the revision 1.8 01/2005 of the SR810 manual). In fact, when we maximize the output signal by “playing” with the reference phase θ_{ref}, the cosine expression is 1 and the output signal is our signal of interest at the reference frequency, provided that the amplitude of our AC reference signal is small;

$$V_{PSD} \approx \frac{1}{2} V_{sig};\ V_{sig} >> V_{ref},\ \theta_{sig} = \theta_{ref}$$

Equation 2-13

Now we know that the lock-in coverts an AC signal into a DC one. Let’s turn to our I/V curve. Around a point V_0 we can express a I(V) through the taylor expansion as;

$$I(V) = I(V_0) + \frac{dI}{dV}(V - V_0) + \frac{d^2 I}{dV^2}(V - V_0)^2$$

Equation 2-14

Now if our I/V curve contains an AC signal of amplitude V_1 with an offset such that $V = V_0 + V_1 \sin(wt)$ we obtain from the previous equation,

$$I(V) = I(V_0) + \frac{dI}{dV} V_1 \sin(wt) + \frac{d^2 I}{dV^2} V_1^2 \sin(wt)^2 + \ldots$$

Equation 2-15

In a second approximation, we hope that if we apply a reference voltage $V_{ref} \sin(wt)$ it will be exactly equal to $V_1 \sin(wt)$. Indeed the applied $V_{ref} \sin(wt)$ signal will serve both as the biasing signal and the PSD reference. Considering the previous, a comparison of **Equation 2-13** and **Equation 2-15** results in;

$$V_{sig} = \frac{dI}{dV} \Rightarrow V_{PSD} \approx \frac{1}{2}\frac{dI}{dV}$$

Equation 2-16

where we note that the last term in **Equation 2-15** translates as a higher harmonic with a different frequency so is not considered (“locked”) by the PSD. Everything up to now assumes two rather safe approximations for obtaining dI/dV directly from the PSD output. There is however two other important considerations: the technical nature of our PSD and the sample conditions. These two are restrained around one variable, which is the frequency of the reference signal applied and detected. First we should establish the minimum working frequency. Indeed, for the ultimate goal of SDTM. The intuitive minimum working frequency corresponds to the one period of the minimum pixel acquisition rate of the image’s scan;

$$\text{inv. scan rate}\frac{[s]}{[nm]}\bullet\text{scan size}\frac{[nm]}{[line]}\bullet\text{resolution}\frac{[line]}{[pixels]}=\text{inv. pixel rate}\frac{[s]}{[pixel]}$$

Equation 2-17

Knowing that minimum scan rate is between 400-600 nm/s, we obtain for a typical 20 nm^2 image a pixel rate of ~100μs/pixel. The lock-in works by integrating the signal over the frequency's period. Knowing that at least 10 periods are needed to obtain a good signal, we need a frequency's period of at least 10μs which translates into a PSD able to work at an applied signal frequency of 100kHz. Besides the choice of a PSD that can work at such high frequencies, most STM equipments must be modified to work at high frequencies without perturbing the feedback system. **Figure 2-2** shows the high-impedance circuit used to decouple the instant current signal (V_{out1}) from the input signal for the external lock-in amplifier (V_{out1}). Also the lock-in reference AC signal V_{ref} sin(wt) must be summed with the normal tunneling bias V_t, via the circuit shown in **Figure 2-3**.

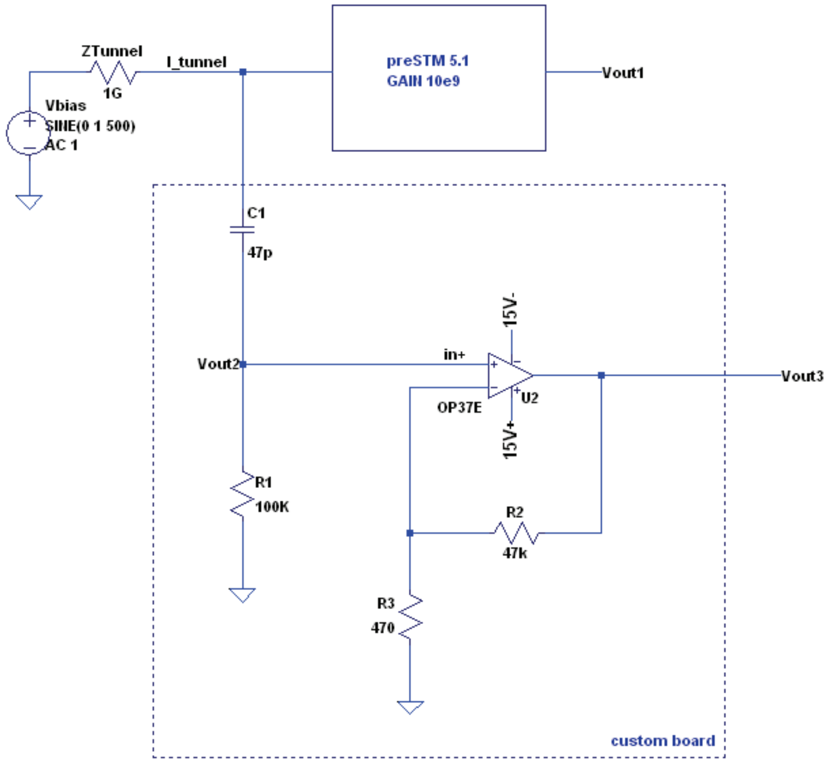

Figure 2-2

Circuit used for decoupling the instant current signal (V_{out1}) from the input signal of the external lock-in amplifier (V_{out3}). The simulation in the respective section of the **Appendix** shows that there is a linear response of the circuit when a 1V reference AC signal, $V_{ref}\,\sin(wt)$, between 1KHz to 100KHz, is applied, using 1GOmhs as a tunnelling resistance. However this behaviour is lost when the tunnelling junction contains a capacitance higher than ~1fF. Courtesy of Stefano Prato, APE Research 2010.

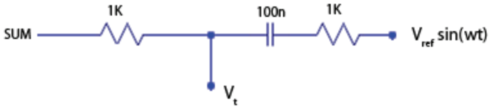

Figure 2-3

Sum circuit for the applied reference signal and the tunneling voltage V_t, such that the applied $V_{ref\text{-}lockin}$ sin(wt) lock-in reference is decrease in amplitude by 96% at 100KHz frequencies. All the values of V_{ref} presented are final (SUM) values applied to the sample which have been corrected *a priori*.

With all the circuits and caveats disclaimed we give the first examples of the SDTM performed at the solid-liquid interface. We use as a first model system highly oriented pyrolytic graphite (HOPG) in 1,2,4-trichlorobenzene solvent (TCB). **Figure 2-4** shows three dI/dV curves acquired during a period of 1h at a set point I_t = 100pA and V_t=100mV. The curves are taken with an integration step of 30ms and 20 averages. Notice the sensitivity of the technique, which besides a consistent trend shows some reproducible features. These features are quantitative characteristics of the system used, and do not belong to graphite *per se*, as we have observed in >100 curves of at least 10 different experiments.

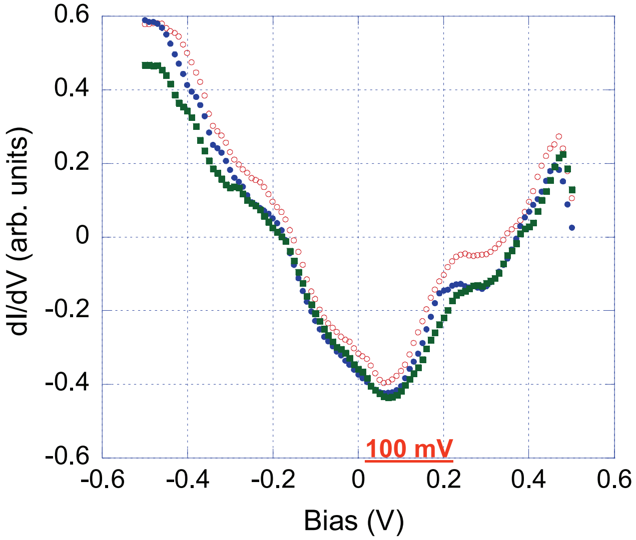

Figure 2-4

Differential dI / dV spectroscopy of HOPG in TCB. I_t = 100pA V_t = 100mV. Modulation Current V_{ref} = 2mV @ 100KHz integration timestep 30ms.

Empirically, the feature that does belong to graphite in **Figure 2-4** is the basin point around 100mV. In fact, such point was present in ~90% (out of hundreds) of dI/dV obtained for the HOPG/TCB system. An important interpretation of the basin point is given when we scan the graphite at that same point. **Figure 2-5** shows the feedback ("topology"), current error and differential tunneling images of HOPG. The feedback gain is set close to zero for the acquisition, to obtain a "constant height" image, although the top left feedback image still features some residual typicall HOPG contrast. The dI/dV image clearly seems to follow the current constrast. Strikingly, it does so only at 100mV bias, which is an interesting phenomenon supporting the evidence that the "basin" of the dI/dV curve corresponds to the HOPG density of states at the equilibrium energy (i.e. at the chemical potential of the system) and assuming a 0.8Å distance from the substrate (Cisternas, Stavale et al. 2009). We highlight that every other atom in graphite is better seen in the dI/dV image. Another important detail is that the image is scanned at 1ms integration timestep. The images' pixel rate is close to 0.2ms per pixel so that an integration timestep of 0.3ms would be already sufficient. However the image is still too noisy at those timesteps and typical 1ms integration timesteps are used.

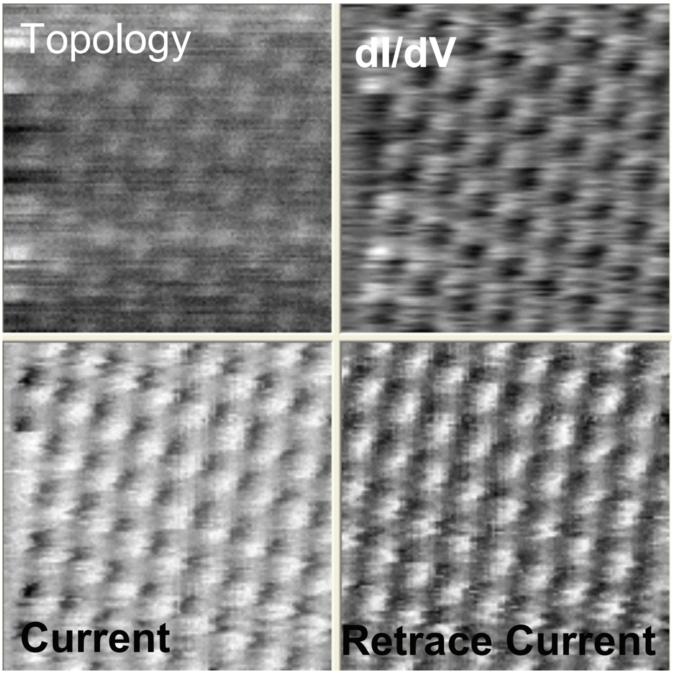

Figure 2-5

Scanning Differential Tunneling Microscopy (SDTM) image of HOPG in TCB solvent. I_t = 100pA V_t = 100mV. Modulation Current V_{ref} = 2mV @ 100KHz with an integration timestep of 1ms.

To finalize we show how the technique can be applied to improve the understanding of a system. The copper phtalocyanine compound **Molecule 1** has been studied at the HOPG/TCB interfase by STM **Figure 2-6**. Preliminary dI/dV spectroscopy over the molecule shows that there is a strong peak at negative biases, -900mV (**Figure 2-7**). It is important to note that at this negative bias at I_t=120pA both topology and current images have no signal. Performing differential tunneling imaging (SDTM) at that bias shows a very localized contrast arising from the metal center of the molecule. On the other hand, if we perform SDTM at biases where the dI/dV is essentially flat (at -450mV and 450mV), we recover the same differential (with noise) contrast as in normal

STM, **Figure 2-6**. Note that the SDTM at -450 and +450mV performed on a “split” image, i.e. first half of the scanning area at one voltage, shows great differences in the current image but not in the SDTM image, as we expect.

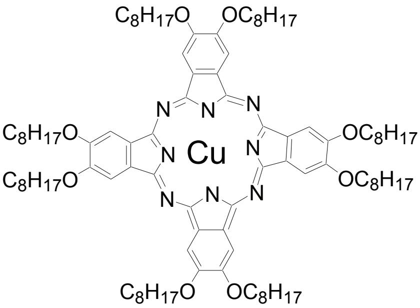

$C_{96}H_{144}CuN_8O_8$
Mol. Wt.: 1601.77

Molecule 1

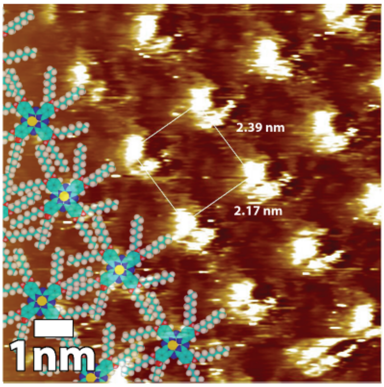

Figure 2-6
STM image of **Mol 1** in TCB. I_t = 26pA V_t = 472mV

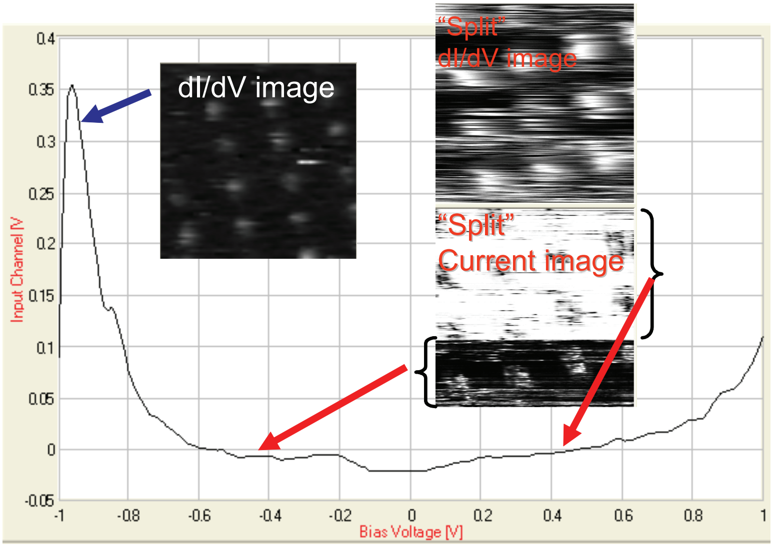

Figure 2-7
Scanning Differential Tunneling Microscopy (SDTM) images embedeed in an dI/dV curve of **Molecule 1** in TCB solvent. I_t = 120pA at V_t -900mV and I_t = 56pA at V_t = -450mV and 450mV (red arrows). Modulation Current V_{ref} = 4mV @ 100KHz with an integration timestep of 1ms and 12dB filter. Image sizes are 10x10nm^2 with a resolution of 256pixels/lines.

2.2 Density Functional Theory (DFT)

Density functional theory (Kohn and Sham 1965) is today the most straightforward and powerful technique to use in conjunction with experimental methods for the analysis of molecular architectures. DFT is in particular powerful in STM and Photophysical investigations. Since STM cannot usually resolve distances under 1Å, some DFT functionals can provide the geometrical accuracy to complement image interpretation.

In addition, DFT is a privileged technique in the simulation of electronic and vibrational spectra, thus becoming a key tool in *supramolecular engineering* for both its potential energy accuracy (which can be used in conjunction with other tools to predict the most stable architecture) and for the characterization of extended architectures via vibrational spectra. Indeed in this section we will witness how DFT may be used to interpret Infrared (IR) spectra and STM images and may be also used to predict adsorption energies on graphene. Moreover, in Chapter 4 we will use DFT to justify the origin of polygonal network formation and polymorphism and phase segregations, while on Chapter 5 we make DFT a point of depart for parameterizing molecular force field energies. In fact once the heaven of DFT is achieved, hybrid DFT/molecular dynamics will benefit from both the accurancy, speed and versatility of the applications of molecular dynamics that we will introduce in the next sections.

2.2.1 Projection of the Local Electronic Density of States

Following the Tersoff-Hamann approximation (Tersoff and Hamann 1983; Tersoff and Hamann 1985) we can extract and ideal case when the STM tip is replaced by a point probe, so the STM current is given simply by;

$$I \sim \sum_{v} \left| \psi_v(\vec{r_0}) \right|^2 \delta(E_v - E_F)$$

Equation 2-18

where ψ_v are all the surface states and r_0 the position of the ideal point probe (with delocalized states, i.e. no Fermi level), such that the current is the sum of the amplitudes of the wave function at the position of the probe, having energies between the state v and the Fermi energy E_F. We inmediatly recognize the right hand side of Equation 2-18 as the density of states at a point r_0 , i.e. the Local Density of States (LDOS). The projection of the LDOS in 2D from the “state of interest” until a certain Fermi energy will then represent a current approximation of the STM current image. Under the equilibrium approximations, the Fermi energy of the system may be approximated by the negative of the applied bias minus plus work function W of the substrate so that ($E_F = -(W + eV_t)$). The STM constant current images (**Figure 2-9**) shows a polygonal supramolecular structure of melamine H-bonded with its corresponding complementary linker, which we will further characterize in Chapter 4. It can be clearly seen that the melamine molecules appear as bright fuzzy spots. The STM image conditions were taken at V_t = -400mV. Under this conditions and assuming the substrates work function energy is ~4.5eV, the simulated image in the system can be acquired by **Equation 2-18** , through summation of the molecular orbitals between the energy E_v we are interested in and the Fermi energy -(4.5eV+400mV)=-4.9eV. **Figure 2-8** shows the energy diagram of the separate molecules and the periodic polygonal crystalline supramolecular structure (center **Figure 2-8**) in vaccum. The figures shows that there are no orbitals in the energy interval we are interested in, which is not surprising considering the calculations were done in vacuum and we assumed an approximated Fermi energy. However, we can see that the HOMO of the melamine molecule (in red) goes up in energy by ~ 200meV becoming -5.22meV with respect to the the vaccum level (**Figure 2-8** right axis), being only ~ 320meV away from the -4.9eV value we expected.

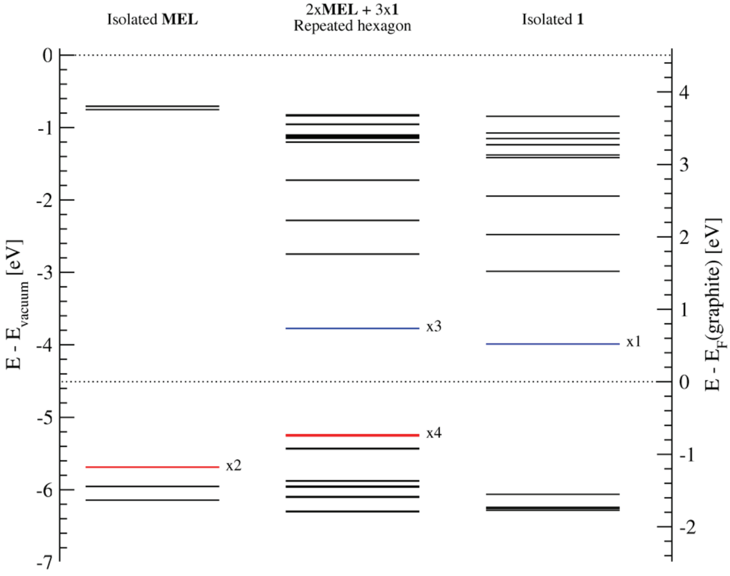

Figure 2-8
Energy level alignment of melamine (**MEL**), and a uracil-like linker (**1**) and a periodic structure of the linker melamine given relative to the respective vacuum level (left energy scale) and relative to the Fermi level of graphite at zero bias assuming the vacuum levels of the weakly physisorbed molecules are aligned with the one of graphite (right scale). The melamine HOMO levels are shown in red, whereas the linker LUMO levels are in blue.

Taking into account that in that region only the HOMO of melamine is closer to the expected value of E_F we may then proceed to simulate the image at $r_0 = 3Å$ above the plane of the molecules. **Figure 2-9b** shows this result, where the melamine molecules present a triangular shape. Unfortunately the resolution of the experimental image does not give a straightforward experiment/theory comparison because the molecules are imaged in room-temperature and at the solid-liquid interface. It is for this reason that the simulation of STM images in dynamic conditions is introduced in the next sections, implemented by Molecular Dynamics. Interestingly, the linker molecule (red) features orbitals densities from three degenerated states at 0.83eV above the work function of graphite, which means that is better imaged at positive biases.

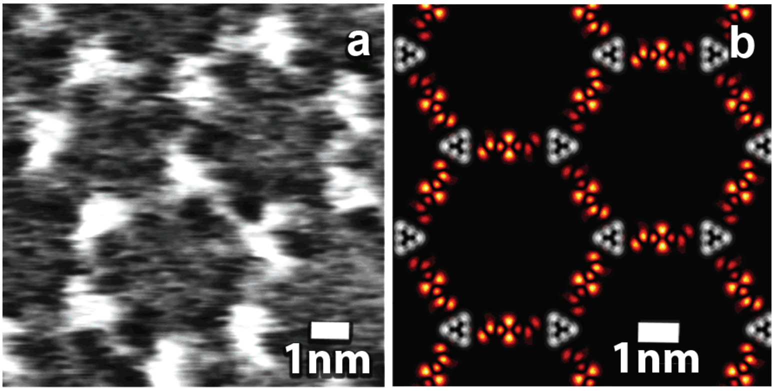

Figure 2-9
(a) Experimental and (b) Simulated STM image or a supramolecular network formed by melamine (cornerstone in white) and a uracyl-like linker.

2.2.2 Infrared Spectra in Network Formation

One sensitive and easily adapted technique at interfaces is Fourier transform infrared spectroscopy (FT-IR). Long-range vibrational states are unique in molecular architectures in the far infrared and terahertz regions. Thus the exact molecular geometry can be quantified and assigned to the coupled vibrational states characteristic of molecular architectures through DFT normal mode analysis. Here we exemplify this principle through the DFT analysis of a covalent molecular network. This first example differs from the focus of this work since the characterization of supramolecular architectures must be done *in situ*. Yet *in situ* characterization of supramolecular networks was unachievable due to limited resources. Thus we proceeded through the characterization of a covalent molecular network which could be formed in solution and precipitated as an amorphous solid. The reaction of **Molecule** 2 with pyromellitic anhydride **Molecule** 3 results in the formation of a polymer network **Network 1**, much like a “Kapton” network.

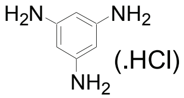

$C_6H_9N_3$
Mol. Wt.: 123.16

Molecule 2

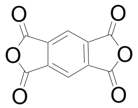

$C_{10}H_2O_6$
Mol. Wt.: 218.12

Molecule 3

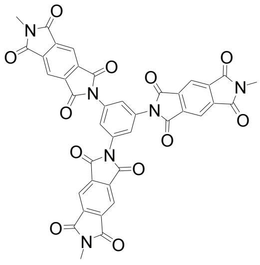

Network1

For the formation of the network polymer, reactions were optimized in 4mL of 30:70 solutions of TCB:DMF with concentrations and ratios ranging from 100µM-400µM at 80ºC for 24hours. The precipates obtained were washed with chloroform and dried under vaccum. **Figure 2-12** shows the IR spectra of the collected precipates in an optimized reaction. The optimized reactions showed no trace of the broad and intense ~3700 cm^{-1} peaks of **Molecule** 2 (**Figure 2-10)** nor of the anhydrade, **Molecule** 3 ~1900 cm^{-1} peaks (**Figure 2-11**).

As previously stated the use of DFT allows us to quantitatively elucidate the formation of a polymer network. However, as we note there are broad peaks in the experimental spectra of **Figure 2-12**, immediately suggesting the presence of many chemical species in the polymer. This means that only a qualitative interpretation of the network may be done at this point, although we expect that in the case of formation of a 2D crystalline or porous network the correlation between experiment and theory will be analytical. In view of the previous we only simulate the IR spectra at the DFT B3LYP/6-31g level (through the commercial package Gaussian '02) using the molecular fragment shown in **Figure 2-12** as a crude representation of the network and not of a periodic structure. Because of this, for sake of simplicity we removed the peaks from the theoretical spectra which clearly belong to the anhydrate in the molecular fragment. Also we note that all theoretical spectra have been offsetted (scaled) batochromically by ~10 to 100cm^{-1} to match the position of the experimental spectra. Unambiguous evidence of the reaction forming the di-imide in **Network 1** comes from the most intense theoretical peak, corresponding to the the N-C aromatic stretch at 1370cm^{-1} which matches perfectly the experimental peak. The second most intense theoretical peak at 1200 cm^{-1} corresponds to the concerted rocking of all the aromatic C-Hs in the fragment. As mentioned, this coincides with the hypothesis of multiple chemical species, since the concerted movement of C-Hs depends on the chemical environment thus broadening the experimental peak in the presence of an heterogeneous polymer composition.

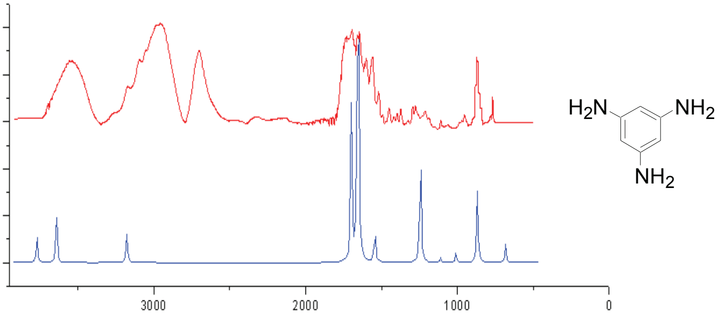

Figure 2-10

Experimental (red line) and theoretical (blue line) IR spectrum of **Molecule** 2. The DTF assignment reveals that the first two peaks ~3700 cm^{-1} correspond to the asymmetrical and symmetrical N-H stretching. The following peaks correspond to the scissoring of the N-Hs and stretching of the aromatic core.

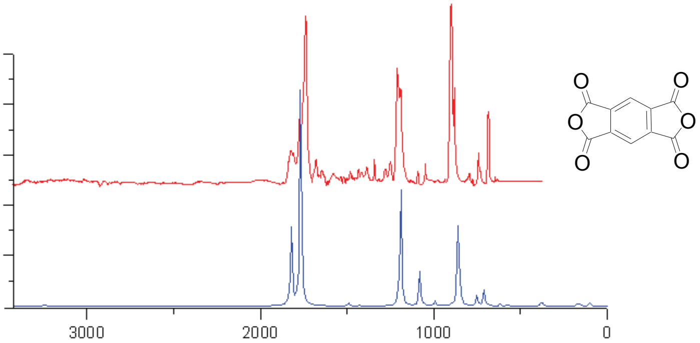

Figure 2-11

Experimental (red line) and theoretical (blue line) IR spectrum of **Molecule** 3. The assignment via DFT reveals that the first two peaks correspond to the symmetrical and assymetrical carbonyl stretching. The third peak at 1990 cm^{-1} corresponds to the coupled symmetrical rocking of the C-Hs while the second at 1077 cm^{-1} to the asymmetrical one. The 856 cm^{-1} is the assymetrical rocking of the C-O-C anhydrade group.

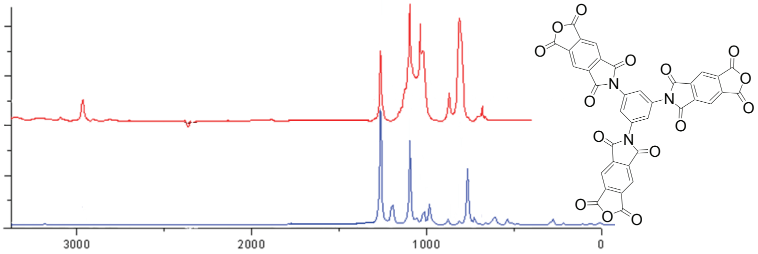

Figure 2-12

Experimental (red line) I.R. spectra of a 1:1 reaction precipitate of **Molecule** 2 with **Molecule** 3. The theoretical (blue line) IR spectrum corresponds to the network fragment shown.

In summary we expect DFT-resolved *in situ* infrared and terahertz spectroscopy to be ubiquitous techniques in the quantitative characterization of ordered 2D and 3D (supra) molecular networks.

2.2.3 **VdW-DF and Adsorption on Graphene**

In spite of the great advantages, DFT suffers up-to-date from a serious drawback; it cannot correctly estimate the dispersive contributions to the potential energy. The previous occurs since by definition, the long-range interactions between regions of poor electronic density vanish because of the exponential decay of electron densities, so that semi-local (Gradient Gradient Approximations) functional theories (Langreth, Dion et al. 2005) fail dramatically for systems where vdW-interactions are significant. Still, the efficient and accurate modeling of non-covalent interactions in large molecular systems remains an outstanding challenge. Their full quantification is at the very heart of subjects such as supramolecular engineering and medicinal chemistry. In these disciplines, the general concept of π–π stacking is used to describe the face-to-face stacking of aromatic systems involved in non-covalent interactions.

In such disciplines, general and exciting concepts are used to understand non-covalent interactions. For instance, it is popular to refer to the planar stacking of aromatic systems as π–π stacking (Hunter, Lawson et al. 2001; Meyer, Castellano et al. 2003; Grimme 2008). Such face-to-face stacking between (poly-)cyclic aromatic hydrocarbons (PAHs) is crucial since it confers unique physico-chemical properties to carbon-based materials, essential for applications in (opto-)electonics, photovoltaics, etc.

To tackle the mentioned drawback, in recent years, there have been many developments towards modeling dispersion interactions, based on both Density Functional Theory (Wu and Yang 2002; Rydberg, Dion et al. 2003; Dion, Rydberg et al. 2004; Grimme 2004; Johnson and Becke 2005; Ortmann, Bechstedt et al. 2006; Gulans, Puska et al. 2009; Pakarinen, Mativetsky et al. 2009; Tkatchenko and Scheffler 2009).These developments may be divided into two schools of thought: empirical and non-empirical. Ab-initio methods also exist (Sherrill, Takatani et al. 2009) but remain computationally too expensive to model large molecular systems. The empirical approach for treating dispersion forces, which is used in all atom force-fields, is a popular *a posteriori* correction to DFT. It involves the use of a pair potential analogous to those of molecular force fields , typically of the form;

$$V_{ij}(R) = C_{6,ij} f_{d,ij}(R) / R^6$$

Equation 2-19

between two atoms *i* and *j* at a distance *R*, to parameterize the dispersion interactions. However the choice and combination of the interaction coefficients $C_{6,ij}$ remain rather arbitrary, relying on atomic polarizability data (Wu and Yang 2002; Grimme 2004; Ortmann, Bechstedt et al. 2006), as well as effective atomic volume (Tkatchenko and Scheffler 2009), or self-consistency within thermodynamical and crystallographic data (Brooks, Bruccoleri et al. 1983; Mackerell, Wiorkiewiczkuczera et al. 1995; Halgren 1996; Ortmann, Bechstedt et al. 2006). Morevover, first-principles determination of the damping function $f_{d,ij}$ introduces an additional difficulty. A non-empirical approach to the dispersion problem is to develop a fully non-local density functional to fix the shortcomings of semi-local DFT. The most widely used formulation (Rydberg, Dion et al. 2003; Langreth, Dion et al. 2005; Gulans, Puska et al. 2009) is based on the revised PBE functional in which the correlation term is replaced by a correction based on the adiabatic connection formula (Zhang and Yang 1998). Such a van der Waals density functional (vdW-DF) was originally derived for layered structures and later on extended to general geometries (Dion, Rydberg et al. 2004).

In this section, we choose to compare the adsorption energies for twelve polyaromatic and five non-aromatic hydrocarbons calculated with the vdw-DF theory (in blue) (Kresse and Furthmuller 1996; Rydberg, Dion et al. 2003; Gulans, Puska et al. 2009), three empirical corrections to density functional theory (Wu and Yang 2002; Grimme 2004; Tkatchenko and Scheffler 2009) and two empirical force fields (Brooks, Bruccoleri et al. 1983; Halgren 1996). **Figure 2-13** shows the adsorption energy normalized per number of adsorbate carbon atom N_C versus the ratio of hydrogen to carbon atoms, N_H/N_C; by definition the latter is equal to 1 through the entire annulene series, while it vanishes when the number of hydrogens tends to zero as for graphene. The results indicate that all models can reasonably describe the data obtained from temperature programmed desorption experiments in ultra-high vacuum (Zacharia, Ulbricht et al. 2004), with the vdW-DF performing exceptionally well. Moreover, the data are well fitted by a linear regression of the normalized adsorption energies so that we can write down a straight forward ansatz for the binding energy of the aromatic compounds to graphene;

$$E_{bind} = N_C E_1 + N_H (E_2 - E_1)$$

Equation 2-20

where E_1 represents the fitted energy normalized per number of carbon of graphene and E_2 the fitted energy normalized per number of carbons of benzene. We note that from **Equation 2-20** it follows that the slope of the linear fits in **Figure 2-13** corresponds to E_2 - E_1, i.e., the difference in binding affinity between a partially saturated aromatic (or benzene-like) carbon and a fully unsaturated aromatic (or graphene-like) carbon.

Notably, the trends followed by all models in **Figure 2-13** are the same. For the empirical corrections (with one exception) this is to be expected (Grimme 2004) since the parameterizations consider only two atom types; one type of carbon and one type of hydrogen. However, for the vdW-DF and TS schemes the result is non-trivial since both depend on the electron density. Except for these two methods, the slopes in **Figure 2-13** are identical. Again, this translates in the following way: The difference $E_2 - E_1$ in the methods with identical slopes is exclusively attributed to the presence of hydrogens (i.e. the binding energy per hydrogen atom), while for the vdW-DF and TS theories the difference is not just the binding energy per hydrogen atom, but it also includes information about the local bonding environment of the carbons.

In other words, carbons in benzene and graphene are chemically distinguishable in non-empirical models, with the former binding stronger to the substrate. With a non-empirical vdW-DF methodology at hand, it is natural to investigate how the chemical environment has an influence on the interaction between planar pi-conjugated systems. To this end, four non-aromatic molecules with $N_H = N_C$ were investigated.

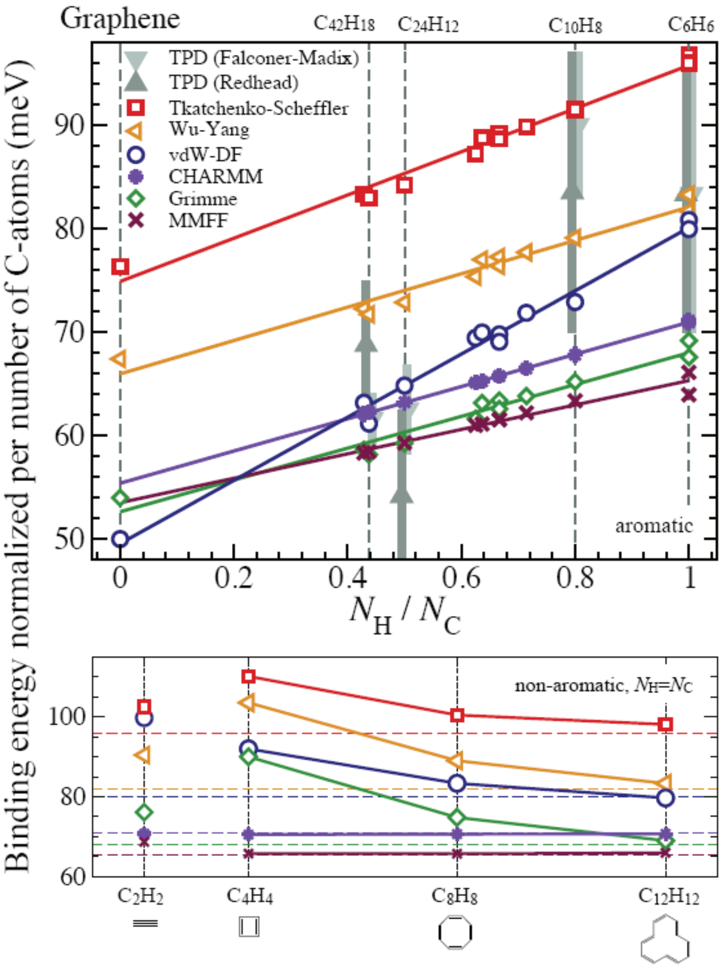

Figure 2-13

Binding energy normalized by number of carbon atoms for aromatic (top) and non-aromatic (bottom) hydrocarbons adsorbed on graphene. The grey error bars show data from temperature-programmed desorption experiments for C_6H_6, $C_{10}H_8$, $C_{24}H_{12}$ and $C_{42}H_{14}$. The lower panel includes three planarized cyclic anti-aromatics and ethyne, with the dashed lines indicating the binding energy for benzene (E_{CH}). The vdWDF binding energies of benzene, naphtalene and graphene agree well with a previous vdW-DF study for these systems.

The bottom panel of **Figure 2-13** compares their binding energy with that of benzene. It is shown that ethyne, [4]-annulene and [8]-annulene deviates significantly from benzene, while [12]-annulene correlates well with the two aromatic annulenes (benzene and [18]-annulene).Interestingly, the theoretical results show that the non-aromatic molecules bind stronger to graphene than the aromatics, thus indicating that pi-conjugation does not favor physisorption.

Given the above, it is of paramount interest to provide a physical interpretation of the phenomenon. To gain insights, the adsorption energies predicted by the vdW-DF model for a series of aromatic and non-aromatic compounds were separated into components and compared (see the corresponding **Appendix** sub-section for details). The total interaction energy, E_{TOT} along with the non-local correlation (or dispersion), $E_{C,nl}$ and electrostatic (Coulomb), E_{ES} components are plotted in **Figure 2-14** as a function of the adsorption height. The decomposition process indicates that the adsorption process is overall (ca. 61%) dispersion-driven at equilibrium distances. Moreover, as shown by **Figure 2-14** the interaction between the investigated compounds and the substrate is entirely described by $E_{C,nl}$ at distances larger than 4.5 Å; note that at these distances the electrostatic contribution is also slightly repulsive. In other words, in the absence of formal charges the initial complex formation is purely governed by dispersion forces, which effectively drive the adsorbate in close proximity to the substrate, and that binding is finalized by short-range electrostatic forces which stabilize the interaction.

Our results show that physisorbing discotics or columnar liquid crystals, would benefit from the use of dendrimer-like structures featuring multiple and strongly interacting moieties (aromatics or non-aromatics with N_H ~N_C) connected by linkers; rather than commonly thought, graphene-like polyaromatics.

In summary, the adsorption properties of polyaromatic and anti-aromatic hydrocarbons on graphene have been investigated as a prototypical system for pi-pi-interactions. Five different models for dispersion have been benchmarked and it was found that descriptions based on a commonly used C_6/R^6-functional form of the interaction give generally fair results, while the comparison of data obtained with the vdW-DF functional resulted in excellent agreement with available experimental data. In particular, a straightforward equation that provides quantitative estimates of the adsorption energy for aromatic hydrocarbons on graphene was introduced. With the interaction energies $E_1 = 49$ meV and $E_2 = 80$ meV predicted by the vdW-DF model at hand, one can obtain a quantitative estimate of the binding energy of any aromatic hydrocarbon by imputing the number of hydrogens and carbons in the equation. We expect **Equation 2-20** to be routinely used among experimentalists in the stage of molecular design. Finally, within currently available theories, we found that pi-pi interactions are of a prevalently dispersive nature. Electrostatic interactions still play a role but effectively contribute to the binding energy only in close proximity to the substrate. We conclude that purely dispersive forces drive the docking of neutral adsorbates on graphene which is finalized by short-range electrostatic interactions.

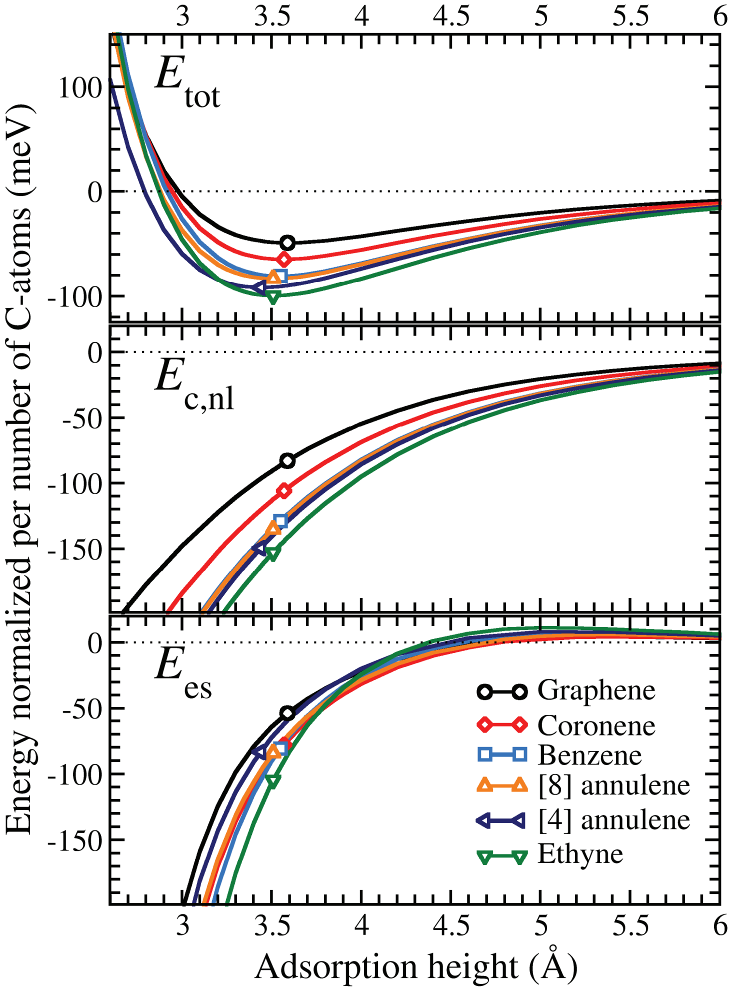

Figure 2-14

Contributions from the non-local correlation energy, Ec;nl, and the electrostatic Harthree energy, Ees, to the total vdW-DF interaction energy, Etot, for a number of representative hydrocarbons adsorbed on graphene. The circles indicate the global energy minima. The repulsive part of Etot comes entirely from the kinetic energy (Pauli repulsion) given in the complete energy decomposition in Fig. S3.

2.3 **Molecular Dynamics (MD)**

Molecular dynamics epitomizes statistical mechanics in its more complete form. In the presence of unlimited technological resources it gives the most accurate prediction and simulation of the thermodynamical ensemble. Reality is otherwise so that systematic approximations and algorithms must be used to describe classical phenomenology, i.e. the integration of Newton's equations of motion in an isothermal distribution must be made in a condition where time averages are equivalent to ensemble averages (ergodic theorem).

Thermostat. The first of these challenges comes by the simulation of a constant molecule-volume-temperature (NVT) ensemble. This ensemble is equivalent to the thermodynamical canonical ensemble which is by pure definition (Toda, Kubo et al. 1992) the submersion of a system into a heat bath so that the temperature of the system remains constant, i.e. an isothermal distribution. In computer simulations, this external heat-bath (thermostat) is only an algorithm that tries to keep the temperature of the system constant. Note that this temperature fluctuates in the canonical ensemble so that it differs from the view of "static" temperature of Boltzmann and Maxwell based on the ideal gas equipartition theorem, i.e. $k_B T = m\langle v_a^2 \rangle$, m and v being the mass and velocity of the particle along its ath component (McQuarrie 1997; Frenkel and Smit 2002). In fact, the game consists in making artificial fluctuations in the velocities of the particles so that the average temperature is that of the thermostat.

Through out the present work, we use the CHARMM program with the Langevin thermostat to control the temperature in all simulations. The latter is based on the Langevin equation of motion (Langevin 1908);

$$F = -\nabla U + (2\gamma k_B T m)^{0.5} \cdot R(t) - \gamma m v$$

Equation 2-21

with U the potential energy, m the mass, γ a frictional coefficient, and $R(t)$ a random force used to control the temperature of the system.(Mccammon, Gelin et al. 1977). The Langevin thermostat effectively controls the temperature, even at the small friction coefficients used in Chapter's 5 simulations, $0.05\mathrm{ps}^{-1}$.

Equations of motion. The idea behind classical determinism is that the evolution of an ensemble is described by its motions at the atomic level. The evolution itself means that such atomic motions will describe what will happen in our timescale of interest, i.e. given by experiments from minutes to milliseconds. It is straightforward to note that when describing the forces acting on a system at a time and position $r(t_0)$ an algorithm needs to be used to compute the new positions at after a time step $r(t_0+\Delta t)$. In classical mechanics, the smallest time step where to compute the new positions Δt is given by the fastest non-linear atomic motion in our system (provided that the algorithm itself behaves ideally). From experiment, non-linear motions happen in the ro-vibrational molecular spectra, so the fastest movement allowed is half of the period of the highest frequency in the characteristic molecular (IR+Raman) spectra.

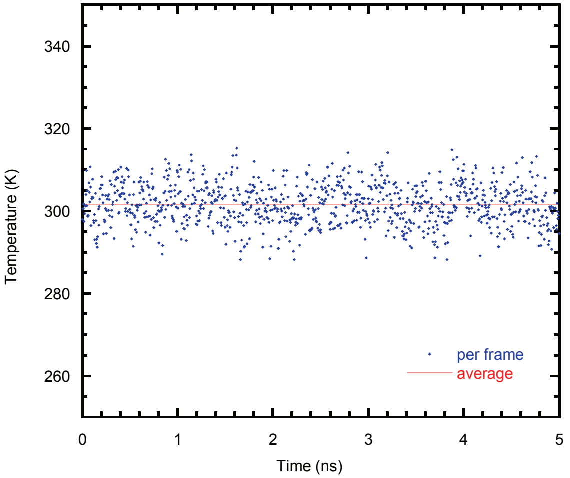

Figure 2-15
Temperature fluctuations for the Langevin thermostat at 300K for 80 molecules under the *standard* simulation setup, details of which we will give in section 5. The thermostat temperature is set to 300K and the average temperature after 5ns is 301.7K.

We saw in the previous section that for a normal molecule the highest frequency corresponds to C-H sp^3 atoms, with ~3000cm^{-1}, which equals 3.5 fs. In practice this timestep depends on the harmonic oscillator parameterized and not the experimental one. For instance, the force constant between an sp3 carbon and a hydrogen in CHARMM is ~330 kcal/molÅ^2 which amounts to 229.39 J/m^2. Using the systems' reduced mass, half of the period of the oscillation yields 0.82 fs. This means that the maximum allowed time step using CHARMM molecular dynamics mass and force parameters is less than 1fs. This means that to recreate 1ms of simulation more that 10^9*(degrees of freedom) integrations of the equations of motions must be made, clearly time consuming. We must rely on a way to increase the integration time step to reduce the 10^9 factor and/or the system's degrees of freedom. In an all-atom approach, this can be done through the constraining of vibrational motions. The SHAKE algorithm (Ryckaert, Ciccotti et al. 1977) can provide accurate constraining of covalent bonds during the simulations. The latter in conjunction with the use of heavy hydrogen atoms greatly improves the efficiency of the calculations and allows for an integration time step of several femtoseconds (fs); again we note that typical timesteps for classical MD are in the order of 1 femtosecond. In all the simulations presented in this work, hydrogens were converted to hydrogen-5 (^{5}H), i.e., the hydrogen mass was increased by 500%, and integration time steps between 7 and 4 fs were employed. While the use of heavy hydrogens is expected to affect the kinetics but not the thermodynamics of self-assembly, an integration timestep of 7 slightly affects the angular density of states, as shown in **Figure 2-16**. The figure shows that, while there is no energy drift in between simulations with constant time step so that the integration of the equation of motions are correct, there is a change of the potential energy towards high integration time steps, (black line) when constraining the bonds length of all atoms and using different integration time steps. It shows a ^{5}H saturated 12-molecule supramolecular hexagon (which we will study in Chapter 4 and 5) at 300K and constant dielectric using a cut-off length of 16 Å. During the course of the simulation the integration time-step is changed every 0.5ns. **Figure 2-16** shows that the total energy change for integration time-steps greater than 4-5fs can be assigned to exclusion of the angle high frequency bending modes. This is evidenced in the red line of **Figure 2-16** which represents the total energy minus the average angle bending energy. Note that high-frequency angle bending modes are not expected to contribute significantly to the free-energy difference between supramolecular entities such that a time-step of 7 fs can be used safely when the free-energy of the structures investigated do not depend on fast angle bending modes.

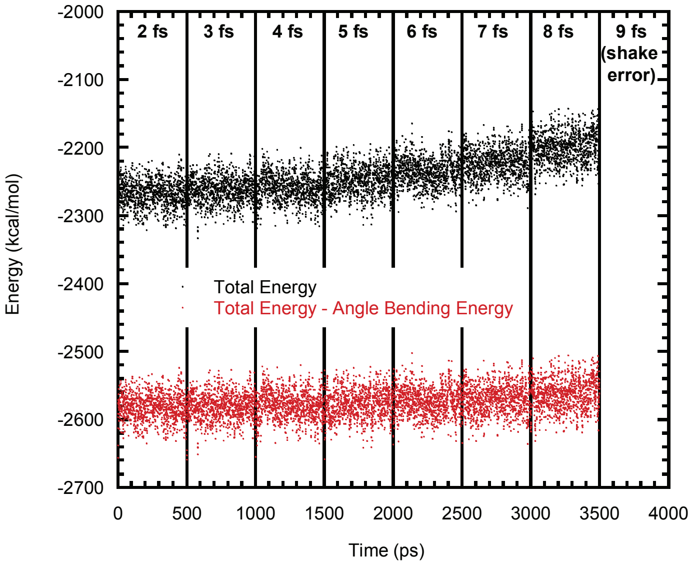

Figure 2-16

Changes in energy with different time steps (bold numbers) in a supramolecular hexagon using SHAKE and heavy ^{5}H hydrogens. The black line represents the total energy and the red line the total energy minus the average angle bending energy, thus identifying the drift in the total energy as a neglection of angle-dependent vibration modes.

In the following sections we will introduce new tools in 2D supramolecular chemistry, from the interpretation of STM images (section 2.31) to free energy calculations. Moreover Chapter 5 epitomizes the use of constant temperature molecular dynamics for the ultimate goal of supramolecular engineering.

2.3.1 Dynamic Tunneling Image Simulation

We have witnessed in the DFT section how the static simulated images with "molecular orbital resolution" have little correlation with STM images acquired at room temperature and in liquid media. This observation comes without surprise, considering that each pixel (~0.2Å^2) in a STM image is taken every 10-600μs, a rate which is ca. 6 orders of magnitude slower than the mean velocity of an ideal gas (using Maxwell-Boltzmann distribution, ~ Å every fs (McQuarrie 1997). In this section we will introduce a new methodology for the simulation of STM images, which we term dynamic tunneling image simulations (DTIS). As a prototypical example we consider the formation of a supramolecular polymer network of a flexible **Molecule 4.**

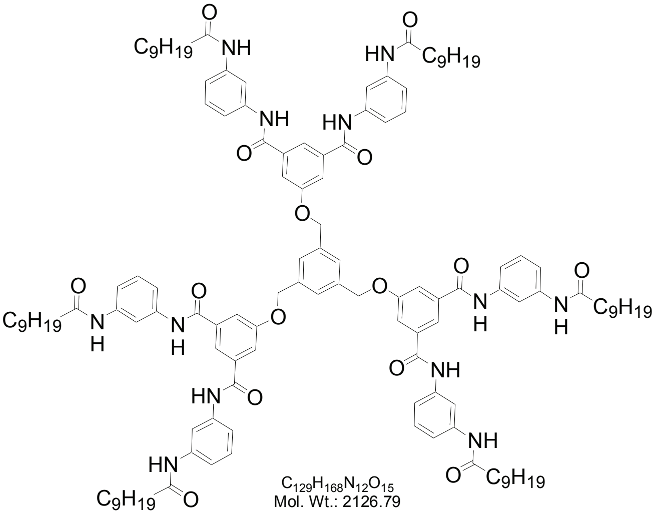

$C_{129}H_{168}N_{12}O_{15}$
Mol. Wt.: 2126.79

Molecule 4

Dynamic image simulation proceeds as follows. First, we perform a molecular dynamics conformational search starting from a structure following the geometrical constraints imposed by the symmetry of the unit cell in the STM experimental image. It is important to note that during this step, a careful diagnosis of the force field must be made, which includes correct parameterization of the hydrogen-bonds involved, of the explicit surface, and the setup of non-bonded interactions. Details on both the conformational search (which involved various 20ns simulations of four initial conformers) and the force field diagnosis are given the **Appendix. Figure 2a** depicts the pairing structure of the conformer found, which will be discussed later on.

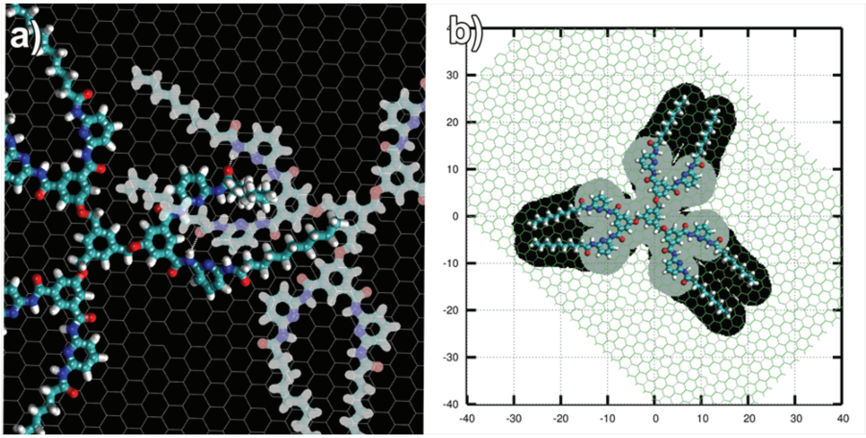

Figure 2-17

(a) Main hydrogen-bond interaction between adjacent dimers found during the conformational search. The primary interaction consist on two simultaneous hydrogen-bonds from two di(acetylamido)pyridine N-H's (bright molecule) to a perpendicular carbonyl in a third di(acetylamido)pyridine fragment (right hand side molecule). The kinetic stability of this interaction was further investigated at 300, 325, 350, 375, 400 and 425 K with explicit surface (ten 20 ns replicas per temperature) (b) Macroscopic $\beta(x,y)$ assignment for the molecular surface of a minimized **Molecule 4.**

Secondly, once the most probable conformer of the molecule is assigned, we need to establish another simplified approximation for the origin of the contrast in the STM images. In the previous sections we saw that this can be done using the Tersoff-Hamann approximation, **Equation 2-7**, but even being the lowest level approximation to the interpretation of STM image its implementation for molecular dynamics would require the merging of thousands of local density of state plots corresponding to each conformation snapshot. A more realistic alternative would be the implementation from the empirical tunneling law, **Equation 2-6**. Indeed, in the case where the molecules are contacted by the tip, we see that each molecule can be characterized by a decay length β also specific of the electrodes used. If we consider that this molecular decay length will be constant even in the case of non-contact, we can reformulate **Equation 2-6** in;

$$I = C_0 \exp\left(-\beta(x,y) z_1(x,y) - \kappa z_2\right)$$

Equation 2-22

where $\beta(x,y)$ is the molecular decay length as a function of the x,y plane (the plane containing the substrate), z_1 is the molecular height from the x,y plane and κz_2 is the decay length of vacuum times the spacing in between the molecule and vacuum. The latter quantity we will consider as a constant for purposes of simulating contrast in the x,y plane. With this information at hand, we turn to the simulation of the feedback image in our instrument, using the last term in **Equation 2-10** and **Equation 2-22** we obtain;

$$Z = P\left(\log(C_0) - \beta(x,y) z_1(x,y) - \kappa z_2\right)$$

Equation 2-23

where again Z is the feedback response, P is the proportional gain and the tunneling current set point I_t has been offsetted to zero for ease of calculation. Then we see that under logarithmic feedback conditions the feedback image reflects the quantity $\beta(x,y)z(x,y)$. While $z(x,y)$ can be obtained from the vdW surface in molecular dynamic force fields, $\beta(x,y)$ must imperatively be obtained for each atom and to a first approximation, we can assign the *beta* factors to experimental macroscopic decay length factors which have been shown to be independent of molecular length, 0.41 for aromatic rings and 0.96 for non-aromatic atoms (Wold, Haag et al. 2002) using gold electrodes. **Figure 2b** depicts the assignment of $\beta(x,y)$ for two atom types using polarizability radiuses in the MMFF parameters.

In the final step, we introduce the concept of molecular dynamics trajectory weighting to simulate every STM feedback image pixel out of the average of ~ns of molecular dynamics simulation, from where we obtain $<\beta(x,y)z(x,y)>$. Although a ns simulation time is still far from the 300 ms/pixel rate acquired for the STM feedback image, we show (see **Appendix**) that the root mean square deviation of molecular movement converges after few ps so that the molecular movements should ideally should have the same statistical weight independently if averaged over picoseconds or milliseconds.

Figure 2-18 shows the experimental STM image as compared to the plot of $<\beta(x,y)>$ averaged over 10ns (and 1000 frames) of a 300 K periodic boundary molecular dynamics simulation of eight **Molecule 4**. The unit cell in the footprint image corresponds to a = 4.4 nm and γ = 60 ° which is in good agreement with the experimental unit cell, being cell a = (4.7 ± 0.2) b = (4.8 ± 0.2) nm γ = (61 ± 3)° . Experimental and Computational details are given in the corresponding section of the **Appendix**.

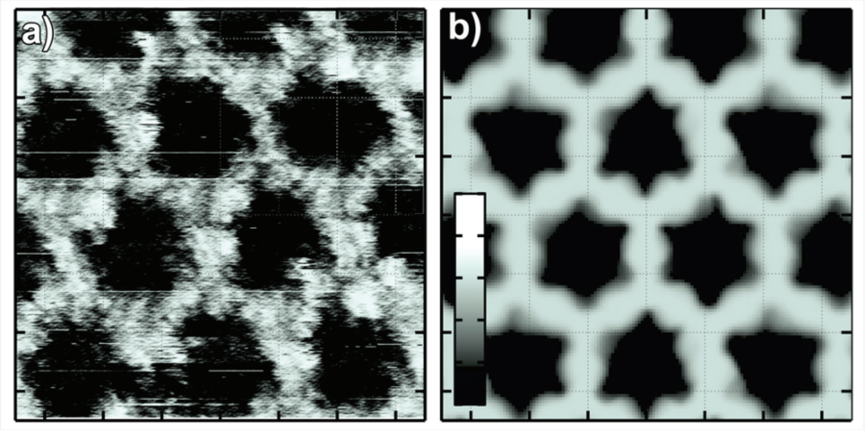

Figure 2-18
(a) Experimental STM feedback image and (b) the simulated image plot of *<β(x,y)>*. Images are 14x14 nm^2 exactly, each mark corresponding to 2 nm.

In summary using a molecular dynamics image simulation protocol we have elucidated and assigned the main interaction between adjacent molecules of a highly dynamic **Molecule 4**. The simple yet powerful protocol which can be further developed for accurate simulation of STM feedback images.

2.3.2 **Free-Energy Calculations**

Through out this chapter we have witnessed the importance of acquiring information on molecular interactions. In the DFT section we saw potential energy as means of establishing the adsorption affinities of a series of polyaromatics in graphene. Potential energy however contains fair information about a *state* in the isothermal distribution characteristic of the (grand)canonical ensemble we live in. For transferring information from and to a *state* we need to use a *thermal* quantity, or *thermal function*. Without entering into the obscure birth of such quantities, the Gibbs free-energy (G) can be effectively used to obtain the statistical weight a certain *state* has in an isothermal distribution. The author defined *state* previously as an atemporal position of atoms in space, for simplicity. Chemically, for one molecule this definition belongs to a conformation. But what exactly is a conformation? We like to think of a conformation as Lewis did in 1916 where the representation of a molecule's conformation can be written down in a piece of paper. The author believes, that in fact a conformation or a general state is not a position of atoms, but exists and is defined by its function. In view of this, the most coherent definition we can give here of a conformation in supramolecular engineering is the time average of its coordinates (X) in space we are interested in, i.e. <X>.

In this section we introduce state of the art techniques for free energy (G) calculations, which give accurate information about conformations <X> in the isothermal distribution. From statistical mechanics, more specifically, using Boltzmann's principle of isothermal distribution (equipartition theorem) and the sum over states (capital Z) principle (Toda, Kubo et al. 1992; Raff 2001) we can express the difference in free energy between two states as the difference between their absolute free energy G;

$$G = -RT \ln\left(\frac{z_{tr} z_{rot} z_{vib} z_{el}}{N} \right)$$

Equation 2-24

where z_i are the respective molecular sum over states or *molecular partition* functions and N is Avogadro's' number. Note that statistical mechanics must assume the separation of the different translational, rotational , vibrational and electronic states in order to give an analytic solution. **Equation 2-24** accentuates our problem in the definition of conformation, since a "state" must then have characteristic vibrational energies, separated from the rotational ones, thus cannot be described by <X>.

One alternative to such an approximated statistical thermodynamic free energy determination is thermodynamic integration, by (Kirkwood 1935).

$$\Delta G = \int_0^1 \left\langle \frac{\partial U(X,\lambda)}{\partial \lambda} \right\rangle_\lambda d\lambda$$

Equation 2-25

where X are the structural coordinates along the projected path parameter λ. Obtaining projected path parameters depends on a creative choice of the potential energy function U(X, λ). If we define a restraining potential U(X, λ)=U_0 + 1/2λk_f|X - $X_0|^2$, where k_f is a restraining constant and X_0 are the reference coordinates of a structure then **Equation 2-25** becomes, setting k = λk_f;

$$\Delta G = \frac{1}{2} \int_0^{k_f} \left\langle |\mathrm{X} - \mathrm{X}_0|^2 \right\rangle_k dk$$

Equation 2-26

which is equivalent computationally to;

$$\Delta G = \frac{1}{2} \int_0^{k_f} \left\langle \mathrm{N} \cdot \mathrm{RMSD}^2 \right\rangle_k dk$$

Equation 2-27

where N is the total number of atoms in the molecule and RMSD is the root mean square deviation from the X coordinates to the X_0 reference structure. Interestingly, we start to note that our creative choice for the potential energy function makes of **Equation 2-26** a free energy difference having by principle the integrated averages RMSD for a portion of the k-spectrum, i.e. from $k=0$ to a final $k=k_f$ of choice. In other words, we are computing the free energy from a “free” state (k~0), or more appropriately, a real “average” conformation $<X-X_0>_{real}$, to a new “restrained” structure $<X-X_0>_{restrained}$ characterized by k_f. In view of this, we may call **Equation 2-26** the free energy of confinement ($\Delta G^{confinement}$). The free energy of confinement for a supramolecular hexagon (see further in this section) is plotted in **Figure 2-19** from k~0 upto different k_f values.

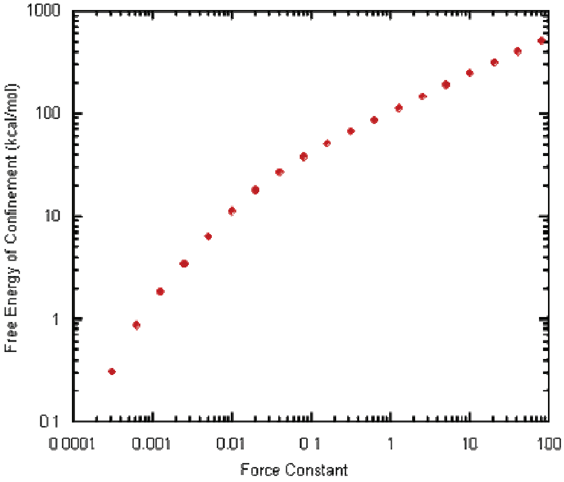

Figure 2-19
Confinement Free Energy of a supramolecular hexagon from integration of the RMSD to the k_f = Force Constant, in a 2 ns simulations at 300K using SHAKE for the Hydrogens (^{1}H).

It is straightforward to note that when $k_f \rightarrow \infty$, $X \rightarrow X_0$ and thus RMSD→0. In the latter case we recover the fully restrained or “frozen” conformation (like the one in paper we like to think of). Again, at high k_f values, such a frozen “zero Kelvin” structure has an analytical absolute free energy given by **Equation 2-24**. We can further approximate **Equation 2-24** by normal mode analysis (NMA) to obtain the vibrational free energy. Then we can compute the conformational free energy between two states A and B as;

$$\Delta G_{BA} = \Delta G^{confinement}_{A(X)\rightarrow A(X_0)} - \Delta G^{confinement}_{B(X)\rightarrow B(X_0)} + \Delta G^{NMA}_{A(X_0)-B(X_0)}$$

Equation 2-28

It may be however intuitive to think that the $\Delta G^{confinement}$ diverges when $k_f \rightarrow \infty$, from looking at **Figure 2-19**. However, it has been shown by its developers (Tyka, Clarke et al. 2006), that the difference between two confinement free energies (first two terms in **Equation 2-8,** converges for $k_f > 10$). In fact, the method has been successfully applied to calculate ΔG between conformational states of the alanine dipeptide (12 atoms) and the β-hairpin from protein G (160 atoms) and was shown to provide estimates with chemical accuracy, i.e., ~ 0.1 kcal/mol, at an affordable computational cost (Cecchini, Krivov et al. 2009). Here, as an example which will serve as critical information in Chapter 5, the conformational free energy of supramolecular polygons, was investigated by the confinement approach at various temperature values. Note this conformational free energy does not include rotational nor translational contributions to the free energy difference, which can be approximated by just using analytical formulae given by the complete form of **Equation 2-24** (Tidor and Karplus 1994; Mammen, Shakhnovich et al. 1998). We proceed by comparing the free energy of a supramolecular hexagon (**Figure 2-20a**) to that of the branched pentagon (**Figure 2-20b**), the former being a potential 2D crystal nucleus, the latter a building block giving rise to polygonal networks. We note that these two supramolecular species have the same number of atoms (i.e., degrees of freedom), so that they can veritably be considered as distinct conformational states, much like two conformers of a protein. The reference structures for the confinement calculation were obtained by strong energy minimization of the two supramolecular polygons extracted from the *fast-annealing* simulations. For this purpose, 30000 steps of steepest descend (SD) and 3000 steps of adopted basis Newton-Raphson (ABNR) were employed until the force gradient was lower than 0.0001 kcal/mol/Å. Each confinement calculation involved eight simulation runs of 0.25ns, for a total sampling of 2 ns per confinement simulation. Only trajectories in which the H-bonds were present were considered for the calculations. The criterion for the presence of the H-bonds was a contact distance of 3.2Å between the heteroatoms involved in the tri-hapto hydrogen bond for the 300K and 400K calculations, while a distance of 5Å was chosen for the 500K, since at that temperature hydrogen-bond are weakened. Note that the heteroatoms distances in the reference structures amounted to ~2.8Å. The error bars were computed as the standard deviation between the eight simulations runs. The confinement runs were carried out with SHAKE only used for the hydrogens, the implicit substrate, an integration time step of 1fs, infinite cutoffs (999.9 Å) and in the presence of an additional restraining potential to the reference structure with an increasing strength. To this aim, force constants ranging from 0.000156 to 82 kcal/mol/Å^2 were employed.

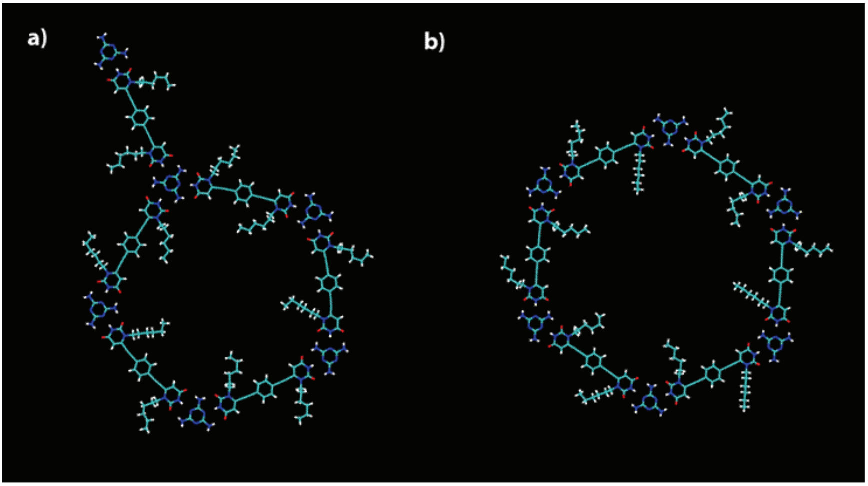

Figure 2-20
Reference structures for the supramolecular polygons that we will study in the next Chapters (4 and 5), (a) the "branched" pentagon and (b) the hexagon. The structures have been deeply minimized at each k_f for the computation of the RMSDs.

The results show that the supramolecular hexagon is lower in free energy in the whole temperature range (**Figure 2-21**) and that the ΔG amounts to 2.3±1.0 kcal/mol at 400K. Under canonical conditions[5], the latter corresponds to a ratio of 18 between the population of the hexagon and that of the pentagon. The origin of the difference in stability predicted by the confinement approach is clearly predominantly enthalpic, favoring the hexagon by -2.0 kcal/mol (red line **Figure 2-21**), despite an equal number of hetero-recognition interactions in the two supramolecular adducts. Out of the -2.0 kcal/mol, -1.0 kcal/mol of the potential energy is due entirely to a better arrangement of recognition elements in the supramolecular hexagon, which is not permitted by the more strained architecture of the pentagon. Comparing to DFT calculations in Chapter 4 this difference was predicted to be -0.46 kcal/mol using PW91 functional with plane waves basis sets (Palma, Bjork et al. 2009); 0.002eV*10 interactions). The majority of the remaining potential energy favoring the formation of the

---

[5] The canonical probability of sampling any system's supramolecular state *A* at the temperature T is proportional to its partition function $Z_a = Sum\_i \ni A \exp(-U_i/k_bT)$, where the sum runs over the ensemble of microstates of *A*, U_i is the internal energy of these microstate, k_b the Boltzmann constant, and T the absolute temperature, and amounts to $p_A = Z_A/Z$, with *Z* the system's canonical partition function. Since the Helmholtz free enegy, $F = -k_bT \ln(Z)$, is by definition proportional to the logarithm of the canonical partition function, the ratio between the populations of two supramolecular states *A* and *B* is given by their difference in free energy as $\Delta F_{AB} = F_A - F_B = -k_bT \ln(p_A/p_B)$, where p_A and p_B are canonical probabilities.

hexagon (-0.8kcal/mol) can be ascribed to the molecular deformation energy, which encompasses both deformation around the interaction centers and bending of the molecular backbone. The energetic contribution to the bending of the backbone was also previously quantified as -0.34 kcal/mol (see Figure S13 in (Palma, Bjork et al. 2009); 0.003eV*5 molecules). There is in fact a good correlation in the potential energies favoring the hexagon, both in DFT and the MMFF Force Field, in view of the former not including dispersion corrections.

Although in this particular example the 2D supramolecular polygons are rigid so their entropy contribution is very small, we conclude that the confinement approach to free energy calculation is a powerful tool in supramolecular engineering.

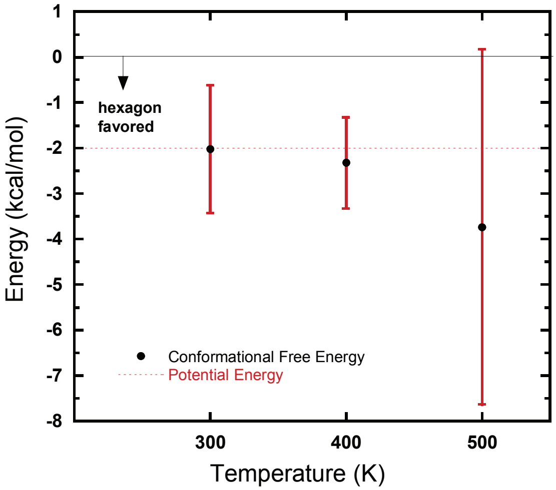

Figure 2-21

Free Energy Differences between branched pentagons and hexagons (negative favors the hexagon). The dotted line indicated the potential energy difference between pentagons and hexagons. Note the high uncertainty in the 500K simulations, due to the weakening of the hydrogen-bonds.

2.4 Isothermal Titration Calorimetry (ITC)

As we have evidenced from the previous modeling sections, our theoretical methods in supramolecular chemistry are technically far away from determinism, thus highly dependent on validation through experimental methods. While DFT is just beginning to account for vdW interactions in intermolecular interactions, molecular dynamics needs ultimately a mean-field parameterization with explicit solvent to output more accurate data. It is obvious and more than timely, that development of ultrasensitive thermochemical methods in solution must be pursued.

Isothermal Calorimetry (ITC) is a method for measuring heat differences between a working and a reference cell at constant temperature. In the working cell a perturbation is introduced in order to register a heat difference between the cells. In biochemistry and supramolecular chemistry, this perturbation is commonly the titration of an analyte into a solution containing the complementary receptor at constant pressure, thus an enthalpy difference (ΔH) of interaction can be obtained for any given conditions. In biology, ITC is the gold standard for measuring biomolecular interactions (Jelesarov and Bosshard 1999), able to determine simultaneously binding parameters (K_{eq} and ΔS) at stoichiometric conditions through the measurement of ΔH. Such powerful use in biochemistry has encouraged the development of ITC instruments capable of measuring millimolar to picomolar binding constants (10^2 to 10^{12} M^{-1}) in sub-milliliter volumes and with reproducible heat differences below tenths of nanocalories per second (Microcal 2010).

While widespread in biomolecular chemistry, the ITC unlimited potential in supramolecular chemistry, where low binding constants of 10^2-10^5 are common (Turnbull and Daranas 2003), has just began to be grasped (Chiad, Stelzig et al. 2009). Moreover it can be successfully employed in measuring non-stoichiometric ΔH such as multi-binding affinities with substrates(Varghese, Ghosh et al. 2009), a key parameter for bottom-up supramolecular nanochemistry. In light of this, we can expect ITC to become the gold standard in supramolecular chemistry and nanochemistry as it has been in biomolecular chemistry in a very near future. A caveat which hinders the extended use of ITC in supramolecular chemistry is the low tolerance of commercial instruments to organic solvents. It is for the previous reason that commercial instruments must be better adapted to organic solvents. We expect that with trivial modifications, commercial instruments may be adapted at an additional cost.

As a practical example, in this section we will introduce the ITC technique for the adsorption of polyaromatics on graphene, a novel methodology which we will describe extensively. We begin by the formulation of exfoliated graphene solutions representative of the graphene substrates. It has been reported (Hernandez, Nicolosi et al. 2008) that sonication of a high-surface energy solvent with pyrolytic graphite flakes (HOPG) will induce the exfoliation of graphene solubilizing micrometer wide single graphene flakes. Indeed we can obtain evidence of the morphology and single-layer composition of the dissolved graphenes via dynamic light scattering (DLS) and Raman spectroscopy. **Figure 2-22** depicts the Raman spectra of the graphite/graphene solution in N-methlylpyrrolidone (NMP). Although we estimate a concentration of 10μg/mL (adsorption cross-section of $20m^{-1}$), since the exact residual weight was not determinated, we note that the graphite/graphene solution was made through the sonication (FB15047 ultra-sound bath,4h) and subsequent centrifugation (6000rpm,1h) of 1.5g of HOPG flakes in 100mL N-methlylpyrrolidone. The Raman spectrum in solution shows a G line at ~1590cm^{-1} and a very broad 2D peak at ~2580cm^{-1}. Since both phonon lines are particular of the conformation of the graphene sheets (Ferrari, Meyer et al. 2006) we cannot infer about the sole presence of single layer graphite. What we can conclude about the Raman spectrum is that there are graphene flakes, since the presence of graphite gives rise only to a sharp 2D peak centered around 2700cm^{-1} (Ferrari, Meyer et al. 2006). Likewise the DLS in **Figure 2-22** shows only one distribution of particle size of Z=147nm which would lead us to conclude that there should be more graphene flakes that graphite particles, if any present. Note that this distribution is obtained by setting the material's refraction index to 1. In the measure that we increase the material's refraction index up to 10, a second peak distribution appears, starting at refraction index of 2.5. The intensity peak at Z=39nm may arise from the conformation of the actual flakes in solution. Indeed cylindrical flakes would have an isotropic refractive index. This hypothesis is left to confirm by future work and from deeper analysis on the correlation caveats introduced by DLS.

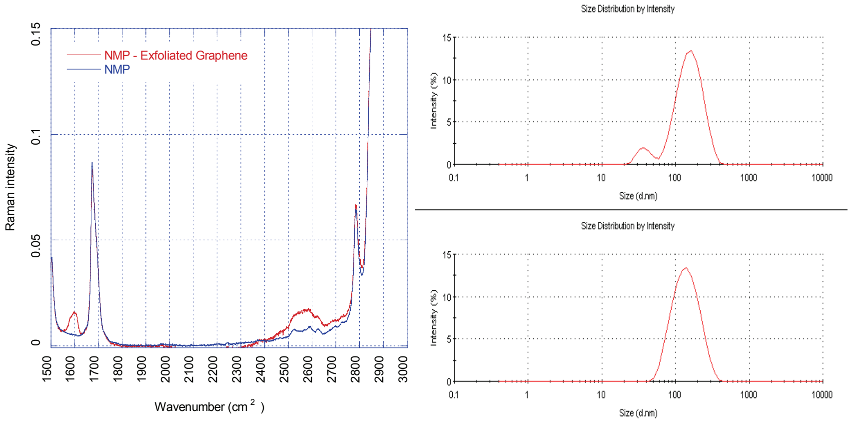

Figure 2-22

Left hand side: Raman spectra of graphene in NMP and the solvent alone. Right hand side: Malvern Zetasizer Nano-S DLS spectra of the same sample with a dispersant refractive index of ten (top) and of one (below). DLS parameters: 1.7cP, 1.47 RI for NMP, 8 attenuation.

With a characterization of our system at hand we turn to the ITC titration of a solution of coronene (the ligand) in NMP to 2mL of our graphene (the subtrate) solution in NMP . Before we continue we must establish the feasibility of ITC determination of adsorption energies. We use a VPITC from Microcal systems, with a reported sensitivity of ~0.030µcal/s. To obtain reasonable results we need to have heat signals of at least 0.300 µcal/s. If we start from the hypothesis that coronene on graphite adsorbs with at least 1eV strength, i.e. 23.0605 kcal/mol and we set a minimum titrant concentration to 600 µM and 5µL in 10s injections, we should titrate heat differences of 6µcal/s, provided that all the molecules adsorb on graphene (**Equation 2-29,** solving for ΔH_{exp}=23.0605 kcal/mol).

$$n \cdot \Delta H_{\mathrm{exp}} = \int_{t_2}^{t_1} \delta Q(t,T)dt$$

Equation 2-29

where *n* is the number of mols of ligand and δQdt is the function output from the ITC. Notice that we have emphasized that δQ is a inexact differential function, whose value may depend in many instrumental parameters. **Equation 2-29** is what the author believes to be the ITC equation for peak integration in a regime where the binding substrate is in excess. Indeed, the condition for adsorption of *n* coronene molecules, which adsorb with an estimated inverse density of $0.33m^2$/µmol, is to have enough substrate available. The occupied portion of substrate under the previous conditions would total $2x10^{-4}$ m^2. This is strikingly a small percentage of the huge area of adsorption that is available in 10µg/mL graphene solutions. Setting a $100nm^2$ flake weight to $9.88x10^{-18}$g we find a surface area of $4x10^{-2}$ m^2 in only 2mL of graphene solution. With such a robust estimation, we proceed to titrate a 2µL of a 641µM coronene solution of NMP into a 2mL solution of graphene/NMP. In such a concentrated solution of NMP in both coronene and graphene there are three fundamental processes happening upon titration. **Figure 2-23** shows the processes in a cartoon and in a real ITC single injection, in green. They consist in the dilution of coronene ($\Delta H_{dil\text{-}C}$), the solvation of graphene ($\Delta H_{solv\text{-}G}$) and finally the adsorption of coronene in graphene ($\Delta H_{ads\text{-}GC}$).

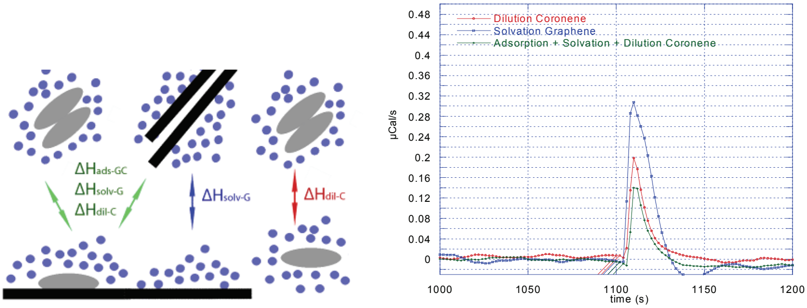

Figure 2-23

Single ligand ITC injection showing the main titration experiment ($\Delta H_{exp,}$ left: green arrows, right: green curve). And two other injections to obtain the $\Delta H_{solv\text{-}G}$ arising from the interaction of the titrated solvent with graphene (left: blue arrow, right: blue curve) and $\Delta H_{dil\text{-}C}$ arising from the increase of volume upon titration of a ligand. Injection parameters: 25ºC, 2µL, 300s wait, 458rpm, 641µM coronene in NMP, graphene concentration ~10µg/mL in 2mL.

Note that since by definition one cannot measure changes in entropy isothermally (unless through a binding curve), the previous solvation and adsorption heats are due mostly to the breaking of intermolecular coronene-coronene and graphene-graphene interactions, thus the main or "exp" titration peak (ΔH_{exp} green curve **Figure 2-23**) will be normally endothermic. There are two ways for obtaining only the adsorption energy. The first one consist on calculating the dilution ($\Delta H_{solv\text{-}G}$, red curve **Figure 2-23**) and solvation curves ($\Delta H_{dil\text{-}C}$, blue curve **Figure 2-23**), such that the heat of adsorption is given by **Equation 2-30**. This can be done through two other titrations as seen in **Figure 2-23**. For the previous we titrate pure NMP into the graphene, while for the latter the NMP/coronene solution into pure NMP solvent.

$$\Delta H_{ads-GC} = \Delta H_{\exp} - \Delta H_{solv\ G} - \Delta H_{dil\ C}$$

Equation 2-30

Using **Equation 2-29** with a triangular δQdt function and solving for $\Delta H_{ads\text{-}GC}$ in **Equation 2-30** we obtain -3.84 kcal/mol as an interaction energy. Note that the injection peak in **Figure 2-23** is only 5 times above our detection limit so this particular value is not certain. The second way for obtaining ΔH_{adsGC} and optimize our previous experiment is to reduce the concentration of graphene to reduce the ΔH_{solvG} contribution. We can do this by sonicating only 1h the graphene for a concentration of ~2µg/mL, which still gives an excess surface area for coronene adsorption (we cannot reduce the the ΔH_{dilC} contribution since coronene starts aggregating at ~50µM concentration and such a concentration will reduce our optimistically expected ITC signal to 0.6µCal/s!). **Figure 2-24** shows the ΔH_{dilC} (left) and ΔH_{exp} (right) injections of two different experiments. Under diluted graphene conditions, the ΔH_{solvG} contribution is below the detection limit so can be neglected. Using **Equation 2-29** and integrating the data between the peaks between a Gaussian fit ranges we obtain -2.6±1.0 kcal/mol, in accordance to the experiment in **Figure 2-23**. We note that the ITC is an extremely sensitive technique and only 30% of the experiments were reproducible. Encouragingly, this is an effect assigned to the changing of solvents so that this percentage may be increased when working long periods of time (<weeks) with only one solvent.

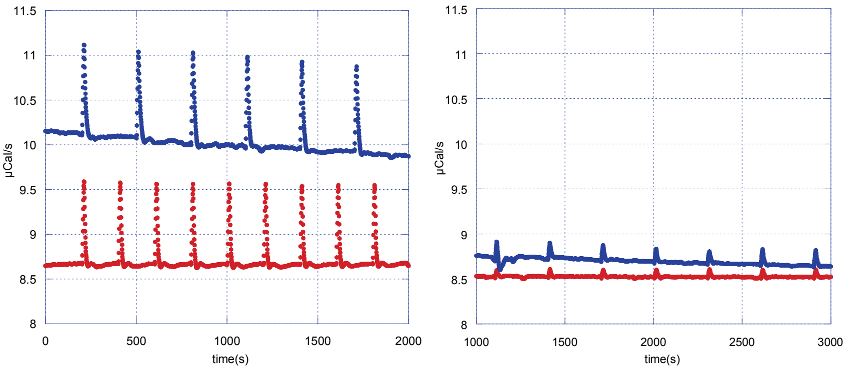

Figure 2-24

ITC experiments showing the dilution experiment ΔH_{dilC} (left hand side) and the main ΔH_{exp} titration experiment (right hand side), when low concentration graphene solutions are used Injection parameters: 25ºC, 5µL, 200s wait, 394rpm. 688µM coronene in NMP, graphene concentration ~2µg/mL in 2mL.

Although we found that the interaction of coronene with graphene was less than 20% what expected, we owe the low enthalpy of adsorption to the high surface energy of NMP solvent (Hernandez, Nicolosi et al. 2008), so that the endothermic desolvation enthalpy is very high. We expect the use of other solvents to give fairly high heats of adsorption for coronene and the polyaromatic series. Altogether we have demonstrated and characterized the ITC technique as a powerful tool for measuring with 50% precision ultra-low (2-3kcal/mol) heats of interaction in supramolecular chemistry.

3 Understanding 2D H-bonded Self-Assembly

A necessary investigation prior to multi-component self-assembly is to put forward a theory of *aufbau* in two dimensions. However, in the early states of engineering, self-assembly remains a highly empirical science. Here we put forward the understanding of 2D H-bonded self-assembly in four steps, each with increasing complexity and, two of which are treated in the present chapter. The conception of 2D self-assembly is based on empirical knowledge of chemistry, the so-called *chemical* intuition, put forward to establish a molecular library of complementary recognition units in order to pre-program self-assembly. Before we can establish the actual pre-programming proof of principle of these libraries which is treated in Chapter 4, we must first introduce basic design and experimental conditions for the self-assembly of the mono-component systems bearing H-bond moieties. This is done through carefull geometrical studies of the molecules.

In a second step, and once introduced the empirical results, a semi-quantitative theory is put forward , with *a priori* knowledge of the phase segregation and polymorphism that present H-bonded molecules on surfaces. We refer to this first semi-quantitative theory as an analytical way of *pre-programming* self-assembly, in contrast to the best level of predictive theory that we can envisage, which we refer to as *supramolecular engineering.* An alternative to our theory of pre-programming self-assembly is given in the Appendix, within the fitting of free energy proposed recently by (Kampschulte, Werblowsky et al. 2008). While essentially equal, we will show later on that the right formulation of the system's free energy may allow to enthalpically *pre-program* the formation of one phase or another. It is important to note however that the subtleties of 2D self-assembly might not be grasped by mean free-energy theories but by a systematic kinetic and non-equilibrium premises. We will discover these premises in Chapter 5.

3.1 STM Characterization of Molecular Libraries

The chosen chemical library features multivalent modules based on the (diacetylamino)pyridines and the uracil-like di-imide moieties. These valency-carrying groups are usually made multi-topical by ethylene linkers, using benzene derivatives as the cornerstones, so that multiple geometries are investigated. Moreover, by analogy to the literature presented in Chapter 1, we may further introduce features which would allow the chemical libraries to physisorb on graphite. In addition, the DFT methods section showed that a benzene ring adsorbs with an energy of 11.06 kcal/mol on graphene in vacuum. In summary, empirically designed libraries for 2D self-assembly must contain benzene rings to favor adsorption (alkyl chains in the case of adsorption onto HOPG), be rigid to minimize entropic loss upon adsorption and symmetric (**Molecule 5** through **Molecule 16)**.

Experimental details in this section are given in the corresponding **Appendix** sub-section. However it is worth resuming *a priori* details of critical importance that are based in the experience encountered during the experiments that we will show. The choice and composition of the solvent is of paramount importance in the processing and formation of supramolecular architectures from a purely practical point of view. In fact, the rule used for the choice of the solvent in the present STM studies is the following: the lowest dielectric constant solvent in which the molecules are soluble. This guarantees ideal dynamic imaging conditions, i.e. reversible conditions and low non-Faradaic currents. As a consecuence,in the present work unless when noted and for the mono-topic studies, most images are reported from solutions <10µM, in 1,2,4-trichlorobenzene(TCB) and 0-2% dimethylsufoxide (DMSO). The reason being that we designed molecules that are conventionally considered rigid and may form multiple hydrogen bonds in the solid state, leading to a solubility typically in the order of 10^{-4}-10^{-6} M even in polar solvents. Because of this, a binary mixture between a polar and relative apolar solvent is mandatory when ternary mixes are to be avoided. However, TCB being an aromatic, it should interact strongly with the graphite itself, disrupting the self-assembly of weakly physisorbed molecules. In fact, when no self-assembly could be evidenced in TCB, the terniary mixtures approach was sought as we will show in the following sections. Moreover, the scanning conditions in TCB are also important. We found that the optimal scanning conditions in our typical STM (veeco multimode with pico-amp booster) solutions are made with a maximum threshold of 1%v/v anhydrous DMSO. Using a higher amount of DMSO results in excessive non-Faradaic currents that may not allow scanning at conditions above 200mV/10pA (i.e. decreasing the current our increasing the voltage). Other solvents tried (DMF, 1,1,2,2 tetrachloroethane, acetonitrile derivatives – Sigma Aldrich >99.9%) decrease the 1%v/v threshold of DMSO, thus making them less suitable for STM imaging. Also note that through out the present work the superimposition error in the molecular models on top of the STM images is below 5%.

3.1.1 **Monotopic H-bond Molecules**

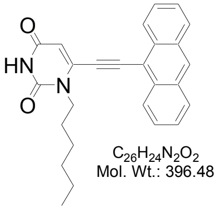

Molecule 5

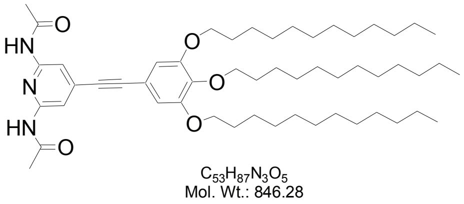

Molecule 6

It is primordial to study self-recognition phenomena before multi-component architectures are sought. These self-recognition phenomena are also called through out this work homo-recognition or homo-association interactions.

The STM images in **Figure 3-1** display the formation of a highly ordered crystalline monolayer, from a solution of **Molecule 5** dissolved in *n*-tetradecane, being readily soluble. Here the bright features are believed to match the anthracene moieties of the molecules, whereas the alkyl chains of molecule are adsorbed in the areas of darker contrast. The corresponding packing motif shown in the cartoon reveals the occurrence of homo-association, *i.e.* the formation of two N–H···O bonds among adjacent molecules, thus forming the (Molecule 5)$_2$ dimer. Similarly, the monolayer formed when molecule (**Molecule 6**) is deposited from n-tetradecane, since it is again readilly soluble (**Figure 3-1c**). The packing is lamellar, where three different type of tunnelling contrasts can be observed: *i*) dark gray parallel lines, which can be ascribed to the alkoxy side-chains, *ii*) brighter rod-like features, that can be attributed to the conjugated moieties, and *iii*) darkest contrast region between two rows of molecules. The arrows shown in the image correspond to the underlying HOPG orientation, which in turn matches the alignment of the aliphatic chains. In these cases, the self-assembly is mostly governed by commensurability of the aliphatic chains with the substrate (see introduction and (McGonigal, Bernhardt et al. 1990; Rabe and Buchholz 1991). Interestingly, there exists some geometrical constraints for the superimposed molecular models proposal in **Figure 3-1c**. In order for the alkoxy chains to adopt the right position and length with respect to the bright conjugated cores, some features are needed. First, one alkyl chain per molecule is not adsorbed on the surface but is rather back-folded in the supernatant solution, in analogy to other organic systems physisorbed at the HOPG-solution interface (Perronet and Charra 2004). Second, a kink occurs in the central alkoxy chain, meaning that the first and fourth CH$_2$ (starting from the oxygen atom) are in an eclipsed conformation, with a dihedral of ~15 degrees. This conformation occurs naturally when flattening the molecule and minimizing the geometry at the MM2 level with a RMS gradient of 0.5 kcal/mol. Third, the STM image also reveals that the molecules facially expose the 2,6-(diacetylamino)pyridine moiety separated by a 1 nm gap featuring a dark contrast.

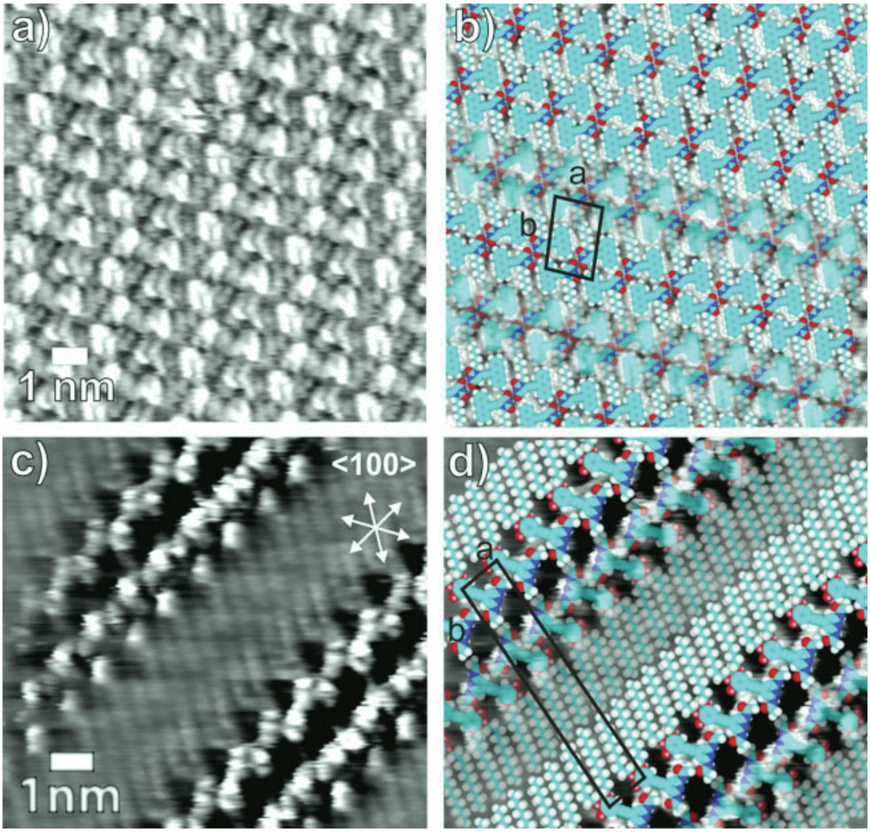

Figure 3-1

STM height image of mono-component monolayers of molecule **Molecule 5** on HOPG. b) Proposed model c) STM current image of **Molecule 6** physisorbed at the solution-HOPG interface. d) Proposed model, one alkoxy chain per molecule is not adsorbed on the surface. Tunneling parameters: a) average tunneling current (I_t) = 5 pA; bias voltage (U_t) = 750 mV. c) I_t = 10 pA; U_t = 1000 mV.

3.1.2 Di-topic H-bond Molecules

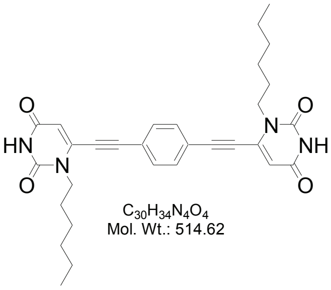

Molecule 7

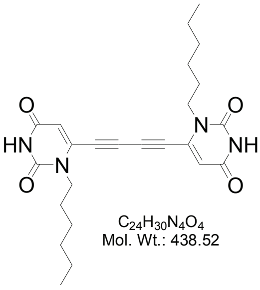

Molecule 10

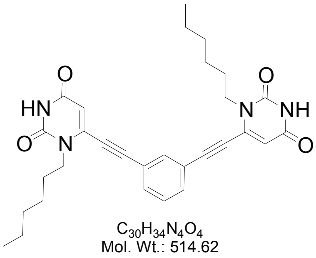

Molecule 8

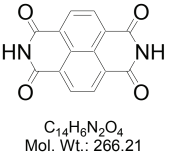

Molecule 11

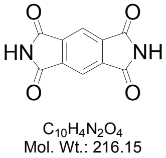

Molecule 12

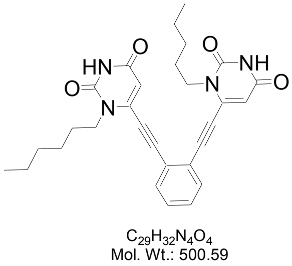

Molecule 9

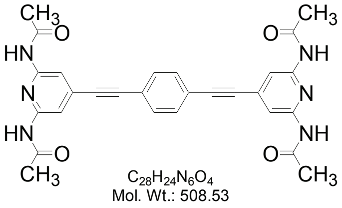

Molecule 13

Extending the principle of mono-topic molecules, the di-topic molecules can homo-recognize to produce architectures with a 1D supramolecular axis, i.e. 1D supramolecular polymers, which may or may not pack into 2D crystals. STM images of **Molecule 7** can be obtained by (40 ± 25 μM) in 1,2,4-trichlorobenzene (TCB) on HOPG surfaces, as displayed in **Figure 3-2**. The system forms highly crystalline monolayers. In the lower part of the **Figure 3-2**, the contrast in the STM image reveals three bright lobes coinciding with the three aligned aromatic rings of molecule. It is interesting to note that the contrast through out the image is not uniform, the upper part of the image appears with a bright arch. It is clear that this bright arch does not correspond to the central body of the molecule, since another contrast for **Molecule 7** is shown in **Figure 3-3**. We may suggest that, as it is clear that the hexyl side-chains are not physisorbed on surface, van der Waals interactions are predominantly occurring between the aromatic cores, so that some contrast maybe due to movement and overlap of hexyl chains and aromatic cores. The unit cell amounts to a = (0.87 ± 0.03) nm, b = (1.79 ± 0.08) nm and α = (65 ± 1)° with an area (A) of (1.4 ± 0.2) nm^2.

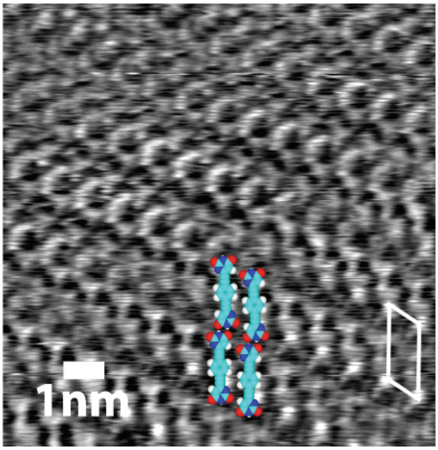

Figure 3-2
STM height images of mono-component assembly of **Molecule 7** on HOPG. Alkyl chains are not shown in the model. Average tunneling current (I_t) and bias voltage (V_t) I_t = 15 pA and V_t = -400 mV.

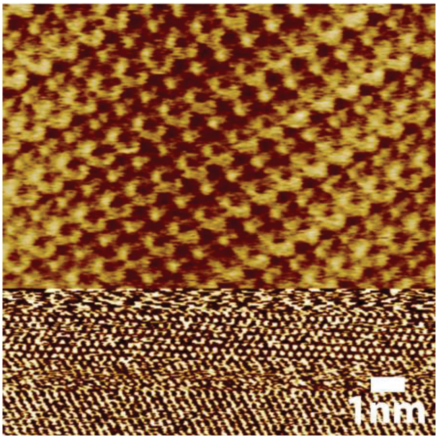

Figure 3-3
STM constant current mode image showing a monolayer pattern of **Molecule 7** at a concentration of 3±2 μM in TCB. Tunneling parameters: V_t = 200mV, I_t = 20pA. Underlying HOPG is also shown.

The critical influence of the aromatic cores in vdW interactions is evident when we compare **Molecule 7** to its shorter analogue **Molecule 10**. **Figure 3-4** depicts the STM image of **Molecule 10.** Exactly six carbon atoms and four hydrogens are missing in the latter and the result in the change of the packing motif when compared to the larger analogue is striking. . We notice immediately that this time the alkyl chains must be adsorbed in the surface, as the bright cores have the sizes and alignment of the homo-interacting conjugated backbones. However an analytical proof of the adsorption of the alkyl chains is not possible since no crystalline structure is formed, i.e. the pattern has a pseudo-periodicity. In fact this pseudo-periodicity is by itself a proof of the adsorption of the alkyl chain since the *syn* isomer of the molecule, i.e. where alkyl chains are adsorbed in the same side, must occur as well as the corresponding *anti* stereoisomer. In view of this, the pattern is considered to be more a 1D supramolecular polymer than a compact 2D architecture.

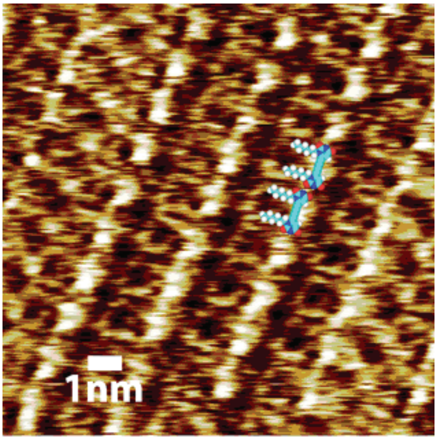

Figure 3-4

STM constant current mode image showing a monolayer pattern of **Molecule 10** at a concentration of 39±3 μM in TCB. We note that the pattern has a pseudo periodicity probably due to substrate commensurability with the alkyl chains, as such, its unit cell could not be extracted. One proposed contrast assignment is show through the superimposed molecular models. Tunneling parameters: V_t= 300mV, I_t = 20pA.

Molecule 7 may be essentially considered as the para derivative of a series of meta (**Molecule 8**) and orto (**Molecule 9**) molecules. From a topological point of view we can expect that the meta and orto derivatives will form a zig-zag type rows of polymers instead of the tightly packed regular motif of the straight para molecules. **Figure 3-5** shows the first packing obtained in TCB solvent of **Molecule 8**. The architectures formed are strikingly discrete porous supramolecular entities. It is remarkable how the hydrogens in the central benzene are in close contact with the two oxygens from different nearby molecules, presumably indicating the formation of weak hydrogen bonds (Desiraju and Steiner 1999). However this last remark remains speculation since, although the STM may resolve under periodic (Fourier transform) conditions up to 1Å, it cannot give analytically distances of weak or strong hydrogen bonds (~3Å), due to the poor resolving of individual contrasts. Again, as introduced, a combined molecular dynamics and STM image analysis may provide the needed resolution. Notice again that the hexyl chains cannot be distinguished and might be either desorbed or adsorbed in the pore cavity. Interestingly, the porous structure appears to contain rapid-diffusing molecules, such as the solvent. Indeed when changing the solvent to 1-phenyloctane, an apparent stripped motif is obtained. This packing was however strongly unresolved and as such is left out of the present work.

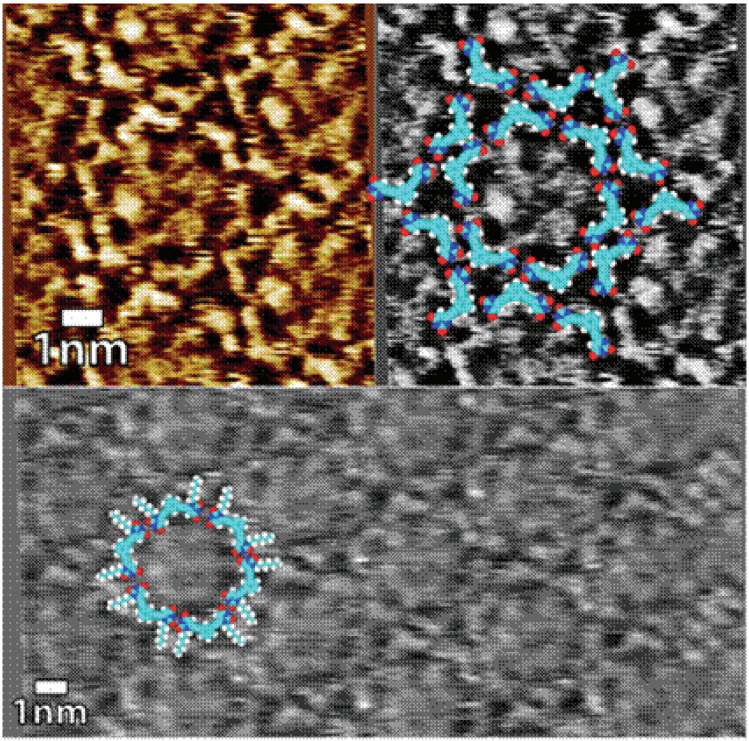

Figure 3-5
Discrete porous networks formed from ~40µM solutions of **Molecule 8** in TCB solvent. I_t = 20pA and V_t = -400mV

For the orto isomer, **Molecule 9**, STM images reveal the formation of rows which correspond to the size of face-to-face homo-interacting molecules (**Figure 3-6**). Notice the large intercolumn voids of low contrast which can be ascribed to the position of the hydrogen-bonds. The fact that hydrogen bonds appear as dark intermolecular voids in TCB solvent can be evidenced very well by comparing figures with different H-bonded rows of molecules, e.g. **Figure**

3-3, **Figure 3-4** and unambiguously in **Figure 3-5**. The red arrows in **Figure 3-6** indicate un-resolved contrast which breaks the 2D periodicity in a random manner so that a unit-cell for the assembly cannot be obtained. Again these rows may feature another 2D stereoisomer of the molecule, dictated by the adsorption/desorption of one or both alkyl-chains.

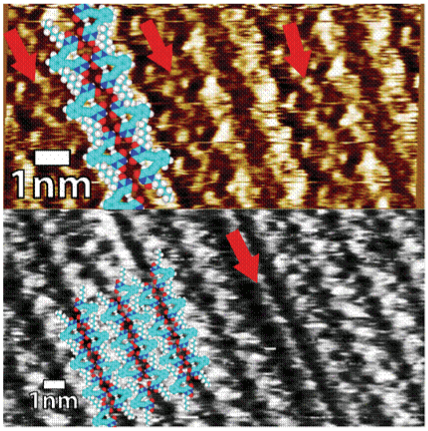

Figure 3-6
Compact structure formed from ~30μM solutions of **Molecule 9** in TCB solvent. I_t = 20pA and V_t = 200mV

In the last of the series of uracil-like molecules stands naphthalene tetracarboxylic di-imide (NTCDI) **Molecule 11** and pyromellitic di-imide, **Molecule 12**. These two molecules were chosen because they are readily soluble in TCB/DMSO mixtures and play a special role in the systematic investigations of Chapter 4. The patterns on HOPG obtained for the mono-component system **Molecule 11** (**Figure 3-7**) surprisingly correlate with architectures observed on Au(111)(Xu, Dong et al. 2007; Silly, Shaw et al. 2008) and Ag/Si(111)(Keeling, Oxtoby et al. 2003; Perdigao, Fontes et al. 2007) substrates (discrepancies in the unit cells being below 20%). Indeed it can be observed that the unit cell encompasses two molecules since there is a tilt between adjacent "polymer" rows, i.e. rows that are homo-associating through H-bonds (**Figure 3-7**). Finally for **Molecule 12,** it was not possible to visualize the mono-component monolayers when deposited using a wide range of solution concentrations, even up to 60 μM. Saturated solutions of **Molecule 12** could not be imaged by STM because of excessive (non-)faradic currents. It is interesting to conclude that **Molecule 12** is the smallest molecule in the di-topic uracil linker series which cannot be tightly physisorbed using TCB solvent. This might be due to both small energy of adsorption and the impossibility of forming close-packed vdW/H-bond 2D crystals.

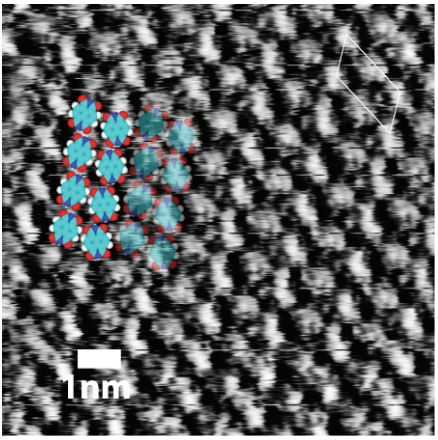

Figure 3-7

STM constant current mode image showing a monolayer pattern of **Molecule 11** at a concentration of 30 µM. Unit cell amounts to a = 1.0 ± 0.1, b = 1.8 ± 0.2 and γ = 56°. This particular pattern was not corrected from the underlying graphite. Tunneling parameters: I_t = 100pA and V_t = 200mV. nm^2.

Finally in the series of di-topic linkers stand the complementary (diacetylamino)pyridine which may recognize the di-imide moieties through the formation of triple hydrogen-bonds. STM investigation were carried out for **Molecule 13**. At the HOPG-TCB interface the time-dependent polymorphism of the assembly is striking. **Figure 3-10** depicts a time series of three images, each 100x100nm^2. The analysis of both polymorphs is shown in detail in **Figure 3-11**. The phases behaved as followed: **Molecule 13** was found to physisorb from diluted (< 10 µM) solutions on HOPG into two different and co-existing self-assembled networks (**Figure 3-11**). In the STM image in **Figure 3-11b** individual **Molecule 13** can be identified in view of their characteristic linear shape, where three aligned bright lobes can be discerned. Each lobe can be attributed to an aromatic core: the central one corresponds to the 1,4-disubstituted phenyl moiety, whereas the peripheral functions correspond to the 2,6-di(acylamino)pyridyl substituents.

The first pattern (left hand side **Figure 3-11b**, unit cell: a = (1.0 ± 0.2) nm, b = (2.5 ± 0.1) nm, α= (65 ± 4)°) shows a lamella-type motif. While molecule-molecule interactions at the intra-lamellar level are of van-der-Waals type, at the inter-lamellar level may or not consist of *H*-bonding. While it is certain that no complemetary hydrogen bond may be formed with the *Z,Z* conformer around the amide bond of the 2,6-di(acylamino)pyridyl (see **Figure 3-8** and **Figure 3-9**), there has been proof that a quadruple hydrogen bond is formed between the *E,Z* conformer in UHV experiments (Matena, Llanes-Pallas et al. 2009). However, the question on whether a quadruple bond is formed, remains unanswered in our investigations.

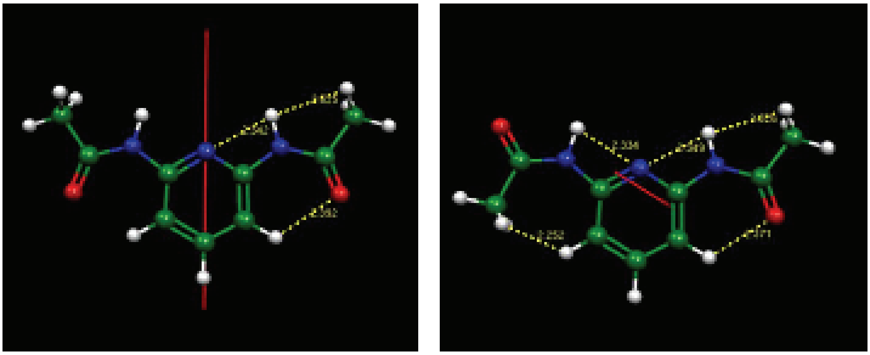

Figure 3-8

Z,Z conformer around the amide bond of 2,6-di(acylamino)pyridine and the *E,Z* (right hand side). The red arrow displays the dipole calculated at the DFT PBE 6-31G (d,p) level by GAMESS, amounting to 4.3 debye and 0.9 debye respectively. The *Z,Z* is preferred by 4.2 kcal/mol at this level of theory.

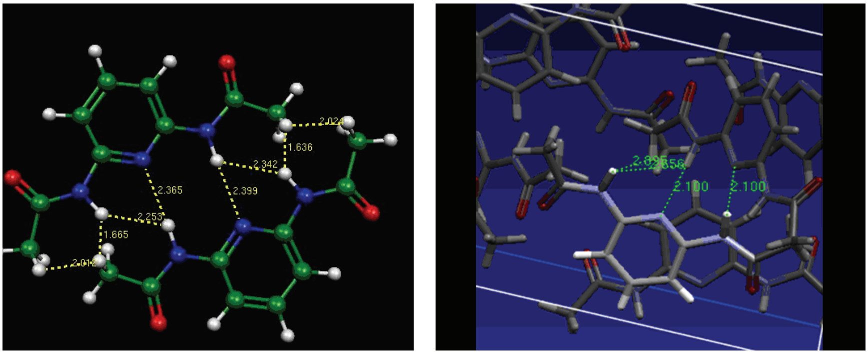

Figure 3-9

The left hand sice shows a DFT PBE 6-31G (d,p) (*Z,Z)* dimer with no strong H-bonds formed (i.e. <2.4Å). The structure is disfavored by ~2.0 kcal/mol. The right hand side shows the crystal structure of the 2,6-di(acylamino)pyridine, showing no H-bonds formed in the plane (Feibush, Figueroa et al. 1986).

In the second pattern (right hand side **Figure 3-11b**, unit cell: a = (3.3 ± 0.2) nm, b = (3.9 ± 0.1) nm, $\alpha = (47 \pm 2)°$), the molecules arrange in a distorted hexagonal structure. The self-assembly the exact packing could not be elucidated from the STM images. Statistical grain analysis on the STM constant-current images reveals that the apparent pores possess a projected surface area of 2.2 nm^2. Notably, the same two patterns were also observed by applying to the surface highly concentrated solutions (> 100 μM), were the evolution was monitored.

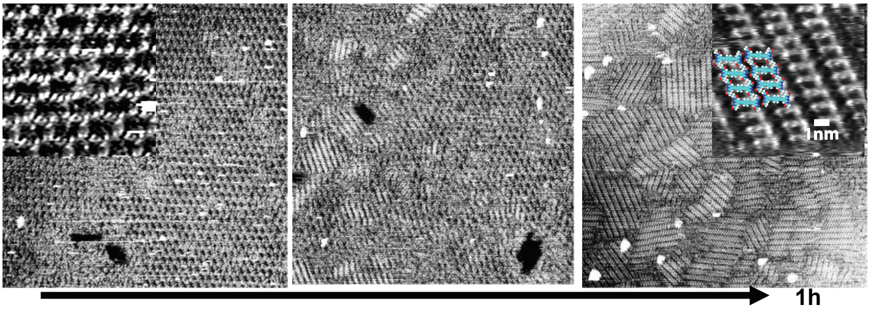

Figure 3-10
Time series large scale images of **Molecule 13** of out the deposition of high concentrated solutions (> 100 µM) at the HOPG interface)

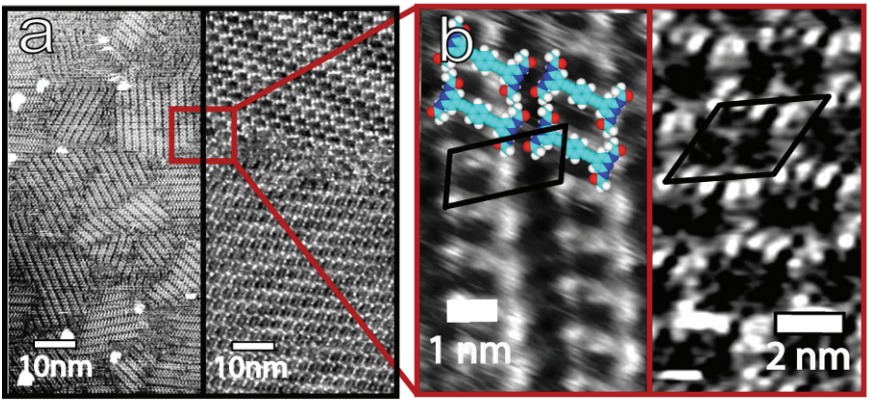

Figure 3-11
Constant current STM images of mono-component monolayers of physisorbed **Molecule 13**. (d1): a = (1.0 ± 0.2) nm b = (2.5 ± 0.1) nm α= (65 ± 4) ° and (d2): a = (3.3 ± 0.2) nm, b = (3.9 ± 0.1) nm, α = (47 ± 2)°. Average tunneling current I_t = 20 pA and sample bias (U_t) between 400 and 800 mV.

3.1.3 Multi-topic H-bond Molecules

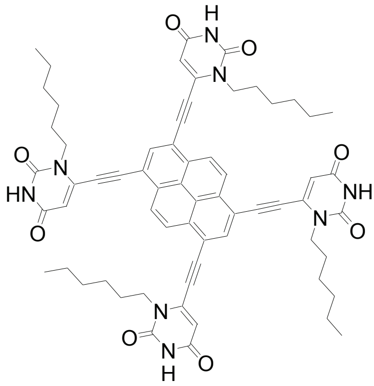

$C_{64}H_{66}N_8O_8$
Mol. Wt.: 1075.26

Molecule 14

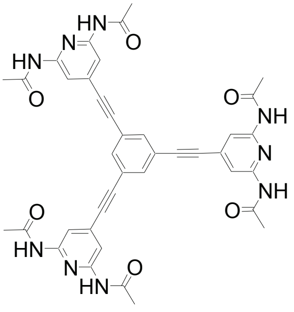

$C_{39}H_{33}N_9O_6$
Mol. Wt.: 723.74

Molecule 15

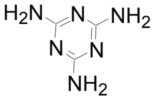

$C_3H_6N_6$
Mol. Wt.: 126.12

Molecule 16

Flat Multi-topic molecules decorated with hydrogen bond homo-associating units are intrinsically two dimensional in their supramolecular interactions and as such offer a good level of pre-programming in their mono-component state. Because of this, their study at the solid-liquid interfaces provides a reliable quantitative structural assignment. On the other hand, it makes the molecules highly insoluble due to their enthalpic gain upon association in close packed trimers and higher order polymers with respect to the di-topic molecules. In fact, as we will see in Chapter 6, the synthesis and design of multi-topical cornerstones is an ongoing challenge in supramolecular chemistry.

Figure 3-12 displays the pattern of a monolayer of pyrene-conjugate **Molecule 14**, prepared by depositing 5 μL of a diluted solution (concentration <10 μM). In the high-resolution image (**Figure 3-12b**) individual molecules within the ordered pattern can be identified by their characteristic cross-shape: the central bright spot corresponds to the pyrene aromatic core and the lateral protrusions correspond to the uracil aliphatic chains. The contrast is ruled by resonant tunneling between the Fermi level of the HOPG substrate and the frontier orbitals of the adsorbed molecules.(Lazzaroni, Calderone et al. 1997) From the proposed model, it clearly appears that neighboring molecules interact with each other through the formation of homo-molecular coupling occurring via the co-existence of two parallel *H*-bonds between their peripheral uracil moieties. The same packing was obtained from more concentrated solutions (> 100 μM) (image not shown). It is interesting to note that in view of the geometry and the uracil moiety homo-association geometry, assemblies of the molecule do not feature medium or long range order. **Figure 3-12a** reveals curved trajectories of molecules. In some sections, a unit cell can be extracted. The unit cell amounts to: a = (2.3 ± 0.1) nm b = (2.2 ± 0.1) nm α= (80 ± 4)°. The area of the unit cell occupied by a single molecule of **Molecule 14**, which amounts to $(4.95 \pm 0.06)\ nm^2$.

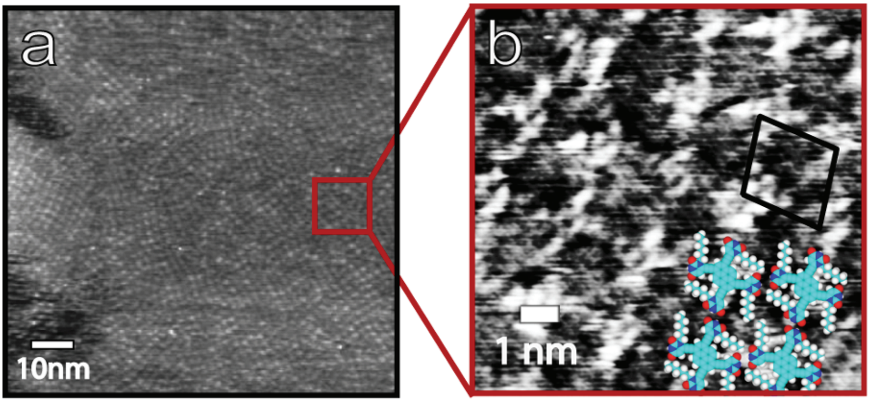

Figure 3-12
Constant current STM images of mono-component monolayers of physisorbed **Molecule 14**. The detail shows the unit cells (b): a = (2.3 ± 0.1) nm b = (2.2 ± 0.1) nm α = (80 ± 4)°, Average tunneling current I_t = 20 pA and sample bias (U_t) between 400 and 800 mV.

Molecule 15 is the only molecule in the chemical library we studied to be centro symmetric, and as such is the best candidate for highly crystalline 2D pattern formation both from mono- and bi- components systems. However the molecule is very insoluble. STM studies performed by Dr. Luc Piot showed that the molecule could be deposited from pure DMSO with subsequent evaporation and addition of TCB. Two polymorph structures were obtained in such a manner, with unti cell of a= 2.9 nm b= 2.7 nm, γ= 123° and a= 3.0 nm b= 2.6 nm, γ= 108.99°. However such a *dry film* approach, while it might be effective for technical studies, is far from the philosophy of equilibrium growth of 2D self-assembled architectures. When STM studies were performed from direct deposition of TCB, featuring 1-2% of DMSO, no ordered structures were obtained on the surface.

In light of this, an alternative molecule was chosen with complementary recognition capabilities to the uracil-like moieties. Melamine or **MEL**, **Molecule 16** with its three-fold symmetry, has been used extensively to engineering multidimensional H-bonded architectures (Seto and Whitesides 1991; Zerkowski, Seto et al. 1992; Arduini, Crego-Calama et al. 2003) both in solution and in the solid state. At the solid liquid interface in TCB solutions containing 1-2% DMSO two polymorphs have been observed **Figure 3-13**. One of this two polymorphs (left hand side of **Figure 3-13**) is better seen at lower concentrations (below 20μM) and surprisingly correlates with architectures observed on Au(111)(Xu, Dong et al. 2007; Silly, Shaw et al. 2008) and Ag/Si(111) (Keeling, Oxtoby et al. 2003; Perdigao, Fontes et al. 2007) substrates (discrepancies in the unit cells being below 20%). It is also of interest for our investigations in the next chapter to characterize the melamine molecule. **MEL** has three conformations, two more stable ones that are nearly degenerate in energy (**Figure 3-14**). We found the conformation with C_{3v} symmetry, where all hydrogens are pointing out of plane in the same direction, to be marginally more stable with about 2 meV than the conformation with C_s symmetry, where one of the NH_2 are pointing out of plane in the opposite direction than the other two. A planar geometry with D_{3h} symmetry, corresponding to a saddle point on the potential energy surface, was found to be 4-8 meV less stable than the C_{3v} symmetry. The right hand side of **Figure 3-14** shows the 0.001 sigma neutron diffraction structure (Varghese, Oconnell et al. 1977), showing that melamine crystallizes into an intermediate structure, featuring one in-plane NH_2 and two out of plane, confirming that the deformation energy of the NH_2 is low and will adapt to the best homo-association structure.

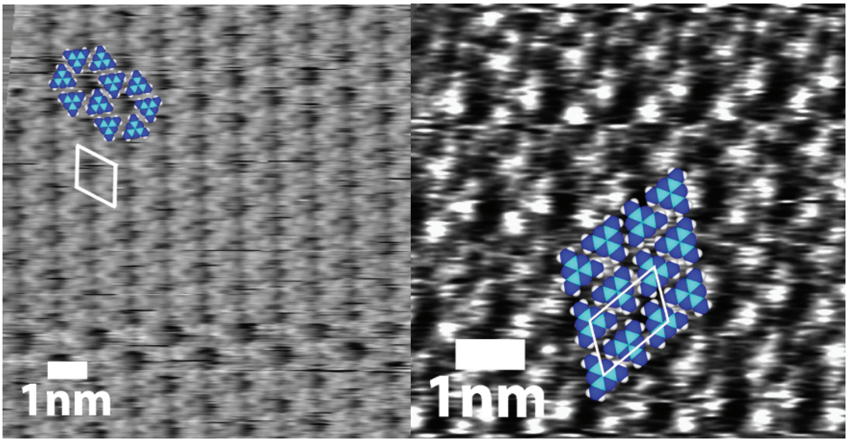

Figure 3-13

STM constant current mode image showing **Molecule 16 (MEL)** *polymorph a* and *polymorph b*, respectively. For *polymorph a* The unit cell is a = 1.2±0.1 nm, b= 0.8 ± 0.1 nm and γ = 58±2°. Tunneling parameters: V_t = 200mV, I_t = 10pA.. The unit cell of the right hand side amounts *a* = (1.1 ± 0.1) nm, *b* = (1.0 ± 0.2) nm, α = (61 ± 3)° with an average tunneling current (I_t) = 16 pA and bias voltage (V_t) = 400 mV.

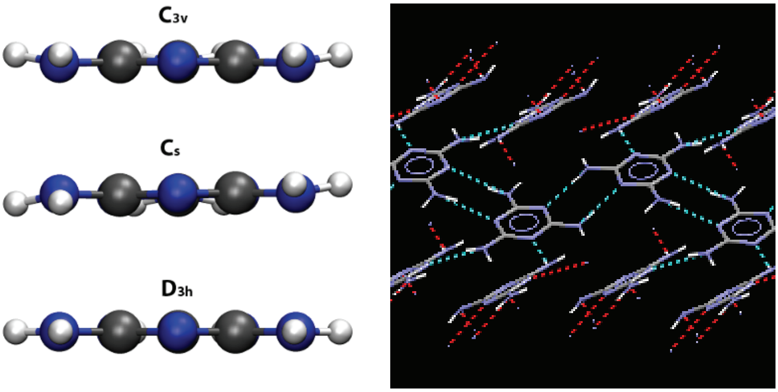

Figure 3-14
Three symmetries of melamine representing its two local geometrical minima (C_{3v} and C_s) and a planar saddle point (D_{3h}). The right hand side shows the conformations found in neutron diffraction experiments (Varghese, Oconnell et al. 1977).

In summary, the STM characterization of chemical libraries represents our first insight into pre-programmed architectures. It came to evidence through out this section that unambiguous assignment of spatial molecular arrangements in mono-component systems is not possible without the help of sophisticated tools such as the *molecular dynamic image simulation* technique introduced in Chapter 2. However the topological information embedded in the molecule will allow us to accurate assign molecular patterns when bi-component systems are sought, with precisions of less than 1Å, in the following chapter.

3.2 Semi-Quantitative Generalities in 2D Self-Assembly

We have witnessed how accurate STM elucidation of structural order with molecular resolution is arbitrary when no complementary recognition units are used. In fact, both accuracy and practical molecular bottom-up construction may be achieved by pre-programming self-assembly. In the present section we put forward a formalism to quantitatively describe the formation of a particular self-assembled phase, thus increasing the probability of its foreseeing.

Polymorphism. We evidenced how a fundamental aspect at solid-liquid interfaces is the unexpected appearance of polymorphs.(Bernstein 2002; Plass, Kim et al. 2004; Desiraju 2008; Lei, Surin et al. 2008). Polymorphism is the existence of two or more crystal structures made from the same molecular building-blocks. The structure’s short and long-range crystalline order depends on the number of contained defects. Beyond impurities, these defects can be regarded either as intrinsic or extrinsic (extrinsic defects are mainly due to kinetic traps or substrate commensurability, and have also been referred to as “pseudopolymorphs”. Moreover, we consider a property to be “intrinsic” (or intensive) when it belongs mostly to the design of a single molecular building block, and “extrinsic” (or extensive) when it belongs to an ensemble. (Plass, Kim et al. 2004; Bernstein 2005) Notably intrinsic defects may lead to the formation of polycrystalline tillings (Blunt, Russell et al. 2008) and glasses(Otero, Lukas et al. 2008). In a first instance a glass can be encompassed inside a broader definition of polymorphism (Greek: *poly* = many, *morph* = form). Formaly, some definitions of a *glass* are available. Kittel (Kittel 1996)defines a glass as a structure featuring local order through molecular connectivity. For instance the combination of components *A* and *B* can originate a rational sequence (*A-B-A-B-A-)* forming a network (Otero, Lukas et al. 2008). Critical phenomena physicists describe it more accurately in term of a frustration of the energy landscape, which traps the solid in amorphous state, a definition which we will use in Chapter 5 (Tanaka, Kawasaki et al. 2010).

Another important aspect of the solid-liquid interface (nanoscopic) that we have evidenced even in monocomponent systems is phase segregation. Phase segregation can be defined both as the co-existence of multiple segregated phases having different chemical composition adsorbed at the surface (type I) or by the adsorption of only one phase at the interface (type II), leaving the other components in the supernatant solution (Baker, Mougous et al. 1999). In fact, in monocomponent systems, phase segregation of type I and polymorphism by coexistence of polymorphic phases are identical concepts. Phase segregation of type II however is intrinsically bi-component, and assuming equilibrium conditions, the favored adsorbed phase at the interface is referred to as the thermodynamically stable phase, leaving the rest of the molecules in solution.

We will see some concrete examples of phase separation in the following Chapter. Again, phase segregation of type I can be defined as the appearance of two usually coexisting phases (despite one being the thermodynamically stable) and of type II for one component remaining in the supernatant solution because it cannot be adsorbed in the surface. Phenomenologically speaking this corresponds to a situation where in a two components system, A and B (which are in solution, in the presence of a substrate S and under equilibrium conditions) a unique bi-component 2D assembly AB_{ad} will not be formed but rather individual adsorption states, i.e.

$$a\mathrm{A}+b\mathrm{B}+\mathrm{S} \rightleftarrows a'\mathrm{A}_{\mathrm{ad}}+b'\mathrm{B}_{\mathrm{ad}}$$

Equation 3-1

for type I phase segregation or;

$$a\mathrm{A}+b\mathrm{B}+\mathrm{S} \rightleftarrows a'\mathrm{A}_{\mathrm{ad}}+b\mathrm{B}$$

Equation 3-2

for type II phase segregation, where the italic and primed letters correspond to different concentrations. Such scenario is commonly favored by tight molecular packing, where molecule-molecule and substrate-molecule interactions per unit area are maximized, giving rise to competitive adsorption phenomena because of the limited surface area available (Baker, Mougous et al. 1999; Kim, Plass et al. 2005; Ma, Wang et al. 2007; Bonini, Zalewski et al. 2009). We may also envisage a situation under non-equilibrium conditions, so that the segregated phase will be composed of the component in the supernatant solution that more quickly crystallizes onto the surface.(Ostwald 1897; Chung, Kim et al. 2008) Such a metastable phase is typically promoted by quick, strong molecule-molecule interactions.

Both polymorphism and segregation concepts are fundamental in pre-programing bi- and multi-component self-assembly. To understand their interplay at the solid-liquid interface, the difference in Gibbs free energy between two systems ***1*** and ***2*** (a system consisting of a substrate, a supernatant solution and physisorbed monolayers) can be ideally described as:

$$\Delta G_{1,2} = G_2 - G_1$$

Equation 3-3

$$G_1 = \sum_i \gamma_i [nm^{-2}] \cdot A_i^{phase} + \sum_j \mu_j [molecule^{-1}] \cdot N_j^{solvated}$$
$$+\gamma_{substrate/solvent}[nm^{-2}] \cdot \left(A^{total} - A^{occupied} \right)$$

Equation 3-4

where γ_i is the free energy per unit area of the i^th^ phase being part of the system ***a***, A_i^{phase} is the area occupied by the i^th^ phase in system ***a***, μ_j is the free energy per molecule in solution of the j^th^ component, $N_j^{solvated}$ is the number of molecules in solution of the j^th^ component, $\gamma_{substrate/solvent}$ is the free surface energy and $A^{occupied} = \sum_i A_i^{phase}$ is the total area occupied by the physisorbed monolayers.

When using molecules that are preferentially physisorbed at the interface, two limiting cases can be drawn. In the first case, by employing highly concentrated solutions, the number of molecules in solution is always much higher than that needed to form a tightly packed monolayer. The occupied area is equivalent to the total available area and the last term in equation *2* tends to zero (since there is no more free surface). The phase's free energy surface term $\gamma_i [nm^{-2}] \cdot A_i^{phase}$ is then minimized through the maximization of the number of molecules and interactions per unit area, i.e. tightly packed phases will be favored. It is worth noting that at saturated concentrations the solution free energy term $\sum_j \mu_j[molecule^{-1}] \cdot N_j^{solvated}$ still plays a dominant role (Kampschulte, Werblowsky et al. 2008).

In the second case, by using extremely low analyte concentrations (i.e. sub-monolayer concentrations, having a number of molecules in solution that is lower than that needed to form a tightly packed monolayer (Lei, Surin et al. 2008; Piot, Palma et al. 2009), the number of molecules in solution $N_j^{solvated}$ is negligible and the third term $\gamma_i[nm^{-2}] \cdot A_i^{phase}$ is dominant. Since the number of molecules is the limiting variable, the area occupied by one phase A_i^{phase} must be expressed as an explicit function of the number of molecules per unit cell in the ith phase, and the total number of adsorbed molecules in the ith phase becomes;

$$A_i^{phase} = \frac{A_i^{unit\ cell}}{\sum_j N_{i,j}^{unit\ cell}} \cdot \left(\sum_j N_{i,j}^{adsorbed} \right)$$

Equation 3-5

where $A_i^{unit\ cell}$ is the unit cell area of the ith phase, $N_{i,j}^{unit\ cell}$ is the number of molecules of the jth component in the unit cell of the ith phase and $N_{i,j}^{adsorbed}$ is the total number of molecules adsorbed in the ith phase. Then the second term of **Equation 3-4** becomes independent of the unit cell area and will be minimized through the maximization of the number of interactions per molecule in the unit cell. This *low-concentration* regime offers many advantages, since it helps us better describe our system. Particulary, the system may now be regarded as having a simplified phenomenological grammar, where both components are a priori adsorbed in the surface, i.e.

$$a\mathrm{A}_{\mathrm{ad}} + b\mathrm{B}_{\mathrm{ad}} \rightleftarrows d\mathrm{AB}_{\mathrm{ad}}$$

Equation 3-6

In the following Chapters we will make use of such approximations extensively and describe how both phase segregation and polymorphism can be attributed to the intrinsic chemical design of the molecular building blocks, by taking into account the enthalpic contributions to the free energies by means of the previous equations, through their intermolecular energies.

In the literature, the awareness of concentration-dependent polymorphism was brought for the first time by De Feyter and co-workers, which parametrized using a mean-field approach, the thermodynamics of the adsorption–desorption processes thus providing a first quantitative insight into the stabilities of these polymorphs (Lei, Tahara et al. 2008). At the same time, Lackinger and co-workers developed a semi-quantitative model to explain polymorphism in H-bonded bi-component networks which we include in the corresponding section of the **Appendix**.

While the statements of free energy in equations **Equation 3-4** and Lackinger's **Equation 8-1** are virtually identical, **Equation 3-4** shows more explicitly how only the surface free energy per unit area is important when the number of molecules in solution can be neglected, whereas **Equation 8-1** is useful for a "top-down" understanding of experimental data. As such, we will see in the next chapter how multiple approximations can be made to transform **Equation 3-4** in a "bottom-up" tool for a priori prediction of the thermodynamically stable phase, thus allowing to *pre-program* self-assembly at a first level. Such a level of approximation can be improved by metropolis monte-carlo or molecular dynamics simulations. The previous has been recently used to unfold a quantitative view of pattern formation in multicomponent systems (Weber, Burkalov et al. 2008), while we introduce for the first time the latter in Chapter 5.

4 2D H-bonded Bi-Component Self-Assembly

In this chapter we will show the characterization of molecules with complementary recognition untis which are combined in order to pre-program 2D self-assembly. The molecules shown are based on the libraries seen in the previous chapter and based on well-known recognition priciples (**Figure 4-1)**. In collaboration with the group of Professor Bonifazi the first library is based on the recognition between uracil with (diacetylamine)pyridil, which was first used by Krager and (Feibush, Figueroa et al. 1986) and then extensively used in supramolecular chemistry by (Hamilton and Vanengen 1987) and Lehn, shown in **Figure 4-1b**, with R=COMe units. At the same time, Diederich and coworkers proposed a library through the use of amidinium with carboxylic acid **Figure 4-1a** and cytosine with iso-cytosine recognition units **Figure 4-1c**. In the present chapter we will focus on the systematic STM characterization of self-recognition 2D self-assembly among Bonifazi's and coworkers library while the Diederich and coworkers library is in active development, concept-molecules of which we will show on Chapter 6. **Figure 4-1d** represents the AAA-DDD recongtion units as effectively introduced by Leigh and coworkers, with a record association constant in solution of 1x10^{12} (Blight, Camara-Campos et al. 2009). This last complementary recongnition unit is featured in a concept molecule which we will introduce in Chapter 5.

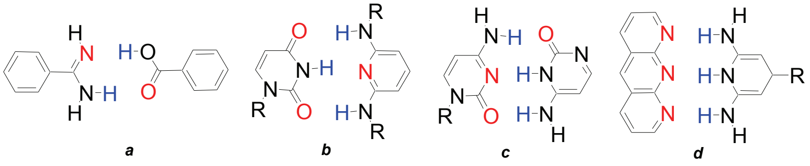

Figure 4-1
Complementary recognition units studied in the following chapters.

4.1 Complementary Recognition into Discrete Architectures

STM measurements have then been performed in order to provide a proof, in the real space, of the formation of bi-component *H*-bonded complexes on atomically flat surfaces. Indeed, titration methods are common in supramolecular chemistry for quantifying the complexation of a monovalent ligand with a receptor. For instance, the stoichiometries and association free energy for the H-bonded dimers of **Molecule 5** and **Molecule 6** in CDCl3 at 295 K amount to 1:1 and 4.158 kcal/mol, through NMR measurements (Piot, Palma et al. 2009).

Given the previously described associating propensity of **Molecule 6** and **Molecule 5** in solution, as proved by NMR and FTIR measurements (Piot, Palma et al. 2009), we extended our investigation to the co-adsorption of the modules at the solid-liquid interface. The solutions of **Molecule 6** and **Molecule 5** have been prepared in a mixture of 1-phenyloctane and toluene in order to increase the solubility of both components and to thus obtain a homogeneous phases. The drop-casting of a 1:1 molar solution of the molecules led to the adsorption of only **Molecule 5** on the basal plane of graphite. This has been evidenced by STM measurements showing the presence of a packing motif identical to that observed for the mono-component monolayers of molecule **Molecule 5** in Chapter 3 **Figure 3-1**. This might be due to both the lower affinity of **Molecule 6** for HOPG and to the stabilization of the monolayer of **Molecule 5** through homo-association forming supramolecular [**Molecule 5·Molecule 5**] dimers. Making use of a solution with a 1:10 molar ratio where **Molecule 6** is in excess (*i.e.,* 0.4 mM of **Molecule 5** and 4 mM of **Molecule 5** in an equi-volume solution), we have observed the formation of a novel self-assembly pattern on the surface (**Figure 4-2**). We refer to this approach of using a different solution stoichiometry to favour the adsorption of both components as the *le Chatellier* principle approach, which we will also use in the next section. Phenomenologically speaking, if two components in solution A and B are in equilibrium contact with the substrate S, the *le Chatellier* principle states that their 2D self-assembly AB_{ad} occurs at non-stoichiometric concentrations, otherwise phase separation occurs, i.e.

$$\text{If a} = \text{b},\ a\text{A}+b\text{B}+\text{S} \rightleftarrows a\text{A} + b\text{B}_{\text{ad}}$$

$$\text{If and only if a} \neq \text{b},\ a\text{A}+b\text{B}+\text{S} \rightleftarrows d\text{AB}_{\text{ad}}$$

Equation 4-1

The STM image in **Figure 4-2** reveals bright rods, the length of which is in good accordance with the cumulative contour lengths of molecule **Molecule 6** and the conjugated fragment of **Molecule 5**, whereas the darker parts of the image corresponds to the alkoxy chain of **Molecule 6**. On **Figure 4-2b** a few molecules (coloured in blue and yellow for **Molecule 6** and**Molecule 5**, respectively) are depicted on the STM image. In combination with the underlying STM image it provides unambiguous evidence for the existence of [**Molecule 5·Molecule 6**] dimers on the surface, each of them being composed by one blue (**Molecule 6**) and one yellow (**Molecule 5**) molecule. Given that such a dimerization through *H*-bonding interactions has been also detected in solution by NMR measurements, it is most likely that the dimers are formed in solution and then transferred to the graphite surface as bi-component entities.

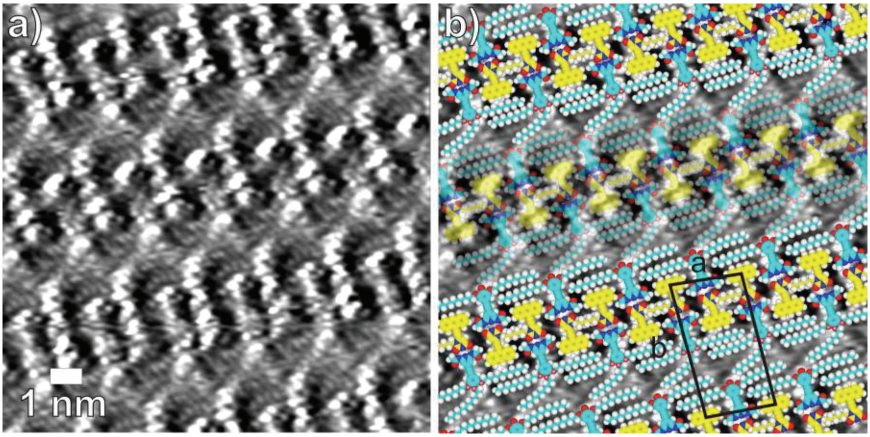

Figure 4-2
a) STM current image of the monolayers formed by mixing molecule **Molecule 5** and **Molecule 6** on the HOPG-solution interface. Each dimer is composed by one **Molecule 5** (yeloow) and one **Molecule 6** (blue). a) The unit cell is depicted in black. b) Proposed model of the assembly. Tunneling parameters: $I_t = 55$ pA; $U_t = 400$ mV.

To prove the general applicability of 2D recognition for the co-deposition of two or more components at the solid-liquid interface, we have extended our study to other molecular modules pre-programmed to generate more complex geometries. In this view, the multidentate system such as **Molecule 14** has been synthesized in order to use a tetrasubstituted pyrene ring as a cornerstone for the self-assembly. According to its geometry, one can expect that the recognition and the combination of each uracil unit at the four extremities of **Molecule 14** with one 2,6-(diacetylamino)pyridine of **Molecule 5** results in the generation of pentameric species [(**Molecule 6**)$_4$·**Molecule 14**]. Upon physisorption of only **Molecule 14** on HOPG, large ordered domains, featuring a porous structure, have been observed. The molecules have been found to interact with their four neighbours via *H*-bonding interactions. The resulting unit-cell is rhombic and contains one molecule, as studied in the previous Chapter. Surprisingly, by exploiting the previously used procedure for the formation of dimers, it has not been possible to obtain any hybrid complexes based on **Molecule 6** and **Molecule 14** on the surface. In fact phase segration occurred at various conditions investigated, it was found that only **Molecule 6** adsorbed on the surface, even at different molar ratios (ranging from 1:1 up to 1:10 of **Molecule**

6: **Molecule 14**), one reason could point towards the insolubility of **Molecule 14**. We have therefore opted to employ a *non-equilibirum* procedure, based on two steps deposition, again making use of the previous notation,

$$1.\ a\mathrm{A}+\mathrm{S} \longrightarrow a\mathrm{A}_{\mathrm{ad}}$$

$$2.\ a\mathrm{A}_{\mathrm{ad}} + b\mathrm{B} \longrightarrow d\mathrm{AB}_{\mathrm{ad}}$$

Equation 4-2

In the experiments, first a monolayer of **Molecule 14** has been formed upon deposition of a drop of a 0.5 mM solution in 1-phenyloctane to HOPG, and the resulting structure has been thoroughly characterized by STM measurements. Then, an additional drop of a solution containing molecule **Molecule 6** in 1-phenyloctane (conc. 0.2 mM) has been deposited on the surface. After being kept overnight at r.t., the wet film has been studied *in-situ* by STM. **Figure 4-3** exhibits a new pattern composed of discrete self-assembled complexes, each of them comprising one **Molecule 14** linked, through triple *H*-bonding interactions, to four surrounding **Molecule 6**, thereby forming the pentameric supramolecular structure [(**Molecule 6**)$_4$·**Molecule 14**]. Three main different contrasts are present in the STM image, the brighter one being mainly attributed to the aromatic residues of both **Molecule 14** and **Molecule 6**, whereas the medium and lower contrast regions correspond to the alkyl chains and to the vacancies of the monolayer, respectively. Since the "cross geometry" of such a complex avoid dense packing on the surface, it is not surprising to observe uncoated areas exposing the HOPG surface. These vacancies are most likely filled with solvent molecules exhibiting a dynamics on a time scale faster than that of the STM scan rate.

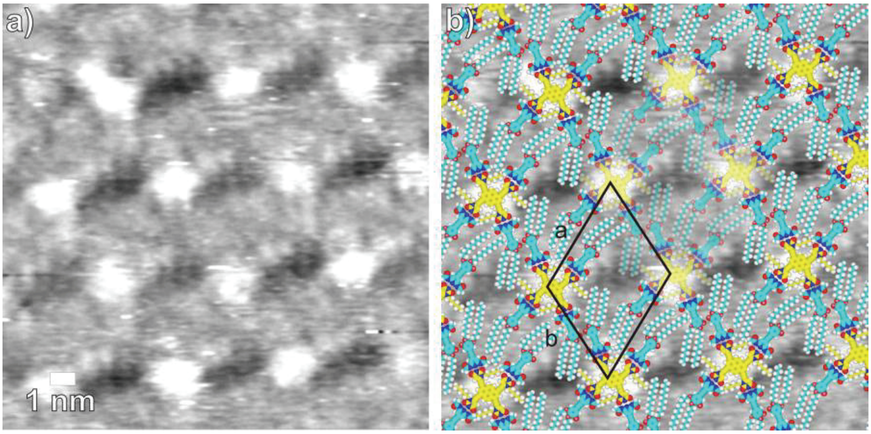

Figure 4-3

a) STM image of the monolayer formed with **Molecule 6** and **Molecule 14**. The addition of a solution of **Molecule 14** on top of an already existing monolayer of

1 is followed by the formation of complexes. b) Proposed model showing that each complex is composed by one **Molecule 14** surrounded by four **Molecule 6**. Tunneling parameters: I_t = 10 pA; U_t = 500 mV.

In summary, we have reported high-resolution images which made it possible to unravel the packing of single *H*-bonded complexes on the surface. Two important hypothesis can be put forward. It appeared that dimers [**Molecule 5·Molecule 6**] have been formed in the solution and then adsorbed on the surface, whereas the [(**Molecule 6**)$_4$·**Molecule 14**] pentamers have been assembled directly on the surface of the sample as evidenced *in-situ* through a titration experiment. The presented results provide evidence for the high flexibility of the approach, which can be used for binding molecules into different polygonal bi-component architectures. This finding represents a proof of principle of the approach and opens perspectives towards the formation of nanoporous and multi-component supramolecular networks that can be used for the confinement of functional molecules at determined locations.

4.2 Complementary Recognition into Amorphous Networks

Following the conclusions of the previous section, it now appears to be possible to extend complex formation in solution or in the surface to create 2D supramolecular architectures mastering the already proven molecular recognition strategy. However the formation of discrete entities and the construction of full architectures, whether appearing in close relationship, represent completely different practical and theoretical phenomena. In a first instance, it must be noted that there does not exist any experimental technique, other than the prototype calorimetric tools described in Chapter 2, to characterize quantitatively (i.e. through thermodynamics, kinetics and order parameters) extended ordered architectures in solution. Solid-state and liquid-crystal techniques might only reveal short-range order parameters. Similarly, construction of 2D extended architectures remains at a first glance elusive. Borrowing concepts from crystal engineering and growth (Desiraju 1989; Desiraju 1995; Hyde, Larsson et al. 1996) the following questions arise: Is the nucleation and/or growth of a self-assembled network equilibrium or non-equilibrium? Does it follow an order? Is it a solution or a surface nucleation/growth phenomenon? Although we have put forward a semi-quantitative thermodynamic theory of polymorph discrimination in 2D in Chapter 3, we stress again that the equilibrium ansatz cannot predict whether or not a 2D architecture can be formed *a priori*. We leave the tentative answers to these questions to Chapter 5, although we advance in this subsection the qualitative principles for effective Supramolecular Engineering.

In the following section, we proceed to combine one ditopic linker **Molecule 13** with the previously studied **Molecule 14** to try and form extended 2D bi-component architectures. Two first obvious factors must be considered in the rational design of such supramolecular architectures: *i*) the symmetry and *ii*) the binding capabilities (thus the valence) of the building blocks. The overall shape of the resulting supramolecular assembly is then a consequence of these parameters (Leininger, Olenyuk et al. 2000). To accomplish this goal, two types of conformational-rigid geometrical modules (angular and linear) are used with multiple complementary *H*-bonding, again specifically, a 1,3,6,8-tetraethynylpyrene exposing four uracil groups (Acceptor-Donor-Acceptor, ADA) positioned at 60° and 120° relative to each other has been designed to interact with a complementary linear module, a 1,4-diethynyl benzene derivative bearing two 2,6-di(acylamino)pyridyl units (Donor-Acceptor-Donor, DAD), through triple *H*-bonds (**Figure 4-4**).

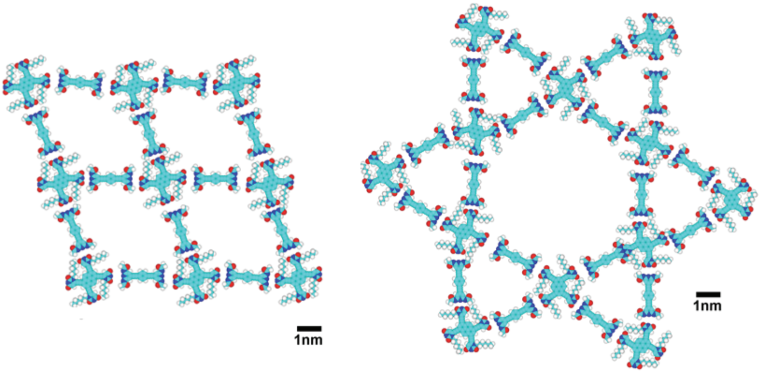

Figure 4-4
Schematic representation of possible polygonal networks which can be obtained combining tetratopic and ditopic modules **Molecule 13** (linker) and **Molecule 14** (corner stone).

Qualitatively, steady-state UV/Vis absorption and emission photophysical measurements can characterize a supramolecular aggregate. Titration measurements suggest the reversible formation of multiple oligomeric species with slightly modulated fluorescence spectra, reflecting the presence of various assemblies between the two polytopic receptors (note that the poor solubility of the *H*-bonding molecules in aprotic solvents did not allow to study the self-assembly process in solution by ^{1}H-NMR spectroscopy). **Molecule 13** and **Molecule 14** are strong absorbers in the UV region with maxima at 345 nm (ε = 37,500 $M^{-1}cm^{-1}$) and 324 nm (ε = 40,600 $M^{-1}cm^{-1}$), respectively, in DMSO. Interestingly, only a clear proof of molecular recognition was obtained in a 1:50 solution of DMSO/1,2,4-trichlorobenzene. Upon addition of one equivalent of molecule **Molecule 13**, the absorption spectrum of the pyrene-like **Molecule 14** in the Vis spectral region undergoes significant changes and clean isosbestic points are found at 435 and 497 nm (**Figure 4-5**). (To rule out the formation of homo-molecular aggregates of linker **Molecule 13** in solution we carried out a control experiment in which the concentration of **Molecule 13** is progressively increased, while absorption and fluorescence spectra are monitored (same solvent mixture as for the titration of **Molecule 14** with linker **Molecule 13**). No spectral changes attributable to the formation of homo-molecular aggregates are observed). The former isosbestic point is slightly shifted to 427 nm after further addition of molecule **Molecule 13 (**up to 2.4 equivalents, **Figure 4-5**). At 2.5 equivalents or higher, extensive formation of suspended aggregates occurs. In parallel to changes in absorption spectra, substantial variations of the fluorescence profiles are detected during the titration. During the initial stage (**Figure 4-5b**) the strong green fluorescence signal of the pyrene derivative is decreased by 80% and a novel emission band, peaked at around 570 nm, grows up with an isoemissive point at 593 nm. During the second titration step, the pyrene-centered fluorescence signal of **Molecule 14** is further decreased down to less than 4 % of its initial value, whereas the intensity of the new emission band is slightly or no affected (**Figure 4-5d**). Notably, the isoemissive point observed during the first stage of the titration is lost, pointing to the formation of more than one emissive species. Note that this complexation does not appear to be due to the formation of a pi-stacked excimer, since control experiments were done to strengthen the hypothesis of H-bond complexation (Llanes-Pallas, Palma et al. 2009).

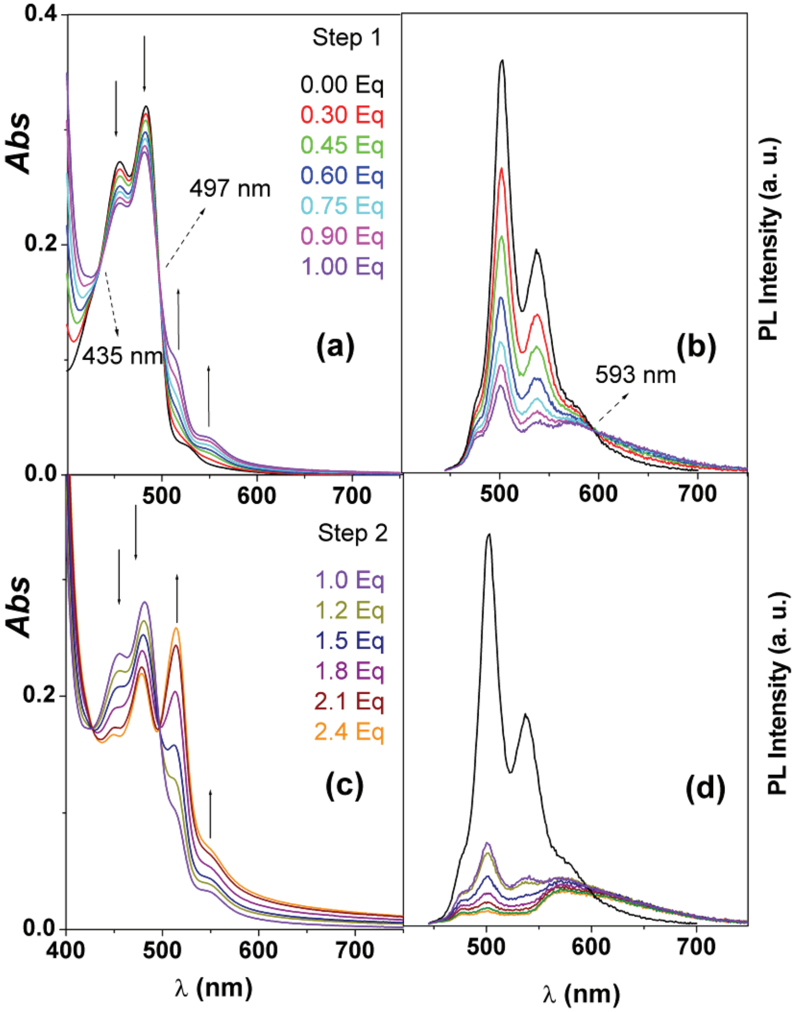

Figure 4-5

Changes of the absorption (left) and fluorescence spectra (right) of a 8.4 × 10^{-6} M solution of module **Molecule 14** in DMSO/1,3,4-trichlorobenzene (1:50) upon addition of increasing amounts of linker **Molecule 13** (from 0 to 2.0 × 10^{-5} M). Stage 1: panels (a) and (b); stage 2: panels (c) and (d). Dashed arrows indicate the isosbestic (a-b) and isoemissive points (c-d). Note that **Molecule 13** absorbs below 435, proved by the isosbestic point at λ_{exc} = 435 nm where the absorbance value is virtually constant throughout the entire titration.

Having qualitatively proof of association in solution, we can use the same conditions to visualize the formation of 2D networks at the HOPG-TCB interface. However, as introduced, there is a particular difference between thermodynamics of formation of supramolecular oligomers in solution and on the surface. We can identify at first the difficulty to direct the deposition of two or more molecules on a surface, because of the difference in adsorption energies

(Wetterer, Lavrich et al. 1998; Zacharia, Ulbricht et al. 2004) of the components and their tendency to minimize the occupied area. Given that adsorption energy is an unknown variable at this point **Equation 3-4** cannot be used to estimate whether or not competitive adsorption will occur. For avoiding such possibility of competitive adsorption we try two approaches, the *Le Chatellier* principle approach described in the previous section, which consist of tuning the relative concentrations of the components to favor the adsorption of both components in the surface and the *low-concentration* approach, also discussed in Chapter 2, and described in **Equation 3-4**. Low-concentrated solutions can be used as a strategy to prevent competitive adsorption,(Kampschulte, Werblowsky et al. 2008; Palma, Bonini et al. 2008; Palma, Bonini et al. 2008) thus operating in a regime where the packing is only ruled by the intermolecular interactions thus minimizing the role of substrate-molecule interactions.

We first proceed through the L*e Chatellier* principle approach. We found that STM images of the self-assembled pattern obtained from films prepared depositing equimolar mixtures of **Molecule 13** and **Molecule 14** on HOPG from concentrated solutions (concentration > 100 μM, supporting information), exactly matches the one obtained for neat films composed of linear unit **Molecule 13**, featuring a unit cell: a = (3.1 ± 0.2) nm, b = (3.7 ± 0.2) nm, α= (50 ± 3)°. This indicates that the formation of **Molecule 13**-based monolayer is thermodynamically favored. Noteworthy no co-existing structured domains containing molecule **Molecule 14** have been imaged from over 100 survey images (*i.e.* mapping an area of 10^4 nm^2), even when exceeding the concentration of **Molecule 14,** which point out to phase segregation of type II, as discussed in Chapter 3, section 2. Therefore under these conditions, **Molecule 14** remains in the supernatant solution. To avoid such a fractionation, we turned to the second strategy, opting to operate in a controlled regime, *i.e.,* by using a concentration below that the one needed to form a full monolayer. Given the difference in adsorption energies of the components and the tendency to minimize the occupied area, it is possible to set a threshold of concentration in which there cannot be competitive adsorption. Thus, we operate in a regime where the packing is dominated mostly by the highly-directional intermolecular interactions and where substrate-molecule interactions contribute less to determining phase formation (Kampschulte, Werblowsky et al. 2008; Palma, Bonini et al. 2008; Palma, Bonini et al. 2008) This approximation holds as long as the molecule-solvent interactions are negligible. By setting the concentration around or below that necessary to form a densely packed monolayer of the different molecular patterns, we can assure that the minimization of the global interfacial energy, **Equation 3-4** (therefore the thermodynamically stable phase) depends only on the intermolecular energies between assemblies of **Molecule 13** and **Molecule 14**. Noteworthy, **Equation 3-4** is a function of the interfacial area, which depends experimentally on the area wetted by the solution. This approach is somewhat analogous to that used for ultra-high vacuum STM experiments, where polymorphism in multicomponent networks is avoided through a careful control of the stoichiometry of the components deposited on the surfaces.(Barth 2007). Thus, the use of very low concentrated solutions (< 10 μM) allowed the simultaneous physisorption of the solutes at the solid-liquid interface, preventing unfavorable (thermodynamically- or kinetically-driven) competitive adsorption between **Molecule 13** and **Molecule 14**. As expected, only operating at concentrations below 10 μM a new **Molecule 13** and **Molecule 14** heterogeneous hybrid phase appears **(Figure 4-6**; large area images are shown in the **Appendix Figure 8-9**). Such a heterogeneous phase was also found to coexist with the two packing modes of **Molecule 13**, which, in this case, remain minority. We remark that the different phase coverages of the **Molecule 13·Molecule 14** phase varied for different experiments and a trend could not be established. This is true even when employing ratios of 1:1 1:2, 1:4 and 1:6 at different concentrations (from ~0.02 μM to ~6 μM) of **Molecule 14** and **Molecule 13**, respectively. Upon annealing of some samples (~50°C, ~2 minutes) phases of **Molecule 13** were only encountered**.** This further confirms that a monocomponent assembly is the thermodynamically stable phase and that the imaging of the heterogeneous phase is kinetically controlled. This kinetic control at low concentrations further extends the hypothesis that the 2D oligomeric species are created in solution and then directly transferred to the surface were they cannot ripe into 2D crystals, thus forming a frustrated 2D pattern. Interestingly, we will see in the Chapter 5 that the condition of growth of a 2D pattern is given under reversible conditions, where oligomers are constantly assembling and dis-assemblying in the surface. Since oligomers have by definition a higher association constant in the surface than in solution, we can conclude that the condition of growth is that weak recognition will happen in solution. This future piece of information comes to strengthen why no 2D pattern formation in the surface can be seen for complexes of (diacetylamino)pyridines and uracils. In other words, their complexation is too strong in solution, thus their interaction is not reversible in the substrate in the timescales needed for self-assembly. This might also explain why monocomponents phases of **Molecule 13** are favored. Rapid growth of **Molecule 13** domains will consume amorphous slow growing domains of bi-component system.

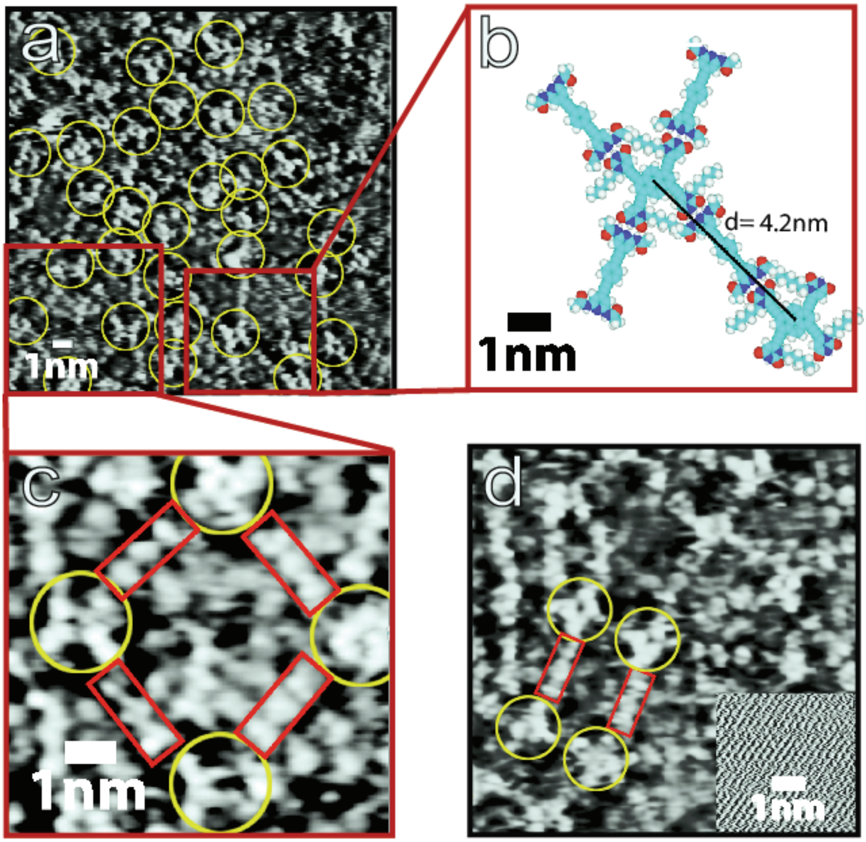

Figure 4-6
Sub-molecularly resolved supramolecular aggregates featuring discrete oligomeric species. (**Molecule 14**)$_m$·(**Molecule 13**)$_n$ prepared from diluted equimolar solutions. Yellow circle identifies a single molecule of tetra-substituted 1,3,6,8-pyrene derivative **Molecule 14** whilst red rectangle a single molecule of **Molecule 13**. b) Model assembly of a hexameric hybrid complex (**Molecule 14**)$_2$·(**Molecule 13**)$_4$ showing the distance values as estimated by MM2-based computational geometry optimization. c, d) Heterogeneous **Molecule 14·Molecule 13** phase images highlighting the presence of rectangular and rhomboidal nanopolygons as consequence of complementary *H*-bonding motifs between molecules **Molecule 14** and **Molecule 13**. The inset in d) shows the underlying graphite. All STM constant current images where recorded at I_t = 20pA and U_t = 400mV.

Only when high-resolution images of the **Molecule 14·Molecule 13** heterogeneous phase (**Figure 4-6**) are obtained, **Molecule 14** and **Molecule 13** can be unequivocally assigned after close inspection. The images reveal several polygonal-like oligomeric species featuring hollow structures in line with the geometries shown in **Figure 4-4**. The high adsorption energies of the modules are also evidenced: polygons featuring large pore areas (**Figure 4-6c**) contain adsorbed molecules of **Molecule 13**. Pores featuring small areas appear empty of any solute molecule (**Figure 4-6d**). As described in the introduction, the structures of the supramolecular complexes are dictated by the pre-designed geometry of the constituting molecular modules. In particular, the structural fingerprints of the single modules can be easily discerned within the formed oligomers. Tetratopic-pyrene **Molecule 14** is imaged as a bright spot exposing four arms (yellow circles) whereas ditopic-linker **Molecule 13** features three aligned bright lobes (red rectangles). The formation of polygonal assemblies composed by complementary **Molecule 14** and **Molecule 13** indicates the *H*-bonding interactions are established. Yet, STM image analysis revealed a low percentage of molecules forming the *H*-bonded pentamers, *i.e.* one **Molecule 14** surrounded by four *H*-bonded **Molecule 13**, as that depicted in Figure 6b, namely about 0.08 pentamers/nm^2 as estimated on 10 different images from different samples. The average angles γ and β in the pentamers relative to the pyrene centers, as determined from the STM images, amount to (71 ± 8)° and (110 ± 7)°, respectively. Indeed, there is some slight discrepancy from the theoretical angles defined relatively to the uracil groups of 60° and 120° because of the elongated pyrene unit. Furthermore, the average distance between two pyrene units in a linear **Molecule 14·Molecule 13·Molecule 14** oligomer was found to be (4.3 ± 0.4) nm, which is in good agreement with the theoretical value of 4.2 nm estimated by MM2-based geometry optimization (**Figure 4-6b**). Noteworthy, once formed, the supramolecular oligomeric motifs revealed to be stable for several minutes, thus no self-healing phenomena were observed in the experiment time scale (see **Appendix Figure 8-10** and **Figure 8-11**). Notably, some homo-molecular **Molecule 14** and **Molecule 13** recognition were also observed as co-existing events.

In summary our STM studies provided fundamental information on the design and engineering of supramolecular discrete patterns at interfaces. Even when preventing competitive adsorption by using low concentrations, the supramolecular (**Molecule 13·Molecule 14**) oligomers could not be observed to ripe into a thermodynamically-stable self-assembled 2D crystalline pattern. Two reasons maybe advanced at this stage: i) module **Molecule 14** is not centro symmetric, *i.e.* exists competing phenomena between the different nucleating nanopolygons in **Figure 4-6**. ii) the monocomponent phase formed by **Molecule 13** intrinsically appears to be both the thermodynamically favored and the fastest growing assembly. We revealed that it is possible to resolve sub-molecularly amorphous 2D phases, which can serve as a strong tool for the studying crystallization phenomena. In such phases, STM can locally probe dynamics (**Appendix Figure 8-10** and **Figure 8-11**) of single molecules, which are relatively decoupled from a densely packed monolayer.

4.3 Complementary Recognition into 2D Networks

Following our previous observations on frustrated amorphous 2D networks, we turn our efforts on choosing a multi-valent system which i) features a centrosymmetric cornerstone ii) does not feature any intrinsic polymorphism. Our task is simplified when we turn to the literature and highlight that the first example of a bi-component 2D network on ultra-high vacuum (UHV) was made exploiting the recognition of a periylene di-imide (PTCDI) with melamine **Molecule 16,** from now on **MEL**. Such a module, mixed with PTCDI, has been used to form highly ordered 2D arrays on Ag/Si(111) as thoroughly characterized by STM in UHV at room temperature (Theobald, Oxtoby et al. 2003).

In this section we report for the first time on the use of **MEL** to direct the generation of bi-component H-bonded networks at the solid-liquid interface. In particular, hexagonal porous networks have been tailored through the co-deposition of solutions containing **MEL** and the bis-functionalized uracil-bearing linear **Molecule 7** (**Figure 4-7**) on highly oriented pyrolytic graphite (HOPG) surfaces. Additionally, detailed STM experiments allowed the semi-quantitative determination of those energetic parameters essential to promote the formation of porous structures over tightly packed monolayers, thus offering a reliable enthalpic prediction of the formation of 2D assemblies at the solid-liquid interface. In the next section we will more explicitly show the enthalpic control principles following the equations in Chapter 3.

Experimental Details are given in the corresponding **Appendix** subsection. In general STM experiments were carried out by preparing and mixing of mother solutions, further diluted with TCB to yield concentrations of 3 ± 2 μM and 2 ± 1 μM of **Molecule 7** and **MEL**, respectively. By applying 5 μL of this new solution to the HOPG surface, a porous network has been obtained at the solid-liquid interface, as visualized by in-situ STM imaging at r.t. (**Figure 4-8**). The unit cell parameters are a = (3.9 ±0.2) nm, b = (3.9 ± 0.2) nm, γ= (60 ± 3)^o and A = (13.4 ± 0.6 nm2). **Figure 4-8b** exhibits a zoom-in of the ordered assembly evidencing the presence of hexagonal pores.

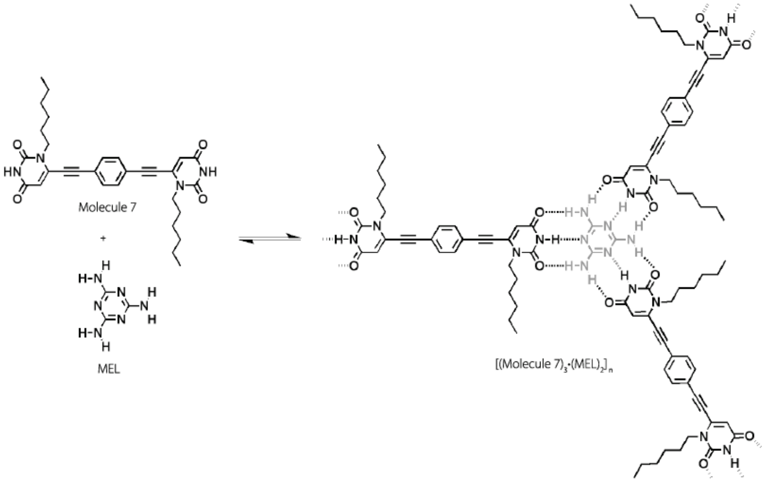

Figure 4-7
Molecular structures of the investigated **Molecule 7** and **MEL**. The formation of the hybrid ([(**Molecule** 7)$_y$·(**MEL**)$_x$]$_n$) assemblies through intermolecular H-bonds at the solid-liquid interface is also depicted.

Although we cannot resolve at the sub-molecular level both components in the images, the shape and size of the hexagonal pores are in perfect agreement with the models depicted in **Figure 4-8d**. However, the combination of these two compounds at the graphite-TCB interface also leads to the generation of other polygonal pores ranging from pentagons to octagons (**Figure 4-8a**). This can be tentatively explained taking into account the geometrical flexibility. In particular, a deviation of -8º or +12° from the ideal value of 120° for the angle between **Molecule 7-MEL-Molecule 7** is sufficient to generate heptagons or pentagons, respectively. Yet in this first example it is not clear if the distribution of the different geometrical shapes is stochastic or phenomenological. Latter on in Chapter 5 we will discover that such polygonal networks are kinetic products. The arrow on **Figure 4-8a** indicates a linear structure germinating from an edge of a polygon. Given that these types of architectures have always been found to nucleate from a melamine edge and that they resemble the arrays of **Molecule 7** at the same magnification, we can ascribe such a structure to a supramolecular assembly composed of **Molecule 7** linearly arranged through homo-coupling H-bonds. Time-resolved evidence of the dynamic nature and growth of such 1D array is shown in the **Appendix Figure 8-12**, proving the high reversibility of these bi-component porous networks. Noteworthy, porous networks have not been observed on films prepared using concentrated solutions, i.e. having a concentration higher than 20 μM. As introduced in the previous sections, due to the emergence of competitive physisorption between **Molecule 7** and **MEL** at the solid-liquid interface, at high concentrations only melamine molecules were found to be physisorbed on HOPG because of its high interaction energy per unit area . In fact, this concept is further developed in the next section.

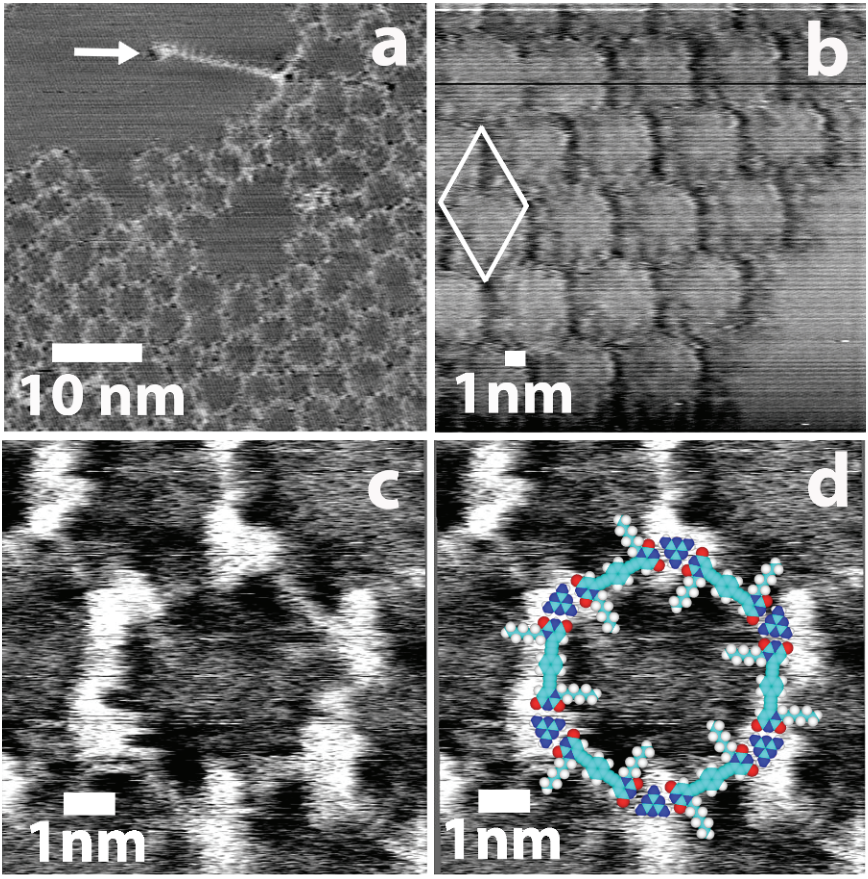

Figure 4-8
STM height images of the self-assembled pattern. (a) Polygonal structure; an arrow indicates the formation of a 1D assembly. (b) Zoomed region of an ordered hexagonal assembly. (c) Detail of a supramolecular hexagon and (d) the proposed assembly model. (a) It = 5 pA and Vt = 400 mV; (b) It = 30 pA and Vt =-600 mV; (c,d) It = 0.5 pA and Vt = -500 mV.

The observed porous architectures displayed in **Figure 4-8** have only been obtained with rather diluted solutions, i.e. featuring a sub-monolayer coverage. We can already recall **Equation 3-5** and taking into account the pattern's unit cell of assembly [(**Molecule 7**)$_3$·(**MEL**)$_2$] featuring an area A = (13.4 ± 0.6 nm2), which consists of three molecules of **Molecule 7** and two molecules of **MEL**, a full monolayer on one cm^2 of flat HOPG substrate contains in total 61 pmol of **Molecule 7** and **MEL**. If we assume a complete physisorption over one cm^2, under our experimental conditions, i.e 5uL of a ~2μM **Molecule 7**: **MEL** solution onto HOPG, there are ca. three times less molecules than those required to fully cover the surface with a self-assembled monolayer. By assuming a sub-monolayer coverage and a complete physisorption of the components at the interface, the prediction of the most stable network is simplified since the number of molecules on HOPG is constant. Noteworthy, the prediction of the molecular packing is not described by the minimization of the free interface energy per unit area, but rather by the total energy of the pattern consisting of N adsorbed molecules and the anisotropic/ isotropic intermolecular interactions (see **Table 4-1.**).

Table 4-1. semi-quantitatively illustrates this principle. The porous network formation is predicted if the concentration used is equivalent (or lower) to that required to form a mixed monolayer of **Molecule 7** and **MEL** on HOPG. Under such conditions, the driving force ruling the molecular packing is the gain in energy per mole of molecules in the adsorbed pattern: in fact, for sub-monolayer coverages, the packing energy density (eV nm^{-2}) does not determine the geometry of the physisorbed assembly. The adsorption energy of the individual components can be also ruled out (as long as it is >>kT), since there is no competitive adsorption between the components. **Table 4-1.** reveals that the H-bonding energy of adsorbed molecules for the $[(\textbf{Molecule 7})_3 \cdot (\textbf{MEL})_2]_n$ pmol phase is higher than that for the monocomponent phases, thus providing unambiguous explanation of the generation of such bicomponent assemblies. On the other hand, at high concentrations, the system tends to minimize its energy per unit area, leading to the formation of a patterned network composed of only **Molecule 7**. Noteworthy, the difference in H-bonding energy between a pmol of assembly **Molecule 7** and that of the hybrid $[(\textbf{Molecule 7})_3 \cdot (\textbf{MEL})_2]_n$ is 0.8×1011 eV (4 kcal mol^{-1}). Thus, if the gain in energy from dipole-dipole, van der Waals or other isotropic interactions in pattern of **Molecule 7** is higher than the latter value, the $[(\textbf{Molecule 7})_3 \cdot (\textbf{MEL})_2]_n$ porous assembly is not the thermodynamically-favored phase. The upper limit in van der Waals interactions hindering the formation of porous networks was previously set to ca. 0.11 eV per molecule (2.5 kcal mol^{-1}) for a melamine PTCDI system (Weber, Burlakov et al. 2008) i.e. lower than the 4 kcal mol^{-1} threshold value here determined. In the following section we will generalize this principle by using the ideas put forward in Chapter 3.

In summary, H-bond recognition among melamine and a linear bis-uracilic module allows the formation of a porous bi-component network at the solid-liquid interface. In analogy to self-assembly under UHV conditions, where the concentration conditions are used to direct polymorphism, we worked at sub-monolayer coverages to promote the formation of porous structures over tightly packed monolayers. Although other critical parameters such as solvent and isotropic molecular interactions should be taken into account to accurately pre-program the formation of multicomponent arrays, our simplified model offers reliable enthalpic prediction of 2D crystal formation at the solid-liquid interface when pre-designed molecular modules are employed.

Table 4-1.

Calculated energies for the formation of an ideal monolayer on HOPG neglecting the molecule-solvent and solvent-substrate interactions. $\mathbf{C_S}$ = surface concentration in a monolayer over an ideally flat HOPG surface; $\boldsymbol{E_H}$ = energy per *H*-bonding interaction; $\boldsymbol{E_A}$ = adsorption energy per molecule; $\boldsymbol{E_T}$ = *H*-bonding and adsorption energy per unit area; $\boldsymbol{E_{HA}}$ = *H*-bonding energy per picomol of adsorbed molecules. When the total number of molecules in the assembly is not controlled, the assembly formation is directed by the total energy per unit area, i.e. $\boldsymbol{E_T}$. In the latter case, the self-assembled network formed by **MEL** is the most stable. When the number of molecules adsorbed is fixed to sub-monolayer coverage (low concentration regime), the expected assembly is that formed by the[(**Molecule 7**)$_3$·(**MEL**)$_2$]$_n$ network.

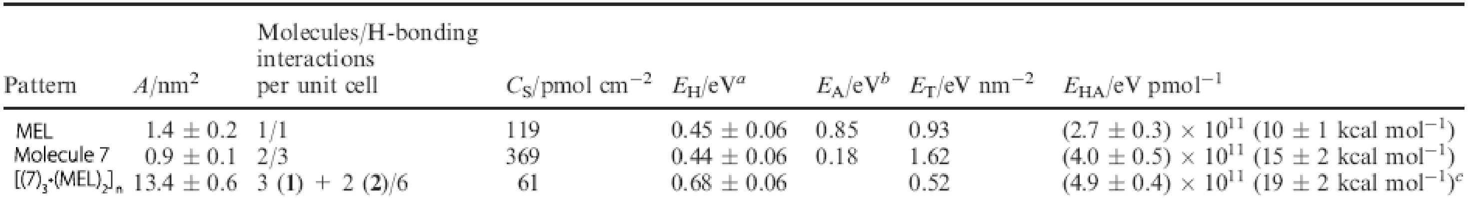

Pattern	A/nm^2	Molecules/H-bonding interactions per unit cell	C_S/pmol cm^{-2}	E_H/eV^a	E_A/eV^b	E_T/eV nm^{-2}	E_{HA}/eV pmol^{-1}
MEL	1.4 ± 0.2	1/1	119	0.45 ± 0.06	0.85	0.93	$(2.7 \pm 0.3) \times 10^{11}$ (10 ± 1 kcal mol^{-1})
Molecule 7	0.9 ± 0.1	2/3	369	0.44 ± 0.06	0.18	1.62	$(4.0 \pm 0.5) \times 10^{11}$ (15 ± 2 kcal mol^{-1})
$[(7)_3{\cdot}(\mathrm{MEL})_2]_n$	13.4 ± 0.6	3 (**1**) + 2 (**2**)/6	61	0.68 ± 0.06		0.52	$(4.9 \pm 0.4) \times 10^{11}$ (19 ± 2 kcal mol^{-1})^c

[a] In-vacuo interaction energy estimated by DFT calculations from melamine and 3H-Pyridine-2,6-dione fragments (Supp Info). The uncertainties are the standard deviations of the melamine H-bond dimer DFT energies reported in references (Perdigao, Perkins et al. 2006; Xu, Dong et al. 2007) and the PBE DFT 6-31G(p,d) calculation in this work, corresponding to values of 0.34, 0.43 and 0.44 eV respectively. [b] Parametrized with 0.061eV for each sp^2 carbon present.[12] [c] The calculation proceeds as follows: for each 2/3 picomols of **Molecule 7** and 1/3 picomols of molecule **MEL** there are 6/5 picomols of *H*-bond interactions worth 0.67 eV each.

4.4 Polymorphism and Phase Segregation in Bi-component Networks

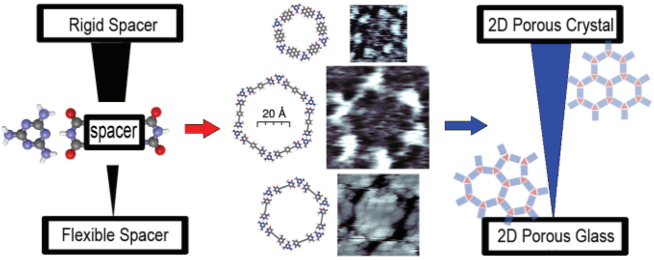

Figure 4-9
Tuning the linker flexibility and length

Here we exploit again the recognition of complementary hydrogen-bond moieties based on the donor-acceptor-donor (DAD) coupling of the melamine molecule with acceptor-donor-acceptor (ADA) imidic moieties as in the previous section. Our interest is however to apply the purely enthalpic theory of Chapter 3 and gain a deeper quantitative understanding on global enthalpy minima which rules the fundamental processes occurring at solid-liquid interfaces such as phase segregation and polymorphism. More importantly, we will try to address the origin of the *polygonal network* observed in the previous section by varying the nature of the linker. We will then show that in multi-component systems, phase segregation and polymorphism are hallmarks of self-assembly at solid-liquid interfaces. Under the right concentration conditions, the 2D porous polymorph of interest can be favored above all. Then it is possible to tune pore sizes in these bi-component nano-patters by modifying the design and length of the component acting as a linker, which are again **Molecule 7** and **Molecule 10**, **Molecule 11**, **Molecule 12**. By using flexible spacers amorphous polygonal networks can also be formed, in equilibrium with crystalline phases. Rigid spacers can form highly crystalline porous patterns, but without the introduction of bulky side groups or side chains the possibility of forming tight-packed polymorphs increases. These processes are explored by *in-situ* scanning tunneling microscopy (STM) at the solid-liquid interface in conjunction with density functional theory (DFT) computations. Experimental Details are given in the corresponding **Appendix** subsection.

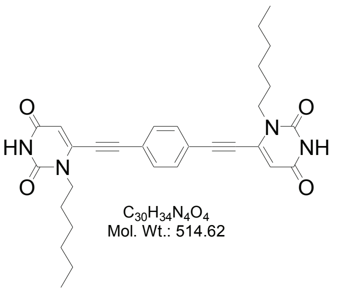

Molecule 7

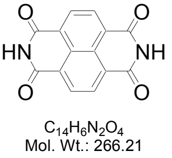

Molecule 11

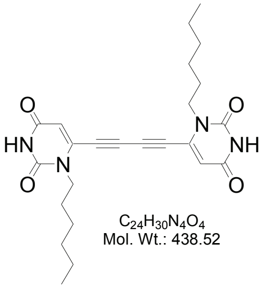

Molecule 10

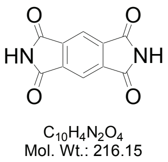

Molecule 12

Figure 4-10
Linkers used with melamine to study phase segregation and polymorphism

Imaging and Self-Assembly of 2D networks Self-assembly of the linkers with melamine **Molecule 16** (from now on **MEL**, for simplicity) into ordered bi-component networks is successfully obtained by applying 6 ± 1 μL. of the proper solutions in a solvent mixture of 1,2,4-trichlorobenzene (TCB) / dimethylsulfoxide (DMSO) to the basal plane of highly oriented pyrolytic graphite (HOPG) surface. This particular volume is chosen since it is the one needed for TCB to completely wet 1 cm^2 of HOPG and giving a scanning window of ~3h before dewetting occurs due to evaporation of the solvent. For the four investigated systems (**Molecule 7**+**MEL, Molecule 10**+**MEL**, **Molecule 11**+**MEL** and **Molecule 12**+**MEL**) an accurate control of the concentration and stoichiometry is needed to favor the formation of a particular bi-component pattern (see Phase Segregation subtitle below). The self-assembly at the solid-liquid interface of the mono-component systems were previously shown in Chapter 3.

STM images of the bi-component pattern structure formed by **Molecule 7**+**MEL**, which has been recently introduced (Palma, Bonini et al. 2008), are further analyzed in **Figure 4-11**. As discussed in Chapter 2, despite the theoretical prediction of a higher contrast of the **MEL** molecules at negative biases, in most cases (ca. 80%) a brighter contrast appears inside the pore areas in the constant current images, under both positive and negative biases (**Figure4-11b,d**). This bright contrast remains elusive and may mostly be ascribed to solvent molecules co-adsorbed at surfaces. The contribution of the solvent molecules co-adsorbed on the surface to the contrast has been already reported on porous structures, (Gutzler, R.; Lappe, et al. 2009) whereas the spontaneous contrast changes in the pores during scans would support the hypothesis of adsorption of molecules on the tip, changing its work-function. This leads to an inversion of the contrast: **MEL** molecules appear thus as wide black spots **Figure4-11c,d**. Similarly, the **Molecule 10+MEL** system on HOPG exhibits self-assembled patterns featuring polygonal structures (**Figure 4-12**). This pattern is characterized by a much higher polygon distribution; it is possible to identify a nonagon (red wire frames) evidenced by nine darker spots acting as corners. As previously discussed, most dark spots correspond to the location of the **MEL** molecules, as also revealed by comparing **Figure 4-12b-d**. Again, a brighter contrast is observed in the pores for the case of the constant current images (**Figure 4-12a,b**). The predicted hexagonal motif with molecular models is shown in **Figure 4-12d** (the red bar corresponds to 2.8 nm). The absence of spatially-extended single crystalline domains did not allow us to determine the unit cell for the predicted hexagonal self-assembled network, also called *polygonal network* or also a *glassy porous network*. Please note that a *glass* is historically used as a frustrated crystal (Zallen 1998), and has to do more to the dynamics than to an order parameter. Thus the glass classification of the polygonal networks is formally given in Chapter 5. Here, the polygonal phases can be better understood when classified in terms of a collection of local polymorph structures, since an order parameter is introduced until Chapter 5 (*vide infra* polymorphism section).

While in the networks obtained with the two previous linkers polymorphism is expressed through the formation of different polygons, in mixtures of **Molecule 11+MEL** polymorphism arises from the co-existence of one-dimensional supramolecular linear assemblies (**Figure 4-13a,b** grey arrow) and porous hexagonal networks (**Figure 4-13a,b** black arrow) formed by alternating units of **MEL** and **Molecule 11**. With increasing concentration of **MEL** in solution (up to 40μM in **MEL** added to 6μM **3+MEL** solutions, *vide infra* in phase segregation section), only the highly ordered hexagonal pattern is formed (**Figure 4-13**), remarkably correlating with the superimposed molecular models (the **Appendix Figure 8-16** shows a zoom-in of the superimposed models in which the super-imposed molecular error is less than 1%). Again, in the constant current images (**Figure 4-13d**), a higher contrast is seen on the inside of the pores. This pore contrast is much brighter and regular than that observed for the assemblies **Molecule 7+MEL** and **Molecule 10+MEL**, which we attribute to the co-adsorption of **MEL** in the hexagon's pores.

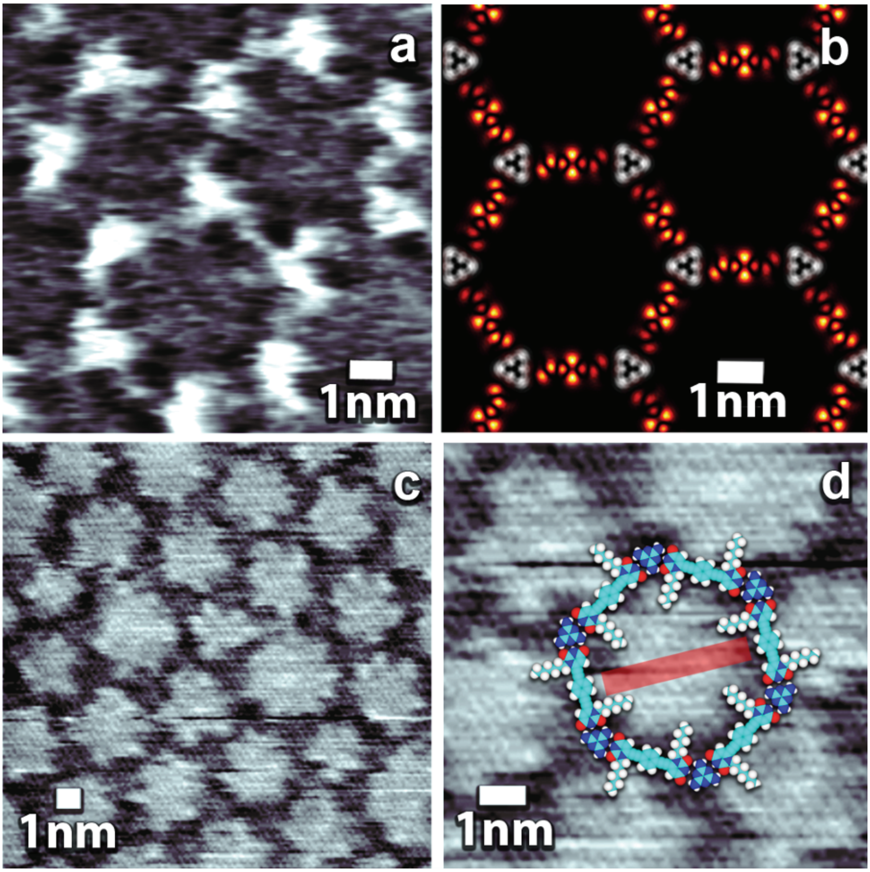

Figure 4-11
(a), (c), (d) Constant current STM images of **Molecule 7**+**MEL**. (a) Zoom-in of a small crystalline domain showing a pentagon defect. (b) Simulated STM images at constant height: in white at (E_F - 0.72) eV and in red at (E_F + 0.83) eV. (c) Survey STM image showing a polygonal motif. (d) Zoom-in with superimposed molecular models; the red bar corresponds to 3.2 nm. Tunneling parameters: (a) average tunneling current $I_t = 0.5$ pA, sample bias voltage $V_t = -500$ mV; (c),(d) $I_t = 5$ pA, $V_t = -500$ mV.

Conversely, a markedly different self-assembly behavior has been observed for the **Molecule 12+MEL** mixture revealing the formation of linear supramolecular polymers (**Figure 4-14**). It is worth noting again, that it was not possible to visualize the mono-component monolayers of **Molecule 12** when deposited using a wide range of solution concentrations, even up to 60 μM. Saturated solutions of **Molecule 12** could not be imaged by STM because of excessive (non-)faradic currents. The linear arrangement obtained with the **Molecule 12**+**MEL** system differs in its structural parameters from that of **Molecule 11+MEL**. Narrow *inter-row* distances allow extra H-bonding interaction of linker **Molecule 12+MEL** with an additional melamine belonging to the adjacent row (**Figure 4-14d**). The tetramer [(**Molecule 12**)$_2$(**MEL**)$_2$] shown in **Figure 4-14d** represents a MM2 force field minimized complex, in which all hydrogen-bond lengths are found to be less than 1.9 Å, being in accordance with typical hydrogen-bond distances. (Jeffrey 1997) The **Appendix Figure 8-19** depicts a DFT minimized [(**Molecule 12**)$_2$(**MEL**)$_2$] tetramer, where the hydrogen bond energy gain between the adjacent melamine and the [(**Molecule 12**)$_2$(**MEL**)] trimer was found was found to be 0.215 eV. Interestingly when a similar tetramer was minimized using linker **Molecule 11**, [(**Molecule 11**)$_2$(**MEL**) $_2$] no H-bond was formed, and the stabilization energy gain was only 0.015 eV, owing to the steric hindrance of the Naphtalene core (see **Appendix**).

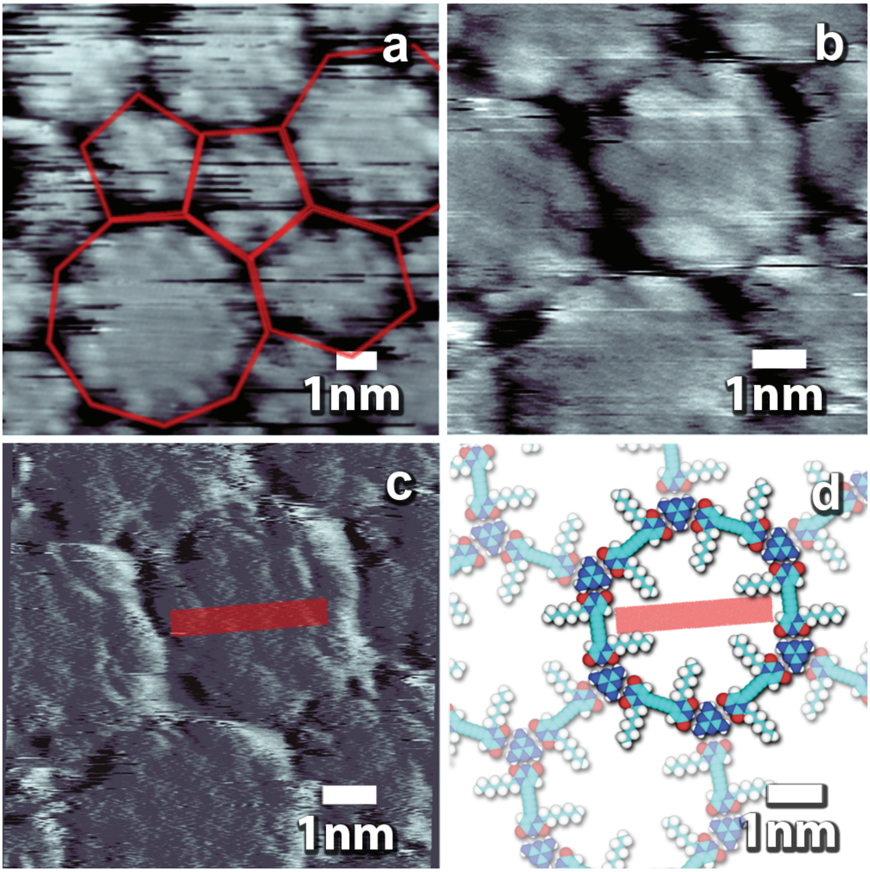

Figure 4-12

STM images of **Molecule 10+MEL** recorded in (a),(b) constant current mode and (c) constant height. (d) Molecular model of a hexagonal structure (red bars correspond to 2.8 nm). (a) A nonagon surrounded by pentagons and a hexagon is shown. Tunneling parameters: (a) $I_t = 4$ pA, $V_t = -900$ mV; (b) $I_t = 5$ pA, $V_t = -900$ mV; (c),(d) $I_t = 5$ pA, $V_t = -900$ mV.

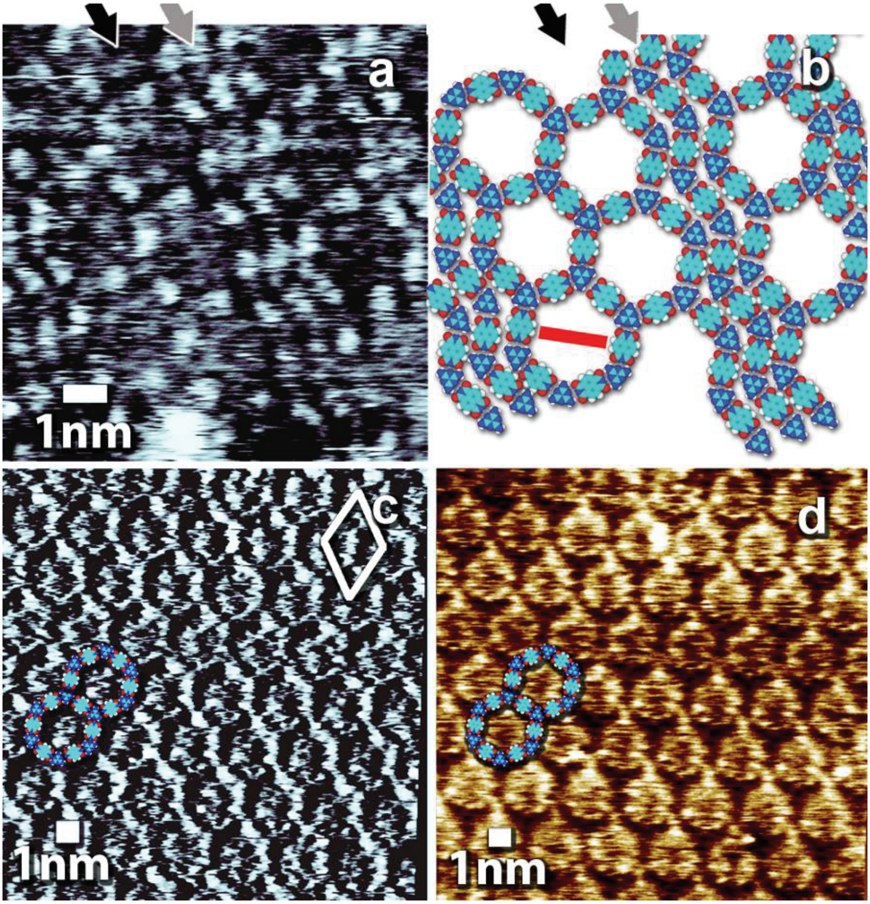

Figure 4-13
STM images of **Molecule 11+MEL** recorded in (a),(c) constant current, and (d) constant height mode. (a) Applying a 6μM solution of **Molecule 11+MEL** in both components segregated the 1D-chain polymorph (grey lines) and the predicted hexagonal motif (black arrows) is obtained. (b) Proposed 2D packing motif. The red bar corresponds to 1.6nm. (c),(d) The long-range highly ordered pattern formed at higher **MEL** concentrations. Unit cell parameters: a = 2.8 ± 0.2 nm, b = 2.8 ± 0.2 nm, with γ = 58 ± 3°. Tunneling parameters: (a) I_t = 10 pA, $V_t = -500$ mV. (c),(d) $I_t = 5$ pA, $V_t = -150$ mV.

Phase segregation in 2D networks. We have seen in the first section of Chapter 3 that pseudo-polymorphs are controlled by the solvent and concentration. Phase segregation at solid-liquid interface is even more dependent on the concentration of the components in the solution and on the type of solvent. In bi-component systems, the enthalpic driving force for the formation of these phases is mostly arising from the competition between homo- and hetero-recognition through hydrogen bonds. The nature itself of the chosen DAD…ADA complementary sequence implies that homo-recognition can occur, leading to mono-component aggregation through dihapto hydrogen bonds. As mentioned in Chapter 3, the formation of multiple phases can be described in terms of phase segregation of type I, due to the presence of multiple components having different chemical composition coexisting on the surface, or type II, where competitive adsorption determines the presence of only one phase physisorbed at the interface. **Figure 4-15** illustrates both types of phase segregation in our systems.

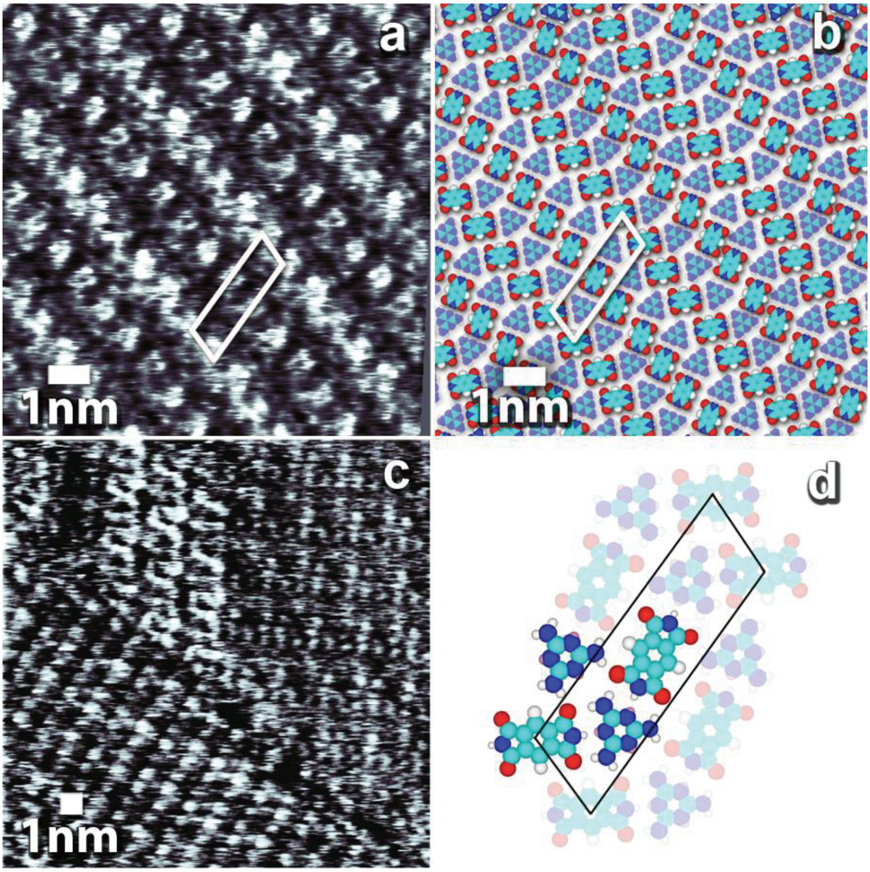

Figure 4-14

a,c) Constant current STM images of the dominant polymorph formed by **Molecule 12**+**MEL**. (a) Unit cell parameters: a = 2.6 ± 0.2 nm, b = 0.8 ± 0.1 nm, γ = 83±3°). (b) Proposed molecular arrangement. (c) An image showing different polymorphic domains of **Molecule 12**+**MEL**. (d) Proposed structure of the molecular assembly. The highlighted [(**Molecule 12**)$_2$(**MEL**)$_2$] tetramer has been planarized and then minimized using the MM2 force field. Tunneling parameters: a) I_t = 15 pA, V_t = 300 mV; c) I_t = 20 pA, V_t = 500 mV.

We have stated in the previous sections that, for pattern **Molecule 7**+**MEL**, competitive adsorption can be suppressed completely by employing low concentration solutions, below monolayer concentrations. The corresponding section in the **Appendix** depicts a phase diagram showing that when the concentration is increased, segregated phases of **MEL** and **Molecule 7** start being observed. These phases coexist with crystal and polygonal structures of **Molecule 7**+**MEL** at equimolar concentration ranges from 12 µM up to 50 µM solutions (see **Appendix Figure 8-16**). Exclusive phases of **Molecule 7**+**MEL** have been found at concentrations around 3 µM.

Similarly, bi-component patterns based of **Molecule 10**+**MEL** have been imaged using equimolar solution concentrations around 15 µM. At equimolar concentrations of **Molecule 10** and **MEL** ranging from 50 µM to 60 µM, only domains of pure **MEL** were found. Note that this phase segregation can be described as type II, since molecule **Molecule 10** was never observed to (co) physisorb at surfaces when equimolar solutions of **Molecule 10**+**MEL** were employed. At even lower concentrations, i.e. 3 µM equimolar, no physisorbed pattern was found at the solid-liquid interface by STM imaging.

Remarkably, in contrast to the previous systems, at low concentrations of **Molecule 11**+**MEL** a tightly packed bi-component pattern has been observed (**Figure 4-13a**, grey lines). At equimolar concentrations of 6 ± 2 µM of **MEL** and **Molecule 11**, linear 1D supramolecular assemblies (**Figure 4-13**) are mostly formed. The porous hexagons shown in (**Figure 4-13a** and **Figure 4-13b** are stochastically observed at phase boundaries. When an excess of **MEL** (5 µL of 43 µM solutions) is added to low-concentrated solutions of **Molecule 11** (6 µL of 6 µM solutions), the linear 1D assembly quickly disappears whereas highly ordered hexagonal networks appear. Finally, at high equimolar concentrations (25 and 50 µM) of **MEL** and **Molecule 11** there is a coexistence of several domains featuring the same hexagonal structures of those depicted in **Figure 4-13c,d**, as indicated in **Appendix Figure 8-15**. As previously argued, this is most probably due to simultaneous co-adsorption of **MEL** with linker **Molecule 11** and is discussed in the polymorphism section below**.**

The coexistence of multiple patterns was often observed for the **Molecule 12**+**MEL** system, a behavior that seemed to be independent on the concentration. At least three different patterns were imaged when using equimolar solution concentrations from 7 to 43 µM, with the dominant pattern being the one shown previously. **Figure 4-14** displays a pattern typical of high concentration solutions of system **Molecule 12**+**MEL**, with the bottom left corner corresponding to the linear supramolecular chains already shown in **Figure 4-14a,b**. Because of the additional ability of **Molecule 12** to form other complexes such as [(**Molecule 12**)$_2$(**MEL**)$_2$] tetramer, alternative configurations can be observed on the surface, thus the packing is of difficult prediction.

As previously introduced, phase segregation and phase transformations can be quantitatively analyzed through the energetic contributions of the respective phases. To a first approximation, in our case the dominant contribution to the enthalpy of the adsorbed phase is given by the hydrogen-bond interaction. This is a very crude approximation so that it is referred to as a first level enthalpic approximation. Although van der Waals (Weber, Burlakov et al. 2008) and dipole-dipole (Ciesielski, Piot et al. 2009) interactions play also an important role, they are usually one order of magnitude lower per molecule than hydrogen-bonds. Under this assumption, the right-hand-side term in **Equation 3-4** can be approximated as the *potential energy per unit area* arising from hydrogen-bond interactions, times the area occupied by the phase A_i^{phase}, and calculated as;

$$\gamma_i[\mathrm{nm}^{-2}]\cdot A_i^{phase} \sim \frac{\sum_n \mathrm{M}_{i,n}^{unit\ cell}\cdot \mathrm{E}_{\text{H-bond}}}{A_i^{unit\ cell}}\cdot A_i^{phase}$$

Equation 4-3

where we take into account nth types of H-bond interaction energies $\boldsymbol{E}_{\textbf{H-bond}}$ and $M_{n,i}^{unit\ cell}$ interactions in a unit cell area $A_i^{unit\ cell}$. The term $\boldsymbol{E}_{\textbf{H-bond}}$ is defined as the gain in energy of formation between the isolated molecules and the 2D architecture of interest. First, the difference between the energies of isolated molecules of interest in their relaxed state and those in the minimized 2D architecture (dimers, trimers, repeated monolayer, etc.) is taken, and $\boldsymbol{E}_{\textbf{H-bond}}$ is then given by this difference divided by the number of consecutive triple or double H-bonds formed. $\boldsymbol{E}_{\textbf{H-bond}}$ energies were calculated through DFT using the PW91 functional and a plane wave basis set (see experimental section). Our level of theory gives similar results for the **MEL-MEL** $\mathbf{D_3}$-dimer; in other works, formation energies being 0.437eV (this work), 0.48eV and 0.44eV by using the PBE functionals.(Mura, Martsinovich et al. 2008; Silly, Shaw et al. 2008) For the system of linker **Molecule 7**, patterns of **Molecule 7** and **MEL** are predicted to be the dominant ones over the porous structure since they have the highest (in absolute values) *potential energy per unit area* - provided that enough molecules are present to satisfy the packing density through the whole area (**Table 4-2**). For system of linker **Molecule 10**, **MEL** is also by far the most favored phase. For linker **Molecule 11**, the close packed polymorphs of **Molecule 11**+**MEL** is predicted, having a similar *potential energy per unit area* to packed structures of **MEL.** The linear assembly of **Molecule 11**+**MEL** is also predicted. Except for the close packed pattern of **Molecule 11**+**MEL** which will be addressed further on**,** the most stable phases predicted are in agreement the observations at (equimolar) solution concentrations higher than a monolayer of the respective lowest-density phase (blue region **Figure 4-15**). It is interesting to note that the phase segregation of component **Molecule 11** is not predicted theoretically, being in agreement with our observations, since at (equimolar) high concentrations the *potential energies per area* of the mixed tightly packed components of **Molecule 11**+**MEL** (1.451eV) are much greater that the single components of **Molecule 11** (0.294eV). Although neither theoretical nor experimental data was available for components **Molecule 10** and **Molecule 12**, a similar behavior to **Molecule 11** is expected, which explains why there is no phase separation of the linker molecules for all the phases other than that of **Molecule 7**.

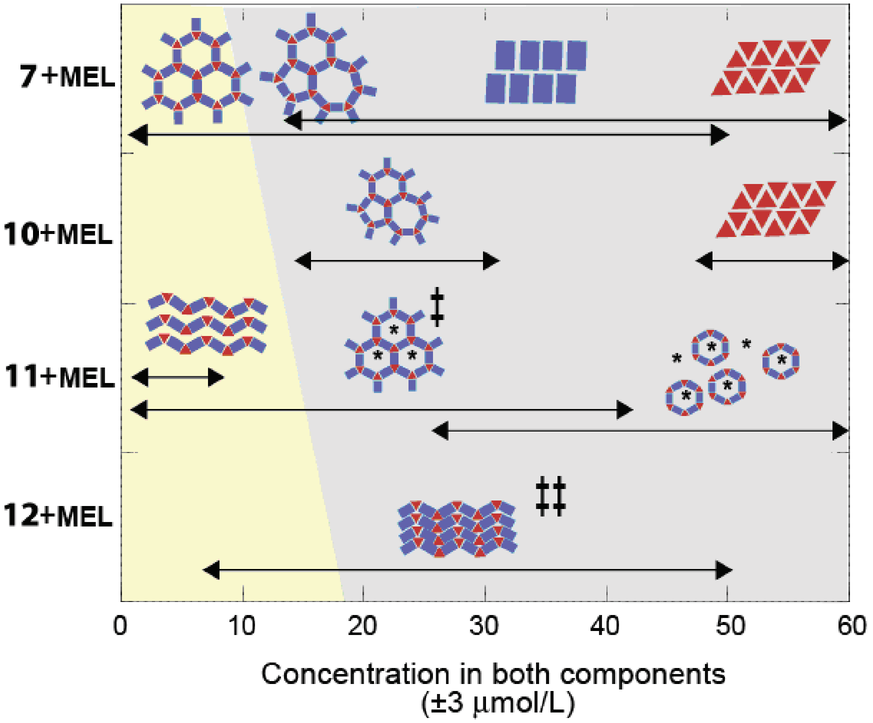

Figure 4-15
Phase segregation in bi-component networks. Illustrations show crystals, polygonal or disordered structures formed by melamine (red triangles) and the linker (blue rectangles) spanning over the concentrations indicated by their corresponding black arrows. Regions where the black arrows overlap depict phase segregation of type I, while regions where the arrows do not overlap are subject to competitive adsorption, i.e. type II phase segregation. (*) Indicates unresolved (pore) areas by STM. (‡) Only when the concentration of the linker is low (see text). (‡‡) Other unresolved segregated polymorphs where observed. The yellow region corresponds to the concentration needed to form full a porous monolayer over 1 cm^2 of substrate by applying 5 µL of solution, and as such coincides with the region where the highest *potential energy per molecule* is predicting the most stable pattern (**Table 4-2**).

When not enough molecules are present at the interface for forming a full monolayer of the lowest-density phase (yellow zone **Figure 4-15**), the system's free energy in **Equation 3-4** $G^{nh\text{ phase}}$ is minimized for those unit cells where the (absolute) *potential energies per molecule* arising from H-bond interactions are maximum; using **Equation 3-5** and **Equation 4-3**:

$$\gamma_i[\mathrm{nm}^{-2}]\cdot A_i^{phase} \sim \frac{\sum_n \mathrm{M}_{i,n}^{unit\ cell}\cdot \mathrm{E}_{\text{H-bond}}}{\sum_j N_{i,j}^{unit\ cell}} \cdot \left(\sum_j N_{i,j}^{adsorbed}\right)$$

Equation 4-4

where multiplication by the total number of adsorbed j^{th} components $\left(\sum_j N_{i,j}^{adsorbed}\right)$, gives out the total potential energy in an i^{th} phase. Again, the calculated *potential energies per molecule* agree very well with our qualitative STM observations, predicting the segregation and formation of a porous network of **Molecule 7**+**MEL** and **Molecule 10**+**MEL** at low concentrations**.** The formation of the tightly packed and porous structures of **Molecule 11**+**MEL** constitutes a fascinating case of polymorphism and is described further on. In **Table 4-2** the difference between theoretical porous phases and tightly packed structures of **Molecule 12**+**MEL** reduces to a few meV. Since van der Waals interactions are expected to be higher for the tightly packed structure, **Figure 4-15**) is also consistent with the predicted formation of tightly packed polymorphs of **Molecule 12**+**MEL** through the whole concentration range.

Table 4-2

Potential energy contributions (as absolute values) from hydrogen bond energies ($E_{H\text{-}bond}$), per unit area and per molecule, from **Equation 4-3** (column 5) and **Equation 4-4** (column 6), respectively. The theoretical and experimental unit cell areas $A^{unit\ cell}$ are given, theoretical values are used for calculation, when available. "-" indicates unavailable or n/a. Notice that for ease of comparison between *potential energy per unit area* and *per molecule*, the columns are multiplied respectively by the total area in a phase A^{phase} which is set to 1 nm^2 and the total adsorbed number of molecules N^{adsorbed} which is set to 1 (i.e. like one single component despite of dealing with bi-components). Label **1** refers to **Molecule 7, 2** to **Molecule 10, 3** to **Molecule 11** and **4** to **Molecule 12.**

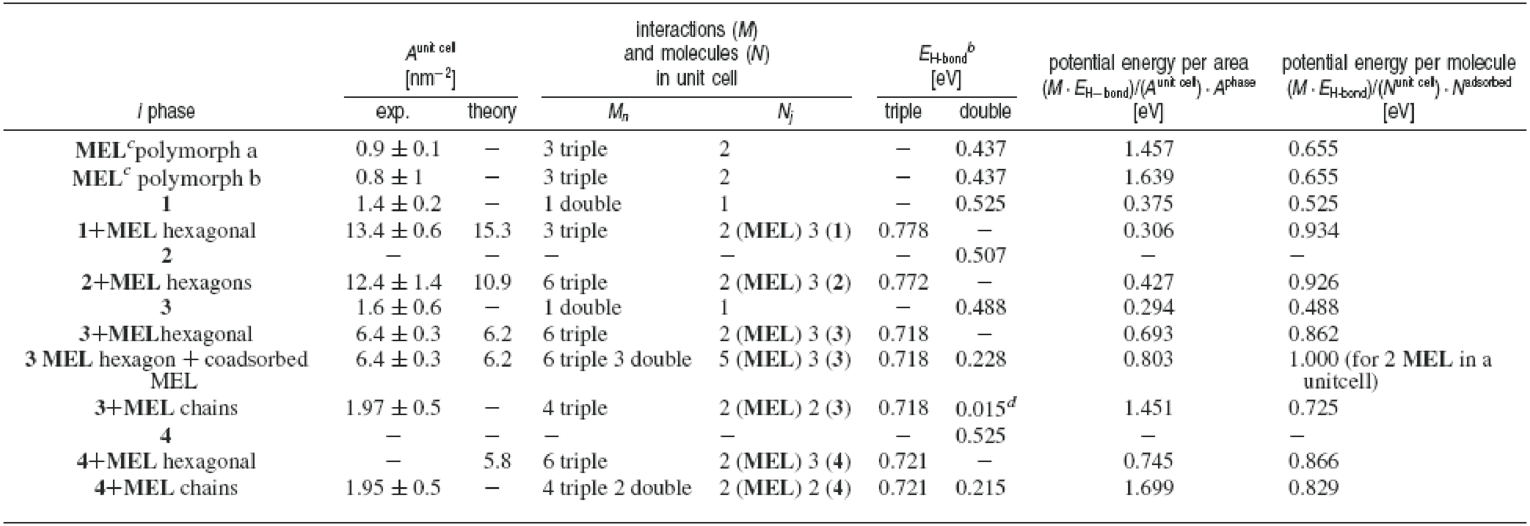

	$A^{\mathrm{unit\ cell}}$ [nm^{-2}]		interactions (M) and molecules (N) in unit cell		$E_{\mathrm{H\text{-}bond}}{}^{b}$ [eV]		potential energy per area $(M \cdot E_{\mathrm{H-bond}})/(A^{\mathrm{unit\ cell}}) \cdot A^{\mathrm{phase}}$ [eV]	potential energy per molecule $(M \cdot E_{\mathrm{H\text{-}bond}})/(N^{\mathrm{unit\ cell}}) \cdot N^{\mathrm{adsorbed}}$ [eV]
i phase	exp.	theory	M_n	N_j	triple	double		
MEL^{c}polymorph a	0.9 ± 0.1	–	3 triple	2	–	0.437	1.457	0.655
MEL^c polymorph b	0.8 ± 1	–	3 triple	2	–	0.437	1.639	0.655
1	1.4 ± 0.2	–	1 double	1	–	0.525	0.375	0.525
1+MEL hexagonal	13.4 ± 0.6	15.3	3 triple	2 (**MEL**) 3 (**1**)	0.778	–	0.306	0.934
2	–	–	–	–	–	0.507	–	–
2+MEL hexagons	12.4 ± 1.4	10.9	6 triple	2 (**MEL**) 3 (**2**)	0.772	–	0.427	0.926
3	1.6 ± 0.6	–	1 double	1	–	0.488	0.294	0.488
3+MELhexagonal	6.4 ± 0.3	6.2	6 triple	2 (**MEL**) 3 (**3**)	0.718	–	0.693	0.862
3 MEL hexagon + coadsorbed MEL	6.4 ± 0.3	6.2	6 triple 3 double	5 (**MEL**) 3 (**3**)	0.718	0.228	0.803	1.000 (for 2 **MEL** in a unitcell)
3+MEL chains	1.97 ± 0.5	–	4 triple	2 (**MEL**) 2 (**3**)	0.718	0.015^d	1.451	0.725
4	–	–	–	–	–	0.525	–	–
4+MEL hexagonal	–	5.8	6 triple	2 (**MEL**) 3 (**4**)	0.721	–	0.745	0.866
4+MEL chains	1.95 ± 0.5	–	4 triple 2 double	2 (**MEL**) 2 (**4**)	0.721	0.215	1.699	0.829

† Except for the hexagonal porous networks, all other $E_{H\text{-}bond}$ energies are approximated as the energy of interaction of single isolated dimers and not of periodic monolayers. ‡ A full description of these two polymorphs can be found in references.(Mura, Martsinovich et al. 2008; Silly, Shaw et al. 2008) *Weak stabilization energy found for the secondary interow **MEL** interaction in a [(**Molecule 11**)$_2$(**MEL**)$_2$] tetramer, see **Appendix**.

Polymorphism and Polygons in 2D networks. The wide variety of hexagonal, glassy and linear structures previously shown represents a clear example of polymorphism in 2D bi-component networks. For the sake of comparison, the self-assembly behavior on a 100×100 nm^2 scale of the studied bi-component systems is shown in **Figure 4-16** while the insets report the respective 2D Fast Fourier Transform (FFT). It reveals that a higher degree of crystallinity is observed in system **Molecule 12+MEL**, in particular if compared to that of **Molecule 10+MEL**. On the other hand, system **Molecule 7+MEL** was found to form hexagonal domains coexisting with relatively disordered areas. Time-dependent STM imaging experiments, using a fluid-cell, revealed that after 12 hours the degree of crystallinity of the **Molecule 7+MEL** system in **Figure 4-1a** remains unchanged (See **Appendix Figure 8-18**). The homebuilt liquid-cell could accommodate 1 cm^2 of HOPG and ~200 μL of solution. A quantitative analysis on the distribution of different polygon structure was not possible in all binary systems since a consistent statistical estimation of the pore areas on large area STM images was beyond the limits of detection. Nevertheless, a semi-quantitative description of the glass-crystal polymorphism in these 2D networks could be obtained by simulating hexagonal and other polygonal structures for each different linkers making use of DFT calculations. **Figure 4-17** depicts the DFT optimized molecular models of hexagons and pentagons engineered combining **MEL** with the linkers. The analysis of the different energetic contributions, in particular in terms of energy needed to change the conformation of the molecular backbone and energy of formation of hydrogen-bonds, reveals that the difference in favoring the formation of pentagons or hexagons is mostly due to the flexibility of the backbone of the linker molecules. The molecular deformation (i.e. all stretching, bending, and rotational changes of groups of atoms within a given molecule.) energy cost, $\boldsymbol{E}_{\mathbf{def}}$, is defined as the difference between the energy of a molecule within a specific 2D architecture, $\boldsymbol{E}_{\mathbf{architecture}}$, and that of a relaxed isolated molecule $\boldsymbol{E}_{\mathbf{isolated}}$. **Table 4-3** shows that $\boldsymbol{E}_{\mathbf{def}}$ remains unchanged within a few meV, for all linkers (**1-4**), in both hexagons and pentagons. This is because $\boldsymbol{E}_{\mathbf{def}}$ features a dominant contribution from the force needed to modify the molecular geometry in the immediate vicinity of the hydrogen bonding moieties (*i.e.*, from the deformation of C=O and N-H bonds, see **Apendix Figure 8-20** The flexibility of the linkers' backbone is then better quantified by defining an angle β between the vectors V_1 and V_2 in the pentagons' linkers in **Figure 4-17**. As expected, for pentagons with **Molecule 7** and **Molecule 10**, β amounts to 12.15° and 11.14°, respectively, while for pentagons with **Molecule 11** and **Molecule 12** β amounts to 2.90° and 2.35°. This means that the backbone flexibility of linkers **Molecule 7** and **Molecule 10** allows the optimal hydrogen-bond configuration, having $\beta = 12^o$.

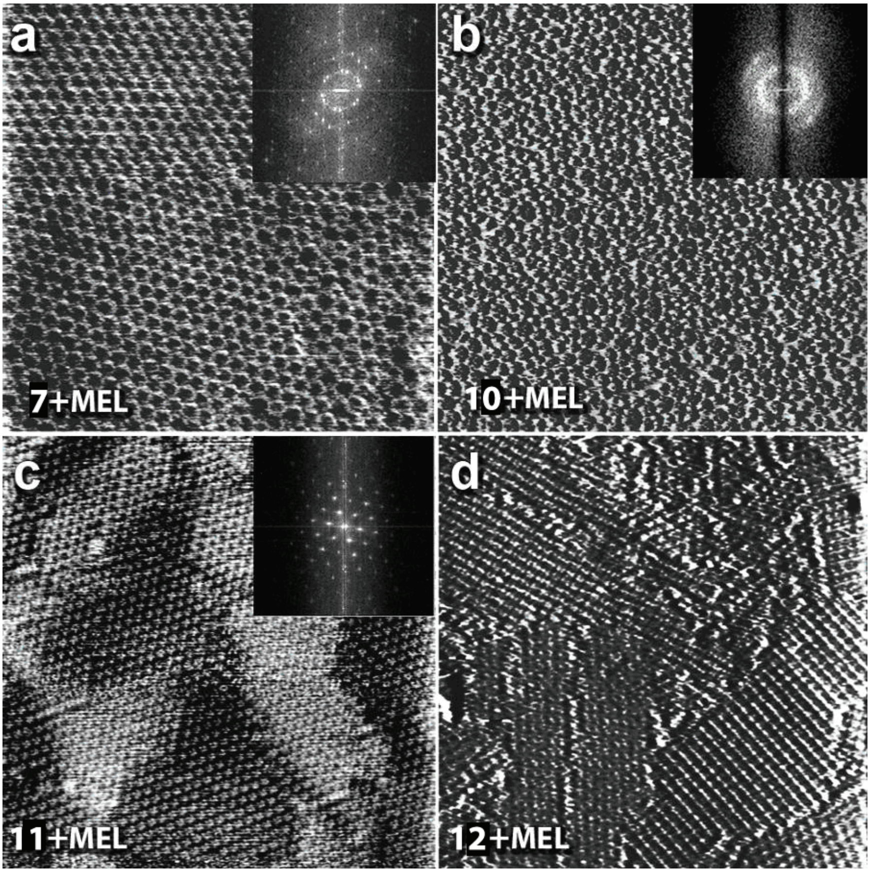

Figure 4-16
STM images recorded in (a), (d) constant current, and (c),(b) constant height mode featuring (i.e. 100×100 nm^2) the four assembling systems of linker+**MEL**. (a) **Molecule 7**+**MEL** deposited from 12µM solutions features crystalline domains at medium length scales. Two highly ordered domains are evidenced from the Fourier transform, corresponding to the left side of the image. (b) **Molecule 10**+**MEL** patterns deposited from 15µM solution exhibiting a high polygonal dispersity. (c) **Molecule 11**+**MEL** patterns from 6µM solution of **Molecule 11** and 21µM solutions of **MEL** were found to exhibiting long-range defect-free crystalline domains. d) **Molecule 12**+**MEL** patterns from 14µM solutions featuring multiple coexisting polymorphs. Tunneling parameters: a) I_t = 1 pA, V_t = –400 mV; b) I_t = 1 pA, V_t = –400 mV; c) I_t = 1 pA, V_t = –400 mV; d) I_t = 20 pA, V_t = 500 mV.

The same trend is seen for the hydrogen-bond distances (**Table 4-3**):for **Molecule 7** and **Molecule 10** they are almost identical in hexagons and pentagons, whereas for linker **Molecule 11** and **Molecule 12** there is a significant difference. $\boldsymbol{E}_{\textbf{H-bond}}$ behaves accordingly in all cases, being less favorable for the formation of a pentagon, and more favorable for the formation of a hexagon. In the first two linkers however, the $\boldsymbol{E}_{\textbf{H-bond}}$ difference between hexagons and pentagons is rather subtle (2 and 18 meV, respectively), whereas it increases to 68 meV for **Molecule 11**. This further confirms that the flexibility of linkers **Molecule 7** and **Molecule 10** allows the system to remain in the optimal hydrogen-bond configuration in both polygons. In contrast, the lower flexibility of linker **Molecule 11** affects the triple H-bond co-linearity in the pentagonal structures, resulting in a less strong intramolecular interaction. Finally, the $\boldsymbol{E}_{\textbf{def}}$ difference between hexagons and pentagons for linker **Molecule 12** is 28 meV. This suggests that if the porous network of **Molecule 12+MEL** were observed, it would have a certain tolerance to different polygon formation, being more crystalline than **Molecule 7+MEL** and **Molecule 10+MEL** but less than **Molecule 11+MEL.**

The origin of the intrinsic tightly packed polymorph of system **Molecule 11+MEL** can be well described in analogy with similar systems studied under Ultra-High Vacuum (UHV) conditions.(Weber, Burlakov et al. 2008) Linear assemblies of **Molecule 11+MEL** are favored because of the additional vdW interactions between adjacent NTCDI cores. In fact linear assemblies are not native from **Molecule 7+MEL** and **Molecule 10+MEL** systems as the side chains prevent close interow interactions so only the porous patterns are predicted (**Table 4-2**). For the **Molecule 11+MEL** system**,** although the *potential energy per molecule* in **Table 4-2** predicts the formation of the hexagonal porous network phase at low equimolar concentrations, it does so by only a 0.13eV margin (0.862 vs. 0.725eV) and as discussed, experimentally the linear **Molecule 11+MEL** was predominantly observed.

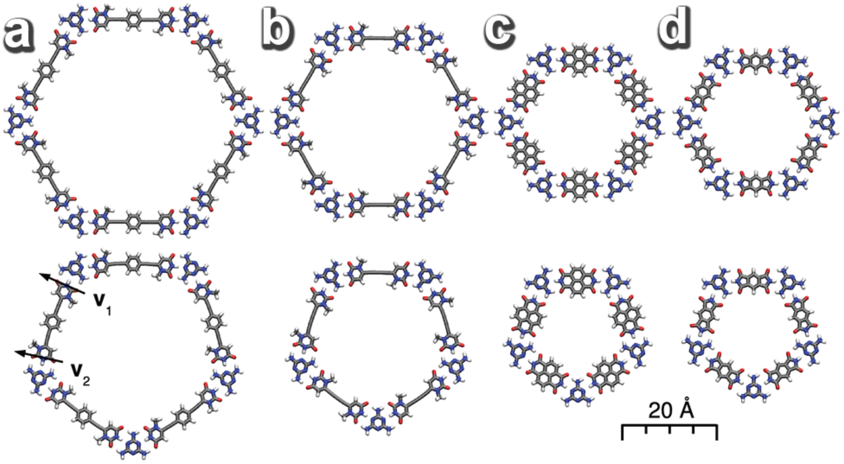

Figure 4-17
DFT optimized structures of isolated hexagonal (top) and pentagonal (bottom) structures with MEL together with the linkers.

Table 4-3

Calculated $E_{\text{H-bond}}$, E_{def}, and H-bond distances of MEL with the bold label **1** referring to **Molecule 7, 2** to **Molecule 10, 3** to **Molecule 11** and **4** to **Molecule 12.** in different polygonal structures. For the isolated pentagons two different bond lengths for the H-bonds with oxygen acceptors have been observed.

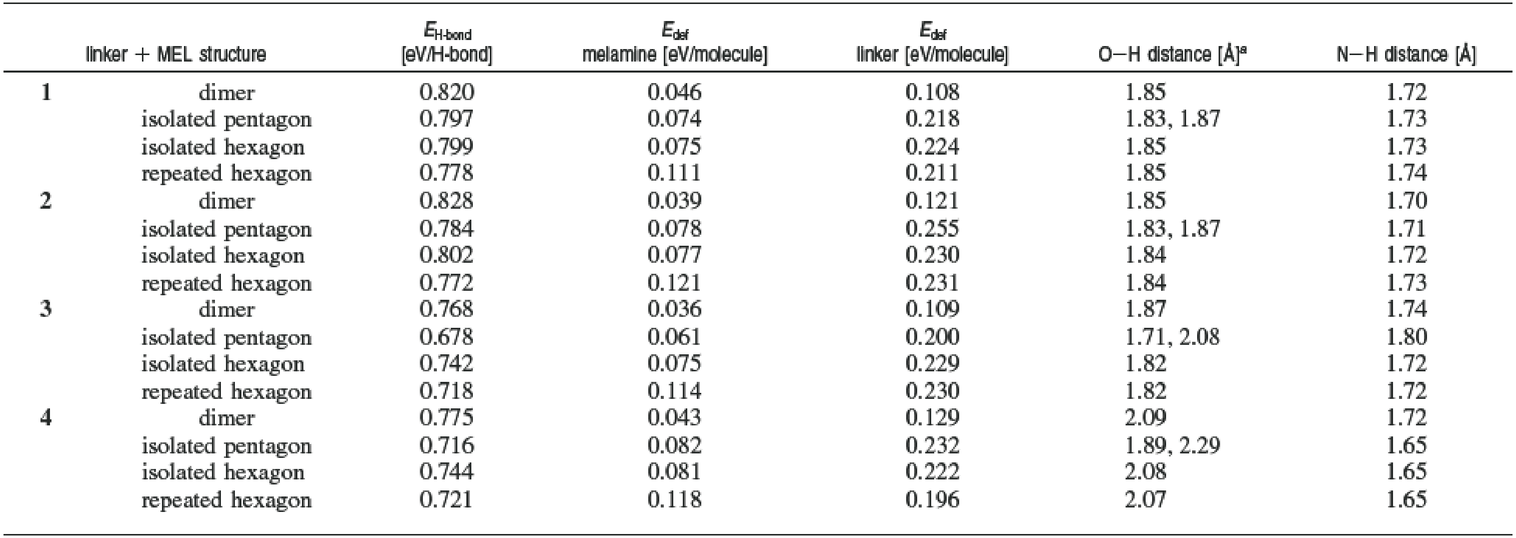

	linker + MEL structure	$E_{\text{H-bond}}$ [eV/H-bond]	E_{def} melamine [eV/molecule]	E_{def} linker [eV/molecule]	O−H distance [Å][a]	N−H distance [Å]
1	dimer	0.820	0.046	0.108	1.85	1.72
	isolated pentagon	0.797	0.074	0.218	1.83, 1.87	1.73
	isolated hexagon	0.799	0.075	0.224	1.85	1.73
	repeated hexagon	0.778	0.111	0.211	1.85	1.74
2	dimer	0.828	0.039	0.121	1.85	1.70
	isolated pentagon	0.784	0.078	0.255	1.83, 1.87	1.71
	isolated hexagon	0.802	0.077	0.230	1.84	1.72
	repeated hexagon	0.772	0.121	0.231	1.84	1.73
3	dimer	0.768	0.036	0.109	1.87	1.74
	isolated pentagon	0.678	0.061	0.200	1.71, 2.08	1.80
	isolated hexagon	0.742	0.075	0.229	1.82	1.72
	repeated hexagon	0.718	0.114	0.230	1.82	1.72
4	dimer	0.775	0.043	0.129	2.09	1.72
	isolated pentagon	0.716	0.082	0.232	1.89, 2.29	1.65
	isolated hexagon	0.744	0.081	0.222	2.08	1.65
	repeated hexagon	0.721	0.118	0.196	2.07	1.65

At higher **MEL** concentrations, the formation of the highly self-healed hexagonal pattern may be only stabilized through additional co-adsorption of melamine. As previously discussed, **Figure 8-16** in the supporting information shows a tentative co-adsorbed configuration; it exhibits three co-adsorbed melamines for every repeating unit, resulting in a hydrogen bond energy gain of 0.228 eV per melamine co-adsorbed. Assuming this stoichiometry to be correct, the formation of a hexagonal pattern is predicted when only five molecules are considered to form the repeating unit, three of type **Molecule 11** and two of **MEL** (1.00 eV total *potential energy per molecule*, **Table 4-2**). When the actual eight molecules making up the assembly are considered, the *potential energy per molecule* of the co-adsorbed hexagonal phase is lower (0.624 eV) and again the linear assembly is predicted (0.725 eV). Our observations (**Figure 4-15**) indeed confirm that at high equimolar concentrations, unresolved areas are present alongside the co-adsorbed hexagonal phase. At these high concentrations, the *potential energies per area* (**Table 4-2**) predict that pure mixtures of **MEL** (*polymorph a* 1.457 eV) and **Molecule 11+MEL** (1.451 eV) should be formed. It is worth highlighting that linker **Molecule 11** and **MEL** have previously been studied under UHV (Perdigao, Fontes et al. 2007) where disordered phases were observed. In turn, an expanded tetracarboxy diimide (PTCDI) exhibited (Staniec, Perdigão et al. 2007) a very similar behavior to that of molecule **Molecule 11** in the presence of co-adsorbed melamine under diluted conditions (**Figure 4-13**) (Silly, Shaw et al. 2008). Note however that PTCDI+MEL mixtures have been reported to form highly crystalline patterns when deposited from pure DMF and imaged at the Au(111)-air interface (Madueno, Raisanen et al. 2008). It is also worth noting that the PTCDI+MEL system could not be studied because of the insolubility of the PTCDI molecule in TCB, even at high concentrations of DMSO. The previous evidence points out that the highly hexagonal pattern of **Molecule 11**+**MEL** is in fact a local (kinetic) minimum.

As introduced in the previous section, molecular pattern **Molecule 12**+**MEL** benefits not only from favorable van der Waals interactions of tightly packed structures, but also from the formation of stabilizing [(**Molecule 12**)$_2$(**MEL**)$_2$] tetramers. Moreover, the intrinsic hydrogen bond formation energies of **Molecule 11**+**MEL** and **Molecule 12**+**MEL** dimers may further disfavor the formation of a nanoporous network over a tightly packed pattern, being 36-62 meV weaker than those for **Molecule 7+MEL** and **Molecule 10+MEL** assemblies. These seemingly small differences are further increased: as patterns become more and more periodic (or crystalline), molecules surrounding melamine are subject to electrostatic repulsions and hydrogen-bond energies are further weakened through depolarization.

The greater crystalline character of some of the **Molecule 7+MEL** domains than those of **Molecule 10+MEL** remains an open question. Theoretically, both systems display similar H-bond and deformation energies between hexagons and pentagons. The FFT image of **Figure 4-16** shows two coexisting crystalline domains, rotated by 14 ± 3 ° relative to their unit cell vectors. In the **Appendix**

Figure 8-18 shows that there is no preferred orientation of crystalline domains with the unit cell vectors of HOPG (which are related by 60°), pointing to a minor role played by the substrate in the crystalline nature of the patterns. A possible explanation for the coexistence of polygonal *glassy* and crystalline phases for system **Molecule 7+MEL** relates to the crystallization dynamics. To this end, the exact crystallization mechanism should be unraveled, albeit this is experimentally not accomplishable on the required nanoscale spatial resolution. To explore the reversible nature of the self-assembly process at the solid-liquid interface, we have performed at such interface an *in-situ* thermal annealing (up to 40 ± 2ºC) through a 2 hour heating ramp starting at 20±1 ºC. The **Appendix Figure 8-14** reveals that the monolayer exhibits a very limited propensity to undergo glass-crystal reorganization (i.e. statistically, the polygonal distribution remained unchanged) even as the pattern appears more and more dynamic (**Figure 8-14c,d**). Likewise, the *ex-situ* temperature-dependent experiments, performed by applying to the HOPG surface a 12 μM solution of linker **Molecule 7** and **MEL** at different temperatures (10, 20, 30 and 40 ± 2 ºC), revealed the presence of the same amount of polygons on the substrate, confirming that the crystallization process is not thermally activated in the explored temperature range. These extrinsic crystallizing conditions (temperature and concentration) do not significantly affect the polymorph distribution of the **Molecule 7+MEL** assemblies. The lower crystallinity of the **Molecule 10+MEL** assemblies compared to that of **Molecule 7+MEL** could be attributed to the increased backbone flexibility of linker **Molecule 10**, raising the probability of formation of larger polygons, such as heptagons and/or octagons. Temperature-dependent experiments with **Molecule 10+MEL** phases could not be performed because the low network stability (limited to tens of minutes) during *in-situ* scanning, which we tentatively ascribed to the low affinity of module **Molecule 10** for HOPG.

In summary the comparative studies of four linkers interacting with melamine via three parallel H-bonds offered new insight on the design of pre-programmable bi-component supramolecular 2D networks. In all the bi-component systems, multiple phases were observed when using solution with concentration below 100 μM, confirming that a concentration-dependent polymorphism and phase segregation are hallmarks of the self-assembled structures at solid-liquid interfaces. An accurate prediction of the multiple phases encountered was achieved by purely enthalpic considerations, through DFT hydrogen-bond formation energies. Furthermore, we have proved that the polymorphism, which can also be expressed through the existence of multiple polygon structures, is an intrinsic feature of molecular design. In particular, three aspects were found to be crucial towards the formation of highly ordered and pre-programmed porous networks at the solid-liquid interface: i) (di)acetylene fragments are not the optimal choice when looking for fully rigid molecular modules, as they introduce sufficient conformational flexibility allowing formation of polymorphic and glassy phases; ii) peripheral functionalization of the linker molecules is needed to avoid strong side-to-side interactions between the module's cores that will drive the formation of tightly packed bi-component patterned assemblies over porous networks and, more likely, hinder the strong adsorption in the pattern's pores; iii) phase segregation and self-recognition in multi-component systems may be avoided pre-programming several molecular modules bearing complementary recognition moieties. Additionally, we have demonstrated that by unraveling the energetic contributions in crystallization, polymorphism, and phase segregation, a dramatic improvement in chemical design, and thus in the molecular engineering, can be achieved. Addressing these issues provide reliable design protocols for the precise and tunable nanopatterning of surfaces. We have also shown that the substrate plays a negligible role in the formation of networks held by tri-hapto hydrogen-bonding interactions, thus paving the way toward the extension of this nano-patterning protocol to a wide variety of substrates. In the limits of chemical design and crystal engineering stand biology which is able to reduce all possible intrinsic degrees of freedom into self-healing and pre-programmable self-assembly.

5 Simulating Self-Assembly

As we have widely stated, molecular self-assembly of artificial architectures with precise 3D arrangements (Whitesides, Mathias et al. 1991; Fujita, Oguro et al. 1995; Lehn 2002; Yaghi, O'Keeffe et al. 2003; Rothemund 2006) is key to the bottom-up fabrication of multifunctional materials. However, despite being the subject of in-depth experimental studies, such articulated phenomena have not been yet been simulated, elucidated in time and space, so as to predict the modeled outcome of the self-assembly. Moreover here we have identified a plethora of structurally diverse self-assembled phases at the (solid-liquid) interface, ranging from 2D amorphous (Otero, Lukas et al. 2008; Palma, Bjork et al. 2009) and polygonal networks (Zwaneveld, Pawlak et al. 2008; Palma, Bjork et al. 2009) to crystals (Theobald, Oxtoby et al. 2003; Schlickum, Decker et al. 2007; Zwaneveld, Pawlak et al. 2008). It has been proposed that the self-assembled architectures at surfaces may actually correspond to either equilibrium (Garrahan, Stannard et al. 2009) or non-equilibrium states, which can be reversible (Palma, Bjork et al. 2009) or irreversible (Zwaneveld, Pawlak et al. 2008). Consequently, any bottom-up material design requires an *a priori* knowledge of both the thermodynamics and the kinetics of molecular self-assembly on the time- and length-scales relevant to the process. The thorough description of the phase diagram of the system as a function of temperature, pressure and relative concentrations of the molecular modules, as well as the transition pathways and barriers to the stable state will ultimately pave the way towards *supramolecular engineering,* thus bridging the gap between the concepts of chemical design and self-assembly into custom architectures with molecular precision .

In this section we seek to develop a molecular dynamics tool for supramolecular engineering (**MolSET**). We come close to this our final goal of full self- prediction through the first simulation of 2D self-assembly of the **Molecule 7-Molecule 16** model bi-component system, i.e., **MEL** and the bis(N_1-hexyl-uracil) **Molecule 7**, exposing complementary recognition sites, from now on **Molecule 7-MEL**, **Figure 5-1a**). The **Molecule 7+MEL** bi-component system is known to form extended porous networks on graphite, which were shown by scanning tunneling microscopy (STM) to feature a variety of polygonal types, including pentagons, hexagons and heptagons (Palma, Bjork et al. 2009). Such a structural diversity offers the opportunity to explore the nature of 2D polygonal networks on the sub-molecular scale and cast light onto the structural evolution to the crystalline phase.

The study of self-assembly at the solid-liquid interface by molecular dynamics is centered on the description of the sequence of events (from molecular recognition to phase properties) in time at an atomic level of detail. We chose Langevin dynamics (Langevin 1908; Brooks, Brooks et al. 2009) with continuum electrostatics in conjunction with a restraining harmonic potential to mimic the presence of graphite, which is referred to as the implicit substrate (SI section 2). The cornerstone (**MEL**) and the linker (**Molecule 7**) were modeled by the Merck molecular force-field (**MMFF**) (Halgren 1996), while atomic charges were modified *ad hoc* to fit the **Molecule 7-MEL** interaction energy profile estimated by Density Functional Theory (see corresponding section in the **Appendix** (Palma, Bjork et al. 2009)). The quality of the implicit substrate was assessed by comparing the life-time and the apparent diffusion constant of pre-formed **Molecule 7-MEL** dimers with those obtained with an all-atom representation of a graphene slab; the latter was reported to yield adsorption energies for a series of aromatic compounds on graphite in good agreement with experimental data (Bjork, Hanke et al. 2010). The analysis confirmed that the implicit model provides a representative description of the substrate, while allowing for microseconds sampling in a few weeks of calculation (**Appendix**). Significantly, the **Molecule 7-MEL** dimers were found to have a lifetime exceeding 100 ns at temperatures below 400K (**Appendix**). Because of this reason all simulations were performed at temperatures above 400K, where self-assembly is reversible and the model mimics the dynamic experimental conditions, Indeed, we have previously reported that the presence of a supernatant solvent in STM studies confers reversibility to self-assembly at the solid-liquid interface (see **Appendix**). In the computations, such a reversibility is achieved by tuning the temperature of the system rather than the effective dielectric constant (**Appendix**). Preliminary results showed that the use of larger frictions (1 or 0.5 ps^{-1}) resulted in the formation of relatively small clusters, never larger than a *12*- to *13*-mers, on dozens of nanoseconds. In fact, cluster growth requires that the collision rate ($k_{collision}$)of complementary modules should be higher than the dissociation rate ($k_{dissociation}$). Since the former includes the random diffusion of the modules ending up into a productive collision encounter, too large values of γ will result in low collision frequencies, which prevent cluster growth on the simulation time scale. The use of small friction coefficients, such that employed in this study, is deemed to be crucial for the investigation of self-assembly by all-atom molecular dynamics. This represents the first fundamental law of self-assembly;

$$k_{collision} > k_{dissociation}$$

Equation 5-1

Although still qualitative, we are actively working on obtaining a quantitative representation for **Equation 5-1**, an important law governing the growth of supramolecular architectures. A second important observation is the proportionality between the rates of macroscopic 2D cluster growth and the rates of dimer dissociation. Apparently contradictory, **Figure 8-31** and **Figure 8-32** show that the weaker the hydrogen bond between **Molecule 7+MEL** is (i.e. at higher temperatures), the faster the cluster grows. This can be represented as;

$$k_{growth}^{macro} \sim k_{dissociation}^{micro}$$

Equation 5-2

In the previous and the following studies, the self-assembly of **Molecule 7+MEL** was investigated by Molecular Dynamics (MD) simulations of an eighty-molecule stoichiometric mixture physisorbed on the substrate. Twenty independent runs were done at 400K for 500 nanoseconds by employing a "fast-annealing" protocol that features temperature spikes at 525K (**Appendix**). Since the **Molecule 7-MEL** dimer dissociates in the sub-ns timescale at 500K (**Appendix**), the procedure results in an efficient conformational search. During annealing, a plethora of discrete supramolecular structures based on *hetero*-mers (hereafter referred as clusters) as large as 70mers rapidly assemble and dis-assemble (**Figure 5-1b**). The motif of a transient cluster extracted at 137 ns is portrayed in **Figure 5-1c**. It shows a *73*-mer combining a pentagon (I), an heptagon (II) and an hexagon (III), as well as the existence of **MEL-MEL** and **Molecule 7-Molecule 7** *homo*-recognition events. When compared with STM images, the correlation between the structure of the simulated clusters and the experimental patterns is striking. **Figure 5-1d-f** shows three structural motifs extracted from the fast-annealing trajectories superimposed on STM recorded images. Interestingly, out of hundreds of clusters composed of *>50*-mers, the largest "crystalline" fragment from the simulations was composed of only three consecutive hexagons, out of nine capable of forming in a condensed 80-molecule crystal (**Figure 5-1f**). Conversely, hexagonal crystalline domains are ubiquitously observed in the experiments. This suggests that large heterogeneous polygonal networks are kinetic products, which suddenly form in the early steps of 2D self-assembly. To confirm this observation, the difference in conformational free energy (ΔG) between potential nuclei of archetypical size, i.e., the smallest polygons, was investigated by the confinement approach (See Chapter 2 Methods (Tyka, Clarke et al. 2006; Cecchini, Krivov et al. 2009)). The free energy of the supramolecular hexagon (**Appendix**), which is structurally compatible with the crystalline pattern, was compared to that of a branched pentagon (**Appendix**), which can be considered a prototypical building block forming polygonal networks. The analysis yields a ΔG of 2.3±1.0 kcal/mol at 400K in favor of the hexagon, implying a theoretical ratio between the populations of the hexagon and the pentagon at equilibrium amounting to 18.

Conversely, the simulations revealed essentially equal populations, their ratio being 0.66 (**Appendix**). These results provide strong evidence that polygonal defects, such as pentagons, are kinetically formed species promoting the formation of non-crystalline phases. Taking into account that crystalline domains extend far beyond polygonal domains in STM images (Palma, Bjork et al. 2009), the hexagonal pattern is supposed to be thermodynamically favored. In light of this, the existence of a structural transition from the network to the crystalline state, i.e. *self-healing,* in the simulations is expected.

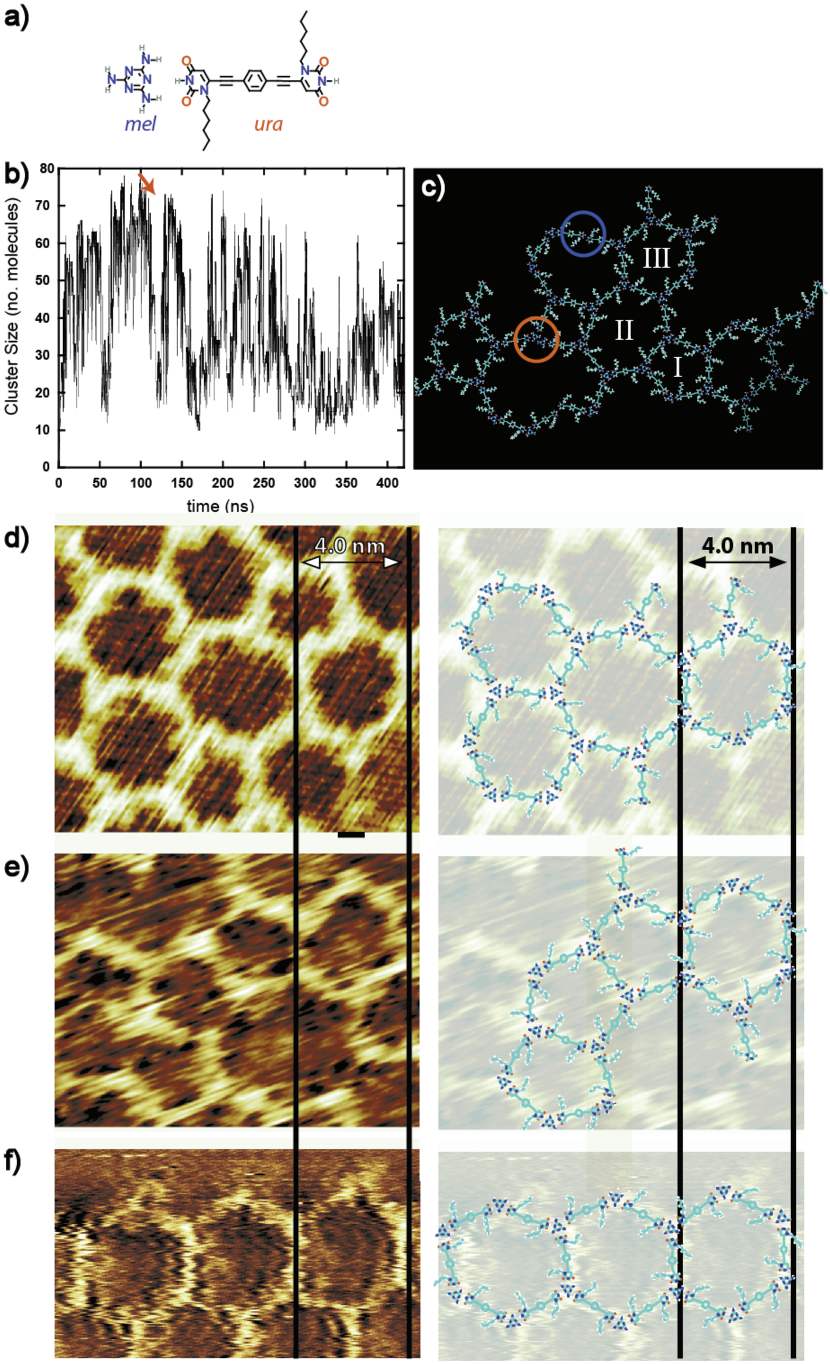

Figure 5-1
Self-assembly simulations of **Molecule 7+MEL**. a) Chemical structure of the complementary *hetero*-dimer. The **Molecule 7-MEL** recognition is based on donor-

acceptor-donor (DAD) coupling with acceptor-donor-acceptor (ADA) imidic moieties. b) Time series of the size (i.e., number of molecules) of the largest supramolecular cluster in a typical fast-annealing trajectory (black line). c) Molecular structure of a *73*-mer cluster extracted at 137 ns (red arrow in Fig. 1b). Roman numbers indicate supramolecular polygons, red and blue circles highlight **MEL-MEL** and **Molecule 7-Molecule 7** *homo*-recognition events, respectively. d-f) Comparison between clusters extracted from the simulations and experimental STM images. On the left-hand side, the supramolecular pattern of experimentally observed polymorphic networks is shown. On the right-hand side, molecular snapshots extracted from the simulations are superposed to the STM images. The correlation between the complex experimental patterns and the simulated assemblies is striking.

To prove the existence of such a transition, we first approached the problem by constant temperature MD simulation of stoichiometric **Molecule 7-MEL**. At 375K the system shows no structural evolution to ordering on the sub-microsecond time scale, leading only to 2D amorphous polymers (**Appendix**). At 420K the system is more dynamic and large molecular clusters spontaneously assemble. Interestingly, the clusters exhibit a steady growth on the ns timescale along with large fluctuations in size on the tens of ns, leading to an overall structural increase on the hundreds of ns (**Figure** 5-2**a**, black line). The comparison of the evolution of the number of *hetero*- and *homo*- recognition events (see **Figure** 5-2**a**) reveals that the former (in blue) inversely *mirrors* the latter (in red). Such an observation suggests that, although *hetero*- hydrogen-bonding has a constant increase with time, continuous replacement of *hetero*-hydrogen-bonding interactions with *homo*- interactions, and vice versa, takes place. This is a consequence of the similar binding energies amounting to 13 kcal/mol for **Molecule 7-Molecule 7** and 11 kcal/mol for **MEL-MEL** if compared to 18 kcal/mol for **Molecule 7-MEL**. Such a competitive interplay gives rise to additional barriers, which effectively trap the system in a glass-like state (Zallen 1998) on the simulation time scale. To test this hypothesis and speed-up the glass to crystal transition *in silico*, the interaction energy of all *homo*-recognition events (i.e. **MEL-MEL** and **Molecule 7-Molecule 7**) was scaled down by a factor of 100, while preserving all other simulation conditions (SI section 6). This corresponds to an idealized system essentially devoid of *homo* recognition, here referred to as **Molecule 7+MEL***. When **Molecule 7+MEL*** is simulated at 420 K, the clusters do not undergo dis-assembly so that fluctuations in the cluster size disappear, as evident from the comparison of the black profiles in **Figure** 5-2**a** and **Figure** 5-2**b**. Moreover, a marked structural evolution to ordering is detected by the appearance of a peak at 41 Å in the radial distribution function *g*(r). Such a peak corresponds to the unit cell of a fully crystalline pattern and its intensity gauges the degree of crystallinity (see **Figure** 5-2**c**). **Figure** 5-2**d** displays the structural evolution of the system revealing a series of intermediates with increased ordering. In the sub-nanosecond range (blue region) the average cluster is composed of three interacting molecules (**A**). Between 1 and 5 ns the cluster size increases and *20*-

mers assemblies appear (**B**, green region). At this stage, a big step in the average cluster size is observed (**C**) followed by a drop in the slope of the *hetero* association rate (blue line). Both the *g*(r) and the cluster size increase until they reach a plateau at about 100 ns (**D**, yellow region). Overall, four main structural transitions are identified. They correspond to: the oligomerization of the melt (**Figure** 5-2**e**); the appearance of a polymeric networks (**Figure** 5-2**f**); the clustering into 2D polygonal networks (**Figure** 5-2**g**); and the relaxation to the crystalline state (**Figure** 5-2**h,i**). The transition from **C** to **D** in **Figure** 5-2 provides the first direct proof of self-healing *in-silico*.

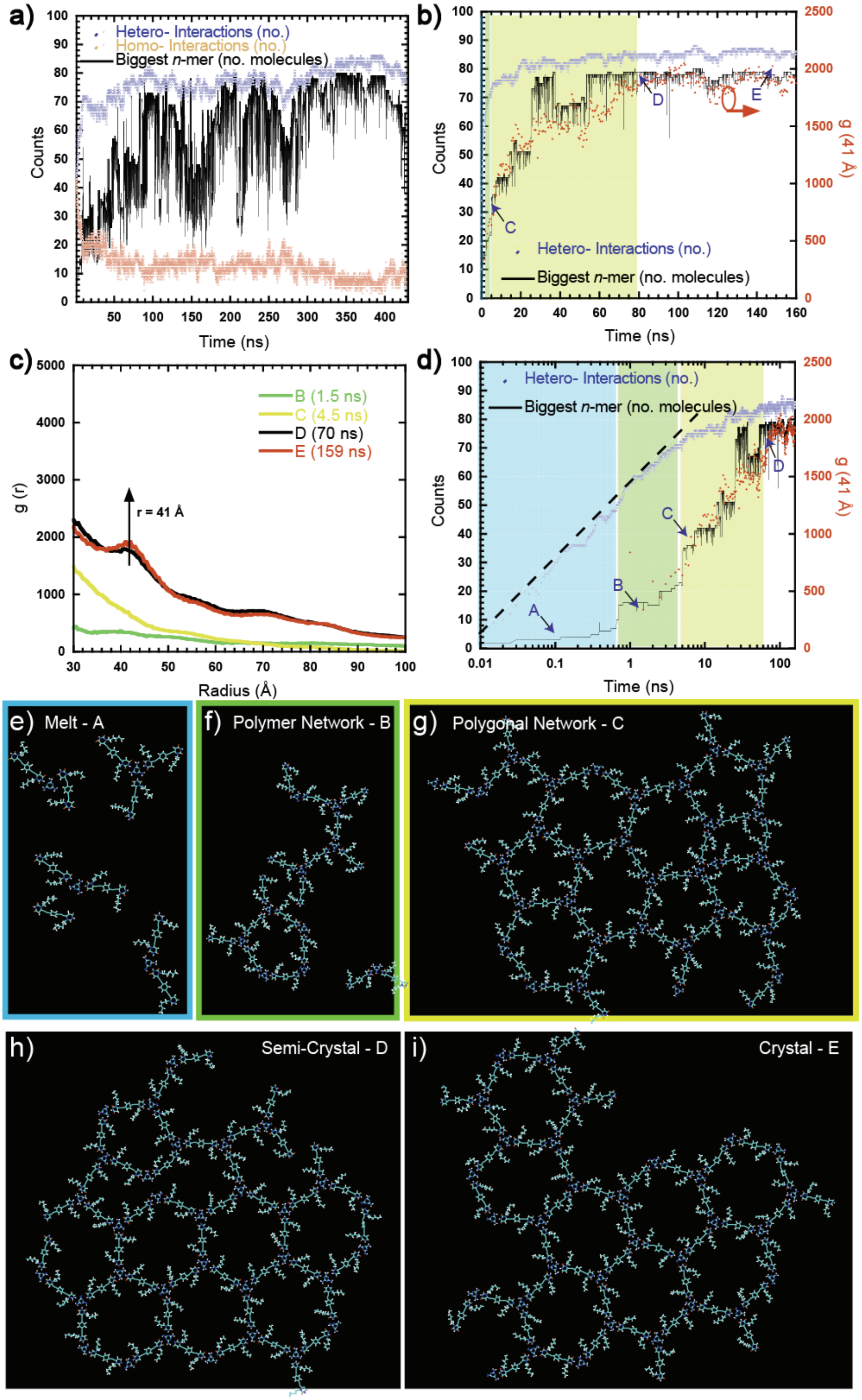
a)
Hetero- Interactions (no.)
Homo- Interactions (no.)
Biggest n-mer (no. molecules)
Counts
Time (ns)
b)
Hetero- Interactions (no.)
Biggest n-mer (no. molecules)
Counts
g (41 Å)
Time (ns)
C
D
E
c)
B (1.5 ns)
C (4.5 ns)
D (70 ns)
E (159 ns)
r = 41 Å
g (r)
Radius (Å)
d)
Hetero- Interactions (no.)
Biggest n-mer (no. molecules)
Counts
g (41 Å)
Time (ns)
A
B
C
D
e) Melt - A
f) Polymer Network - B
g) Polygonal Network - C
h) Semi-Crystal - D
i) Crystal - E

Figure 5-2

Self-assembly simulations of **Molecule** 7+**MEL**(*). a) Time evolution of **Molecule** 7+**MEL** at 420K. The time series of the size of the largest cluster and those of the number of *hetero*- and *homo*-recognition events are shown in black, red, and blue, respectively. b) Time evolution of **Molecule** 7+**MEL*** at 420K. The size of the largest cluster (black) and the number of *hetero*-recognition events (blue) are shown. By construction, *homo*-recognition events are absent (see Main Text). The Figure also shows the time series of *g*(r) at r = 41Å (red dots). c) Radial distribution function, *g*(r), determined at different time frames of the **Molecule** 7+**MEL*** simulation. d) Logarithmic plot of (b). Four distinct phase behaviors are apparent. e-i) Structural representation of the intermediate states identified in (d).

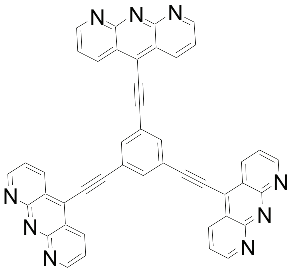

$C_{45}H_{21}N_9$
Mol. Wt.: 687.71

Molecule 17

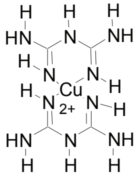

$C_4H_{14}Cl_2CuN_{10}$
Mol. Wt.: 336.67

Molecule 18

Following the principles emerged from the analysis of **Molecule 7+MEL***, we turn our attention to the supramolecular engineering of a bi-component featuring improved self-healing ability, through enthalpic control. Enthalpic control refers to the removal of the non-cooperative enthalpic *homo*-interactions. For this purpose, we *de novo* designed a system naturally devoid of homo-recognition. This was achieved by identifying two complementary molecules, the former exposing three parallel hydrogen bond donors that recognize three parallel hydrogen bond acceptors belonging to the second molecule (**Molecule 17+Molecule 18**, **Figure 5-3a**). For the sake of computational simplicity the metal in the **Molecule 18** module was replaced with an artificial bond bridging the two biguanide moieties. In such a system, *hetero* recognition results in the remarkably strong dissociation energy of 52 kcal/mol. By following the strategy used for **Molecule 17+Molecule 18**, the self-assembly of an eighty-molecule **Molecule 17+Molecule 18** bi-component was simulated at 520K and dielectric constant of 2.5. For the system, the dielectric constant was changed to reduce the dissociation energy (E_{diss}) of the dimer to 20 kcal/mol. Also, the temperature was increased to 520K to have kT/E_{diss} of ~22, comparable with that of **Molecule 7+MEL** (See **Appendix**). **Figure 5-3b-e** shows the structural evolution of the system in a typical simulation trajectory. The melt phase rapidly aggregates into a 2D amorphous glass in tenths of picoseconds until a stable cluster is formed (**3b**). The cluster rearranges into a 2D glassy network in about 100 ns (**3c**), evolves into a polygonal network (**3d**) and finally undergoes a spontaneous transition to a semi-crystal featuring five hexagonal pores (**3e**). The latter further evolves into a six hexagons structure in about half microsecond. Strikingly, the *de novo* designed **Molecule 17+Molecule 18** bi-component shows the spontaneous transition to the semi-crystalline phase observed for the model system **Molecule 7+MEL*** (see **Figure 5-3f-g**).

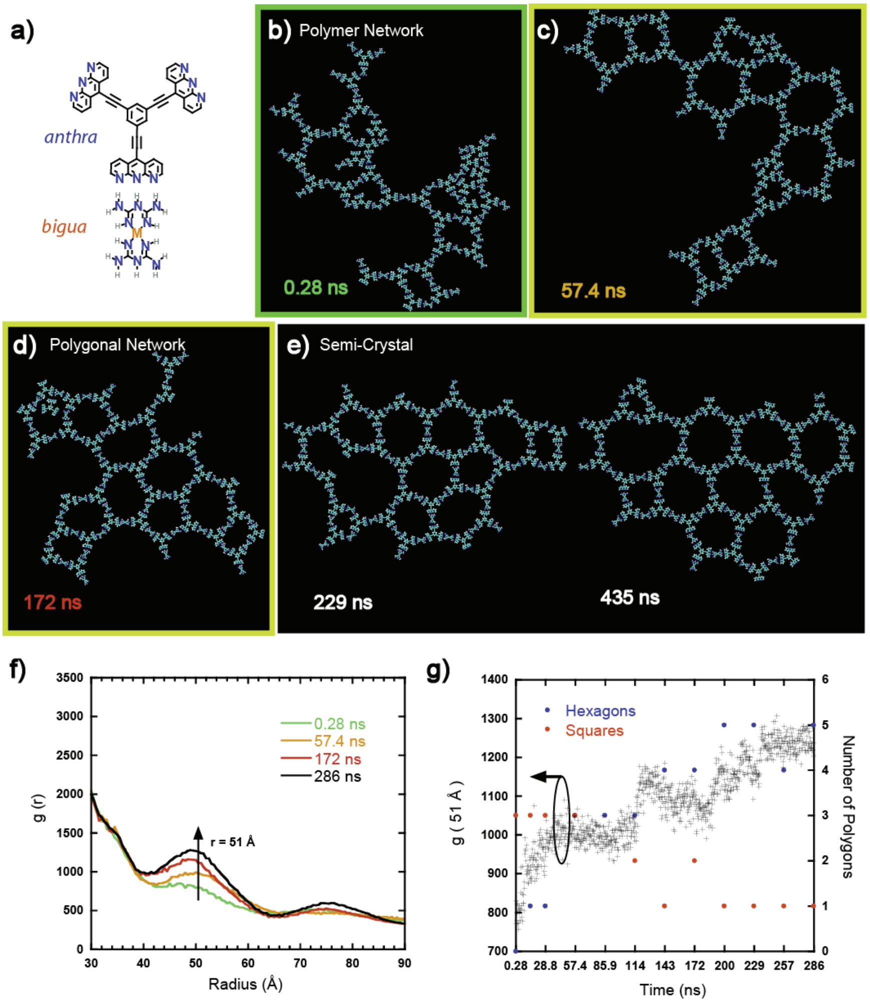

Figure 5-3

Self-assembly simulations of **Molecule 17+Molecule 18**. a) Chemical structure of the complementary *hetero*-dimer. The **Molecule 17+Molecule 18** recognition is based on donor-donor-donor (DDD) coupling with acceptor-acceptor-acceptor (AAA) triazaanthracene moieties. The metal (M) of the **Molecule 18** module was replaced by an artificial bond in the simulations. b-e) Molecular snapshots extracted from a typical self-assembly simulation depicting the structural intermediates leading to the semi-crystalline phase. f) Radial distribution function, *g*(r), at chosen times. The band centered at r = 51 Å, which corresponds to the unit cell vector length for a fully crystalline pattern, shows the evolution of the system to ordering. g) Time series of *g*(r) at a distance of 51 Å. Blue and red dots, respectively, correspond to the number of hexagons and squares sampled in the simulation as a function of time.

Computer-assisted self-assembly represents a milestone in supramolecular engineering. We demonstrated that knowledge of the free-energy landscape can be exploited to elucidate bi-component self-assembly into crystalline networks *in silico*. The reversible nature of the self-assembly process was evidenced by monitoring the self-healing of a 2D polygonal network into a 2D crystal. We captured the molecular origin of the frustration of the underlying free energy surface and used it to design a novel bicomponent with improved self-healing ability. These findings are an important step in *de-novo* material design, where understanding the link between the chemical nature of the building blocks and the properties of the resulting architectures is of paramount importance. This problem is highly reminiscent of the relationship between primary sequence and three-dimensional structure of proteins .

6 Towards Function

As our understanding of self-assembly grows through the supramolecular tools brought forward in the previous chapter, functional molecular libraries require active parallel developing. So far, we have extensively characterized and given four linkers capable of forming 2D self-assembled monolayers with different levels of ordering, domains of which extend hundreds of nanometers. In this regard, we have established a protocol to position linkers in space, which we now quantitatively and qualitatively know need to comply with certain criteria for creating crystalline, polygonal, amorphous or phase-separated phases. This chapter deals with the conception of linkers for a specific function. Section 5.1 introduces chromophores of technological importance, while section 5.2 deals with the conception of photo-responsive monolayers.

In the closing section of the present work, we put forward the foundations of device self-assembly (**Figure 6-1**), introducing 3D bottom-up self-assembly via the design and ongoing development of platform-like supramolecular networks.

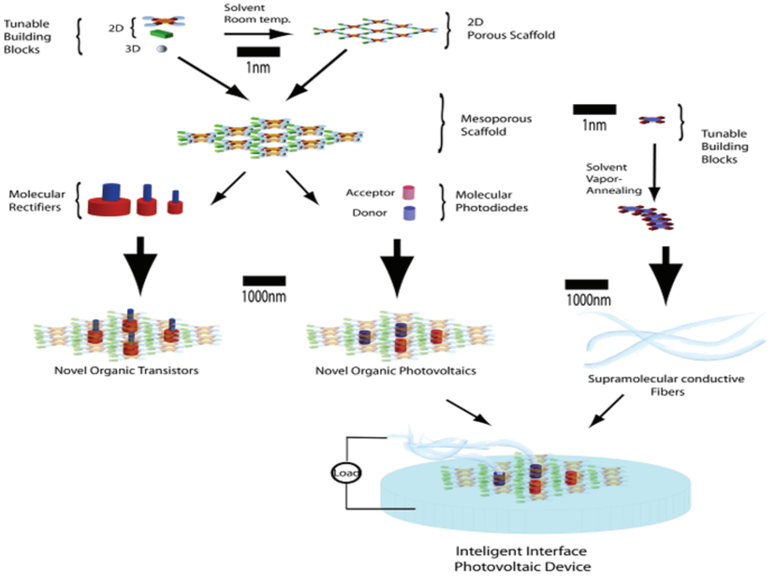

Figure 6-1
A convergent approach towards device self-assembly. Conducting fibers and functional scaffolds are self-assembled and then converge in a single photovoltaic device.

6.1 Functional Di-imide Linkers

In this section, we develop functional di-imide linkers exploiting the well establishment of the **Linker+MEL** hexagonal 2D pattern. As such, we can continue to develop linkers with different properties to enrich the molecular toolbox.

6.1.1 Photo-responsive Linkers

In 2D self-assembly, besides the wide utilization of 2D monolayers for tuning the electronic properties, the ability of molecules to respond nanoscopically to an stimulus we can control in the macroscopic world has captivated the attention of scientists. In particular, any conformational change of a molecular induced by electromagnetic radiation is highly sought for the latter purpose. The ability of stilbenes of changing their conformation from *E*→*Z* about the N=N double bond upon light irradiation has been well known since at least 50 yrs (Zimmerman, 1958). It was found that one analogue of stilbene, diphenyldiazene, more commonly known as azobenzene, could change its conformation using shorter wavelengths and in a higher yield of the kinetic *Z* product. It is for this reason and their ease of synthesis that we will dedicate this section to the understanding of the azobenzene functionality upon adsorption into HOPG.

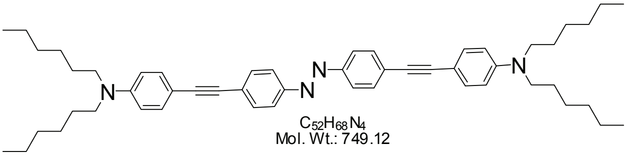

Molecule 19

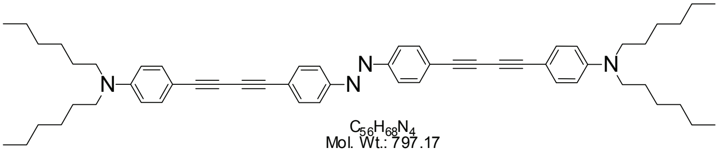

Molecule 20

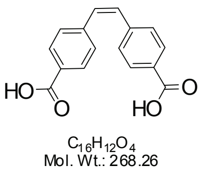

Molecule 21

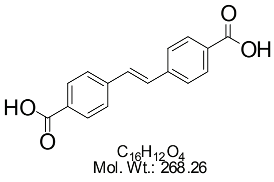

Molecule 22

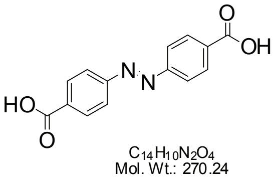

Molecule 23

Before we continue we must mention that the *E* and *Z* conformation are geometrically misleading in azobenzenes since the dihedral angle in the "*Z*" conformation may vary from 0 º to ~25º. For this reason, we introduce the azimuthal angle as a characteristic of the "Z" conformation. **Figure 6-2** shows that the azimuthal angle, defined as the angle between a plane containing a phenyl ring and the next immediate carbon after the azide, varies only few degrees for both theory and experiment.

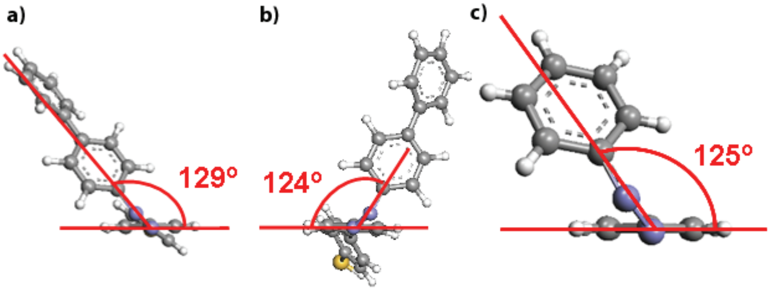

Figure 6-2
Some (*E*)-azobenzenes in two theoretical steepest descent gradient minimization from a) DFT B3LYP/6-311d,p and b) MMFF Force Field and an experimental c) neutron diffraction structure (Mostad and Rømming 1971).

Experimental Details are given in the corresponding **Appendix** subsection. However, there exists experimental details that cannot pass by without special attention. The power and geometry of the irradiating source is of key importance and is often disregardedt reported in photoswitching experiments. For solution experiments in the left hand sides of **Figure 6-3** and **Figure 6-5,** Armaroli and coworkers use a 150 W argon lamp power supply model C1-X8P, the excitation wavelength was selected by means of Andover Corporation optical bandpass filters (10 ± 2 nm) with unknown irradiation power to the samples. For the rest of STM and solution experiments we use a Pen-Ray 360nm lamp model 11SC-1L with a reported power ratio of 1.3mW/cm^2 at 2 cm from a the target, which is our usual irradiation geometry (from the tip of the lamp to the HOPG for the STM experiments and using the body of the lamp against a standard quartz cuvet for the optical measurements). Owing to the high electrical noise introduced with the Pen-Ray, we latter on implemented the use of a ~0.7 mW/mm^2 340nm T9F34C diode from Seoul Optodevices.

Owing to their extended conjugated back-bone and alkyl chains, **Molecule 19** and **Molecule 20** were provided by Bonifazi and coworkers for physisorbtion experiments on HOPG. STM investigations for both molecules were carried out in solutions of pure phenyloctane solvent, the right hand side of **Figure 6-3** shows the adsorption of the *E* isomer on the basal plane of HOPG, with the proposed superimposed molecular models. In the photophysical studies, the molecules were found out to isomerize in cyclohexane solvent by Armaroli and coworkers. The photoisomerization of **Molecule 19** is shown on **Figure 6-3**, showing that, assuming that Beer's-law holds in the concentration range, the photoisomerization *Z* yield is at least >60%. With such a good photoisomerization yield we irradiated the a ~10µL dropcasted solution *in situ* for more than one hour. While during the first hour there was no apparent change in the physisorbed pattern, we noticed a quick desorption of the monolayer after 100 min of irradiation (**Figure 6-4)**. Note that the monolayers is stable in the dark for more than 5 hours. In fact if at the desorption point the irradiation is stopped, the initial pattern is recovered in a few minutes. The same results were found for a sequence of experiments. Indeed, we may attribute this behavior to two possible hypotheses: i) The *E* photoisomer is formed on the surface and as a consequence the monolayer gets desorbed. ii) The *E* isomer is forming in solution and at a certain point there is a strong chemical potential gradient that induces the desorption of the *Z* isomer. To address these two fundamental questions we must pursue the photoswitching study of a series of analogous molecules at the solid-liquid interface. Unfortunately, the next molecule in the series, **Molecule 20** appears to present a very low photoswitching yield, as evidenced by the small changes in the adsorption spectrum in **Figure 6-5**, making it unsuitable for persistent STM photoisomerization experiments.

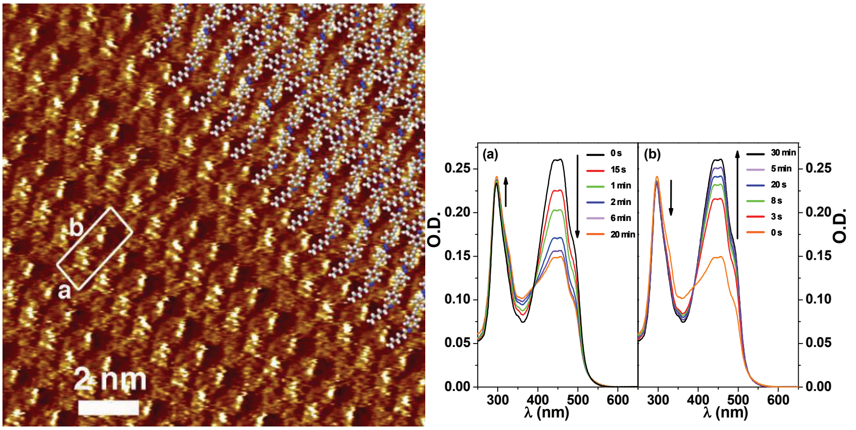

Figure 6-3

Left hand side: STM current image of the monolayer formed by **Molecule 19** in 1-phenyloctane at the HOPG-solution interface. Image size: 9×9 nm2. Tunneling conditions: average tunneling current (I_t) = 10 pA, bias voltage (V_t) = 500 mV. The CPK molecular models and the unit cell are superimposed (unit cell parameters: a =1.01 ± 0.05 nm, b = 2.52 ± 0.05 nm, a,b = 97 ± 1°). Right hand side: Time evolution of the absorption spectra of a 58 µM solution of **Molecule 19** in cyclohexane under 450 nm light irradiation, until the photostationary state is reached. (b) Back reaction observed over time under 300 nm light irradiation. The initial ***E*-Molecule 19** spectrum is fully recovered showing complete reversibility.

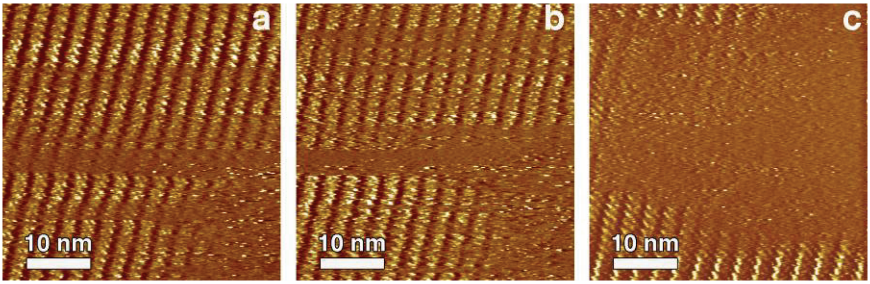

Figure 6-4
STM image of the ***E*-Molecule 19** after 100 min (a), 110 min (b) and 120 min (c) of irradiation *in-situ*. The SAM is slowly getting desorbed from the surface. Tunneling conditions: (I_t)=10 pA, (V_t)=500 mV.

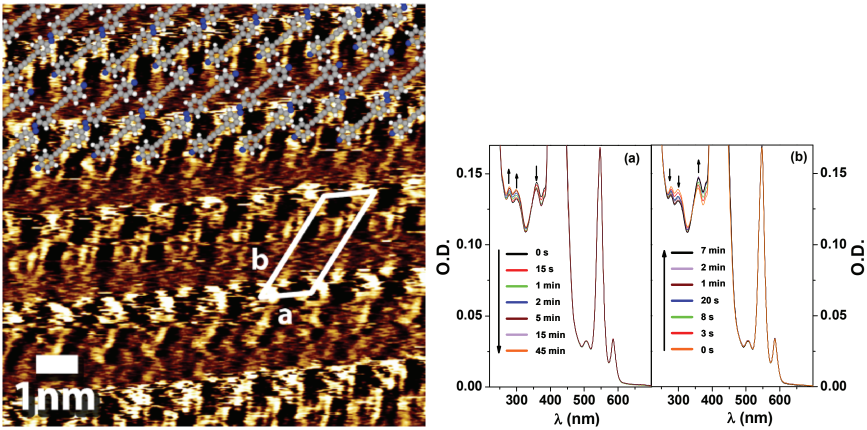

Figure 6-5
Left hand side: STM current image of the monolayer formed by **Molecule 20** in 1-phenyloctane at the HOPG/solution interface (N-alkyl chains are not shown for clarity). Tunneling conditions: average tunneling current (I_t)=10 pA, bias voltage (V_t)=300 mV. The CPK molecular models and the unit cell are superimposed (unit cell parameters: a =1.23 ± 0.05 nm, b=2.48 ±0.05 nm, γ = 59º).Right hand side: Time evolution of the absorption spectra of a 60μM solution of **Molecule 20** in cyclohexane under 360 nm light irradiation, until the photostationary state is reached. (b) Back reaction observed over time under 289 nm light irradiation. The initial **Molecule 20**spectrum is fully recovered showing complete reversibility.

In view of the previous observations, we then turn our attention to an archetypical azo-benzene ***E*-Molecule 23** kindly provided by Mayor and coworkers. The photoisomerization experiment in DMSO showed that >50% photoswitching yield can be optained after only 2 minutes of irradiation at 340nm, making it an excellent candidate for STM investigations. **Figure 6-6** shows the high-resolution STM experiment in TCB solvent alongside the photophysical investigation. It is worth noting that the substrate appears to “bend” the molecule, such that the superimposed models must be scaled down by 20% to fit the periodic pattern and the unit cell. The origin of this phenomenon was not clear but may relate to conmesurate effects of the molecule with the underlying graphite substrate. Despite of the good photoisomerization yield, the patterns could not be photoisomerized *in situ, i*.e. irradiation at 340nm for ~2h did not show any significant changes in the observed domains of ***E*-Molecule 23**. We have to add that, unlike studies in phenyloctane, the TCB solvent is almost completely evaporated after ~3h of scanning thus longer irradiation experiments are not feasible.

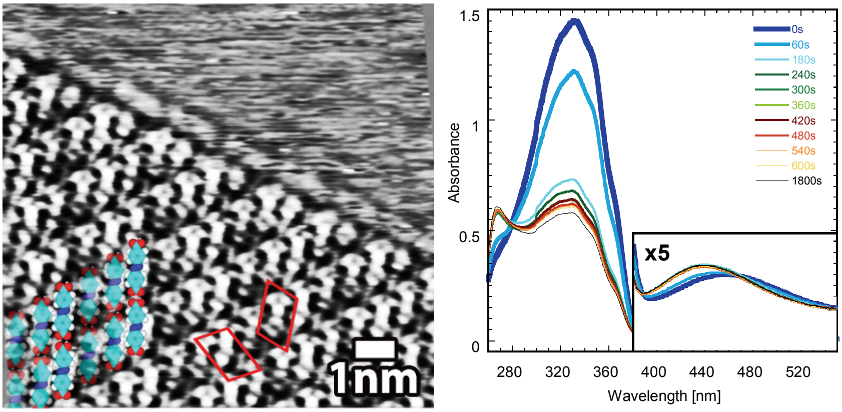

Figure 6-6

Left hand side: STM images of ***E*-Molecule 23**. No evidence of switching was obtained in solutions from 3-300 µM irradiating with the 340nm diode. Again models are scaled by 80%. Right hand side: Time evolution of the absorption spectra of a 57 µM solution of in DMSO under 360 nm light irradiation

To give further proof that the *Z* form cannot be physisorbed, we opted to utilize commercially available *Z* and *E* stilbenes with purities of >95%, ***Z*-Molecule 21** and ***E*-Molecule 22**, respectively. Our results shows that only the ***E*-Molecule 22** is physisorbed in the surface. **Figure 6-7** shows two molecular packings that have been found from both ***E*-Molecule 22** and ***Z*-Molecule 21** solutions, of concentrations 14µM and a 23µM in TCB, respectively. The unit-cell are a = 0.90 b = 0.68 nm (**Figure 6-7** Left hand side) and a = 1.25 b = 0.70 nm (**Figure 6-7** Right). Interestingly, like in **Figure 6-6**, in one domain the molecular models had to be scaled down by 80% while in the other they were scaled down by 95%.

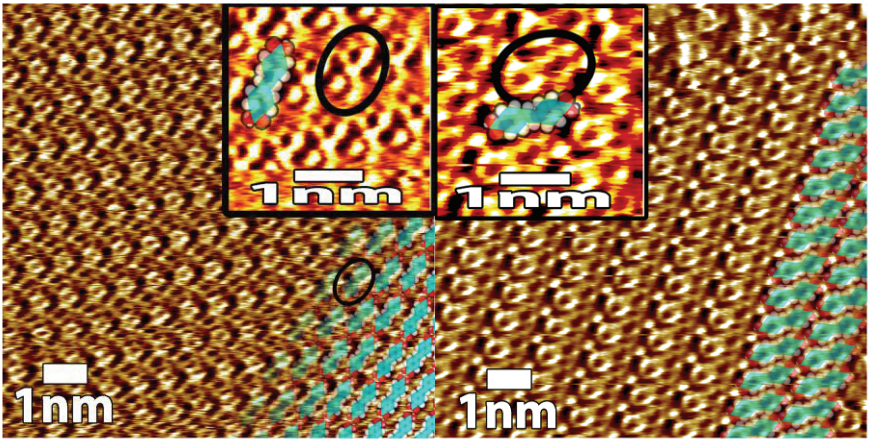

Figure 6-7
STM packings found in solutions of ***E*-Molecule 22** and the **Z-Molecule 21** (95%) stilbene attributed exclusively to the *E* isomer.

We can conclude that physisorbed molecules won't undergo *E*→*Z* isomerization when their adsorbed state is highly stabilized either by H-bonds, in the case of like in the case of ***E*-Molecule 23** or by adsorption energy and low *E*→*Z* yield like in the case of **Molecule 16**. More details on the photo-isomerization of physisorbed can be obtained introducing two new linkers, **Moleculer 24** and **Molecule 25**.

Figure 6-8 depicts the STM images of the pristine compounds in TCB solvent. The packing in the left hand side image belonging to **Molecule 24** could not be resolved and appears to form hexagonally distorted macrocycles. The observation is in line with the results previously obtained for **Molecule 13**, in Chapter 3, where the kinetic pattern was not elucidated. The right hand side of **Figure 6-8** depicts the packing of **Molecule 25**, showing clearly closed-packed rows of molecules, featuring the azobenzene moiety in high-contrast. No changes in neither pattern were observed upon irradiation with 340nm T9F34C diode the of the molecules in 6µL drops <4µM solutions for 1h.

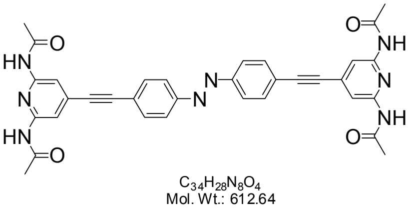

Molecule 24

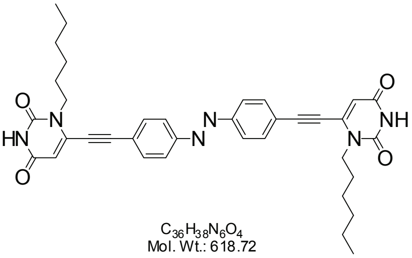

Molecule 25

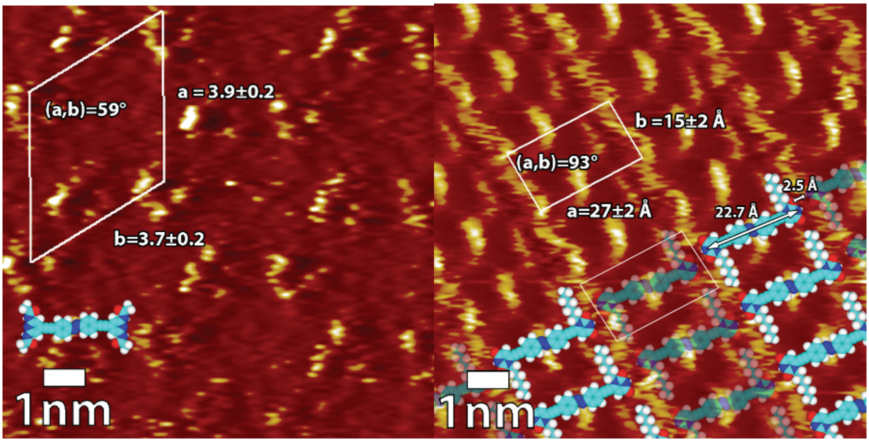

Figure 6-8

STM image of pristine components right hand side **Molecule 24** It = 7pA, Vt = 490mV and b) **Molecule 25** It = 5pA, Vt = -275mV in 1,2,4-trichlorobenzene/0.1%DMSO. The error in the model superimposition is below 2%. The 512x512 pixels images were smoothed by a 3x3pixel mean.

We are particularly interested in the photoswitching in binary mixtures of the molecules, following our studies on Chapter 5. In view of this **Molecule 24** can be naturally mixed with **Molecule 14** (the tetratopic uracil-like corner stone) to try and form 2D networks, under similar conditions discussed previously for **Molecule 13 Molecule 14**. The outcome of these investigations showed no difference from our previous results in Chapter 5, i.e. only amorphous and frustrated networks were observed. For the second azobenzene linker, **Molecule 25**, distorted polygonal architectures are successfully obtained when blending 6µL of 2.5µM of each solution separately *in-situ* **Figure 6-9*a***. Unfortunately neither this pattern showed any response towards irradiation *in-situ*, even when 100µL of 5µM solutions were for the STM scanning setup, achieved with the help of a teflon fluid-cell. Note that with the teflon unit-cell irradiation can be prolonged for up to five hours since TCB solvent will not evaporate (6µL-10µL TCB solutions will evaporate in only 2-3h).In another essay, **Molecule 24** and **Molecule 25** are mixed to try to obtained bi-component polymers at the solid-liquid interface. Again no binary mixtures were observed from multiple attempts, e.g. by using of 100µL fluidcells, *in-situ* heating to 30ºC, ex-situ heating at 40ºC over 2-3hours, etc. **Figure 6-9a** shows a phase-separated image of 5µL of 4.0µM solutions of **Molecule 24** and 6µL 3.3µM of **Molecule 2.5**

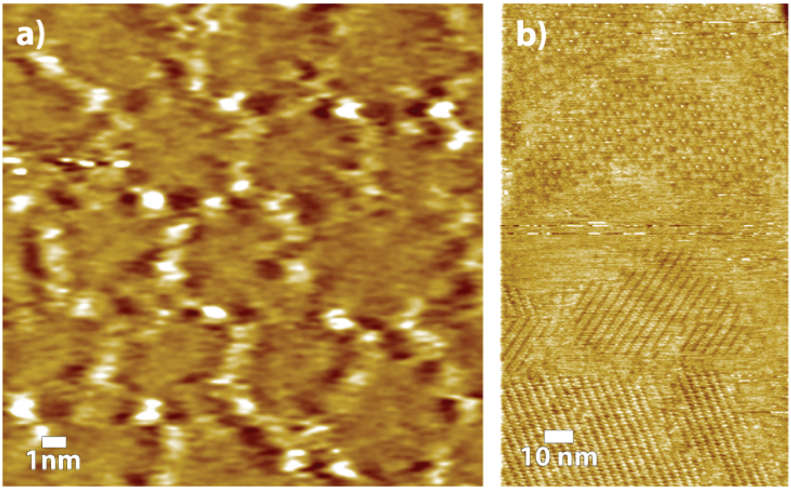

Figure 6-9
Binary solutions of a) **Molecule 25 +MEL** I_t = 6pA V_t = 200mV showing the formation of a polygonal network and b) **Molecule 24** and **Molecule 25** showing phase separation: Upper part **Molecule 24**, lower part **Molecule 25** unit-cell. I_t = 8.7pA V_t = 335mV. Solutions in 1,2,4-trichlorobenzene/1-2%DMSO, Mean 3x3 pixel filters.

6.1.2 Electro-opical Linkers

From Chapter 4, we can foresee that both the goal of crystallinity and electro-optically active molecules can be expanded through the use of larger naphthalene di-imides. Larger conjugated molecules will present a red shift in the visible spectrum. Such low bandgap molecules are important absorbers for solar cell devices, provided that their lowest unoccupied molecular orbital (LUMO) is high enough for being an effective electrochemistry type charge donor (see Markus theory in Bard and Faulkner 2001).

Topologically speaking, the first strategy would be to increase the conjugation through the length for the molecules. For this, naphthalene can become perylene and even terrylene di-imide, which are a member of the important family of rylene dyes (Herrmann and Mullen 2006). The importance of rylenes goes beyond molecular rigidity - they present the interesting electronical properties that we are looking for and which can be tuned by altering the substuents in the bay area and are excellent light absorbers. With an estimated LUMO and HOMO from their half wave redox potentials (Bullock, Vagnini et al. 2010) of -4.00 and 5.12 and an adsorption maximun at 650nm (**Figure 6-10**), terrylene di-imide seems like an excellent candidate for solar cells, provided that its LUMO is at least 0.3eV above the electron acceptor level (Cheng, Yang et al. 2009).

A second strategy would be to increase the size of the molecule. This can be done for instance by using coronene families of molecules instead of rylenes to increase the molecular conjugation.

With that in mind, we set forth to formation of highly crystalline hexagonal lattice formation of mixtures of (**MEL**) and the terrylene-core. Prof. Dr. Klaus Mullen and coworkers designed two molecules based on both strategies, **Molecules 26** and **27.**

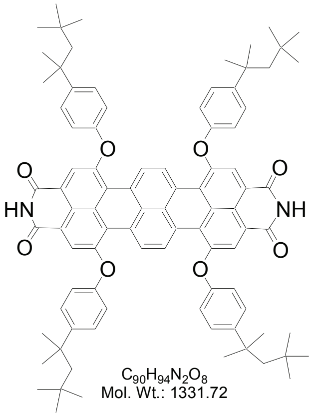

Molecule 26

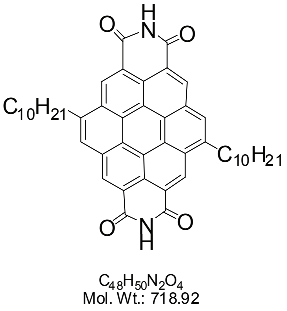

Molecule 27

Figure 6-10 shows the **Molecule 26** self-assembled monolayer at the TCB/HOPG interface. The so-formed self-assembled pattern was shown to be highly crystalline in the microscale (by scanning multiple 100nm-areas), a property encouraging electronic applications. Nevertheless the exact packing with sub-Å precision (i.e. with the subtle detail of the interface with the substrate) must yet be elucidated, as images on smaller scales could no be recorded.

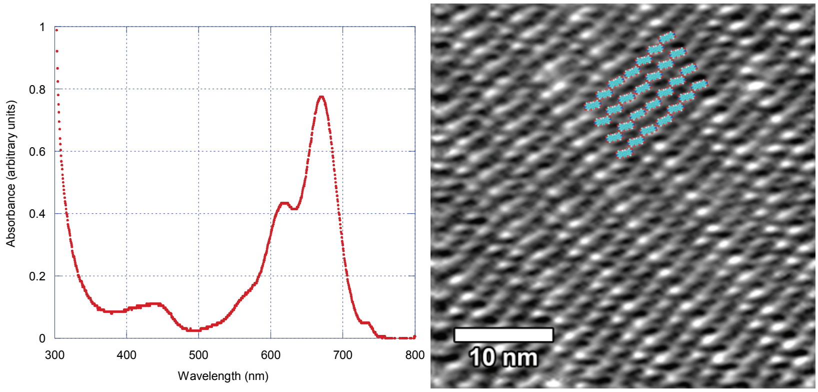

Figure 6-10

Left: Adsorption spectra of in TCB:1%DMSO (note the TCB adsorption onset ~320nm). Right: STM image at the solid-liquid interface of KM-T01 monolayer of 10µM solution on HOPG/TCB 2%DMSO. I_t = 0.20pA V_t = 200mV

For the formation of bi-component networks, a typical self-assembled experiment involved applying 6 µL of diluted (4± to 20± µM) solutions in TCB of **Molecule 26**+**MEL** to a freshly cleaved HOPG interface. Interestingly, hexagon-like structures (**Figure 6-12a**) appear after a few minutes of approaching the STM tip to the surface, exclusively in solutions around 7±µM and only at current set points (I_t) below 5 pA (for details of other structures at higher concentrations see the **Appendix**). **Figure 6-12b** depicts the minimized (to a GRMS of 0.01 kcal/mol, using an explicit surface potential, see **Appendix**) molecular models of two fused hexagons of **Molecule 26+MEL**. The models remarkably superpose with the STM image in **Figure 6-12a.** It was puzzling that no long-range nor defect-free images were observed in neat solutions of **1+MEL** in all five different experiments with concentrations of 7±µM. However we can observe small network fragments that are quickly disrupted by the STM imaging. We can hypothesize that, because alkyl chains cannot adsorb on graphite and because the molecule features a twisted backbone its self-assembled pattern is not robust enough *per-se.* This is illustrated in **Figure 6-11**. When we simulate the **Molecule 26** structure through 300K with the backbone constrained in space and ontop of the graphene slab, we notice that the alkyl chain conformations change radically. In fact when the **Molecule 26** is simulated without a surface the most populated states of the alkyl chains are in what we name the **1**-up **4**-down **1'**-down **4'**-up conformation. The *all-up* conformation (the one that must exist in the surface) exists in a very small percentage.

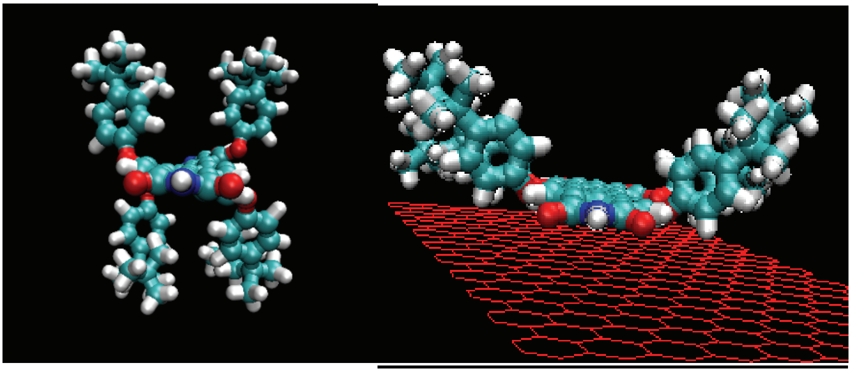

Figure 6-11
Molecule 26 simulated via molecular dynamics, free in "solution" at 300K and ontop of a graphene slab.

Interestingly, when applying to the unstable pattern of **Molecule 26+MEL**, *in-situ* solutions of coronene and fullerene (C_{60}), 1.1mM and 5mM respectively, highly crystalline long range images can be then readily imaged (**Figure 6-12c**) featuring also high-current contrast islands which we tentatively ascribe to C_{60} clusters (**Figure 6-12c in red circles**). We rationalize the successful imaging of extended crystals only upon addition of coronene+C_{60} as follows. From one side, coronene favors thermodynamically the pattern. From another side, C_{60} is an electron scavenger that successfully allows imaging with STM parameters at higher current set points. Also, although large, defect-free domains where normally formed with co-adsorption of coronene+C_{60} (Compare the 2D Fast-Fourier Transform in **Figure 6-12d** with **Figure 6-12c**), in one out of four experiments defects were formed. We assign this defect formation to a melamine deficient domain, which leads to homo-coupling interactions between **Molecule 26**.

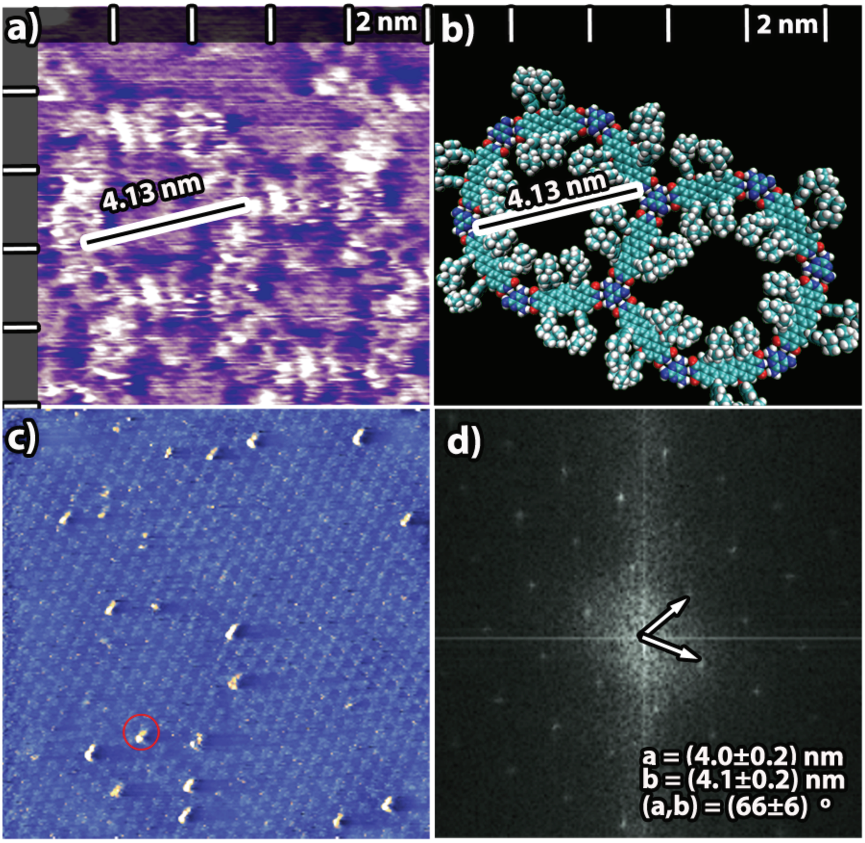

Figure 6-12

(a) STM constant current image of a 7µM solution in **Molecule 26** and 10µL in MEL. I_t = 0.08pA V_t = 150mV The bar represents 4.13 nm, which corresponds to the diameter (carbonyl to carbonyl) from a **(b)** Double hexagon molecular model minimized by the MMFF force field. **(c)** STM constant height 100nm^2 image of the same solution after addition of a C_{60}/Coronene solution. I_t = 0.41pA V_t = 791mV The red circle identifies presumable C_{60} clusters adsorbed within the hexagonal structure. **(d)** 2D Fast Fourier transform of c showing the high crystalline of the assembly.

6.1.3 Combined Approaches

The high conformational change found in the position of the side-chains of , **Molecule 26** (particularly the *all-up* side-chains) makes similar compounds interesting candidates for becoming molecular platforms, i.e. molecules that can symmetrically reach the third dimension with functional units.

Towards 3D prone architectures by means of azobenzenes. We have witnessed that azo-benzenes cannot readily interconvert from *E*→*Z* in their adsorbed form. By changing the side-chains of **Molecule 26** by azo-benzene moieties equipped with moieties which can undergo recognition events, a steady bi-state molecule may be created. This would make it possible to access new types of molecular cages. **Figure 6-13** shows how these particular type of molecular cage can be opened and closed through external stimuli. This complex functional system may be for instance applied to information storage. In the latter case, **Figure 6-14** reveals how the cage in a closed conformation experiences a higher tunneling current in a molecular junction probed by STM, thus e reversible writing with light or tip stimuli may be accomplished.

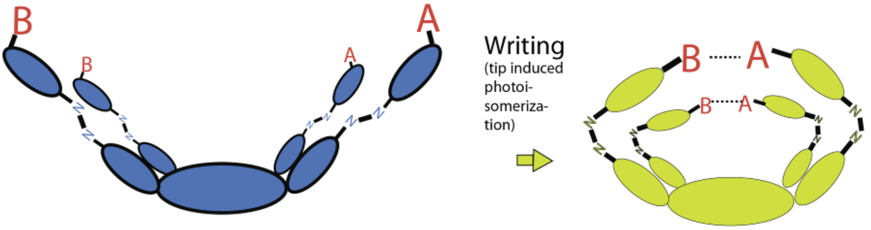

Figure 6-13
Conception of a Bi-stable switch, an azo-benzene-functionalized Terrylene. The functionalities A and B are used to create a bi-stable (OPEN-CLOSE) conformation which is only reversible by using the tip and/or by strong UV-light. The voltage applied locally with the STM tip may be employed as a stimuli to trigger azobenzene isomerization, thus controlled surface patterning.

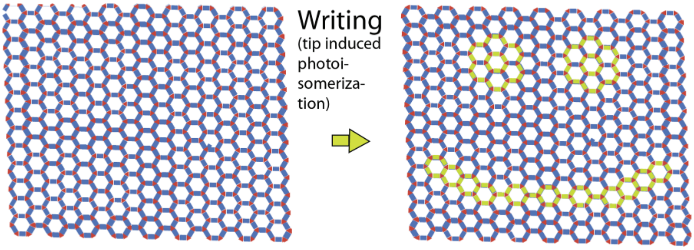

Figure 6-14
An applied example of 2D monolayers functionalized with 3D-prone azobenzenes for information storage by tip-induced writing in highly crystalline monolayers.

The design of a molecule that may undergo this type of recognition (**Figure 6-13**) is crucial and is currently being developed with the group of Prof. Dr. Klaus Müllen. In parallel, the tools developed in Chapter 5 can be applied to understand the possible formation of such a cage. **Figure 6-15** depicts a concept molecule where the A,B positions have been replaced by CH_2COOH moieties. Interestingly, the first disadvantage of this design is not the eventual insolubility of the carboxyl units but are the bay-area phenyl groups, which make the torsion of the azo-benzene, i.e. an eventual CLOSE position, impossible.

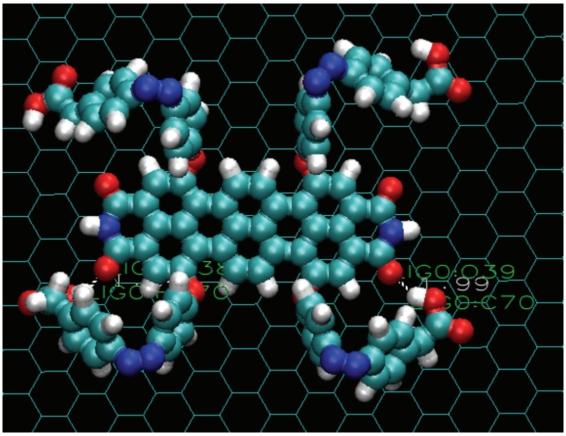

Figure 6-15
10ns Molecular Dynamics Simulation of A,B = CH_2COOH system in *Z* configuration. The all- *Z* conformation shows that the side-chains do not CLOSE on top of the molecule since the first benzene most favorable position is perpendicular to the surface. Notice the intramolecular hydrogen bond between the imides and carbonyls.

In view of the previous, we show how molecular dynamic tools are mandatory for complex molecular design. For instance, current modeling shows that a second phenyl ring might be necessary for achieving an all-*Z* CLOSED conformation. This molecule is currently being modeled with R= CH_2COOH. Close collaboration and feedback might allow a joint design of the best “R” groups for a reasonable synthetic procedure that can afford a molecule for achieving a bi-stable all-*Z* closed conformation.

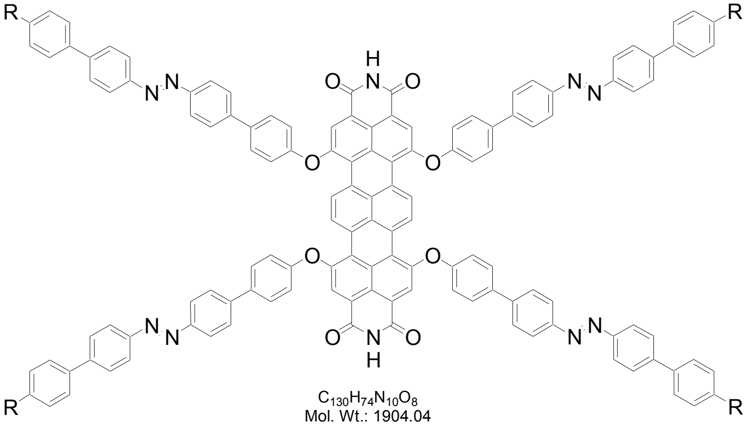

Figure 6-16
Second design of a bi-stable switch. Simulations on this molecule are currently being carried out, again whit the groups R=CH_2COOH.

6.1.4 **Ion-responsive Linkers**

A second strategy for tuning monolayers through external stimuli may include conformational changes in response to a third component in solution. Besides the solvent, the third component can be an ion or a guest molecule. While guest molecules may not be readily directed by external stimuli, Lehn an coworkers have shown that ions may be complexed and extracted using cryptands through pH modulation, and the process repeated many cycles (Barboiu and Lehn 2002). This principle has just been recently applied to monolayers at the solid-liquid interface (Ciesielski, Lena et al. 2010). Because of this, actively developing of linkers and cornerstones is mandatory. In a collaboration with Prof. Dr. Alan Rowan, a library of modules have been proposed, featuring crown ethers that can respond differently to multiple ions (Glendening, Feller et al. 1994).. For this goal, **Molecule 28** and **Molecule 29** were designed with embedded [18]O[6]-crown units. Interestingly, the use of [18]O[6]-crown allows not only a response from Li^+, to Na^+ and K^+ but it also may complex Cs^+ to form “sandwich” complexes with the immediate consequence of the formation of bilayers.

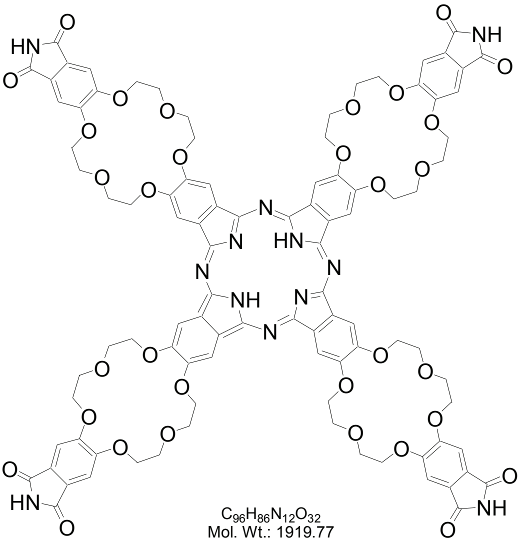

Molecule 29

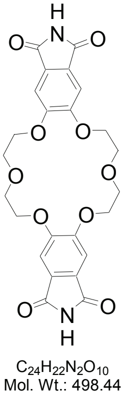

Molecule 28

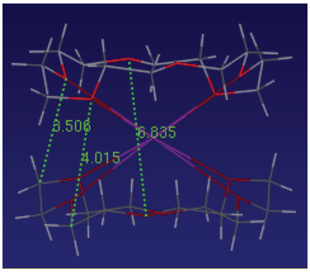

Figure 6-17

The ([18]O[6])$_2$Cs+ solid-stae complex, taken from (Dawes, Ward et al. 1986).

6.2 Towards 3D Device Self-Assembly

In this closing section we will try to grasp all the different possibilities that we have in order to create working functional devices through supramolecular engineering. While the **Linker+MEL** system has served as a model system to introduce the field of supramolecular engineering and to exemplify the unlimited flexibility of a bi-component system to tune function, it lacks one important characteristic. It is not three-dimensional. Through the acquired empirical knowledge of the previous chapters and with the help of the newly developed 2D molecular dynamics supramolecular engineering tool (MolSET) we will now venture into the supramolecular engineering (and future self-assembly) of complex 3D devices.

This section will present preliminary results in the creation of a new library of compounds based on porphyrins, synthesis which has been undertaken by the author under the supervision of Michael Schär, Petra Fesser and Prof. Dr. François Diederich.

While there is now unambiguous proof that two separate components may self-assemble into highly-ordered 2D architectures, there is no reason to believe that two separate components won't form 3D architectures. The most intuitive way of having full conformation control over 3D architectures is through the use of a symmetric platform and a metal center. The metal center would then allow for the coordination of an axial ligand and its interchange for the tuning of coordination strength. **Figure 6-18** depicts this principle through the use of a D_{4h} molecular platform.

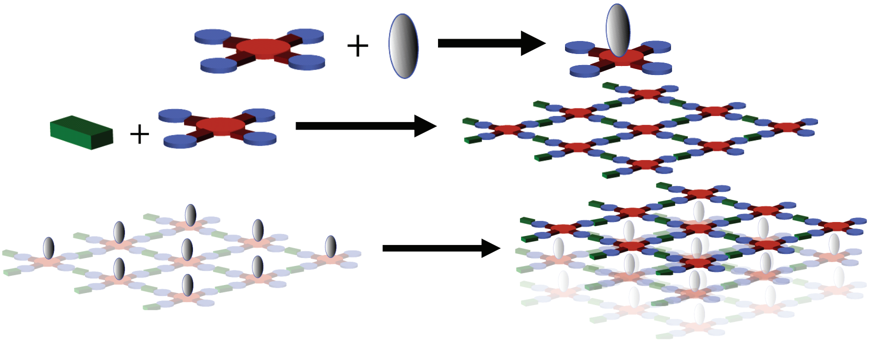

Figure 6-18
The reversible platform approach, showing the 2D linker (in green) and the 3D linker (in gray).

It is straightforward to note that such natural coordination platforms may be represented by phtalocyanines and porphyrins. With this in mind we proceed to the design of a bi-component molecular system, each bearing distinct recognition moieties based on the complementary units introduced in Chapter 4, **Figure 4-1**. Because of the previous aggregation problems in the (diacetylamino)pyridil units, we proceed to synthesize a porphyrin which is able to form hydrogen bonds with a complementary 2D linkers through the cytosine-isocytosine pair. An important alternative to this complementary recognition moiety would also be the amidinium-carboxylic acid pair. Despite its simpler synthesis, such a recognition pair could pose problems due to the basicity of the amidinium unit (conjugated pka ~ 11), an important factor when dealing with metal centers. In this regard, we propose the synthesis of cornerstone porphyrin **Molecule 30** along its complementary linker **Molecule 31**. While **Molecule 30** would serve as the "zero" level template, a third component featuring **Molecule 30**'s complex with Cobalt, would serve as the platform for the successive layers.

We note that the 2D linker **Molecule 31** is readily available in mg quantities from Dr. Michael Schär.

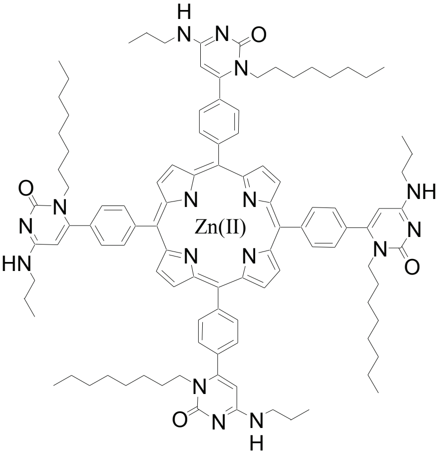

$C_{104}H_{128}N_{16}O_4Zn$
Mol. Wt.: 1731.62

Molecule 30

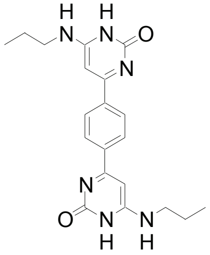

$C_{20}H_{24}N_6O_2$
Mol. Wt.: 380.44

Molecule 31

Once the synthetic blueprints established, we proceed to the simulation of a 80 molecule stoichiometric mixture of **Molecule 30 + Molecule 31** though the use of the 2D molecular dynamics supramolecular engineering tool (MolSET). Strikingly, our preliminary simulations show that only after 10ns at 400K, stable supramolecular polygons are readily formed **Figure 6-19** . This sole result is indicative that the system is far more performing that the two other systems we have studied in the previous chapter. We can prematurely interpret the origin of the improvement. While we developed earlier the notion of self-healing through enthalpic control, here we rediscover self-healing through entropic control. The red circles in **Figure 6-19** mark the different conformations of the N-alkyl chains in the cytosine and isocytosine moieties. This rotation disfavors strong aggregation through homo- and hetero- coupling even at low temperatures. A natural evolution of the assembly will slowly bring the system towards the formation of crystalline architectures.

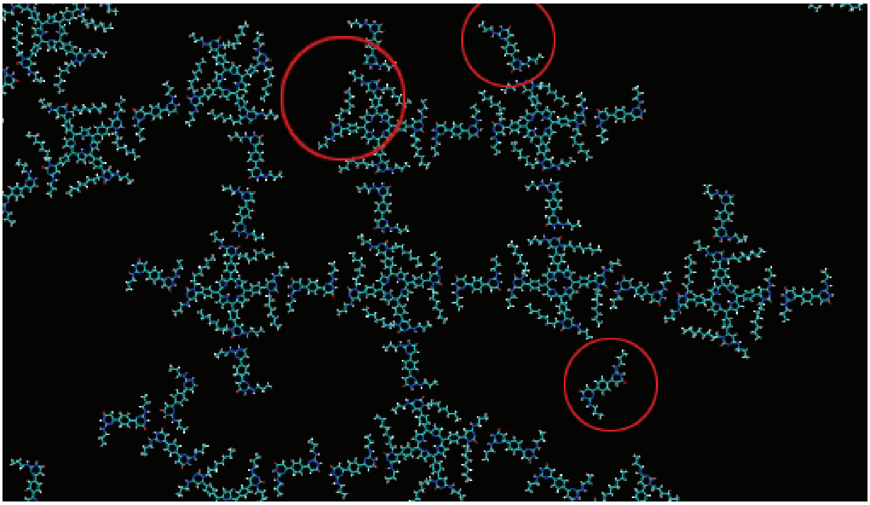

Figure 6-19
Preliminary use of the molecular dynamics supramolecular engineering tool (MolSET) for the design of a new 3D-prone multi-component system. A Supramolecular square extracted from 10ns molecular dynamics simulations of an stoichiometric mixture is shown, along side different conformations of the N-alkyl chains allowed by the implicit surface.

The synthesis of the molecular fragments **Molecule 30*i*** and **Molecule 30*iv*** for ultimately obtaining molecule **Molecule 30** is currently being carried out (see corresponding section in the **Appendix**).

We have grasped one of thousand of possibilities that can be investigated under the scope of supramolecular engineering using the preliminary tool MolSET. We expect, that, with a joint scientifically effort, such exciting 3D self-assembled devices will flood many areas of science in the near future.

7 Conclusions

In summary in the present work we inferred three qualitative phenomenological principles and developed one deterministic molecular dynamics tool (MolSET) for the ultimate goal of prediction and formation of supramolecular architectures, i.e. *Supramolecular Engineering*. For the formation of a sought 2D (anisotropic) architecture to occur, all kinetic criteria below must be obeyed while the thermodynamic criterion is not absolutely necessary when the time scale of interest is kinetically fulfilled. Moreover, we gave interesting perspectives towards future development of *Device Self-Assembly*.

1- **Kinetic Growth Conditions of 2D Supramolecular Architectures**: "The growth rate of a 2D pattern is proportional to the dissociation of its respective dimer. A structure must grow faster than it is dissolved.".

$$k_{growth}^{macro} \sim k_{dissociation}^{micro} \ \& \ b \cdot k_{collision}^{micro} > k_{dissociation}^{micro}$$

where $k_{collision}$ is the collision rate of the uncomplexed molecules or clusters with the architecture, $k_{dissociation}$ is the dissociation of dimers of the sought architecture and *b* is a constant accounting for the association cooperativity effects. k^{macro} is the macroscopic growth of the cluster.

2- **Enthalpic Control of 2D Supramolecular Architectures**: "A multi-component architecture can be predicted if it is thermodynamically favored with respect to its respective monocomponent architectures"

$$\left| \frac{\Delta H^{unit\ cell}}{N_{i,j}^{unit\ cell}} \cdot N_{i,j}^{adsorbed} \right| > \left| \frac{\Delta H's^{unit\ cell}}{N's_{i,j}^{unit\ cell}} \cdot N's_{i,j}^{adsorbed} \right|$$

where in the "low concentration regime" the potential energy of the sought architecture in a unit cell $E^{unit\ cell}$ divided by the number of molecules in the unit cell times the total number of adsorbed molecules is higher than the same expression for all unwanted architectures (symbolized by an apostrophe).

3- **Non-equilibrium 2D Oswald Ripening**: "A thermodynamically favored or unfavored multi-component 2D Supramolecular architecture must grow much faster than the respective mono-component architectures."

$$k_{dissociation} > k's_{dissociation}$$

where $k_{dissociation}$ is the molecular dissociation rate constant of the uncomplexed dimers of the sought architecture and $k's_{dissociation}$ are the rate constants of the unwanted architectures.

8 Appendix

In this section we give in depth details on the procedures shown in the main investigations comprised in Chapters 2 to 6

.

8.1 Chapter 2

8.1.1 Molecular Dynamics

All simulations were performed with the general force field MMFF (Halgren 1996) as implemented in the package CHARMM 35 (Karplus and Porter 1970). Details about the different calculation setups are given in the following sub-sections. Explicit graphene was setup as in Chapter 2 pg 42 which has been shown to describe very well adsorption energies unto HOPG substrate. Density Functional Theory calculations were performed with the commercial package Gaussian 06.

The identical unit cells of two compounds studied, **Molecule 4** and an analogous molecule featuring C_4 alkyl chains instead of C_9 assigns the nature of the intermolecular interactions between adjacent molecules to self-associating hydrogen bonds between the six 2,6-di(acetylamido)pyridine endgroups per molecule. In this section, we will focus our endeavor in elucidating with atomistic detail the geometrical configuration of these hydrogen bonds. We begin by exploring hydrogen-bond conformations that have been previously reported in **Figure 3-8**. We showed two conformers, the *Z,Z* and *Z,E* conformations (around CO-NHR bond) of the amidic functional groups are possible, in Chapter 6. According to both conformations, we can envisage two self-recognition fragments, which we will name the $(Z,Z)_2$ featuring two hydrogen bonds and the $(Z,E)_2$ featuring four hydrogen bonds. We initially prepare a six-molecule hexamer and minimize it onto a graphene sheet, in which the H-bond configuration between adjacent molecules is arranged in analogy with the $(Z,Z)_2$ and $(Z,E)_2$ isomers in **Figure 8-1**. **Table 8-1** summarizes typical distances used as geometrical criteria for hexamer building. The main criteria is the predispotion of the conformers to form an hexagonal macrocycle of dimensions close to those observed in the experiment. Since the graphene plane breaks the symmetry of each of the hexagons (which we will also refer to as $(Z,Z)_2$ and $(Z,E)_2$) two stereoisomers have to be considered for each $(Z,Z)_2$ and $(Z,E)_2$ isomers. We then construct the initial structures of the four hexagons, which we term the (*Z,Z*)$_2$ -up (**Figure 8-1a)**, (*Z,Z*)$_2$ -down (**Figure 8-1b)**, (*Z,E*)$_2$-up (**Figure 8-1c)** and (*Z,E*)$_2$-down (**Figure 8-1d)**, configurations. The terminology makes reference to the alkyl-chain substituents which are in contact with the graphene (down) in one configuration and half of them which are back-folded in the other (up).

Table 8-1

Geometrical criteria for hexamer construction. Distances correspond to the distances in **Figure 8-1** where the structures were minimized onto a graphene sheet by the MMFF.

	Side of Hexagon (nm) (atom-to-atom distance shown in **Figure 8-1**)	**Diagonal of Hexagon (nm)** (atom-to-atom distance shown in the insets **Figure 8-1)**
Experimental	2.4 ± 0.1	4.8 ± 0.2
(*Z,Z*)$_2$ -up (**Figure 8-1a)**	2.46	4.93
(*Z,Z*)$_2$ -down (**Figure 8-1b)**	2.58	5.25
(*Z,E*)$_2$-up (**Figure 8-1c)**	2.65	5.05
(*Z,E*)$_2$-down (**Figure 8-1d)**	2.67	5.09

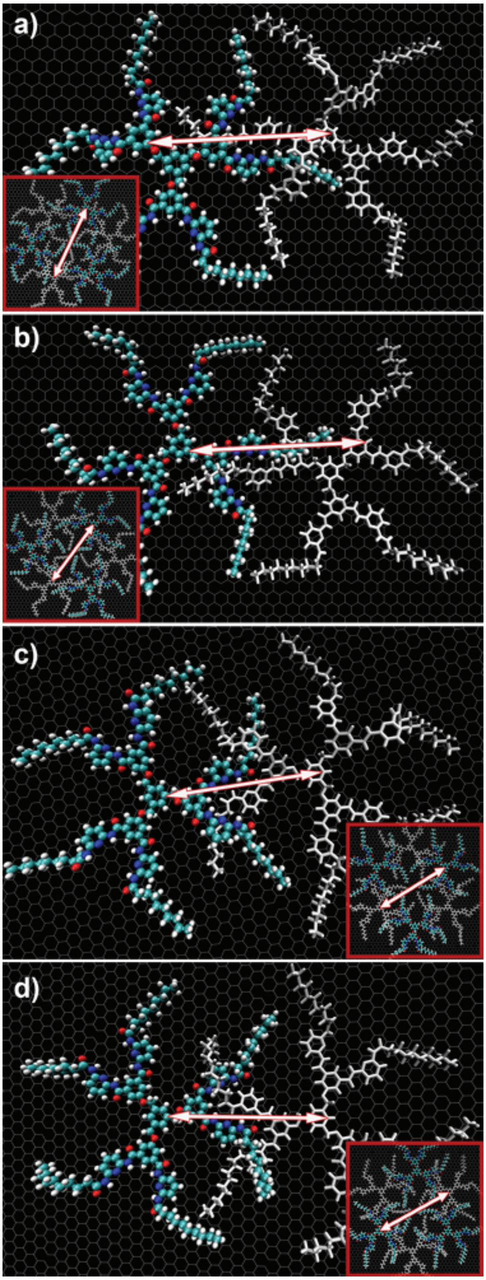

Figure 8-1

Force Field considerations. The different conformers are built and minimized with the program CHARMM, where the molecules were parameterized within the MMFF force field. Before the simulations are run, it is important to diagnose the molecular force field use to parameterize the di(acetylamido)pyridine moieties of **Molecule 4**. We do this by comparing the energies of dissociation of the H-bonds in the MMFF parameterization and in the DFT B3LYP/6-311G++(d,p) level of theory. We treat non-bonded interactions in the CHARMM-program as follows: NBONDS ELEC ATOM **CDIE** SHIFT VDW VATOM VSHIFT CUTNB 30; SHAKE BOND PARA TOLE 1.0E-6. Notice that constant dielectric (**CDIE**) and R-dielectric (**RDIE**) values of **1** were used in every energy computation through out the paper. Both **CDIE** and **RDIE** dielectrics must be used during the calculations since we found out that **RDIE** is describing better triple and quadruple hydrogens bonds when the H-bonds have been only parameterized for single or double H-bond interactions. **Table 8-2** reports the hydrogen-bond dissociation energies for DFT and MMFF, where the asterisk (*) refers to the values obtained using **RDIE**. It is strinking to see that the energy of quadruple hydrogen-bond formed by the $(Z,E)_2$ dimer is described with **RDIE** almost as the exact DFT energy. In contrast, the double-hydrogen bond of the $(Z,Z)_2$ dimer is dissociated when using **RDIE** in the calculations. In a parallel diagnosis, we computed the stability of the *Z,Z* conformation vs. the *Z,E* conformation and found out that difference in stabilization energy favoring the *Z,Z* conformer in the MMFF parametrization is in agreement with the DFT B3LYP/6-311G++(d,p) level of theory. The theories predict 6.6 kcal/mol and 6.8 kcal/mol, respectively.

Table 8-2

Comparison between molecular dynamics and ab-initio parameters in 2,6-di(acetylamido)pyridine dimers of conformation $(Z,Z)_2$ and $(Z,E)_2$ featuring quadruple or double hydrogen bonds, respectively. *Refers to molecular mechanics parameters using the r-dielectric decay (RDIE).

	Dissociation Energy (kcal mol^{-1})		**Hydrogen Bond distances (Å)**	
	DFT	**MMFF**	**DFT**	**MMFF**
$(Z,E)_2$	-24.0	-18.4 -24.5*	1.90(N-H…N)	1.70 (O…N-H) 2.48 (N-H…N) 1.60 (O…N-H)* 1.94 (N-H…N)*
$(Z,Z)_2$	-13.0	-10.5 -3.4*	2.04 (N-H…N)	2.24 (N-H…N) 3.12 (N-H…N)*

Conformational Search. Once the conformers are built and minimized (**Figure 8-1**), 20 ns simulations onto a graphene sheet are conducted, using a Langevin thermostat, and friction coefficient 1, treating non-bonded interactions as mentioned in the previous paragraph except with cut-offs CUTNB of 999.9, CTONNB 12 and CTOFNB 14.0. The fast routine was applied, which will be described in detail later in the **Appendix,** with a time step of 7fs using SHAKE to all bonds and with heavy hydrogens. Interestly during the first nanoseconds of simulations at 300 K onto graphene and in vacuum conditions, two out of four conformers melt.

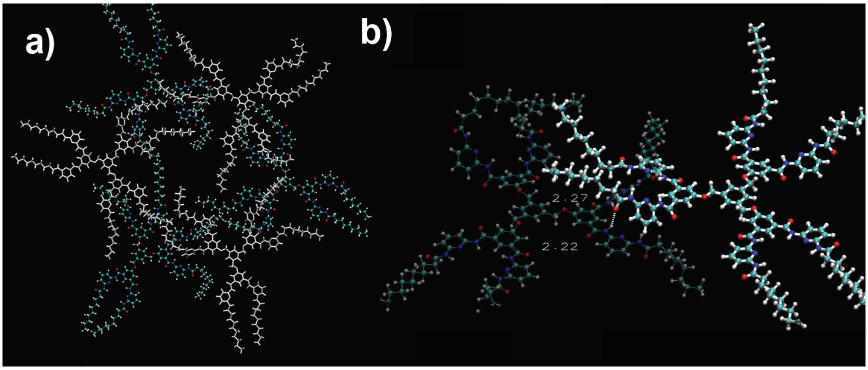

Figure 8-2
Conformer found in the 2 independent 20ns molecular dynamics runs at 300K on graphene (using CDIE setup) starting from the $(Z,Z)_2$-down conformation(**Figure 8-1b)**. This new H-bond conformer is termed the $(Z,Z)_3$ tetramer.

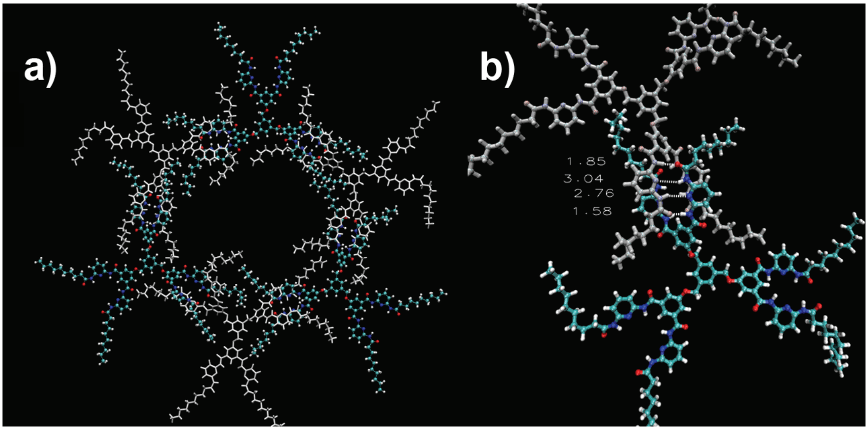

Figure 8-3
Conformer found in the 2 independent 20ns molecular dynamics runs at 300K on graphene (using RDIE setup) starting from the $(Z,E)_2$-up conformation (**Figure 8-1c)**. This new H-bond conformer is termed the bis-$(Z,E)_2$.

Figure 8-2 depicts the one of the final stable structures found after the 20ns trials, the now termed $(Z,Z)_3$ H-bond configuration, since it consists on one end-carbonyl interacting with two amines from two opposed 2,6-

di(acetylamido)pyridine units. Unexpectedly, the second stable conformer found seen in **Figure 8-3** is formed by an extraordinary double stacking of quadruple hydrogen-bonds, as observed in **Figure 8-3b,** which we now term bis-(*Z,E*)$_2$. The graphene is not shown in the figures for clarity. **Table 8-3** gives important data on the potential energy (without the presence of graphene) of the interacting new structures found, using both R-dielectrics and constant dielectric. Note that since the van der Waals contribution is very different in both dimers, only the electrostatic stabilization energy is given as a rational for hydrogen-bond strength. Interestingly, while it is clear that the double decker 8-hydrogen-bond bis-(*Z,E*)$_2$ conformer, ΔE(electrostatic)° = -41.4 kcal/mol is more than twice as stable than the (*Z,Z*)$_3$, ΔE(electrostatic)° = -18.1 kcal/mol, the highly strained conformation of bis-(*Z,E*)$_2$ makes it less favorable by 57 kcal/mol, compared to the (*Z,Z*)$_3$ dimer. Note that since **Table 8-3** assigns the same energy for the (*Z,Z*)$_3$ dimer whether RDIE or CDIE dielectric is used, the simulations were done using a RDIE dielectric. RDIE conditions also approximate the substrate and solvent interactions used in the experiment. The latter energy difference of 57 kcal/mol is further amplified when a sheet of graphene is present. **Figure S8** shows the time series of the fluctuation of the potential energy in 10 averages of 4ns simulation of (*Z,Z*)$_3$ and bis-(*Z,E*)$_2$ dimers. It shows that the difference in potential energy favoring the (*Z,Z*)$_3$ dimer is now amplified to 100 kcal/mol, which is explained by the fact that there are more parts of the molecule in close proximity to the graphene. The previous potential energies differences, discard the bis-(*Z,E*)$_2$ conformer as a generator of the highly crystalline pattern of **Molecule 4**.

Table 8-3

Important energetic and geometrical data for the most stable hexamers found

	Electrostatic contribution (kcal mol^{-1})	**Hydrogen Bond distances (Å)**
bis-(*Z,E*)$_2$ (**Figure** 8-3)	-41.4 -52.9*	1.76 (O…N-H) , 1.59 (O…N-H)* 2.70 (N-H…N), 2.50 (N-H…N)* 2.80 (O…N-H), 2.57 (O…N-H)* 1.86 (N-H…N), 1.66 (N-H…N)* Note: only the upper (*Z,E*)$_2$ distances are given
(*Z,Z*)$_3$ (**Figure** 8-2)	-18.1 -18.0*	2.38 (O…N-H), 2.46 (O…N-H)* 2.06 (O…N-H), 1.92 (O…N-H)* 2.10 (O…N-H), 1.97 (O…N-H)*

Moreover, the stability of the (*Z,Z*)$_3$ conformation can be addressed through dissociation kinetics in temperature. This effectively mimics what the TCB solvent would do if present, since the solvent is a natural disruptor of vdW interactions. In this regard, **Figure 8-4** depicts the average survival probability of (*Z,Z*)$_3$, were only 10 replicas were simulated for each temperature using the same RDIE and fast routine conditions as above. It is remarkable to note that, conformer (*Z,Z*)$_3$ has a high kinetic stability. Moreover, no new conformers were found during the dissociation or the $(Z,Z)_3$ dimer, reinforcing our previous conformational search.

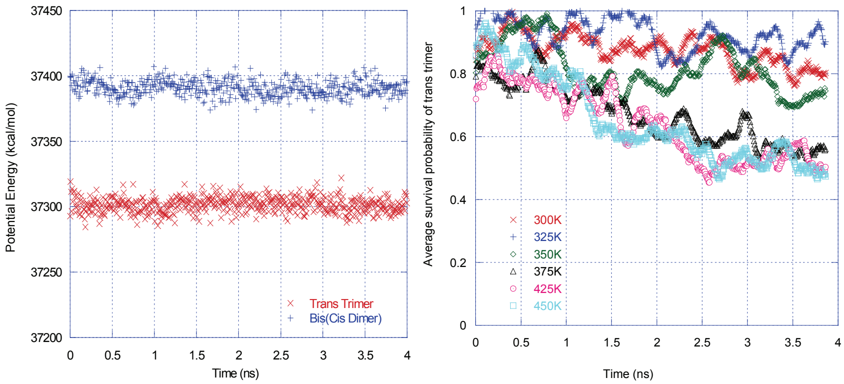

Figure 8-4

Left hand side: Average potential energy fluctuations in 10 differet simulations of 4ns simulation of $(Z,Z)_3$ (in red) and bis-$(Z,E)_2$ (in blue) with explicit graphene. Right hand side: Average survival probability in temperature of 10 replicas of $(Z,Z)_3$ from 300K to 450K.

Simulation of STM molecular footprints. Simulation of STM images proceeded through averaging 1000 snapshots of the molecular dynamics simulations, each corresponding to 2ps of molecular dynamics simulation time. Ideally, according to equation **Equation 2-23** in Chapter 2 the averaging should consist on the product of the height times the *beta* factor per atom in each snapshot. However, due to ongoing development of the current methods, the computation of this product has not been yet optimized. Thus, The averaging consisted on assigning two *beta* values to the 2D projection of the MMFF polarizable atomic radius, thus giving only a “molecular footprint” of the STM images. In this projection, the lowest *beta* value is assigned the highest priority, meaning that when overlap of the projection would occur, the contrast will be given by only the value of the lowest *beta* value. Again, note that there is no averaging of the beta value within a single snapshot, i.e. the superposition of two atoms with different *betas* will only result in the assignment of the *beta* value with the highest priority. This procedure is coherent in that *beta* should be independent of the height of the molecule (z_1). **Figure 8-5** shows the $\langle \beta(x,y) \rangle$ assignment of a simulated hexagonal hexamer bis-$(Z,E)_2$ of onto a single layer of graphene.

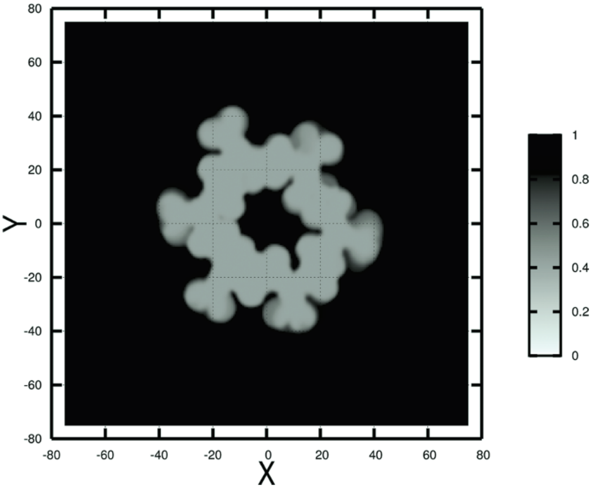

Figure 8-5
The x,y plot of β for a 2ps simulated hexagonal hexamer bis-$(Z,E)_2$ onto graphene

After the simulation of the hexagonal hexamer of bis-$(Z,E)_2$ the simulation is set up to reproduce a crystalline pattern of **Molecule 4** through periodic boundary conditions. An eight-molecule unit cell is constructed and minimized. However, since the unit cell is not commensurable with the underlying graphene super cell, the minimization with periodic boundaries is done without a substrate, in which case the best-fit rectangular unit cell is found to be a= 87Å, b= 76Å. The primitive unit cell of this assembly is found to be a = 4.4 nm , γ = 60º; i.e. a featuring a 10% discrepancy with the experimental unit cell. To decrease this difference, which is due to the lack of planarity of molecules when simulated without a surface, we performed simulations with an implicit harmonic 2D potential, through the CHARMM input: GEO PLAN ZDIR 1 FORCE 10 DROF 0 SELECT AROM END, where the "AROM" keyword designates the ensemble of aromatic carbons. In the former case, an expansion of the eight-molecule unit cell was tolerated to a= 89Å, b= 78Å, corresponding to a primitive unit cell of a = 4.5 nm, γ = 58º, as depicted in **Figure S11**.

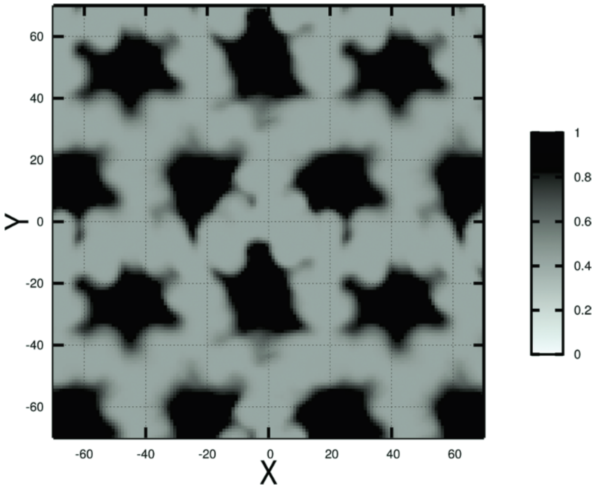

Figure 8-6
The x,y plot of β for a 2ps simulated periodic hexagonal pattern of Molecule 4 onto graphene. Notice that there are small deviations with respect to **Figure 2-18** in Chapter 2 due to the presence of the graphene substrate. Indeed, there is no convergence of molecular movements on the picosecond timescale when graphene is present so the substrate in **Figure 2-18** has been removed for illustration purposes.

STM measurements of **Molecule 4** were performed using a Veeco scanning tunneling microscope (multimode Nanoscope III, Veeco) at the interface between highly oriented pyrolitic graphite (HOPG) and a supernatant solution. Diluted solutions of Molecule 4were applied to the basal plane of the surface. The STM tips were mechanically cut from a Pt/Ir wire (90/10, diameter 0.25 mm). The raw STM data are processed by the application of background flattening and the drift is corrected using the underlying graphite lattice as a reference. The latter lattice is imaged underneath the molecules by lowering the bias voltage to 20 mV and raising the current to 65 pA. **Molecule 4** was dissolved in dimethyl sulfoxide (DMSO) and diluted with 1,2,4-trichlorobenzene (TCB) to give 30±1 μM and 5±1 μM solutions respectively. Monolayer pattern formation was achieved by applying 4μL of a warm (30-40ºC) solution onto freshly cleaved HOPG.

8.2 Chapter 3

8.2.1 Semi-quantitative Generalities in Pre-programming Self-Assembly

A recent contribution by Lackinger and co-workers represents also a crucial towards the understanding of polymorphism and a formal treatment for polymorphism. Authors focused their endeavor on the formation of multiple phases as a function of concentration in 2D monolayers obtained from the deposition of two components namely 1,3,5-benzenetribenzoic acid (BTB) and 1,3,5-tricarboxybenzene trimesic acid (TMA). Six different phases have been detected, their formation being directed only by the concentrations of the two molecular modules **Figure 8-7**.

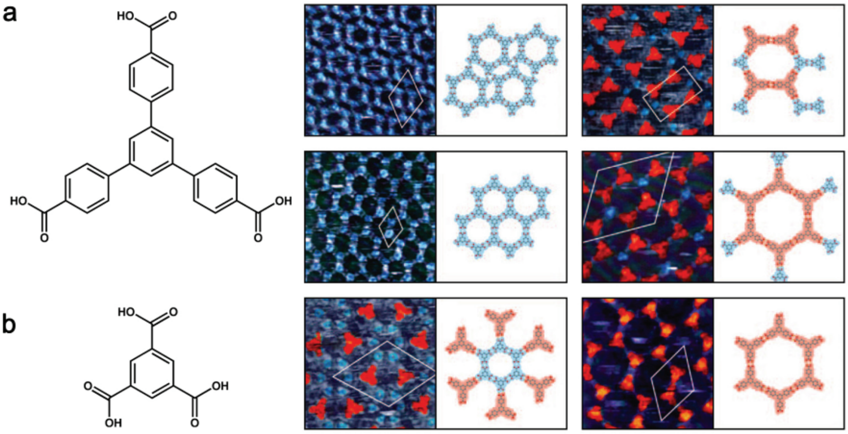

Figure 8-7
Polymorphism in a bicomponent system. *On the left:* chemical structures of the two components, (*a*) BTB and (*b*) TMA. STM-images of the different phases are shown, with the respective molecular mechanics simulations right next to them. Molecular building blocks are intuitively superimposed to STM images. TMA molecules are colored blue, BTB molecules are colored orange.

They then developed a slightly different thermodynamic equilibrium model to semi-quantitatively explain the structural versatility of the binary TMA + BTB system. In Lackinger model, Gibbs free energy *G* is calculated under the assumption of thermodynamic equilibrium, i.e. the chemical potential μ(phase) of each molecule is the same on the surface and in solution. The Gibbs free energy of each phase at a concentration c_i is then calculated as:

$$G = \left[\sigma_{TMA}(phase) \cdot \mu_{TMA}(c_{TMA}) + \sigma_{BTB}(phase) \cdot \mu_{BTB}(c_{BTB}) + e_{solvent} \cdot \rho_{pore}(phase)\right] A$$

Equation 8-1

where σ is the area density (molecules/unit area), μ is the chemical potential, $e_{solvent}$ is the additional free energy per unit area associated to the adsorption of solvent molecules within the pore and ρ is the area fraction occupied by pores. Then they proceeded to calculate the chemical potential at the concentration point c_i;

$$\mu_{\mathrm{i}}(c_i) = \mu_0 + \varepsilon(1 - c_i)^2 + k\mathrm{T}\ 1\mathrm{n}\ c_i$$

Equation 8-2

where the first term $\mu_{0,i}$ is the standard chemical potential of the respective compound, the second term accounts for the enthalpy of mixing, and the third term stands for the entropy of mixing.

With this approximation of the chemical potential at hand, the authors proceeded to obtain the values of μ_{TMA} and μ_{BTB} at the concentration point (c_{TMA}, c_{BTB}) to evaluate the total free energy G of the monolayer according to **Equation 8-1**. To produce a phase diagram, the specific point in the two-dimensional (c_{TMA}, c_{BTB}) concentration space was assigned to the phase with the lower value in the free energy G. The free parameters (μ_0) and e_{solvent} were iterated to produce the best fit of the experimental points **Figure 8-8**.

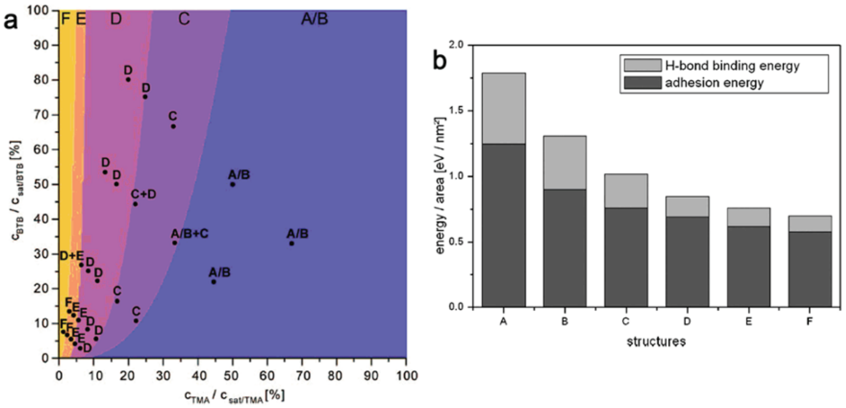

Figure 8-8

(a) Phase diagram of the polymorphs. (b) Total binding energy per unit area of the different phases as obtained by molecular mechanics calculations. Adhesion energy between the molecules and the surface and the intermolecular H-bonding energies are also shown.

8.3 Chapter 4

8.3.1 Complementary Recognition into Amorphous Networks

Compound synthesis of the molecules can be obtained from (Llanes-Pallas, Matena et al. 2008, Llanes-Pallas, 2009 #8).

STM measurements at the liquid-solid interface have been carried out both in constant height and in constant current modes using a DI Multimode microscope. The STM tips are mechanically cut from a Pt:Ir (80:20) wire. Samples have been prepared by depositing a droplet of solution on freshly cleaved highly oriented pyrolytic graphite (HOPG). The first solution containing **Molecule 5** (0.5mM) is prepared by mixing few droplets of $CHCl_3$ with 5 ml of ultra pure *n*-tetradecane while the solution containing molecule **Molecule 5** (0.6 mM), as well as the solution containing the [**Molecule 5·Molecule 6**] dimers (4 mM of molecule **Molecule 5** and 0.4mM of molecule **Molecule 6**), are obtained from few droplets of toluene mixed with 5 ml of 1-phenyloctane.The preparation of the pentamer monolayer is done first by forming one monolayer of **Molecule 5** on HOPG followed by the consecutive deposition of **Molecule 6** from a solution made of 300 µl of toluene, few droplets of DMSO and 3 ml of 1-phenyloctane.The raw STM data are processed by the application of background flattening and the drift is corrected using the underlying graphite lattice as a reference. The latter lattice is imaged underneath the molecules by lowering the bias voltage to 20 mV and raising the average tunnelling current to 65 pA.

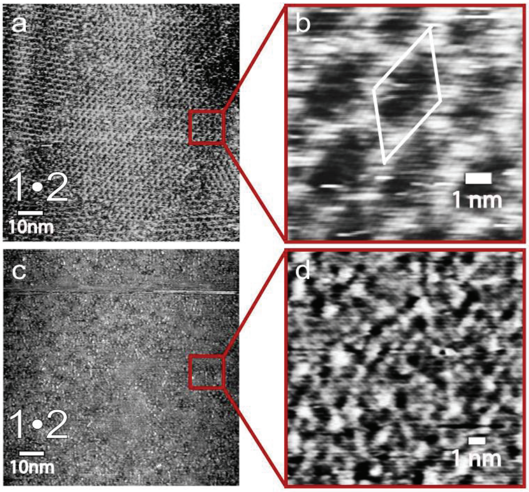

Figure 8-9

Large scale constant current STM images showing the mixture components **Molecule 14 Molecule 13** obtained from (a,b) high (>100 µM) and (c,d) low (<10 µM) concentration solutions deposited on HOPG. Figures (a,b) feature the same self-assembled pattern as the single component 2 and can therefore be ascribed to component 2. Figures (c,d) show an amorphous pattern. High-resolution images reveal that this pattern is composed of oligomers **Molecule 14 Molecule 13**. The detail shows the unit cells (b): a = (3.1 ± 0.2) nm, b = (3.7 ± 0.2) nm, α = (50 ± 3)°. Average tunneling current I_t = 20 pA and sample bias (U_t) between 400 and 800 mV.

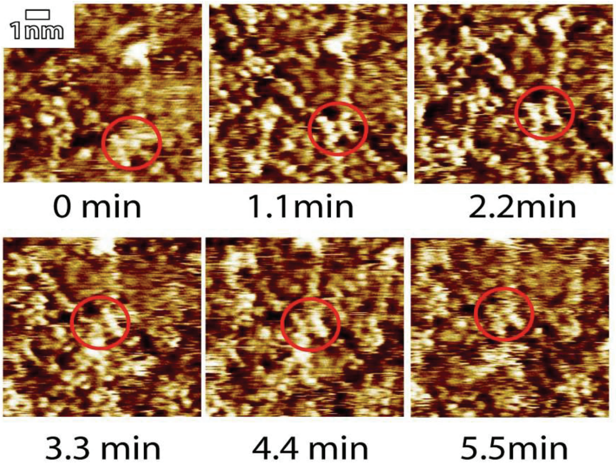

Figure 8-10
Transient STM constant-height images of the pentamer in the main figure. The images are shown unfiltered. Marked areas encircle one molecule of 1. Average tunneling current I_t = 20 pA and sample bias (U_t) between 800 mV.

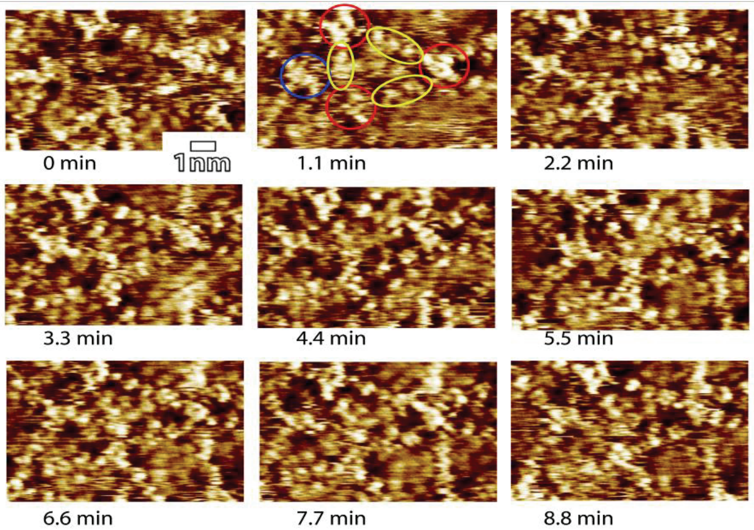

Figure 8-11
Transient STM constant-height images of a triangular motif. Images are shown unfiltered. At 1.1 minutes, three **Molecule 14** along with three **Molecule 13** are shown forming a triangle. At 2.2 minutes a desorption of **Molecule 13** is clearly seen and the network is stabilized by the neighboring molecule of **Molecule 14**. The molecule is

adsorbed back again in the next image. Average tunneling current I_t = 20 pA and sample bias (U_t) 800 mV.

8.3.2 Complementary Recognition into 2D Networks

STM measurments. Melamine (>99.0%) was obtained from Sigma-Aldrich and used without further purification. Mother solution of melamine was dissolved in DMSO and diluted with trichlorobenzene (TCB) to give solutions 40±25 and 2±1 μM respectively. Preparation of **Molecule 7** has been described elsewhere [A. Llanes-Pallas, M. Matena, T. Jung, M. Prato, M. Stöhr, and D. Bonifazi, In Press]. The molecule was readily soluble in DMSO, diluted with TCB and used with concentration of 29±19 and 3±2 μM. Pattern formation was achieved by applying 5 μL of a vigorously shaked and warm (40-50º) solution 3±2 μM in **Molecule 7** and 2±1 μM in **MEL** onto freshly cleaved HOPG. Uncertainties values are derived from the standard deviation for the "limit values" of the balance's linearity (XS105 Mettler Toledo ®) for maximum confidence. "Typical values" are reported as one order of magnitude lower. STM tip was approached and the solution imaged before the solvent was completely evaporated (~3h). Imaging of the patterns occurred within minutes. Over 200 images from at least 3 different experiments were obtained for each monolayer pattern. Unit cells were corrected by the underlying graphite, except for unit cell of the porous network 1+2 pattern in which the unit cell was just averaged over 6 images. All images with superimposed molecular models were also corrected by the underlying graphite and the models were minimized with Chem3D at the MM2 level. Unit cell errors correspond to the standard deviation multiplied by a factor of 2. DFT calculations for hydrogen bond interaction between 3H-Pyridine-2,6-dione fragments and melamine fragments were performed with the quantum mechanical package GAMESS 04 at the PBE 6-31G(d) level, where geometries converged typically to <0.0002 Hartrees. Unit cell determination and plane correction were made by the SPIP program. No filtering of any kind was applied to any of the images herein reported. The images in the supporting information were rendered with the help of the Gwyddeon Program.

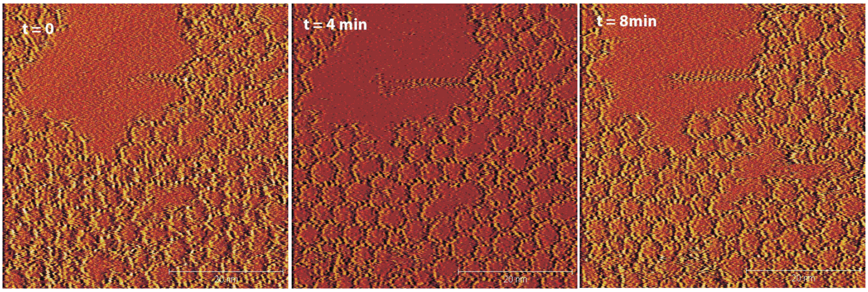

Figure 8-12
50x50 nm STM constant height images of the porous network showing the dynamic nature and evolution in a 1D array.

8.3.3 Polymorphism and Phase segration in Bi-component Networks

Compounds synthesis of the **Molecule 7** (Llanes-Pallas, Matena et al. 2008) and **Molecule 10** (Llanes-Pallas and Bonifazi 2009) are described elsewhere. 1,4,5,8-naphtalenetetracarboxylic acid dyanhydride (70300, purum >95%) and melamine (**MEL**) (63600, purum >99.0%) were purchased from Fluka and used without further purification. Pyromellitic di-imide (P1153, >95%) was obtained from TCI Chemicals Europe. 1,2,4-Trichlorobenzene (spectrophotometric grade 99%) and anhydrous DMSO (99.9%) were obtained from Alfa Aesar and Sigma-Aldrich, respectively.

Computational details. All calculations were done within the framework of density functional theory (DFT) with periodic boundary conditions using the Vienna Ab-initio Simulation Package (VASP) (Kresse and Furthmüller 1996) The ion-core interaction was described by the projector augmented waves method.(Blüchl 1994; Kresse and Joubert 1999) Generalized gradient approximation (GGA) through the Perdew Wang 91 (PW91) functional (Perdew, Chevary et al. 1992) was used to describe exchange-correlation effects. The plane wave basis has been expanded up to a cut-off energy of 400 eV and only the gamma-point was used to represent the *k*-point grid. Structural optimization was done until the force acting on each atom is below 0.01 eV/Å. The 1 and 2 linker molecules were simplified by replacing the dangling alkane chains with methyl groups to reduce the computational cost. The simulated STM images were based on the Tersoff-Hamann approximation (Tersoff and Hamann 1983; Tersoff and Hamann 1985) where *dI/dV* is proportional to the local density of states (LDOS). The images in Fig. 1b are contour plots of the densities for molecular orbitals in the energy range from the specified energy to the Fermi energy at a constant height of 3 Å above the 1+**MEL** repeated hexagons in vacuum. As no substrate was included in the calculations, we assume that the vacuum levels of the weakly physisorbed molecules and the HOPG substrate are aligned. Energies are given relative to the Fermi energy of graphite, as obtained from the calculated work function of a single graphene sheet.

STM imaging. Mother solutions of molecules the linkers and **MEL** were prepared by dissolution of an exact weighted amount of the respective product in 500-1000μL of DMSO. Uncertainties values are derived from the standard deviation for the “limit values” of the balance’s linearity (XS105 Mettler Toledo ®). Intermediate solutions were then prepared to the respective concentrations with 1,2,4-trichlorobenzene (TCB). These solutions where then combined in different ratios to afford the bi-component solutions (linker + MEL) between 1 and 100 μM (see main text for specific concentrations) used for the STM experiments. The assembly formation is typically obtained by applying 6 μL of vigorously stirred and warm (except when noted in the main text, 30-40 ºC) solutions onto freshly cleaved HOPG. STM imaging was done in a commercial instrument, Veeco Multimode (Nanoscope III controller). STM tip was approached and the solution imaged before the solvent was completely evaporated (~3h, except in the cases where a fluid cell was used, where the solvent evaporated after 2-3 days). Imaging of the patterns occurred within minutes. Unit cells were corrected by the underlying graphite. All images with superimposed molecular models were also corrected by the underlying graphite, except for linker **Molecule 12** (NTCDI) in Supporting Information, where no reference could be imaged. Unit cell errors correspond to the standard deviation multiplied by a factor of 2. The models were minimized with Chem3D at the MM2 level. Unit cell determination and plane correction were made by the SPIP program. No filtering other than line-wise levelling was applied to the images herein reported, except for the images in Fig. 5c and in Fig. 7 were a low pass filter was applied. No high voltage (i.e. >1V) pulses where applied at any time during image acquisition.

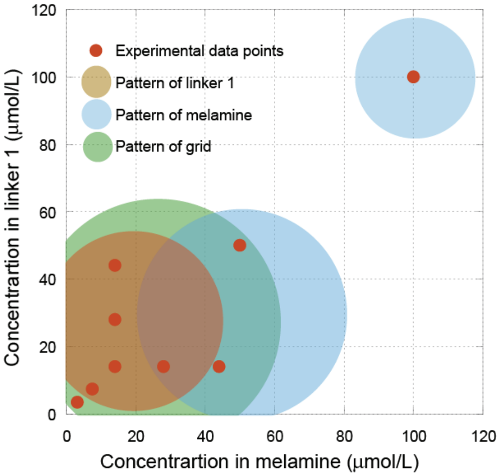

Figure 8-13

Schematic phase diagram for the linker **Molecule 7+ MEL** system. Each point was acquired from three different experiments and exploring different substrate areas, by preparing a solution of the shown concentration and ratio in **Molecule 7** and **MEL** and applying it unto the basal plane of HOPG. The colored circles are illustrative, representing that at least in one experiment out of three a coexistence of different phases was observed. Previously it was reported (Palma, Bonini et al. 2008) that patters of **Molecule 7+ MEL** could not be found at concentrations greater than 20μM in both components, however a wider sampling revealed that patterns of **Molecule 7+ MEL**, **MEL** and **Molecule 7** could be found coexisting up to concentrations of 50μM.

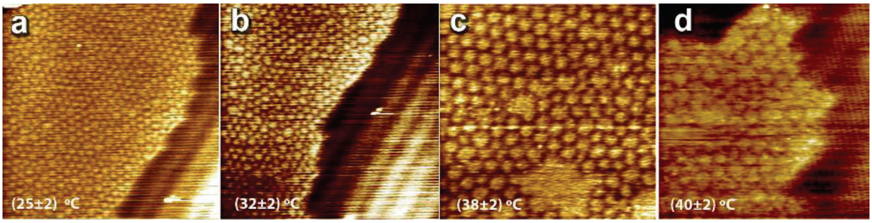

Figure 8-14

In-situ temperature-dependent STM images of **Molecule 7+ MEL** phase at a concentration of ~20µM in ~200µL of TCB. (a) 100 × 100 nm^2, T = (25±2) ºC; (b) 100 × 100 nm^2, T = (32±2) ºC; (c) 50×50 nm^2, T = (38±2) ºC; (d) 50 × 50 nm^2= (T = 40±2).

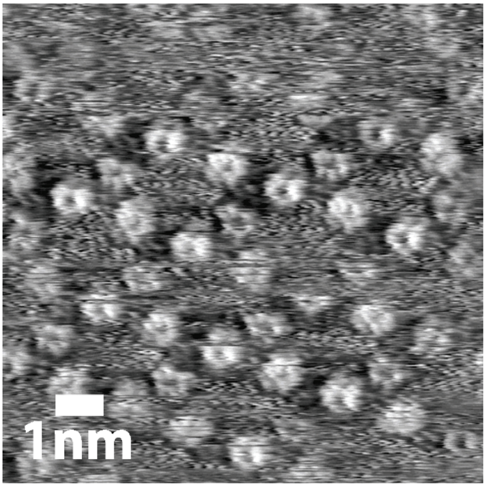

Figure 8-15

STM constant current mode image showing 10×10nm^2 image of a polymorph structure of linker **Molecule 11+MEL** featuring bright "doughnuts", from a highly dynamic image sequences when high concentrations where employed: 60µM in **Molecule 11** and 55µM in **MEL**. This polymorph dynamically changed into a structure resembling that reported in the main section, but with a much higher contrast in the pores, here seen as bright doughnuts ~0.6nm in diameter. Tunneling parameters: I_t = 10 pA, V_t = 20 mV.

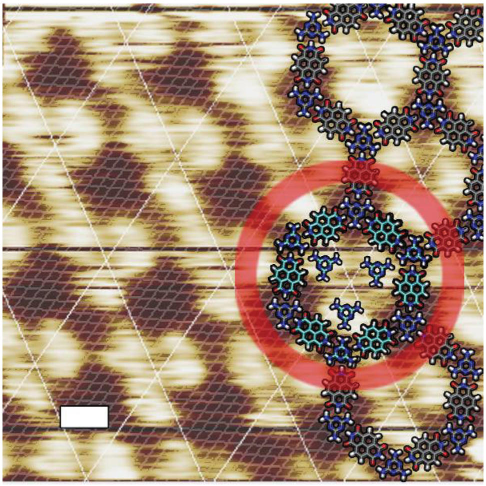

Figure 8-16

STM constant current mode image showing another contrast for the structure of linker **Molecule 11**+**MEL**. We used a high contrast for clarity; the inverted contrast corresponds to that shown in fig. 3d in the main text. The image partially supports the hypothesis that 3 melamine molecules can adsorb into the pores for stabilizing the highly crystalline structures of **Molecule 11**+**MEL**, however it is not clear why co-adsorbed melamine should have a preferential adsorption site. These "doughnuts" resemble the ones reported on Fig S8. The superimposed models have a low error as they were DFT minimized (The N-N distance of a **Molecule 11** 3 is 0.7nm in the image, corresponding ith the theoretical distance) and the underlying graphite unit cell is shown (small rhomboids), following the crystallographic axis of the monolayer (large rhomboids).

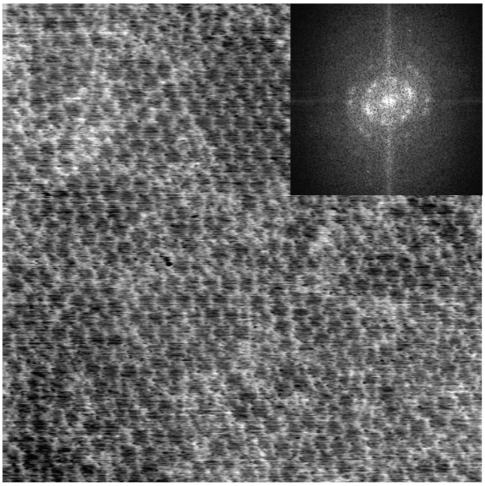

Figure 8-17

STM constant current mode image showing a 100x100 nm^2 pattern of **Molecule 7**+ **MEL**. The image corresponds to the same image sequence in Chapter 3. Polycrystalline domains are observed embedded in the glass matrix after 12 hours of continuous scanning in an open aluminium fluid cell of volume ~ 0.3mL.

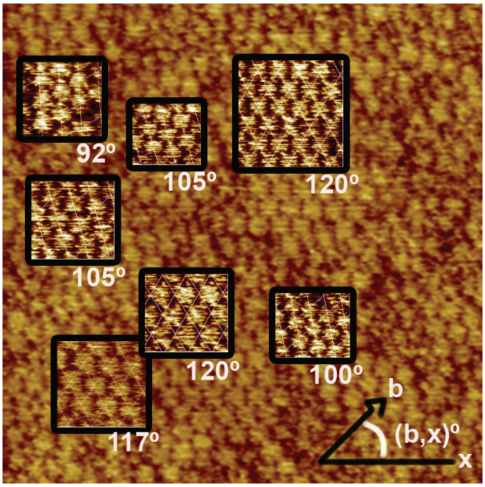

Figure 8-18
A closer look into the previous STM constant current mode image showing the unit cells of the crystalline domains. The angles (±1.5) correspond to the angles between the vector "b" of the hexagonal unit cell referenced to the horizontal of the image. It is straightforward to note that the orientation between unit cell vectors spawn the long of the hexagonal 30 ° mirror relationships, meaning that there is a very small commensurability with the substrate.

1. Details on the VASP DFT calculations.

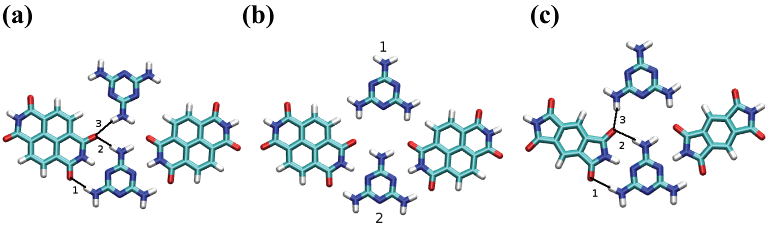

Figure 8-19
Calculated structures for (a) **Molecule 11** and **MEL** conformation for the co-adsorbed melamine, Distance 1: 1.85 Å; Distance 2: 1.92 Å; Distance 3: 2.30 Å, (b) **Molecule 11** and **MEL** , interow conformation, Distance 1: 1.83; Å Distance 2: 2.00 Å; Distance 3: 2.49 Å and (c) **Molecule 12** and **MEL** interrow conformation, Distance 1: 2.01 Å; Distance 2: 2.14 Å; Distance 3: 2.07 Å. Homomolecular dimer hydrogen bond distances (from H atom to respective hydrogen bond acceptor) **Molecule 7-Molecule 7** Dimer: 1.81 Å , **Molecule 10-Molecule 10** Dimer: 1.84 Å, **Molecule 11-Molecule 11**Dimer: 1.82 Å, **Molecule 12-Molecule 12** Dimer: 1.82 Å, **MEL-MEL** Dimer: 1.92 Å

Linker	Decoupled bending energy [eV]	Total deformation energy [eV]
1	0.003	0.218
2	0.016	0.255
3	0.005	0.200
4	0.001	0.232

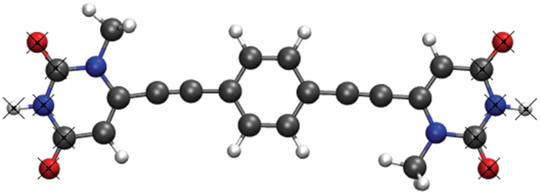

Figure 8-20
Decoupled bending energy (i.e. mostly arising from the backbone flexibility) [eV] versus the total deformation energy (column 2 table 4.1 main section) [eV] of . The deformation energy cost due to bending was found to be insignificant compared to the total deformation energy cost. The bending energy is defined as the energy difference between a fully relaxed molecule and the geometrically constrained molecule where only the 2 C=O groups and the N-H group were allowed to relax while the rest of the molecule was kept in the "bent" state found in the pentagon (The atoms which were able to relax in the case of linker 1 are indicated by crosses).

Further details deformation energies

The table in the main text uses the most stable conformation with C_{3v} symmetry as a reference structure for calculating the hydrogen bond and deformation energies. The deformation and H-bond energies using a melamine with D_{3h} symmetry as reference were also computed and are given in **Figure 8-4**.

Table 8-4

$E_{H\text{-bond}}$ and E_{def} energies found when using the D_{3h} melamine symmetry as a reference structure.

Linker Structure	$E_{H\text{-bond}}$ [eV/H-bond]	E_{def} melamine [eV/molecule]	E_{def} linker [eV/molecule]	O - - H distance [Å]	N - - H distance [Å]
Molecule 2mer 7	0.828	0.038	0.108	1.85	1.72
Isolated pentagon	0.800	0.067	0.218	1.83, 1.87	1.73
Isolated hexagon	0.803	0.068	0.224	1.85	1.73
Repeated hexagon	0.781	0.104	0.211	1.85	1.74
Molecule 2mer 10	0.836	0.032	0.121	1.85	1.70
Isolated pentagon	0.788	0.071	0.255	1.83, 1.87	1.71
Isolated hexagon	0.806	0.070	0.230	1.84	1.72
Repeated hexagon	0.774	0.114	0.231	1.84	1.73
Molecule 2mer 11	0.774	0.030	0.109	1.87	1.74
Isolated pentagon	0.681	0.055	0.200	1.71, 2.08	1.80
Isolated hexagon	0.745	0.069	0.229	1.82	1.72
Repeated hexagon	0.720	0.108	0.230	1.82	1.72
Molecule 2mer 12	0.781	0.038	0.129	2.09	1.72
Isolated pentagon	0.719	0.077	0.232	1.89, 2.29	1.65
Isolated hexagon	0.747	0.075	0.222	2.08	1.65
Repeated hexagon	0.723	0.112	0.196	2.07	1.65

8.4 Chapter 5

STM Experiments proceeded as reported in (Palma, Bjork et al. 2009). A STM Multimode with a Nanoscope III controller and a pico-boost module (*Veeco*) was used in conjunction with a mechanically cut Pt/Ir (80:20) tip (*Goodfellow*, ND = 0.25 mm) to scan under 6µL of working solutions of the molecules deposited onto freshly cleaved highly ordered pyrolitic graphite (HOPG, *ZYH Material Quartz Inc.)*Mother solutions were prepared by dissolution of a weighted amount of the respective product (melamine <99% 1289303 *Fluka*, see (Llanes-Pallas, Matena et al. 2008) for preparation of the **Molecule 7** linker) in 500-1000 µL of anhydrous DMSO (*Sigma-Aldrich*). Solutions were diluted to intermediate concentrations with 1,2,4-trichlorobenzene (TCB, *Alfa-Aesar*). The intermediate solutions were combined in stoichiometric ratios to afford the working solutions used for the STM experiments, with concentrations between 1 and 100 µM. The fake-color images shown in the the Main section depict the polygons contours with bright contrasts. Line-wise leveling filter was applied to all images and a low pass filter was applied to only one image. The STM images were acquired with tunneling parameters of I_t = (1 to 5) pA and V_t = (-400 to -500) mV.

Table 8-5

Modified Charges on the **MEL** self-assembly module.

MMFF atom type	Atom Name	Ad hoc Charges	MMFF charges @CHARMM	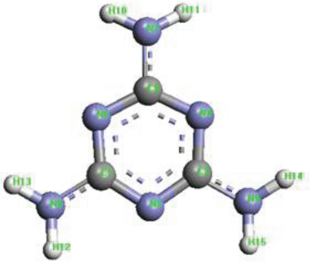
37	C1	0.520000	0.720000	
38	N2	-0.620000	-0.620000	
37	C3	0.520000	0.720000	
38	N4	-0.620000	-0.620000	
37	C5	0.520000	0.720000	
38	N6	-0.620000	-0.620000	
40	N7	-0.700000	-0.900000	
28	H8	0.400000	0.400000	
28	H9	0.400000	0.400000	
40	N10	-0.700000	-0.900000	
28	H11	0.400000	0.400000	
28	H12	0.400000	0.400000	
40	N13	-0.700000	-0.900000	
28	H14	0.400000	0.400000	
28	H15	0.400000	0.400000	

Parameterization. Parameterization of all molecules studied in this work was done through the MMFF94 automatic module implemented in CHARMM (Halgren 1996; Brooks, Brooks et al. 2009). Although the MMFF electrostatic charges were shown to describe fairly well the dissociation energies for single and double hydrogen-bond interactions (Halgren 1999), they apparently fail for the triple H-bonds on the **Molecule 7-MEL** dimer. Therefore, the atomic charges of the **MEL** module (**Figure S1**) were fitted to reproduce the formation energy of the **MEL-Molecule 7** dimer obtained from DFT calculations using the PW91 exchange functional (Table 2 in (Palma, Bjork et al. 2009). These results are shown in

Table 8-5 and **Figure 8-21**. With the new parameterization, the **Molecule 7-MEL** dissociation energy was determined by pulling apart an energy-optimized preformed dimer along the axis of the central hydrogen bond (N-H---N) connecting the complementary modules. By treating the non-bonded interactions as described in section *b* and in the presence of the implicit substrate (see section *d)*, dissociation energy of 18.5 kcal/mol at a distance of 10Å from the equilibrium position is obtained for the **MEL-Molecule 7** dimer. We note that since the present parameterization does not consider the D_{3v} geometry as a stable molecular state, the **MEL** module was constrained to a fully planar conformation during partial charge optimization. Interestingly, with the new parial charges on melamine the homo **MEL-MEL** dimer dissociation energy automatically increases from ~7 to 10.5 kcal/mol, in excellent agreement with calculated DFT values in the literature (~10.1 kcal/mol) (Mura, Martsinovich et al. 2008).

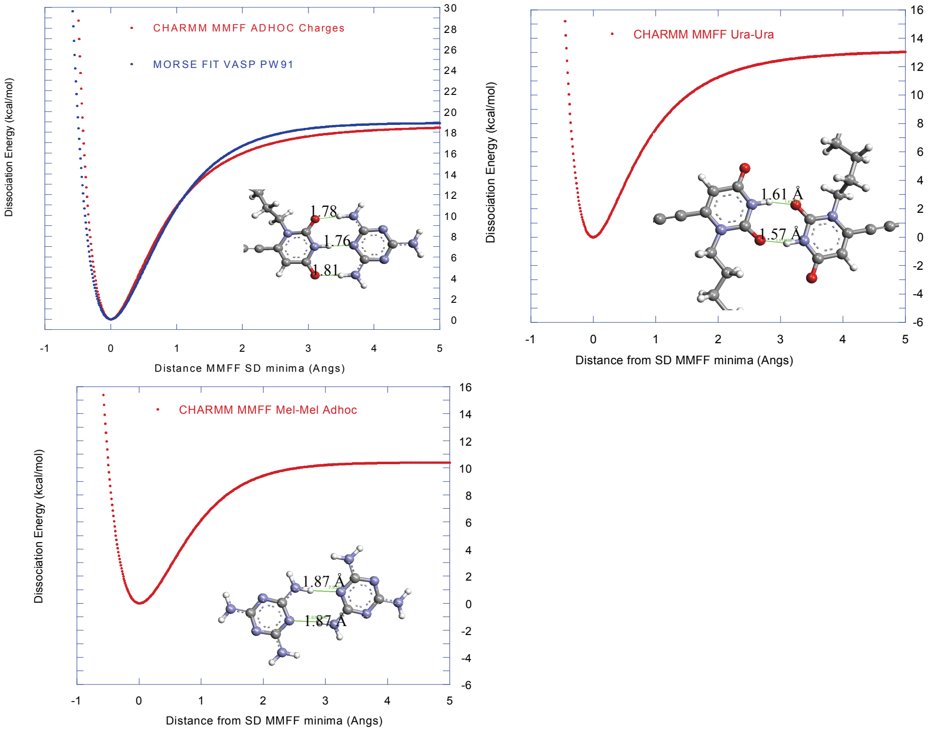

Figure 8-21
H-bond dissociation energy for: (a) the **Molecule 7-MEL** hetero-dimer, (b) the **Molecule 7-Molecule 7** homo-dimer, and (c) the **MEL- MEL** homo-dimer. The blue line in panel a) was generated by fitting the quantum mechanical dissociation energy for the **Molecule 7-MEL** dimer (18.5 kcal/mol) with a Morse potential function.

<u>CHARMM KEYWORDS</u>
SCALAR CHARGE SET -0.7 SELECT ATOM MEL * N7
SCALAR CHARGE SET -0.7 SELECT ATOM MEL * N10
SCALAR CHARGE SET -0.7 SELECT ATOM MEL * N13
SCALAR CHARGE SET 0.52 SELECT ATOM MEL * C1
SCALAR CHARGE SET 0.52 SELECT ATOM MEL * C3
SCALAR CHARGE SET 0.52 SELECT ATOM MEL * C5

Non-Bonded Interactions and Cut-off's. The calculation of the non-bonded interactions in molecular dynamics is costly and normally constitutes the bottleneck in the speed of the simulations. To lower the computational cost, cut-off values for the non-bonded interactions are commonly employed; they speed up the simulations by reducing the effective number of interacting atoms without lowering the accuracy of the calculations. However, the choice of the cutoff is critical, especially when the simulations are performed in a highly apolar medium. **Figure 8-22** shows the histogram of the potential energy corresponding to 100ps Langevin dynamics in vacuum for 1x**MEL** and 3x**Molecule 7** modules physisorbed on the implicit substrate. The simulations were carried out using an integration time step of 2fs and a friction coefficient of 1 ps^{-1}, as described in the following sections. The effect of changing the cutoff from 9.5 Å to infinite (99.5 Å in a 100x100 Å box) is apparent. The average potential energy sampled with a cutoff of 9.5 Å is about 10% off the correct value. To avoid systematic errors of this kind, which may strongly bias the simulation results, a cutoff of 18Å in conjunction with the SHIFT and VSHIFT cut-off functions were used; the latter are recommended for the MMFF Force-Field. A layer 2 Å was finally imposed between the cutoff used to compute the energy (CTOFNB) and the cutoff to update the non-bonded list (CUTNB). The latter allows for an efficient heuristic update during the simulations.

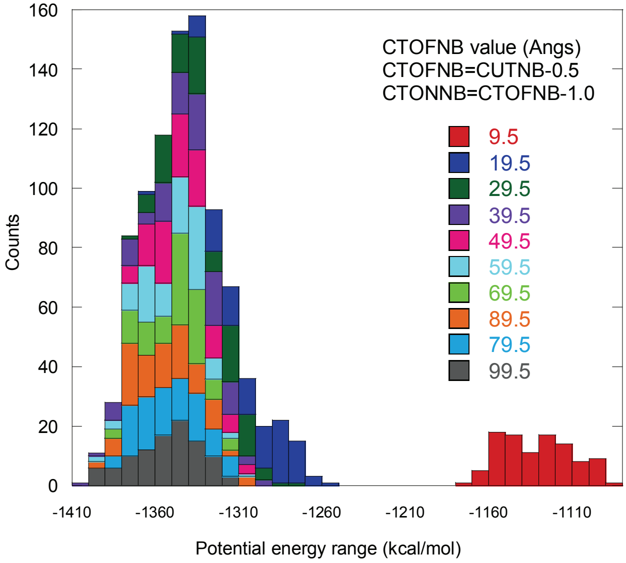

Figure 8-22

Non-bonded cut-offs (CTOFNB) Potential Energy Bar histograms.

CHARMM KEYWORDS

NBONDS ELEC ATOM CDIE SHIFT VDW VATOM VSHIFT -
CUTNB 20.0 CTOFNB 18.0 CTONNB 16.0 CTIMG 22.0

Implicit Substrate Model. In 2D molecular self-assembly the substrate plays a critical role. *In primis*, it reduces the dimensionality of the problem to 2D, thus strongly reducing the entropic cost of association (Tidor and Karplus 1994), *in secundis*, it may template the formation of specific supramolecular architectures by site selective physisorption (Lei, Wang et al. 2004). It is thus clear that any computational investigation of 2D self-assembly must rely on a proper description of the substrate as well as the interaction with the self-assembly modules. Given that the experimental STM imaging of **Molecule 7-MEL** self-assembly was performed on graphite (Palma, Bonini et al. 2008), the most natural choice for modeling the substrate is an all-atom representation of a graphene slab; referred to as the *explicit* substrate model. Importantly, such an explicit substrate has been recently shown to provide adsorption energies for a series of aromatic compounds that correlate well with the experimental adsorption energies on graphite (Bjork, Hanke et al. 2010). Nevertheless, an all-atom representation of the substrate dramatically increases the effective number of interacting centers, thus reducing the efficiency of the calculations. The explicit representation of a graphene slab introduced 10800 additional atoms, which corresponds to a 73% increase in system's size. An alternatively and more efficient approach is based on a mean field description of the substrate. Within this framework the presence of graphite can be mimicked by an effective attractive potential with a given depth well at the equilibrium distance and desorption barrier on a longer range; the former accounts for the interaction between the substrate and the physisorbed modules, the latter for solvation effects. Such a simplified description, which is referred to as the *implicit* substrate model, is a crude but very efficient representation, which effectively reduces the dimensionality of the system to a 2D space at no extra cost. In the current *simulation setup*, the desorption barrier was neglected and the *implicit* substrate was simply modeled by a 2D harmonic well, whose width was adjusted to confine the self-assembly modules to a layer of 3-4 Å from the surface. In this implementation, the width of the potential well is a key parameter that needs to be optimized. The latter, in fact, is related to the steepness of the energy gradient in the direction perpendicular to the plane and determines both the adsorption geometry of the self-assembly modules (structural property) and their diffusion (dynamics) on the surface. The parameterization of the implicit substrate is shown in **Figure 8-23** which shows the effective width of the physisorbed layer at various harmonic strengths (*k*) for 3x**Molecule 7** and 1x**MEL** modules forming a *4*-mer. It is shown that for a restraint strength of 1.5 kcal/mol/Å^2 the energy gradient is so steep that a change of 30 kcal/mol is needed for an out-of-plane movement of 1Å. By contrast, for *k* equal to 0.1 kcal/mol/Å^2, the small energy change of 4 kcal/mol is sufficient to move the whole structure by 1 Å. Since the kinetic energy of the *4*-mer is about 100 kcal/mol at 420K, we estimate that a harmonic strength of 0.5 kcal/mol/Å^2 is best suited to confine the molecules onto a physisorbed layer of 3-4 Å. This value of *k* has been used in the *standard simulation setup* throughout the study. It is important to note that in the current implementation, the *implicit* substrate model incorporates no intrinsic ruggedness. Thus, all molecules are free to diffuse isotropically on the substrate, which is conferred no templating ability. More sophisticated modeling that includes ruggedness at the surface as well as tunable desorption barriers will be left for future investigation.

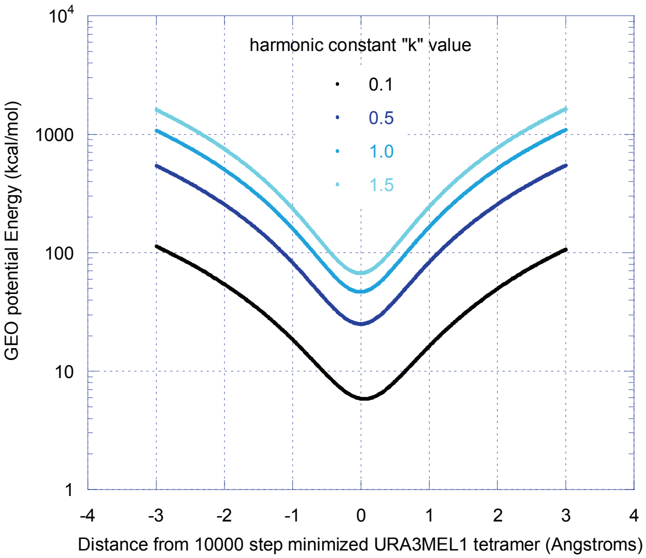

Figure 8-23

Restraining Harmonic Potential Energy vs. out-of-plane distance for different harmonic constants. To produce the plot the flat tetramer was moved perpendicularly to the surface from its minimized structure.

The quality of the current *implicit* substrate model was judged by comparing the lifetime and the apparent diffusion constant for the **Molecule 7-MEL** dimer with values obtained with an *explicit* representation. The diffusion coefficients were computed from ten independent runs of a **Molecule 7-MEL**, each of which was 5ns long. The time series of the MSD (mean square displacement with respect to the initial absolute positions of the atoms) were first computed and averaged over the ten runs. Finally, the two dimensional diffusion coefficient, *D*, was determined by linear fit of equation (Frenkel and Smit 2002),

$$MSD = 4Dt$$

Equation 8-3

Error bars were calculated from the standard deviation of multiple fits to the linear part of the same MSD. The results of the analysis are plotted in **Figure 8-24**. It is shown that the simplified *implicit* approach reproduces reasonably well the diffusion coefficient on a graphene slab, as well as the overall trend in temperature. However, the "apparent" diffusion[6] of the **Molecule 7-MEL** dimer

---

[6] Note that Langevin Dynamics cannot be used to estimate real diffusion coefficients since the dragging force artificially draws momentum at the atomic scale. Therefore, diffusion coefficients obtained from the simulations are termed "apparent".

is faster on the implicit substrate. Given the fact that both implicit and explicit substrate simulations were based on Langevin dynamics employing the same friction coefficient ($0.05ps^{-1}$), it indicates that the interactions between the self-assembly modules and the graphene slab provide extra friction, which may slow down the association kinetics and reduce the overall sampling efficiency. Therefore, despite the higher accuracy of the explicit substrate model, the implicit model appears to be superior in sampling.

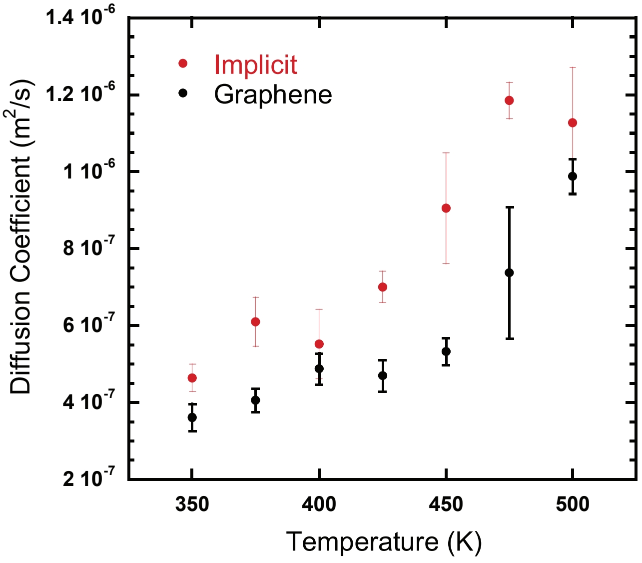

Figure 8-24
Apparent Surface Diffusion Coefficient vs. Temperature for both implicit and graphene substrates.

<u>CHARMM KEYWORDS</u>

```
MMFP
GEO PLANE -
   XREF 1 YREF 1 ZREF 0 ZDIR 1.0 -
   FORCE @i DROFF 0 SELECT ALL END
END
```

Complement: Dimer Life-times. The lifetime of the **Molecule 7-MEL** dimer was estimated by performing two series of 10 independent simulations at temperatures ranging from 350 to 500K. A preformed **Molecule 7-MEL** dimer physisorbed on the implicit (or explicit) substrate was simulated for 5ns, while monitoring the number of hydrogen bonds (N) as a function of time. The hydrogen bonds number was identified by the default WORDOM H-bond detection module in the case of implicit substrate and the default CHARMM H-bond detection module for the graphene slab (see **Scripts**). By averaging the time series of the number of hydrogen bonds over various MD runs, the dimer lifetime was obtained by fitting the exponential part of N(t) to,

$$N(t) = N_0 * \exp\left(-\frac{t}{\tau}\right)$$

Equation 8-4

where N_0 is the initial number of hydrogen bonds and τ the dimer lifetime. Error bars were estimated from the standard deviation of τ between two series of simulations.

A critical aspect in the investigation of molecular self-assembly by computer simulations regards the reversibility of the process on the time scales accessible by the calculations. In fact, conformational sampling by molecular dynamics is statistically meaningful only if the conformational states visited during the simulation trajectory are in thermal equilibrium. Under these conditions, the system evolves to the thermodynamically more stable states, which according to their Boltzmann factor are sampled more often. Therefore, to properly study the self-assembly of hundreds of modules *in silico*, it is critical to identify the simulation conditions that guarantee full reversibility of the recognition events. **Figure 8-25** and **Figure 8-26** show that reversibility of the *hetero*-recognition on the nanosecond time scale is achieved by increasing either the temperature (physical acceleration) or the dielectric constant of the medium (chemical acceleration). In fact, increasing the temperature provides extra thermal energy that helps the system to cross barriers, while increasing the dielectric constant reduces the strength of the *hetero* recognition and lowers the dissociation barrier. Accordingly, **Figure 8-25** and **Figure 8-26** show that at temperatures higher than 400K or dielectric constant larger than 2 the **Molecule 7-MEL** dimer disassembles in a few nanoseconds. Both ways can be effectively exploited to enhance sampling efficiency. For the scope of the paper, we decided to play with the temperature and to run all **Molecule 7-MEL** simulations at values larger than 400K. Consequently, a dielectric constant of 1 was used throughout the study, except when specified (i.e., for **Molecule 17+Molecule 18**).

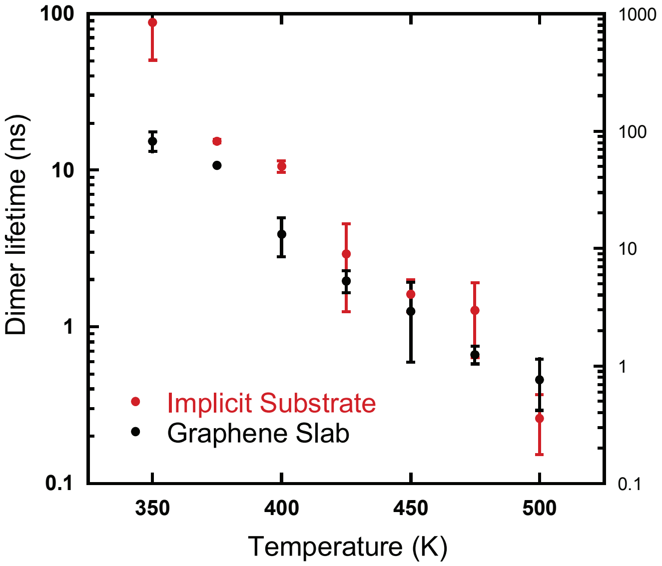

Figure 8-25
Molecule 7-MEL dimer dissociation lifetimes vs.temperature for implicit substrate and a graphene slab representative of the used graphite substrate.

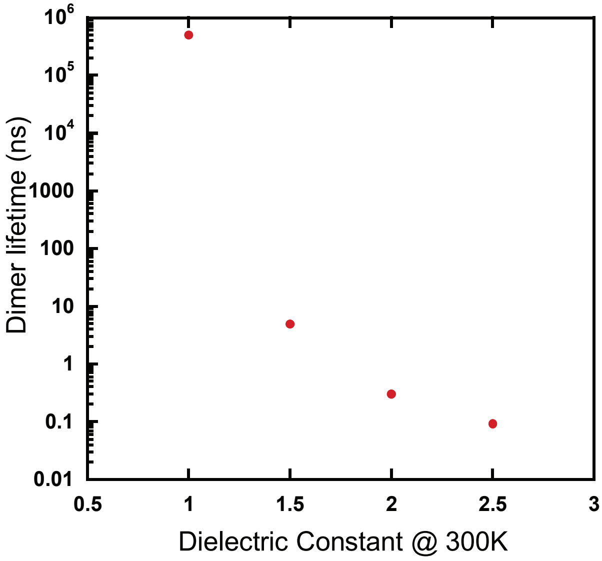

Figure 8-26
Molecule 7-MEL dimer dissociation lifetimes vs. relative dielectric constant for both implicit and graphene surfaces.

Along with the diffusion constant results, we conclude that the *implicit* model provides a reasonable and extremely efficient representation of the substrate, which allows for microseconds sampling in a few weeks of calculation.

Periodic Boundary Conditions. As stated in the Chapter 5, mastering the thermodynamics of multi-component self-assembly implies the full knowledge of the system's phase diagram in temperature and concentration. It follows that to simulate multi-component self-assembly, the range of concentrations of the modules for which self-assembly may actually occur must be first identified. This information is used to setup the size of the simulation box as well as the number of modules to be simulated. In STM experiments, we have shown that self-assembly occurs at sub-monolayer coverages (Palma, Bonini et al. 2008). Thus, we chose a system density that corresponds to half a monolayer. This choice is justified as follows. At lower coverages self-assembly is less likely to occur on the simulation time scale because seeding nuclei might not form. Moreover, too low concentrations (using *extended* periodic boundary conditions) may effectively reduce the probability of productive collision encounters, thus slowing down the association kinetics (compare for instance clustering figures insets in the following sections). By contrast, at higher densities the system may easily get trapped into extrinsic structural defects unable to relax on the sub-microsecond scale. This issue is expected to be even more severe in conjunction with the use of an *implicit* substrate model, which does not account for the adsorption-desorption equilibrium and intrinsically favors kinetic trapping.

Moreover, to avoid finite-size effects and provide the system with a critical size that is able to trigger self-assembly, the number of molecules to be simulated should be maximized. The latter, of course, lowers the efficiency of the calculations. With 80 molecules (ca. 4000 atoms), a single MD run on four IBM sp6 CPUs samples 1ns per hour, thus yielding half a microsecond sampling in about 20 days. In light of the above, the *standard setup* involves simulations of a stoichiometric mixture of 80 self-assembly modules (32 molecules of **MEL** or the trihapto cornerstone and 48 of **Molecule 7** or the biguanide linker modules) in a rectangular box with periodic boundaries conditions; the latter is a multiple of the rectangular super-cell highlighted in **Figure 8-27.** In particular, the side lengths of the box amounts to *b*= 207.8 Å, *a*= 216 Å for **Molecule 7-MEL**, and *b*= 255.5 Å, *a*= 265.5 Å for **Molecule 17-Molecule 18**. The use of a stoichiometric mixture of 80 modules instead of the theoretical value of 150, which can fully tile the chosen super-cell, corresponds to a monolayer coverage of 0.53. The initial structures for the simulations were obtained by creating alternate rows of **MEL** (or **Molecule 17**) molecules and **Molecule 7** (**Molecule 18**) molecules and then extracting a snapshot from simulation every 25 picoseconds at 800K and a relative dielectric constant of 20 to randomly distribute the molecules. It is important to note that only one stereoisomer of the *ura* module was used in the simulations, where the alkyl chains are *anti* with respect to the main molecular axis. In addition, given that **Molecule 7-MEL*** cluster very rapidly, the simulations were performed with an *extended* box with periodic boundaries conditions, i.e., a squared box with a side length of 500 Å. The latter was shown to favor the crystalline architecture over the semi-crystalline one (see below).

The super-cells were obtained by multiplying the magnitude of the 10-molecule elementary rectangular unit cell vectors (i.e. the smallest rectangular unit cell) by 5 and 3. The dimension of the elementary rectangular unit cell was obtained by the formulas ***b***= 2**t**cos(π/3) and ***a***= 3*t*, were *t* is the size of the hexagonal side measured in the simulations. The hexagonal side obtained for **Molecule 17-Molecule 18** and **Molecule 7-MEL** amount to 29.5 and 24 Å, respectively; the latter results in the primitive hexagonal unit cell area of 15 Å^2 in agreement with DFT calculations (Palma, Bjork et al. 2009). We note that under these conditions, full crystalline packing involves 88 recognition events. The combination of stoichiometric mixtures and rather high densities was shown to yield the best compromise in terms of simulation time and structural evolution to ordering.

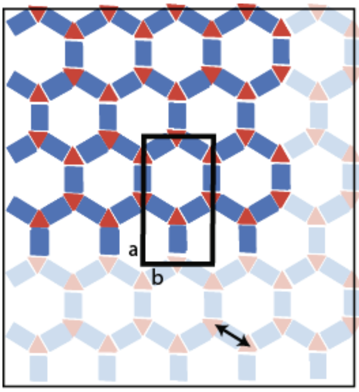

Figure 8-27

Rectangular supercell used for the calculations, based on multiples of the elementary rectangular unit cell (in black). The 80 dark molecules are the ones actually used in the calculation, leaving the supercells partially empty. Supercell b= 207.8 Å a= 216 Å for **Molecule 7-MEL** and b= 255.5 Å and a= 265.5 Å for **Molecule 17-Molecule 18**.

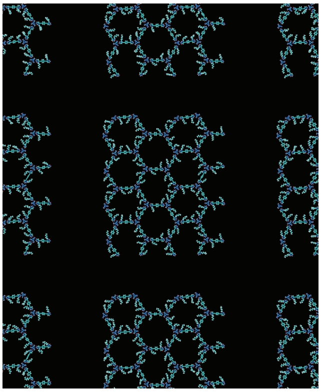

Figure 8-28
View of the pre-formed **Molecule 7-MEL** crystal *80*-mer of **Figure 8-27** with periodic boundary conditions applied and showing the three possible linker steroisomers induced by adsorption. Only one *anti* enantiomer was used in the present study.

CHARMM KEYWORDS

```
CRYSTAL DEFINE TRICLINIC 207.8 216 1000 90 90 90
CRYSTAL BUILD CUTOFF 216 NOPERATIONS 0
IMAGE BYSEG XCEN 0 YCEN 0 ZCEN 0 SELE ALL END
```

These data confirms our previous work (Palma, Bjork et al. 2009), such that playing with the internal flexibility of the self-assembly modules may offer an alternative strategy to favor the desired supramolecular architecture. The latter, which essentially involves an optimization of the entropic term, may extend the available chemical space in previously unexplored directions. Most importantly, the computational tools presented and employed in this study can be effectively used for a quantitative control of such subtle aspects.

Molecule 7-MEL Fast-Annealing Simulations Fast-annealing simulations consisted in 500ns molecular dynamics at 400K in which every 0.5ns two temperature spikes are consecutively applied, one of 0.05ns at 475K followed by another one of the same time length at 525K. Since the **Molecule 7-MEL** dimer dissociates in the sub-ns timescale at 500K (see **Figure 8-25**), the fast-annealing strategy results in a quite efficient conformational search. During annealing a plethora of discrete supramolecular structures mainly based on *hetero*-mers were sampled.

Cluster and Macrocycle Detection. To perform a statistical analysis of the supramolecular adducts that spontaneously assemble and dis-assemble on the simulation time scale, a clustering procedure based on the *hetero*-interactions was developed (see **Scripts**). For this purpose, the number of *hetero*-interactions were computed by the program WORDOM (Seeber, Cecchini et al. 2007) in each simulation snapshot. The latter was used to monitor the occurrence of *hetero*-recognition events and most importantly to build up a connectivity matrix, which was used to identify the supramolecular clusters. The criterion for the identification of one hetero- recognition event was a contact distance of 3 Å between the H-bond donor nitrogen of melamine and the H-bond acceptor hydrogen of **Molecule 7**. For the **Molecule 17-Molecule 18** system a contact distance of 4 Å was used instead of 3 Å. Finally, the structural analysis proceeds as presented below, which allowed to monitor the time-evolution of the system towards ordering and collect statistics on the supramolecular polygons formed at the substrate's surface.

A color spread algorithm is used to identify molecules that belong to the same supramolecular group for any given snapshot of the simulation trajectory. Once the snapshot is decomposed into supramolecular groups, or clusters, the largest adduct is identified and used to monitor the cluster size as a function of time (see **Figure 8-29**). The large fluctuations in **Figure 8-29** indicate that relatively large clusters form and dissolve on the nanosecond time scale but none of them attains the maximum cluster size of 80 molecules. Overall, the average size of the largest cluster per frame amounts to 40±17 molecules, i.e. clusters have enough molecules for creating 2-3 polygons.

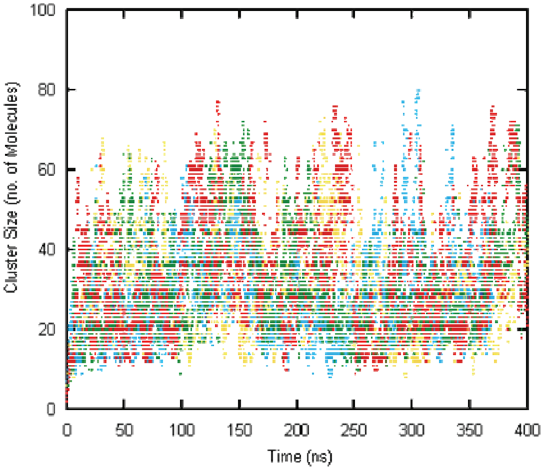

Figure 8-29

Largest cluster size evolution as measured in four independent "fast-annealing" **Molecule 7-MEL** simulation trajectories. The data correspond only to the low-temperature (i.e., 400K) simulation segments, i.e. they do not include the annealing cycles at 475 and 525K.

Concerning the macrocyle analysis, only one macrocycle is identified per supramolecular group for each frame through a combinatorial procedure. Note that only one polygon is identified per supramolecular group to avoid any *tiling* preferential artifacts that may occur in clusters bigger than ~20 molecules.

Figure 8-30 shows the average of macrocycle population per simulation from twenty "fast-annealing" independent runs of 500 ns.

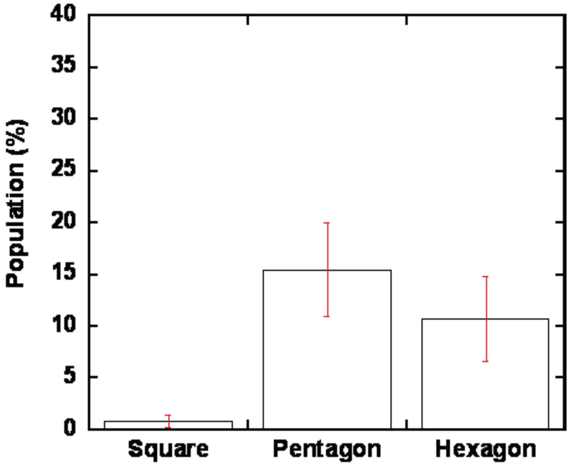

Figure 8-30
Average populations of indistinguishable macrocyles from twenty independent runs, each of which was 500 ns long. Only the trajectories corresponding to the simulations at 400K are analyzed.

Molecule 7-MEL 420K & 375K Simulations. Ten simulations of a **Molecule 7-MEL** stoichiometric mixture were carried out at the constant temperatures of 375K and 420K using the *standard simulation setup*. **Figure 8-31** and **Figure 8-32** show the largest cluster size evolution in four independent simulations. As stated in Chapter 5, on the sub-microsecond time scale the system shows little structural evolution to ordering at 375K (**Figure 8-31**), whereas it appears more dynamic at 420K (**Figure 8-32**). In the former case, only 2D amorphous polymers are sampled; in the latter, large molecular clusters spontaneously assemble and slowly evolve to highly ordered structures; i.e., on the hundred of nanoseconds time scales.

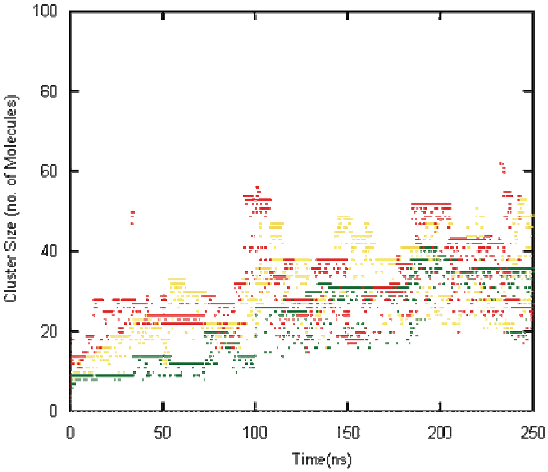

Figure 8-31
Largest cluster size evolution at 375K for three independent runs.

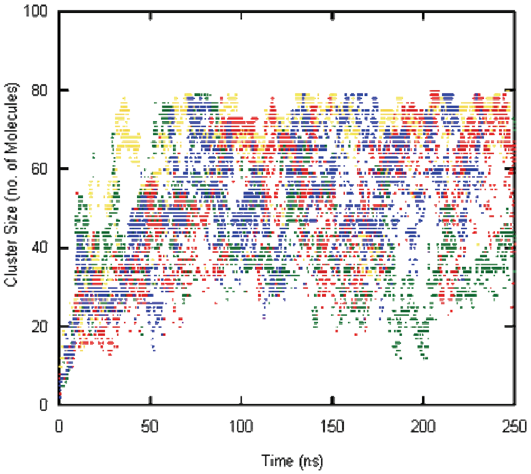

Figure 8-32
Largest cluster size evolution at 420K for four independent runs.

Molecule 7-MEL* Simulations. To explore the role of *homo* recognition in **Molecule 7-MEL** self-assembly, the model system **Molecule 7-MEL*** was introduced. The model system **Molecule 7-MEL*** is chemically analogous to **Molecule 7-MEL** apart from the fact that all *homo*-recognition events are scaled down by a factor of 100. The latter was implemented by using the BLOCK facility in CHARMM, which allows the user to scale the interaction energy between suitably defined portions (or *blocks*) of the system.

In the present implementation eighty blocks were identified, one per molecule. The energy scaling factors for all intra-block interactions (internal molecular energy) and the inter-block interactions, which involve chemically heterogeneous modules (*hetero* interactions), were set to 1.0, while those for the inter-block interactions, which involve chemically homologous modules (*homo* interactions), were set to 0.01. The decomposition of the system into blocks allows for an effective scaling of the *homo* non-bonded interactions, while preserving the energetics of the individual molecules. The choice of a small but non-zero scaling factor for the *homo* non-bonded interactions avoids any structural overlap between chemically homologous modules and thus preserves the effective volume accessible to the system. The present implementation effectively corresponds to an idealized self-assembly system essentially devoid of *homo* recognition; see below for the CHARMM code. With the new setup, fifteen simulations were carried out at a constant temperature of 420K, ten using *standard* periodic boundary conditions (**Figure 8-33**) and five using *extended* periodic boundaries with a=b=500 Å (**Figure 8-34**). As previously discussed the *extended* boundaries favor the formation of a fully crystalline pattern, at the expense of a lower nucleation rate (~2 ns vs. ~30 ns for reaching the maximum molecular cluster size, see respective insets).

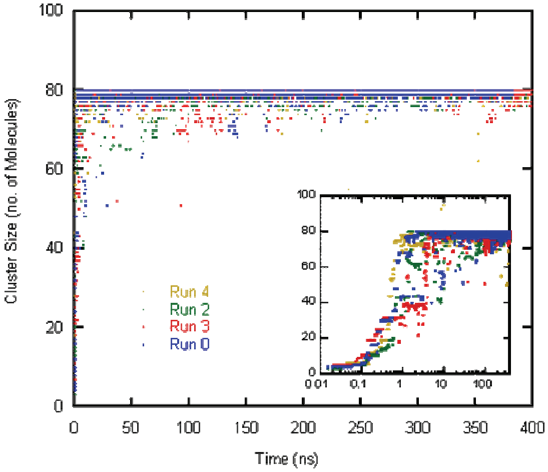

Figure 8-33

Largest cluster size evolution at 420K for four independent runs in the **Molecule 7-MEL*** setup with *standard* periodic boundary conditions of b= 207.8 Å a= 216 Å. The inset shows the plot on the semi-logarithmic scale.

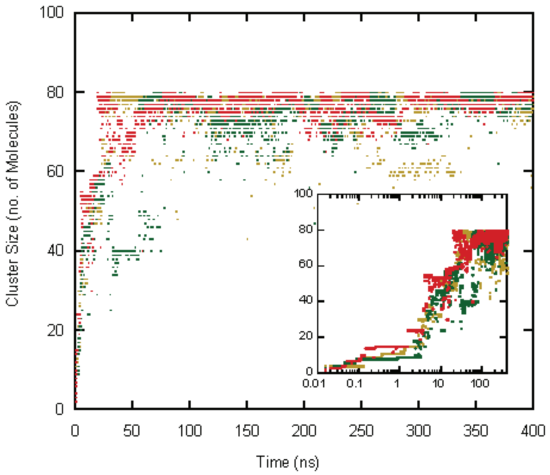

Figure 8-34
Largest cluster size evolution at 420K for three independent runs in the *mel·ura** setup with *extended* periodic boundary conditions a=b= 500 Å. The inset shows the figure in semi-logarithmic plot.

CHARMM KEYWORDS:

```
BLOCK 80
CALL 1   SELE  SEGID ME1  END
CALL 2   SELE  SEGID ME2  END
…
CALL 79  SELE  SEGID UR47  END
CALL 80  SELE  SEGID UR48  END
COEFF  1   1 1.00
COEFF  1   2 0.01
…
COEFF  1 79 1.00
COEFF  1 80 1.00

COEFF  2   1 0.01
COEFF  2   2 1.00
…
COEFF  2 79 1.00
COEFF  2 80 1.00

COEFF  80  1 1.00
COEFF  80  2 1.00
…
COEFF  80 79 0.01
COEFF  80 80 1.00
END
```

From a theoretical perspective, it should be noted that **Molecule 7-MEL*** is reminiscent of the Go models for protein folding (Taketomi, Ueda et al. 1975). In the latter, the frustration of the folding free energy landscape is effectively smoothed out by the introduction of a structure-based potential, which drives the system toward its native state. Despite their success, Go models are strongly biased since they strictly rely on the knowledge of the native structure and the definition of the "native contacts", which are used to bias the conformational search of the model protein; native contacts are a list of residues, which are interacting in the native state. Here, following a somewhat similar idea the knowledge of the crystal structure is used to bias the self-assembly into a fully crystalline pattern. However, by contrast to the Go models our definition of *hetero* interactions, which is the analogous of the native contacts, is not structurally univocal due to the presence of multiple and totally equivalent interaction centers. It follows that the idealized **Molecule 7-MEL*** system is more general than a Go model and therefore is expected to be less biased. Along this line, one could state that while Go models should be categorized as structure-based approaches, simplified models such as **Molecule 7-MEL*** should be referred to as chemistry-based approaches, with the latter extending the former.

Molecule 17+Molecule 18 520K Simulations. Fifteen independent simulations were carried out at a constant temperature of 520K and a dielectric constant of 2.5. Among them, ten employed the *standard simulation setup* featuring periodic boundaries conditions of b= 255.5 Å and a= 265.5 Å, while five featured extended boundaries a=b=500Å. To maintain a comparable ratio between the strength of the *hetero*-recognition and the thermal energy in the simulations ($E_{\text{interaction}}$/kT) to that characteristic of the **Molecule 7-MEL** system, **Molecule 17-Molecule 18** would require temperature values >>900K;. Such temperatures, however, are hardly compatible with our simplified description of the substrate, because promote large fluctuations on the out-of-plane direction. Hence, we decided to reduce the strength of the interaction energy by tuning the dielectric constant. The use of a dielectric constant of 2.5 effectively lowers the **Molecule 17-Molecule 18** hetero-recognition from 50 to 20 kcal/mol. Interestingly, the **Molecule 17-Molecule 18** system simulated at 520K with a dielectric constant of 1.0 behaves as an amourphous compact solid because isotropic electrostatic interactions are of the order of 10 kcal/mol. **Figure 8-35** shows the evolution of the cluster size with the standard boundaries (b= 255.5 Å and a= 265.5 Å), while Figure S21 the evolution with extended boundaries (a=b=500Å). In contrast to **Molecule 7-MEL***, **Molecule 17-Molecule 18** system remains dynamic even in the extended simulation box, as evidenced by the large fluctuations in **Figure 8-36**, i.e. it shows a constant interconversion of supramolecular polygons, i.e., pentagons, hexagons, as well as other polygons. By contrast, in the standard box the system features structural evolution towards the semi-crystalline pattern, and the fluctuations are damped (**Figure 8-35**). We conclude that although this material presents fast self-healing properties in the high-density regime, self-healing is not homogeneous in the entire concentration space.

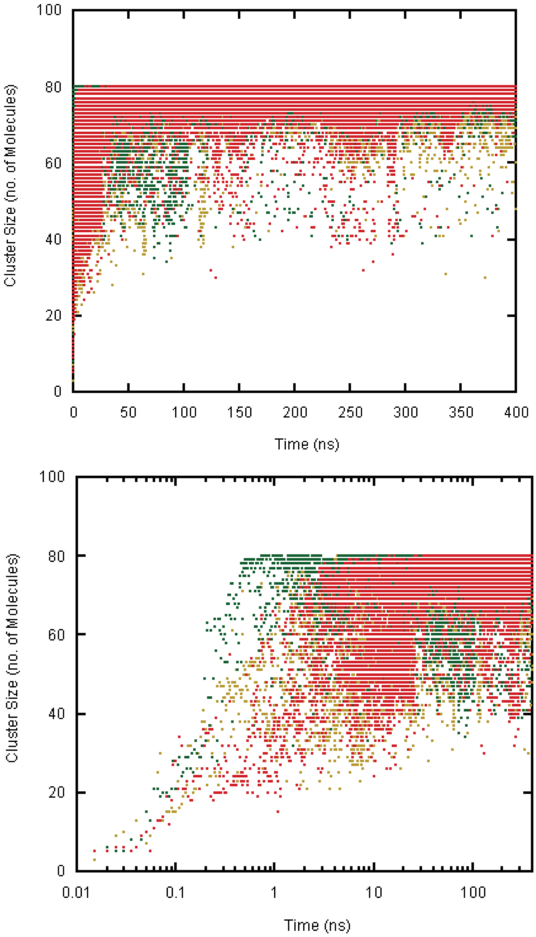

Figure 8-35

a) Largest cluster size evolution at 520K for three independent runs in the *bigua-anthra* setup with *extended* periodic boundary conditions of b= 255.5 Å and a= 265.5 Å b) The figure in semi-logarithmic plot

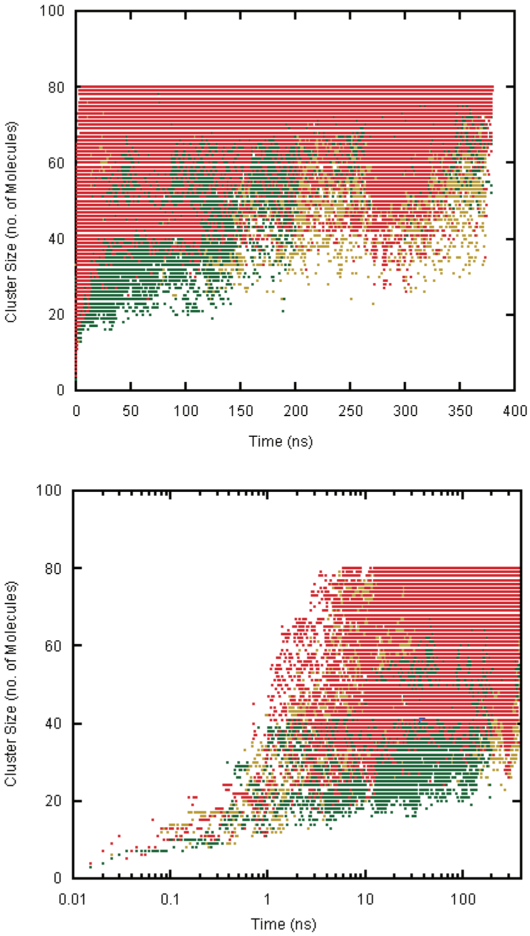

Figure 8-36

a) Largest cluster size evolution at 520K for three independent runs in the *bigua-anthra* setup with *extended* periodic boundary conditions a=b= 500 Å b) The figure in semi-logarithmic plot

Movies are available in the video section of the nanochemistry website: http://www-isis.u-strasbg.fr/nanochem/videos

8.5 Chapter 6

8.5.1 Functional Di-imide Linkers

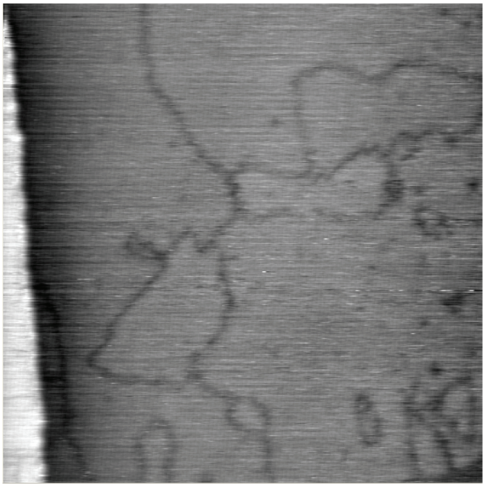

Figure 8-37

100nm x 100nm STM image at the solid-liquid interface of **Molecule 26** with **MEL** monolayer on HOPG (trichlorobenzene solvent). By applying to the surface a highy concentrated solution, i.e. containing more molecules that that need to form a monolayer of tightly packed molecules, melamine is only visualized (gray contrast). Here, **Molecule 26** homomeric networks (black contrast) appear to a first approximation to be embeded in the melamine sea. Concentration 15±3 micromolar in MEL and 6±3 **Molecule 26** - used 6uL of solution. This result is highly reproducible.

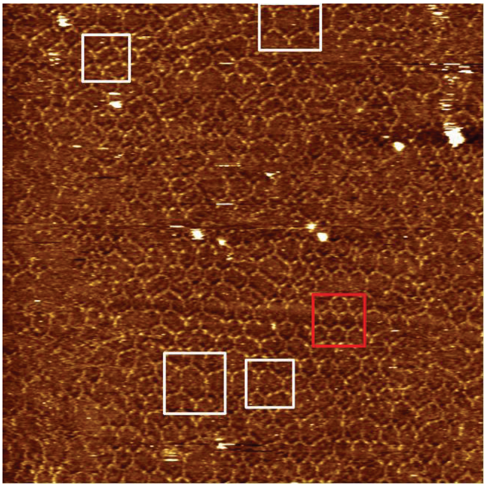

Figure 8-38

STM image at the solid-liquid interface of **Molecule 26** with **MEL** monolayer on HOPG (trichlorobenzene solvent) at low concentration. By applying to the surface a diluted solution, i.e. containing less molecules than those needed to form a monolayer of tightly packed molecules, in particular with a concentration of 4 micromolar in **MEL** and 5 micromolar in **Molecule 26**, a polygonal architecture is observed, featuring interesting polygon structures (white rectangles) that can be ascribed to the melamine defiency. Meanwhile a cristalline hexagonal bit is also shown (red rectangle).

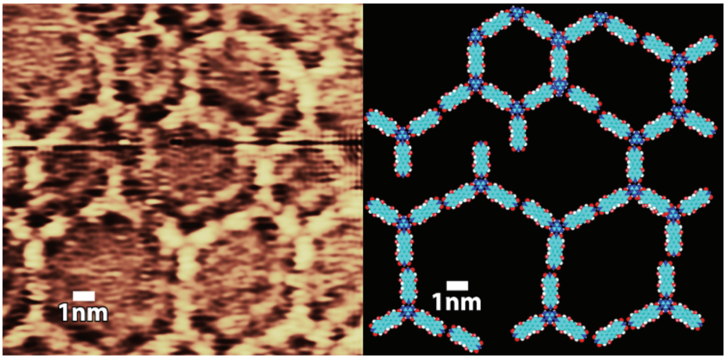

Figure 8-39
STM image at the solid-liquid interface zoom-in in the defect domain of **Molecule 26+MEL**. The deficiency of melamine is evident from the constructution of higher order polygons through heterocoupling of **Molecule 26** dimers. An apparent "double-tip" effect inside the polygon structure is being investigated by an statistical analysis of the multiple polygons.

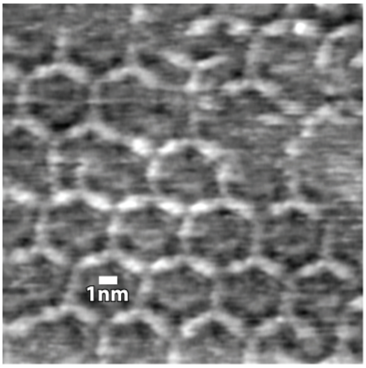

Figure 8-40
STM image at the solid-liquid interface zoom-in of **Molecule 26+MEL** ordered domain. Small hexagonal network domains are also seen within the monolayer.

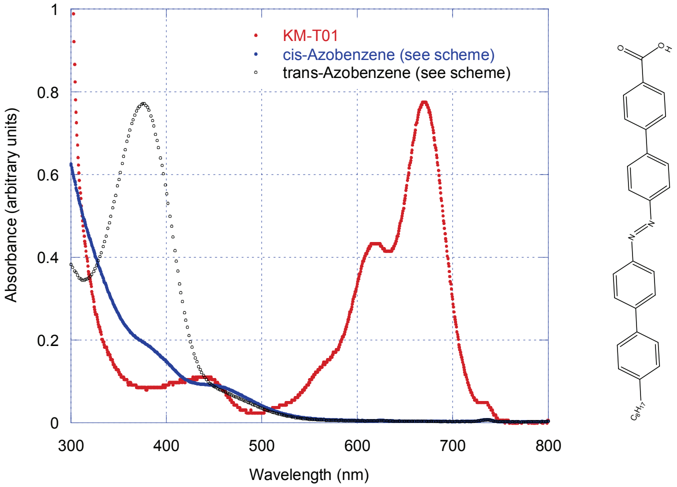

Figure 8-41

Absorption spectra of **Molecule 26** and the *Z* and *E* of the azobenzene observed in the right hand side. The spectra shows that the main absorption bands are decoupled, showing that the *Z* →*E* isomerization is possible even in the presence of terrylene core (band from 600 to 700nm), by using 375nm light to isomerize the *trans* into the *cis* without degradation of the **Molecule 26** compound.

8.5.2 **Towards 3D Device Self-Assembly**

Synthesis of **Molecule** 31 was carried out by Dr. Michael Schar. Currently, only two fragements of **Molecule 30** have been synthetized, fragment **Molecule 30i** and **Molecule 30iv**.

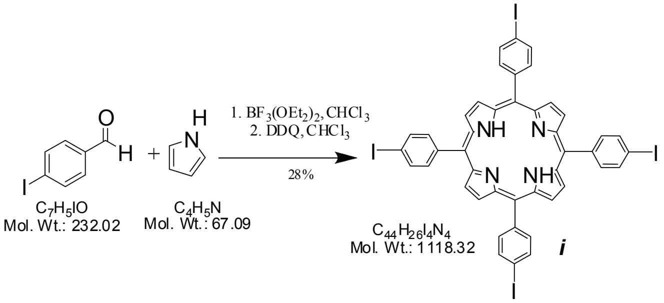

Scheme 8-1

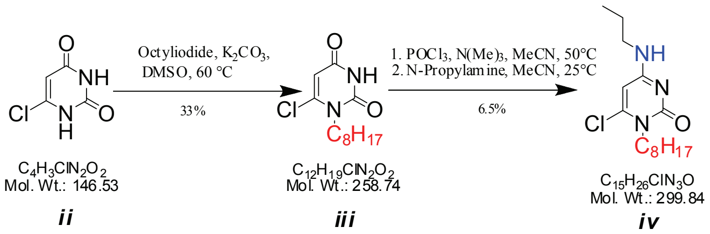

Scheme 8-2

Molecule 30*i*

A 1L round flask is triply heated and purged with N2. 400mL of CH3Cl3 are added and the mixture degassed for 1h30. 0.922grams (4mmol) of iodobenezene and 283mL of pyrrrole are added. The solution is degased for 2h more, then 1mL of BF3-Oet is added. The reaction is left protected from light at r.t. under agitation and after 2 hours 5g of DDQ are added and left overnight. Workup of the reaction mixture with three consecutive silica plugs of CH2Cl2 and then EtOAc yields 125mg of **Molecule 30*i*,** (28% yield). **.** Kd=0.72 in DCM eluant. ^{1}H NMR (400MHz D_6-$CDCl_3$): δ -2.88ppm (s, 2H, N-H) δ 7.91ppm (d, 8H, Ar-H), δ 8.1ppm (d, 8H,Ar-H), δ 8.8ppm (s, 8H, pyrrole-H).

Molecule 30*iii*

A 100ml round flask is triply heated and purged with N2. 4.43g (30mmol) of Moleculer 26ii (supplied by Michael Schar) and 2.06 (0.015mmol) k2CO3 are added. Under argon balloon 20mL dry DMSO are added and 6mL (d=1.32, 30mmol) of octyliodine (Aldrich, stabilized with copper) are added. The mixture is stirred at 60-70. After 2 hoursreaction, 20mL of NaOH 4% is added to the hot mixture. Workup of the reaction mixture involved extracting the aquous phase twice with toluene, evaporating and passing the disolved residue in 250mL CH2Cl2 through a silica plug and repeating the procedure for 250mL of EtOAc yields 2.8g (10mmol, 33%) of **Molecule 30*iii*.** Kd=0.6 EtOAc eluant, ^{1}H NMR (400MHz D_6-DMSO): δ 11.6ppm (s, 1H, N-H) δ 5.91ppm (s, 1H, vinylic C-H), for C_8H_{17}: δ 3.86ppm (tr, 2H), δ 1.56ppm (broad, 2H), δ 1.24ppm (broad, 12H), δ 0.84ppm (broad, 3H).

Molecule 30*iv*

A 100ml three-neck round flask is triply heated and purged with N2. 0.8g (3.1mmol) of **Molecule 30*iii*** are added. 30mL of dry ACN are added and the reaction heated at possitive N2 pressure until dissolved.0.5mL of POCl3 (4 eq.) are added and the reaction left fro 4 hours. The mixture is then evaporated slowly at 0.5 torr until dryness. Then 20mL of ACN with 0.246mL of ethanamine (3.1mmol, d=0.719, MM 59.11) is added. After 4h agitation and reaction at room temperature reaction is stopped and quenched with 30mL of EtOAc. The solution is washed with 3x15mL of brine. The ACN fraction is dried with MgSO4 and filtrated. A 6cm silica flash chromatography column with EtOAc separated the ~4 products. The first 4x5mL fractions yielded 60mg of **Molecule 30*iv*** (1.95mmol, 6.5%). Kd=0.8 EtOAc eluant. ^{1}H NMR : (400MHz D_6-DMSO): δ 5.881ppm&5.81ppm (s, 1H, vinylic* C-H), δ 3.87ppm (tr, 2H, CH_2-C_7H_{17}),δ 4.73ppm (tr, 2H, CH_2-C_2H_5), for the rest of C_8H_{17}&C_8H_{17}: 1.56ppm (broad, 4H), δ 1.24ppm (broad, 12H), δ 0.84ppm (broad, 6H). **Note, this split due to a possible rotamer of **Molecule 30*iv*** is under investigation.

Index of Molecules

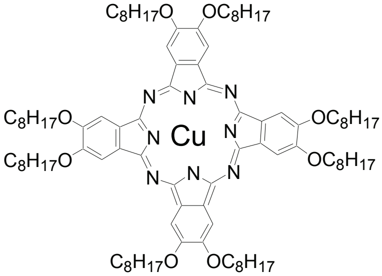

$C_{96}H_{144}CuN_8O_8$
Mol. Wt.: 1601.77

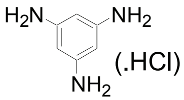

$C_6H_9N_3$
Mol. Wt.: 123.16

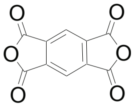

$C_{10}H_2O_6$
Mol. Wt.: 218.12

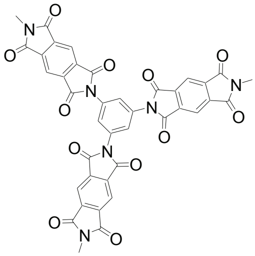

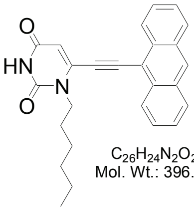

$C_{26}H_{24}N_2O_2$
Mol. Wt.: 396.48

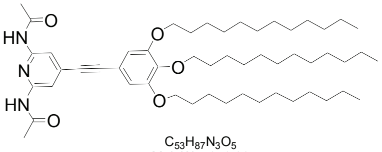

$C_{53}H_{87}N_3O_5$
Mol. Wt.: 846.28

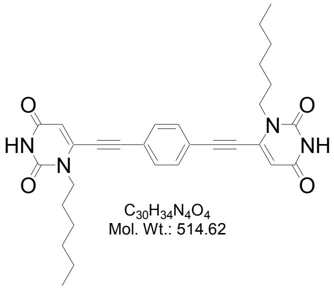

$C_{30}H_{34}N_4O_4$
Mol. Wt.: 514.62

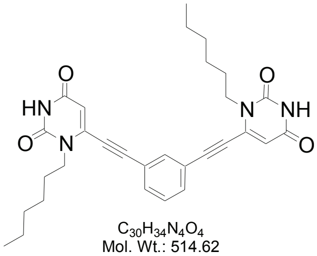

$C_{30}H_{34}N_4O_4$
Mol. Wt.: 514.62

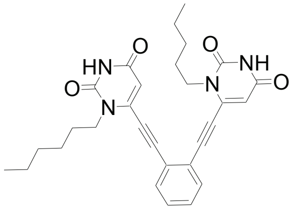

$C_{29}H_{32}N_4O_4$
Mol. Wt.: 500.59

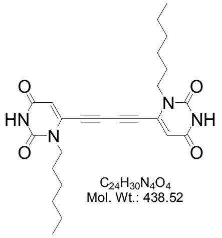

$C_{24}H_{30}N_4O_4$
Mol. Wt.: 438.52

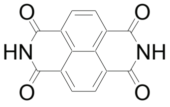

$C_{14}H_6N_2O_4$
Mol. Wt.: 266.21

Index of Molecules

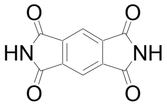

$C_{10}H_4N_2O_4$
Mol. Wt.: 216.15

Molecule 12 73

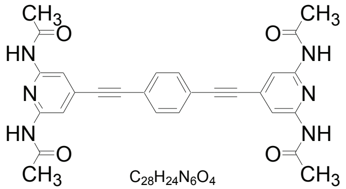

$C_{28}H_{24}N_6O_4$
Mol. Wt.: 508.53

Molecule 13 73

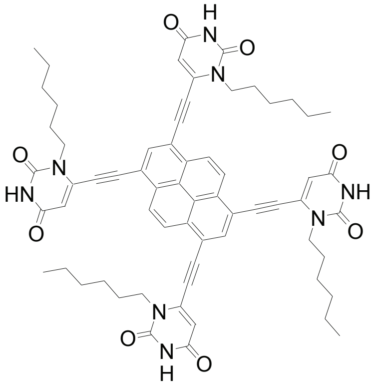

$C_{64}H_{66}N_8O_8$
Mol. Wt.: 1075.26

Molecule 14 81

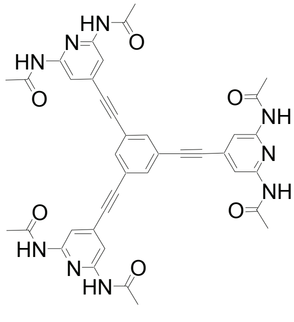

$C_{39}H_{33}N_9O_6$
Mol. Wt.: 723.74

Molecule 15 81

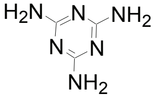

$C_3H_6N_6$
Mol. Wt.: 126.12

Molecule 16................................81

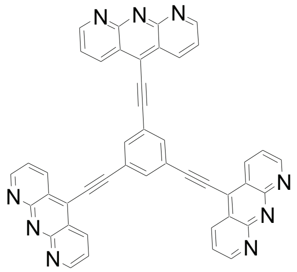

$C_{45}H_{21}N_9$
Mol. Wt.: 687.71

Molecule 17.............................. 134

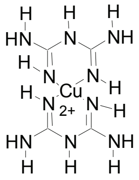

$C_4H_{14}Cl_2CuN_{10}$
Mol. Wt.: 336.67

Molecule 18.............................. 134

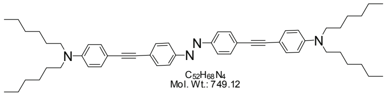

$C_{52}H_{68}N_4$
Mol. Wt.: 749.12

Molecule 19.............................. 138

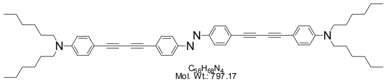

$C_{56}H_{68}N_4$
Mol. Wt.: 797.17

Molecule 20.............................. 138

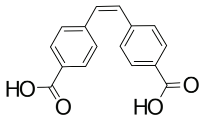

$C_{16}H_{12}O_4$
Mol. Wt.: 268.26

Molecule 21.............................. 138

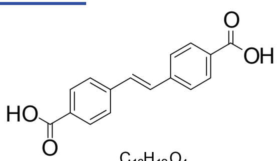

$C_{16}H_{12}O_4$
Mol. Wt.: 268.26

Molecule 22.............................. 138

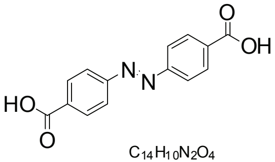

$C_{14}H_{10}N_2O_4$
Mol. Wt.: 270.24

Molecule 23 138

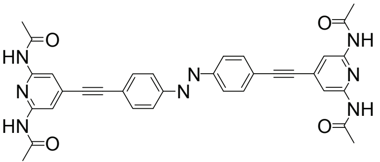

$C_{34}H_{28}N_8O_4$
Mol. Wt.: 612.64

Molecule 24 144

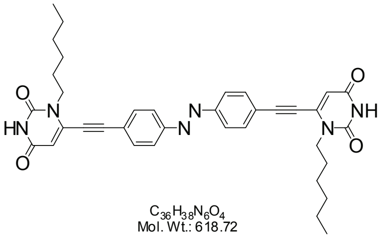

$C_{36}H_{38}N_6O_4$
Mol. Wt.: 618.72

Molecule 25 144

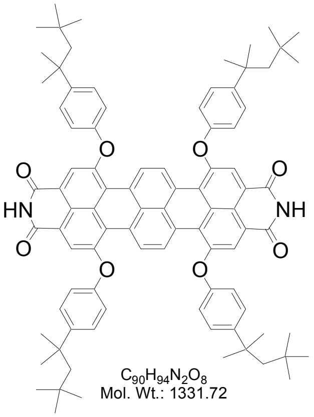

$C_{90}H_{94}N_2O_8$
Mol. Wt.: 1331.72

Molecule 26 146

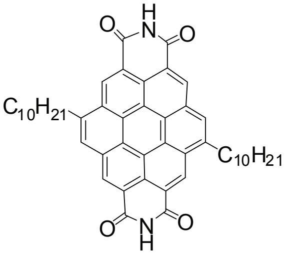

$C_{48}H_{50}N_2O_4$
Mol. Wt.: 718.92

Molecule 27..............................146

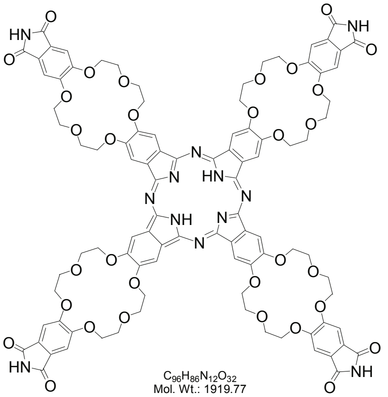

$C_{96}H_{86}N_{12}O_{32}$
Mol. Wt.: 1919.77

Molecule 28..............................152

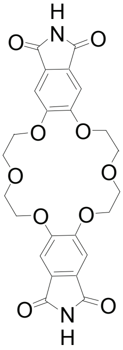

$C_{24}H_{22}N_2O_{10}$
Mol. Wt.: 498.44

Molecule 29..............................152

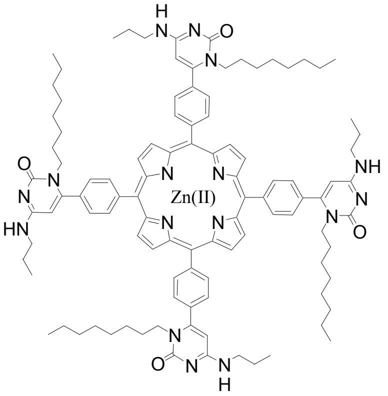

$C_{104}H_{128}N_{16}O_4Zn$
Mol. Wt.: 1731.62

Molecule 30..............................154

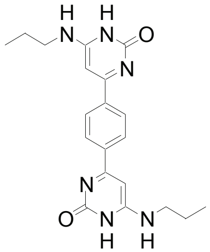

$C_{20}H_{24}N_6O_2$
Mol. Wt.: 380.44

9 References

Adisoejoso, J., K. Tahara, et al. (2009). "Two-Dimensional Crystal Engineering: A Four-Component Architecture at a Liquid-Solid Interface." Angew. Chem. Int. Ed **48**: 7353 –7357

Arduini, M., M. Crego-Calama, et al. (2003). "Novel type of hydrogen-bonded assemblies based on the melamine-cyanuric acid motif." Journal of Organic Chemistry **68**(3): 1097-1106.

Arico, A. S., P. Bruce, et al. (2005). "Nanostructured materials for advanced energy conversion and storage devices." Nat. Mater. **4**(5): 366-377.

Aviram, A. and M. A. Ratner (1974). "Molecular rectifiers." Chem. Phys. Lett. **29**(2): 277-283.

Baisch, B., D. Raffa, et al. (2009). "Mounting Freestanding Molecular Functions onto Surfaces: The Platform Approach." J. Am. Chem. Soc. **131**(2): 442-443.

Baker, R. T., J. D. Mougous, et al. (1999). "Competitive Adsorption, Phase Segregation, and Molecular Motion at a Solid−Liquid Interface Studied by Scanning Tunneling Microscopy." Langmuir **15**(14): 4884-4891.

Balaban, T. S. (2005). "Tailoring Porphyrins and Chlorins for Self-Assembly in Biomimetic Artificial Antenna Systems." Acc. Chem. Res. **38**(8): 612-623.

Barboiu, M. and J. M. Lehn (2002). "Dynamic chemical devices: Modulation of contraction/extension molecular motion by coupled-ion binding/pH change-induced structural switching." PNAS **99**(8): 5201-5206.

Bard, A. J. and L. R. Faulkner (2001). Electrochemical Methods, John Wiley & Sons

Barth, J. V. (2007). "Molecular Architectonic on Metal Surfaces." Annu. Rev. Phys. Chem. **58**(1): 375-407.

Barth, J. V. (2007). "Molecular architectonic on metal surfaces." Annu. Rev. Phys. Chem. **58**: 375-407.

Bernstein, J. (2002). Polymorphism in Molecular Crystals, Oxford University Press, USA.

Bernstein, J. (2005). "...And another comment on Pseudopolymorphism." Cryst. Growth Des. **5**(5): 1661-1662.

Binnig, G., H. Rohrer, et al. (1982). "Tunneling through a controllable vacuum gap." Appl. Phys. Lett. **40**(2): 178-180.

Bjork, J., F. Hanke, et al. (2010). "Adsorption of Polyaromatics in Graphene." (in preparation).

Bleger, D., D. Kreher, et al. (2008). "Periodic Positioning of Multilayered [2.2]Paracyclophane-Based Nanopillars." Angew. Chem. Int. Ed. **47**(44): 8412-8415.

Bleger, D., D. Kreher, et al. (2007). "Surface noncovalent bonding for rational design of hierarchical molecular self-assemblies." Angew. Chem. Int. Ed. **46**(39): 7404-7407.

Blight, B. A., A. Camara-Campos, et al. (2009). "AAA-DDD Triple Hydrogen Bond Complexes." J. Am. Chem. Soc. **131**(39): 14116-14122.

Blüchl, P. E. (1994). "Projector augmented-wave method." Phys. Rev. B **50**(24): 17953-17953.

Blunt, M. O., J. C. Russell, et al. (2008). "Random Tiling and Topological Defects in a Two-Dimensional Molecular Network." Science **322**(5904): 1077-1081.

Blunt, M. O., J. C. Russell, et al. (2008). "Random Tiling and Topological Defects in a Two-Dimensional Molecular Network." Science **322**(5904): 1077-1081.

Bonifazi, D., S. Mohnani, et al. (2009). "Supramolecular Chemistry at Interfaces: Molecular Recognition on Nanopatterned Porous Surfaces." Chem. Eur. J. **15**(29): 7004-7025.

Bonini, M., L. Zalewski, et al. (2009). "Competitive physisorption among alkyl substituted p-conjugated oligomers at the solid-liquid interface: towards prediction of self-assembly at surfaces from a multicomponent solution." Small doi: 10.1002/smll.200801901.

Braga, D., F. Grepioni, et al. (1998). "Crystal Engineering and Organometallic Architecture." Chem. Rev. **98**(4): 1375-1406.

Bransden, B. H. and C. J. Joachain (2000). Quantum Mechanics, Pearson Education.

Brooks, B. R., C. L. Brooks, et al. (2009). "CHARMM: The Biomolecular Simulation Program." J. Comp. Chem. **30**(10): 1545-1614.

Brooks, B. R., R. E. Bruccoleri, et al. (1983). "Charmm - a Program for Macromolecular Energy, Minimization, and Dynamics Calculations." J. Comp. Chem. **4**(2): 187-217.

Brunsveld, L., B. J. B. Folmer, et al. (2001). "Supramolecular polymers." Chem. Rev. **101**(12): 4071-4097.

Bullock, J. E., M. T. Vagnini, et al. (2010). "Photophysics and Redox Properties of Rylene Imide and Diimide Dyes Alkylated Ortho to the Imide Groups." J. Phys. Chem. B **114**(5): 1794-1802.

Campbell, J. (1973). Grammatical Man, Simon & Schuster

Cecchini, M., S. V. Krivov, et al. (2009). "Calculation of Free-Energy Differences by Confinement Simulations. Application to Peptide Conformers." J. Phys. Chem. B **113**(29): 9728-9740.

Cheng, Y. J., S. H. Yang, et al. (2009). "Synthesis of Conjugated Polymers for Organic Solar Cell Applications." Chemical Reviews **109**(11): 5868-5923.

Chiad, K., S. H. Stelzig, et al. (2009). "Isothermal Titration Calorimetry: A Powerful Technique To Quantify Interactions in Polymer Hybrid Systems." Macromolecules **42**(19): 7545-7552.

Chiang, C. K., C. R. Fincher, et al. (1977). "Electrical Conductivity in Doped Polyacetylene." Phys. Rev. Lett. **39**(17): 1098-1098.

Chung, S.-Y., Y.-M. Kim, et al. (2008). "Multiphase transformation and Ostwald/'s rule of stages during crystallization of a metal phosphate." Nat. Phys. **5**: 68-73.

Ciesielski, A., S. Lena, et al. (2010). "Dynamers at the Solid-Liquid Interface: Controlling the Reversible Assembly/Reassembly Process between Two Highly Ordered Supramolecular Guanine Motifs." Angew. Chem. Int. Ed. **49**(11): 1963-1966.

Ciesielski, A., L. Piot, et al. (2009). "Molecular Tectonics at the Solid/Liquid Interface: Controlling the Nanoscale Geometry, Directionality, and Packing of 1D Coordination Networks on Graphite Surfaces." Adv. Mater. **21**(10-11): 1131-1136.

Ciesielski, A., G. Schaeffer, et al. (2009). "STM Insight into Hydrogen-Bonded Bicomponent 1D Supramolecular Polymers with Controlled Geometries at the Liquid-Solid Interface." Angew. Chem. Int. Ed. **48**(11): 2039-2043.

Cisternas, E., F. Stavale, et al. (2009). "First-principles calculation and scanning tunneling microscopy study of highly oriented pyrolytic graphite (0001)." Phys. Rev. B **79**(20): -.

Cyr, D. M., B. Venkataraman, et al. (1996). "STM Investigations of Organic Molecules Physisorbed at the Liquid−Solid Interface." Chem. Mater. **8**(8): 1600-1615.

Datta, S., W. D. Tian, et al. (1997). "Current-voltage characteristics of self-assembled monolayers by scanning tunneling microscopy." Phys. Rev. Letters **79**(13): 2530-2533.

Dawes, S. B., D. L. Ward, et al. (1986). "1st Electride Crystal-Structure." J. Am. Chem. Soc. **108**(12): 3534-3535.

De Gennes, P. G. and J. Prost (1993). The Physics of Liquid Crystals. Paris, Oxford Science Publication.

Decher, G. (1997). "Fuzzy Nanoassemblies: Toward Layered Polymeric Multicomposites." Science **277**(5330): 1232-1237.

Desiraju, G. R. (1989). Crystal Engineering. The Design of Organic Solids. Amsterdam, Elsevier.

Desiraju, G. R. (1995). "Supramolecular Synthons in Crystal Engineering - A New Organic Synthesis." Angew. Chem. Int. Ed. **34**: 2311-2327.

Desiraju, G. R. (2008). "Polymorphism: The Same and Not Quite the Same." Cryst. Growth Des. **8**(1): 3-5.

Desiraju, G. R. and T. Steiner (1999). The Weak Hydrogen Bond, Oxford Science Publications.

Dion, M., H. Rydberg, et al. (2004). "Van der Waals density functional for general geometries." Phys. Rev. Letters **92**(24): -.

Djurdjevic, S., D. A. Leigh, et al. (2007). "Extremely strong and readily accessible AAA-DDD triple hydrogen bond complexes." J. Am. Chem. Soc. **129**(3): 476-477.

Dorogi, M., J. Gomez, et al. (1995). "Room-temperature Coulomb blockade from a self-assembled molecular nanostructure." Phys. Rev. B **52**(12): 9071-9071.

Elemans, J. A. A. W. and S. De Feyter (2009). "Structure and function revealed with submolecular resolution at the liquid-solid interface." Soft Matter **5**(4): 721-735.

Elemans, J. A. A. W., S. B. Lei, et al. (2009). "Molecular and Supramolecular Networks on Surfaces: From Two-Dimensional Crystal Engineering to Reactivity." Angew. Chem. Int. Ed. **48**(40): 7298-7332.

Fan, E., C. Vicent, et al. (1994). "Molecular Recognition in the Solid-State - Hydrogen-Bonding Control of Molecular Aggregation." Chem. Mater. **6**(8): 1113-1117.

Fan, F. R. F., J. P. Yang, et al. (2002). "Charge transport through self-assembled monolayers of compounds of interest in molecular electronics." J. Am. Chem. Soc. **124**(19): 5550-5560.

Feibush, B., A. Figueroa, et al. (1986). "Chiral Separation of Heterocyclic Drugs by Hplc - Solute Stationary Phase Base-Pair Interactions." J. Am. Chem. Soc. **108**(12): 3310-3318.

Feng, X., V. Marcon, et al. (2009). "Towards high charge-carrier mobilities by rational design of the shape and periphery of discotics." Nat. Mater. **8**(5): 421-426.

Feng, X., W. Pisula, et al. (2009). "Controlled Self-Assembly of C3-Symmetric Hexa-peri-hexabenzocoronenes with Alternating Hydrophilic and Hydrophobic Substituents in Solution, in the Bulk, and on a Surface." J. Am. Chem. Soc. **131**(12): 4439-4448.

Ferrari, A. C., J. C. Meyer, et al. (2006). "Raman spectrum of graphene and graphene layers." Phys. Rev. Letters **97**(18): -.

Fouquey, C., J.-M. Lehn, et al. (1990). "Molecular recognition directed self-assembly of supramolecular liquid crystalline polymers from complementary chiral components." Adv. Mater. **2**(5): 254-257.

Fowler, R. H. and L. Nordheim (1928). "Electron emission in intense electric fields." Proceedings of the Royal Society of London. Series A, Containing Papers of a Mathematical and Physical Character **119**(781): 173-181.

Frenkel, D. and B. Smit (2002). Understanding Molecular Simulation, Academic Press.

Fujita, M., D. Oguro, et al. (1995). "Self-Assembly of 10 Molecules into Nanometer-Sized Organic Host Frameworks." Nature **378**(6556): 469-471.

Garrahan, J. P., A. Stannard, et al. (2009). "Molecular random tilings as glasses." PNAS **106**(36): 15209-15213.

Geim, A. K. and K. S. Novoselov (2007). "The rise of graphene." Nat Mater **6**(3): 183-191.

Gellman, A. J. and K. R. Paserba (2002). "Kinetics and Mechanism of Oligomer Desorption from Surfaces: n-Alkanes on Graphite." J. Phys. Chem. B **106**(51): 13231-13241.

Gesquiere, A., P. Jonkheijm, et al. (2004). "2D-Structures of quadruple hydrogen bonded oligo(p-phenylenevinylene)s on graphite: Self-assembly behavior and expression of chirality." Nano Lett. **4**(7): 1175-1179.

Glendening, E. D., D. Feller, et al. (1994). "An Ab-Initio Investigation of the Structure and Alkali-Metal Cation Selectivity of 18-Crown-6." J. Am. Chem. Soc. **116**(23): 10657-10669.

Gomez-Segura, J., I. Diez-Perez, et al. (2006). "2-D Self-assembly of the bis(phthalocyaninato)terbium(iii) single-molecule magnet studied by scanning tunnelling microscopy." Chem. Commun.(27): 2866-2868.

Greef, T. F. A. and E. W. Meijer (2008). "Materials science - Supramolecular polymers." Nature **453**(7192): 171-173.

Grimme, S. (2004). "Accurate description of van der Waals complexes by density functional theory including empirical corrections." J. Comp. Chem. **25**(12): 1463-1473.

Grimme, S. (2008). "Do Special Noncovalent pi-pi Stacking Interactions Really Exist?13." Angew. Chem. Int. Ed. **47**(18): 3430-3434.

Grobis, M., K. H. Khoo, et al. (2005). "Spatially dependent inelastic tunneling in a single metallofullerene." Phys. Rev. Letters **94**(13): -.

Grobis, M., A. Wachowiak, et al. (2005). "Tuning negative differential resistance in a molecular film." Applied Physics Letters **86**(20): -.

Gulans, A., M. J. Puska, et al. (2009). "Linear-scaling self-consistent implementation of the van der Waals density functional." Phys. Rev. B **79**(20): -.

Halgren, T. A. (1996). "Merck molecular force field .1. Basis, form, scope, parameterization, and performance of MMFF94." J. Comp. Chem. **17**(5-6): 490-519.

Halgren, T. A. (1999). "MMFF VII. Characterization of MMFF94, MMFF94s, and other widely available force fields for conformational energies and for intermolecular-interaction energies and geometries." J. Comp. Chem. **20**(7): 730-748.

Hamadani, B. H., D. A. Corley, et al. (2006). "Controlling Charge Injection in Organic Field-Effect Transistors Using Self-Assembled Monolayers." Nano Lett. **6**(6): 1303-1306.

Hamilton, A. D. and D. Vanengen (1987). "Induced Fit in Synthetic Receptors - Nucleotide Base Recognition by a Molecular Hinge." J. Am. Chem. Soc. **109**(16): 5035-5036.

Hernandez, Y., V. Nicolosi, et al. (2008). "High-yield production of graphene by liquid-phase exfoliation of graphite." Nature Nanotechnology **3**(9): 563-568.

Herrmann, A. and K. Mullen (2006). "From industrial colorants to single photon sources and biolabels: The fascination and function of rylene dyes." Chemistry Letters **35**(9): 978-985.

Hipps, K. W. and L. Scudiero (2005). "Electron tunneling, a quantum probe for the quantum world of nanotechnology." J. Chem. Educ. **82**(5): 704-704.

Hipps, K. W. and D. R. Vij (2006). Handbook of Applied Solid State Spectroscopy, Springer-Verlag.

Hosseini, M. W. (2005). "Molecular Tectonics: From Simple Tectons to Complex Molecular Networks." Acc. Chem. Res. **38**(4): 313-323.

Hunter, C. A., K. R. Lawson, et al. (2001). "Aromatic interactions." Journal of the Chemical Society-Perkin Transactions 2(5): 651-669.

Hyde, S., K. Larsson, et al. (1996). The Language of Shape, Elsevier B.V.

Iijima, S. (1991). "Helical microtubules of graphitic carbon." Nature **354**(6348): 56-58.

Ilan, B., G. M. Florio, et al. (2008). "Scanning Tunneling Microscopy Images of Alkane Derivatives on Graphite: Role of Electronic Effects." Nano Lett. **8**(10): 3160-3165.

Israelachvili, J. (1992). Intermolecular & Surface Forces. London, Academic Press.

Itaya, K. (1998). "In situ scanning tunneling microscopy in electrolyte solutions." Prog. Surf. Sci. **58**(3): 121-247.

Ito, S., M. Wehmeier, et al. (2000). "Synthesis and Self-Assembly of Functionalized Hexa-peri-hexabenzocoronenes." Chem. Eur. J. **6**(23): 4327-4342.

Jäckel, F., U. G. E. Perera, et al. (2008). "Investigating Molecular Charge Transfer Complexes with a Low Temperature Scanning Tunneling Microscope." Phys. Rev. Lett. **100**(12): 126102-4.

Jäckel, F., Z. Wang, et al. (2004). "Nanoscale array of inversely biased molecular rectifiers." Chem. Phys. Lett. **387**(4-6): 372-376.

Jackel, F., M. D. Watson, et al. (2006). "Tunneling through nanographene stacks." Phys. Rev. B **73**(4): 1-6.

Jäckel, F., M. D. Watson, et al. (2004). "Prototypical Single-Molecule Chemical-Field-Effect Transistor with Nanometer-Sized Gates." Phys. Rev. Lett. **92**(18): 188303-188303.

Jeffrey, G. A. (1997). An Introduction to Hydrogen Bonding, Oxford University Press.

Jelesarov, I. and H. R. Bosshard (1999). "Isothermal titration calorimetry and differential scanning calorimetry as complementary tools to investigate the energetics of biomolecular recognition." Journal of Molecular Recognition **12**(1): 3-18.

Joachim, C., J. K. Gimzewski, et al. (2000). "Electronics using hybrid-molecular and mono-molecular devices." Nature **408**(6812): 541-548.

Joachim, C., J. K. Gimzewski, et al. (1998). "Physical principles of the single-C60 transistor effect." Phys. Rev. B **58**(24): 16407-16407.

Joachim, C. and M. A. Ratner (2005). "Molecular electronics: Some views on transport junctions and beyond." PNAS **102**(25): 8801-8808.

Johnson, E. R. and A. D. Becke (2005). "A post-Hartree-Fock model of intermolecular interactions." Journal of Chemical Physics **123**(2): -.

Kampschulte, L., M. Lackinger, et al. (2006). "Solvent induced polymorphism in supramolecular 1,3,5-benzenetribenzoic acid monolayers." J. Phys. Chem. B **110**(22): 10829-10836.

Kampschulte, L., T. L. Werblowsky, et al. (2008). "Thermodynamical equilibrium of binary supramolecular networks at the liquid-solid interface." J. Am. Chem. Soc. **130**(26): 8502-8507.

Karplus, M. and R. Porter (1970). Atoms and Molecules, W.A. Benjamin.

Kastler, M., W. Pisula, et al. (2005). "Influence of alkyl substituents on the solution- and surface-organization of hexa-peri-hexabenzocoronenes." J. Am. Chem. Soc. **127**(12): 4286-4296.

Keeling, D. L., N. S. Oxtoby, et al. (2003). "Assembly and Processing of Hydrogen Bond Induced Supramolecular Nanostructures." Nano Lett. **3**(1): 9-12.

Kim, K., K. E. Plass, et al. (2005). "Structure of and Competitive Adsorption in Alkyl Dicarbamate Two-Dimensional Crystals." J. Am. Chem. Soc. **127**(13): 4879-4887.

Kirkwood, J. G. (1935). "Statistical mechanics of fluid mixtures." The Journal of Chemical Physics **3**: 300-300.

Kittel, C. (1996). Introduction to Solid State Physics, John Wiley & Sons.

Klymchenko, A. S., J. Sleven, et al. (2006). "Two-Dimensional Self-Assembly and Phase Behavior of an Alkoxylated Sandwich-Type Bisphthalocyanine and Its Phthalocyanine Analogues at the Liquid−Solid Interface." Langmuir **22**(2): 723-728.

Kohn, W. and L. J. Sham (1965). "Self-consistent equations including exchange and correlation effects." Phys Rev A **140**: 133-1138.

Kresse, G. and J. Furthmüller (1996). "Efficient iterative schemes for ab initio total-energy calculations using a plane-wave basis set." Phys. Rev. B **54**(16): 11169-11169.

Kresse, G. and D. Joubert (1999). "From ultrasoft pseudopotentials to the projector augmented-wave method." Phys. Rev. B **59**(3): 1758-1758.

Kunz, H. (2002). "Emil Fischer-Unequalled Classicist, Master of Organic Chemistry Research, and Inspired Trailblazer of Biological Chemistry." Angew. Chem. Int. Ed. **41**(23): 4439-4451.

Lackinger, M., S. Griessl, et al. (2004). "Self-assembly of benzene-dicarboxylic acid isomers at the liquid solid interface: Steric aspects of hydrogen bonding." J. Phys. Chem. B **108**(36): 13652-13655.

Lackinger, M. and W. M. Heckl (2009). "Carboxylic Acids: Versatile Building Blocks and Mediators for Two-Dimensional Supramolecular Self-Assembly." Langmuir **25**(19): 11307-11321.

Lang, N. D. (1986). "Spectroscopy of Single Atoms in the Scanning Tunneling Microscope." Phys. Rev. B **34**(8): 5947-5950.

Langevin, P. (1908). "Sur la théorie du mouvement brownien." Comptes-Rendus de l'Académie des Sciences **146**: 530-532.

Langreth, D. C., M. Dion, et al. (2005). "Van der Waals density functional theory with applications." International Journal of Quantum Chemistry **101**(5): 599-610.

Lazzaroni, R., A. Calderone, et al. (1997). "Electronic structure of molecular van der Waals complexes with benzene: Implications for the contrast in scanning tunneling microscopy of molecular adsorbates on graphite." J. Chem. Phys. **107**(1): 99-105.

Lehn, J.-M. (1990). "Perspectives in Supramolecular Chemistry - From Molecular Recognition towards Molecular Information Processing and Self-Organization." Angew. Chem. Int. Ed. **29**(11): 1304-1319.

Lehn, J.-M. (1995). Supramolecular chemistry: concepts and perspectives, VCH New York.

Lehn, J. M. (2002). "Toward self-organization and complex matter." Science **295**(5564): 2400-2403.

Lei, S., M. Surin, et al. (2008). "Programmable Hierarchical Three-Component 2D Assembly at a Liquid−Solid Interface: Recognition, Selection, and Transformation." Nano Lett. **8**(8): 2541-2546.

Lei, S., K. Tahara, et al. (2008). "One Building Block, Two Different Supramolecular Surface-Confined Patterns: Concentration in Control at the Solid-Liquid Interface13." Angew. Chem. **120**(16): 3006-3010.

Lei, S., K. Tahara, et al. (2008). "Molecular Clusters in Two-Dimensional Surface-Confined Nanoporous Molecular Networks: Structure, Rigidity, and Dynamics." J. Am. Chem. Soc. **130**(22): 7119-7129.

Lei, S. B., C. Wang, et al. (2004). "Site selective adsorption and templated assembling: Effects of organic-organic heterogeneous interface studied by scanning tunneling microscopy." J. Phys. Chem. B **108**(4): 1173-1175.

Leininger, S., B. Olenyuk, et al. (2000). "Self-Assembly of Discrete Cyclic Nanostructures Mediated by Transition Metals." Chemical Reviews **100**(3): 853-907.

Lewis, G. N. (1916). "THE ATOM AND THE MOLECULE." J. Am. Chem. Soc. **38**(4): 762-785.

Liscio, A., G. De Luca, et al. (2008). "Photovoltaic Charge Generation Visualized at the Nanoscale: A Proof of Principle." J. Am. Chem. Soc. **130**(3): 780-781.

Llanes-Pallas, A., M. Matena, et al. (2008). "Trimodular engineering of linear supramolecular miniatures on Ag(111) surfaces controlled by complementary triple hydrogen bonds." Angew. Chem. Int. Ed. **47**(40): 7726-7730.

Llanes-Pallas, A., C. A. Palma, et al. (2009). "Engineering of Supramolecular H-Bonded Nanopolygons via Self-Assembly of Programmed Molecular Modules." J. Am. Chem. Soc. **131**(2): 509-520.

Lukin, O. and J. Leszczynski (2002). "Rationalizing the strength of hydrogen-bonded complexes. Ab initio HF and DFT studies." J. Phys. Chem. A **106**(29): 6775-6782.

Ma, Z., Y.-Y. Wang, et al. (2007). "Star-Shaped Oligofluorenes End-Capped with Carboxylic Groups: Syntheses and Self-Assembly at the Liquid–Solid Interface." ACS Nano **1**(3): 160-167.

Macdonald, J. C. and G. M. Whitesides (1994). "Solid-State Structures of Hydrogen-Bonded Tapes Based on Cyclic Secondary Diamides." Chem. Rev. **94**(8): 2383-2420.

Mackerell, A. D., J. Wiorkiewiczkuczera, et al. (1995). "An All-Atom Empirical Energy Function for the Simulation of Nucleic-Acids." J. Am. Chem. Soc. **117**(48): 11946-11975.

MacLeod, J. M., O. Ivasenko, et al. (2007). "Stabilization of exotic minority phases in a multicomponent self-assembled molecular network." Nanotechnology **18**(42): -.

Madueno, R., M. T. Raisanen, et al. (2008). "Functionalizing hydrogen-bonded surface networks with self-assembled monolayers." Nature **454**(7204): 618-621.

Mammen, M., E. I. Shakhnovich, et al. (1998). "Estimating the entropic cost of self-assembly of multiparticle hydrogen-bonded aggregates based on the cyanuric acid center dot melamine lattice." Journal of Organic Chemistry **63**(12): 3821-3830.

Mann, S. (2009). "Self-assembly and transformation of hybrid nano-objects and nanostructures under equilibrium and non-equilibrium conditions." Nat. Mater. **8**: 781 - 792.

Margenau, H. (1939). "Van der Waals Forces." Rev. Mod. Phys.(11): 1-35.

Matena, M., A. Llanes-Pallas, et al. (2009). "Conformation-controlled networking of H-bonded assemblies on surfaces." Chemical Communications(24): 3525-3527.

Mativetsky, J. M., M. Kastler, et al. (2009). "Self-Assembly of a Donor-Acceptor Dyad Across Multiple Length Scales: Functional Architectures for Organic Electronics." Adv. Funct. Mater. **19**(15): 2486-2494.

May, V. and O. Kühn (2004). Charge and Energy Transfer Dynamics in Molecular Systems, Wiley-VCH.

Mccammon, J. A., B. R. Gelin, et al. (1977). "Dynamics of Folded Proteins." Nature **267**(5612): 585-590.

McGonigal, G. C., R. H. Bernhardt, et al. (1990). "Imaging alkane layers at the liquid/graphite interface with the scanning tunneling microscope." Appl. Phys. Lett. **57**: 28.

McQuarrie, D. A. (1997). Physical Chemistry, University Science Books.

Meirovitch, H. (2007). "Recent developments in methodologies for calculating the entropy and free energy of biological systems by computer simulation." Curr. Opin. Struct. Biol. **17**(2): 181-186.

Mena-Osteritz, E. and P. Bäuerle (2006). "Complexation of C60 on a Cyclothiophene Monolayer Template." Adv. Mater. **18**(4): 447-451.

Merzbacher, E. (2002). "The early history of quantum tunneling." Physics Today **55**(8): 44-49.

Metzger, R. M. (2008). "Unimolecular electronics." J. Mater. Chem. **18**(37): 4364-4396.

Meyer, E. A., R. K. Castellano, et al. (2003). "Interactions with aromatic rings in chemical and biological recognition." Angew. Chem. Int. Ed. **42**(11): 1210-1250.

Microcal. (2010). "http://www.microcal.com/products/itc/default.asp."

Millikan, R. A. and C. F. Eyring (1926). "Laws governing the pulling of electrons our of metals by intense electrical fields." Phys. Rev. **27**: 51-67.

Mostad, A. and C. Rømming (1971). "A refinement of the crystal structure of cis-azobenzene." Acta Chemica Scandinavica **25**: 3561-3568.

Mujica, V., M. Kemp, et al. (1996). "Current-voltage characteristics of molecular wires: Eigenvalue staircase, Coulomb blockade, and rectification." J. Chem. Phys. **104**(18): 7296-7305.

Mura, M., N. Martsinovich, et al. (2008). "Theoretical study of melamine superstructures and their interaction with the Au(111) surface." Nanotechnology **19**(46): -.

Mura, M., N. Martsinovich, et al. (2008). "Theoretical study of melamine superstructures and their interaction with the Au(111) surface." Nanotechnology **19**(46): 465704-465704.

Murray, T. J. and S. C. Zimmerman (1992). "New Triply Hydrogen-Bonded Complexes with Highly Variable Stabilities." J. Am. Chem. Soc. **114**(10): 4010-4011.

Nicol, J., S. Shapiro, et al. (1960). "Direct Measurement of the Superconducting Energy Gap." Phys. Rev. Letters **5**(10): 461-461.

Ortmann, F., F. Bechstedt, et al. (2006). "Semiempirical van der Waals correction to the density functional description of solids and molecular structures." Phys. Rev. B **73**(20): -.

Ostwald, W. Z. (1897). "Studies on formation and transformation of solid materials." Z. Phys. Chem **22**: 289-330.

Otero, R., M. Lukas, et al. (2008). "Elementary structural motifs in a random network of cytosine adsorbed on a gold(111) surface." Science **319**(5861): 312-315.

Pakarinen, O. H., J. M. Mativetsky, et al. (2009). "Role of van der Waals forces in the adsorption and diffusion of organic molecules on an insulating surface." Phys. Rev. B **80**(8): -.

Palermo, V. and P. Samorì (2007). "Molecular self-assembly across multiple length scales." Angew. Chem. Int. Ed. **46**(24): 4428-4432.

Palma, C.-A., M. Bonini, et al. (2009). "Supramolecular Crystal Engineering at the Solid-Liquid Interface from First Principles: Toward Unraveling the Thermodynamics of 2D Self-Assembly." Adv. Mater. **21**(13): 1383-1386.

Palma, C. A., J. Bjork, et al. (2009). "Tailoring Bicomponent Supramolecular Nanoporous Networks: Phase Segregation, Polymorphism, and Glasses at the Solid−Liquid Interface." J. Am. Chem. Soc. **131**(36): 13062-13071.

Palma, C. A., M. Bonini, et al. (2008). "Pre-programmed bicomponent porous networks at the solid-liquid interface: the low concentration regime." Chem. Commun.(42): 5289-5291.

Palmer, L. C., Y. S. Velichko, et al. (2007). "Supramolecular self-assembly codes for functional structures." Philosophical Transactions of the Royal Society A: Mathematical, Physical and Engineering Sciences **365**(1855): 1417-1433.

Pan, G.-B., X.-H. Cheng, et al. (2006). "2D Supramolecular Structures of a Shape-Persistent Macrocycle and Co-deposition with Fullerene on HOPG." J. Am. Chem. Soc. **128**(13): 4218-4219.

Pascual, J. I., J. Gomez-Herrero, et al. (2000). "Seeing molecular orbitals." Chemical Physics Letters **321**(1-2): 78-82.

Perdew, J. P., J. A. Chevary, et al. (1992). "Atoms, molecules, solids, and surfaces: Applications of the generalized gradient approximation for exchange and correlation." Phys. Rev. B **46**(11): 6671-6671.

Perdigao, L. M. A., G. N. Fontes, et al. (2007). "Coadsorbed NTCDI-melamine mixed phases on Ag-Si(111)." Phys. Rev. B **76**(24): 245402-6.

Perdigao, L. M. A., E. W. Perkins, et al. (2006). "Bimolecular networks and supramolecular traps on Au(111)." J. Phys. Chem. B **110**(25): 12539-12542.

Perronet, K. and F. Charra (2004). "Influence of molecular–substrate interaction on the self-assembly of discotic liquid crystals." Surface Science **551**(3): 213-218.

Piot, L., D. Bonifazi, et al. (2007). "Organic reactivity in confined spaces under scanning tunneling microscopy control: Tailoring the nanoscale world." Adv. Funct. Mater. **17**(18): 3689-3693.

Piot, L., A. Marchenko, et al. (2005). "Structural Evolution of Hexa-peri-hexabenzocoronene Adlayers in Heteroepitaxy on n-Pentacontane Template Monolayers." J. Am. Chem. Soc. **127**(46): 16245-16250.

Piot, L., C.-A. Palma, et al. (2009). "Selective Formation of Bi-Component Arrays Through H-Bonding of Multivalent Molecular Modules." Adv. Funct. Mater. **19**(8): 1207-1214.

Plass, K. E., K. Kim, et al. (2004). "Two-Dimensional Crystallization: Self-Assembly, Pseudopolymorphism, and Symmetry-Independent Molecules." J. Am. Chem. Soc. **126**(29): 9042-9053.

Qiu, X., C. Wang, et al. (2000). "Alkane-Assisted Adsorption and Assembly of Phthalocyanines and Porphyrins." J. Am. Chem. Soc. **122**(23): 5550-5556.

Rabe, J. P. and S. Buchholz (1991). "Commensurability and Mobility in Two-Dimensional Molecular Patterns on Graphite." Science **253**(5018): 424-427.

Raff, L. M. (2001). Physical Chemistry, Prentice Hall.

Reed, M. A., C. Zhou, et al. (1997). "Conductance of a Molecular Junction." Science **278**(5336): 252-254.

Rothemund, P. W. K. (2006). "Folding DNA to create nanoscale shapes and patterns." Nature **440**(7082): 297-302.

Ryckaert, J. P., G. Ciccotti, et al. (1977). "Numerical-Integration of Cartesian Equations of Motion of a System with Constraints - Molecular-Dynamics of N-Alkanes." Journal of Computational Physics **23**(3): 327-341.

Rydberg, H., M. Dion, et al. (2003). "Van der Waals density functional for layered structures." Phys. Rev. Letters **91**(12): -.

Samorì, P., A. Fechtenkötter, et al. (2001). "Supramolecular Staircase via Self-Assembly of Disklike Molecules at the Solid−Liquid Interface." J. Am. Chem. Soc. **123**(46): 11462-11467.

Samorì, P. and J. P. Rabe (2002). "Scanning probe microscopy explorations on conjugated (macro)molecular architectures for molecular electronics." J. Phys. Condens. Matter **14**(42): 9955-9973.

Samorì, P., N. Severin, et al. (2002). "Epitaxial Composite Layers of Electron Donors and Acceptors from Very Large Polycyclic Aromatic Hydrocarbons." J. Am. Chem. Soc. **124**(32): 9454-9457.

Samorì, P., C. D. Simpson, et al. (2002). "Ordered monolayers of nanographitic sheets processed from solutions via oxidative cyclodehydrogenation." Langmuir **18**(11): 4183-4185.

Samorì, P., X. M. Yin, et al. (2004). "Self-assembly of electron donor-acceptor dyads into ordered architectures in two and three dimensions: Surface patterning and columnar "double cables"." J. Am. Chem. Soc. **126**(11): 3567-3575.

Schlickum, U., R. Decker, et al. (2007). "Metal-organic honeycomb nanomeshes with tunable cavity size." Nano Letters **7**(12): 3813-3817.

Seeber, M., M. Cecchini, et al. (2007). "Wordom: a program for efficient analysis of molecular dynamics simulations." Bioinformatics **23**(19): 2625-2627.

Seto, C. T. and G. M. Whitesides (1991). "Self-Assembly of a Hydrogen-Bonded 2 + 3 Supramolecular Complex." J. Am. Chem. Soc. **113**(2): 712-713.

Shannon, C. E. and W. Weaver (1963). The Mathematical Theory of Communication, Board of Trustees of the University of Illinois.

Shekhah, O., H. Wang, et al. (2009). "Controlling interpenetration in metal-organic frameworks by liquid-phase epitaxy." Nat Mater **8**(6): 481-484.

Sherrill, C. D., T. Takatani, et al. (2009). "An Assessment of Theoretical Methods for Nonbonded Interactions: Comparison to Complete Basis Set Limit Coupled-Cluster Potential Energy Curves for the Benzene Dimer, the Methane Dimer, Benzene-Methane, and Benzene-H2S." J. Phys. Chem. A **113**(38): 10146-10159.

Sherrington, D. C. and K. A. Taskinen (2001). "Self-assembly in synthetic macromolecular systems via multiple hydrogen bonding interactions." Chem. Soc. Rev. **30**(2): 83-93.

Silly, F., A. Q. Shaw, et al. (2008). "Achiralpin wheel supramolecular network driven by the assembly of PTCDIandmelamine." Chem. Commun.(16): 1907-1909.

Silly, F., A. Q. Shaw, et al. (2008). "Melamine Structures on the Au(111) Surface." J. Phys. Chem. C **112**(30): 11476-11480.

Silly, F., U. K. Weber, et al. (2008). "Deriving molecular bonding from a macromolecular self-assembly using kinetic Monte Carlo simulations." Phys. Rev. B **77**(20): 201408-4.

Smilowitz, L., N. S. Sariciftci, et al. (1993). "Photoexcitation spectroscopy of conducting-polymer–C60 composites: Photoinduced electron transfer." Phys. Rev. B **47**(20): 13835-13835.

Son, Y.-W., M. L. Cohen, et al. (2006). "Half-metallic graphene nanoribbons." Nature **444**(7117): 347-349.

Söntjens, S. H. M., R. P. Sijbesma, et al. (2000). "Stability and lifetime of quadruply hydrogen bonded 2-ureido-4[1H]-pyrimidinone dimers." J. Am. Chem. Soc. **122**(31): 7487-7493.

Stabel, A., P. Herwig, et al. (1995). "Diode-Like Current-Voltage Curves for a Single Molecule-Tunneling Spectroscopy with Submolecular Resolution of an Alkylated, Pericondensed Hexabenzocoronene." Angew. Chem. Int. Ed. **34**(15): 1609-1611.

Staniec, P. A., L. M. A. Perdigão, et al. (2007). "Hierarchical Organisation on a Two-Dimensional Supramolecular Network." ChemPhysChem **8**(15): 2177-2181.

Subramanian, S. and M. J. Zaworotko (1994). "Exploitation of the Hydrogen-Bond - Recent Developments in the Context of Crystal Engineering." Coord. Chem. Rev. **137**: 357-401.

Surin, M. and P. Samorì (2007). "Multicomponent monolayer architectures at the solid-liquid interface: Towards controlled space-confined properties and reactivity of functional building blocks." Small **3**(2): 190-194.

Tahara, K., S. Lei, et al. (2008). "Site-selective guest inclusion in molecular networks of butadiyne-bridged pyridino and benzeno square macrocycles on a surface." J. Am. Chem. Soc. **130**(21): 6666.

Tahara, K., S. Lei, et al. (2008). "Giant molecular spoked wheels in giant voids: two-dimensional molecular self-assembly goes big." Chem. Commun.(33): 3897-3899.

Takami, T., D. P. Arnold, et al. (2006). "Two-Dimensional Crystal Growth and Stacking of Bis(phthalocyaninato) Rare Earth Sandwich Complexes at the 1-Phenyloctane/Graphite Interface." J. Phys. Chem. B **110**(4): 1661-1664.

Taketomi, H., Y. Ueda, et al. (1975). "Studies on Protein Folding, Unfolding and Fluctuations by Computer-Simulation .1. Effect of Specific Amino-Acid Sequence Represented by Specific Inter-Unit Interactions." International Journal of Peptide and Protein Research **7**(6): 445-459.

Tanaka, H., T. Kawasaki, et al. (2010). "Critical-like behaviour of glass-forming liquids." Nature Materials **9**(4): 324-331.

Tchebotareva, N., X. Yin, et al. (2003). "Ordered Architectures of a Soluble Hexa-peri-hexabenzocoronene−Pyrene Dyad: Thermotropic Bulk Properties and Nanoscale Phase Segregation at Surfaces." J. Am. Chem. Soc. **125**(32): 9734-9739.

Tersoff, J. and D. R. Hamann (1983). "Theory and Application for the Scanning Tunneling Microscope." Phys. Rev. Lett. **50**(25): 1998-1998.

Tersoff, J. and D. R. Hamann (1985). "Theory of the scanning tunneling microscope." Phys. Rev. B **31**(2): 805-805.

Theobald, J. A., N. S. Oxtoby, et al. (2003). "Controlling molecular deposition and layer structure with supramolecular surface assemblies." Nature **424**(6952): 1029-1031.

Tidor, B. and M. Karplus (1994). "The Contribution of Vibrational Entropy to Molecular Association - the Dimerization of Insulin." J. Mol. Biol. **238**(3): 405-414.

Tkatchenko, A. and M. Scheffler (2009). "Accurate Molecular Van Der Waals Interactions from Ground-State Electron Density and Free-Atom Reference Data." Phys. Rev. Letters **102**(7): -.

Toda, M., R. Kubo, et al. (1992). Statistical Physics I, Springer-Verlag.

Turnbull, W. B. and A. H. Daranas (2003). "On the value of c: Can low affinity systems be studied by isothermal titration calorimetry?" J. Am. Chem. Soc. **125**(48): 14859-14866.

Tyka, M. D., A. R. Clarke, et al. (2006). "An efficient, path-independent method for free-energy calculations." J. Phys. Chem. B **110**(34): 17212-17220.

van der Waals, J. D. (1920). "The equation of state for gases and liquids." Nobel Lecture.

Varghese, J. N., A. M. Oconnell, et al. (1977). "X-Ray and Neutron Crystal-Structure of 2,4,6-Triamino-1,3,5-Triazine (Melamine)." Acta Crystallographica Section B-Structural Science **33**(Jul15): 2102-2108.

Varghese, N., A. Ghosh, et al. (2009). "Selectivity in the Interaction of Electron Donor and Acceptor Molecules with Graphene and Single-Walled Carbon Nanotubes." J. Phys. Chem. C **113**(39): 16855-16859.

Visser, J., N. Katsonis, et al. (2009). "Two-Dimensional Molecular Patterning by Surface-Enhanced Zn-Porphyrin Coordination." Langmuir **25**(10): 5980-5985.

Wasielewski, M. R. (2006). "Energy, Charge, and Spin Transport in Molecules and Self-Assembled Nanostructures Inspired by Photosynthesis." J. Org. Chem. **71**(14): 5051-5066.

Watson, M. D., F. Jäckel, et al. (2004). "A hexa-peri-hexabenzocoronene cyclophane: An addition to the toolbox for molecular electronics." J. Am. Chem. Soc. **126**(5): 1402-1407.

Weber, U. K., V. M. Burlakov, et al. (2008). "Role of Interaction Anisotropy in the Formation and Stability of Molecular Templates." Phys. Rev. Lett. **100**(15): 156101-4.

Wetterer, S. M., D. J. Lavrich, et al. (1998). J. Phys. Chem. B **102**: 9266.

Wetterer, S. M., D. J. Lavrich, et al. (1998). "Energetics and Kinetics of the Physisorption of Hydrocarbons on Au(111)." J. Phys. Chem. B **102**(46): 9266-9275.

Whitesides, G. M., J. P. Mathias, et al. (1991). "Molecular Self-Assembly and Nanochemistry - a Chemical Strategy for the Synthesis of Nanostructures." Science **254**(5036): 1312-1319.

Wiesendanger, R., H. J. Guntherodt, et al. (1992). Scanning Tunneling Microscopy II. Basel, Springer-Verlag.

Winfree, E., F. R. Liu, et al. (1998). "Design and self-assembly of two-dimensional DNA crystals." Nature **394**(6693): 539-544.

Wold, D. J., R. Haag, et al. (2002). "Distance dependence of electron tunneling through self-assembled monolayers measured by conducting probe atomic force microscopy: Unsaturated versus saturated molecular junctions." J. Phys. Chem. B **106**(11): 2813-2816.

Wu, Q. and W. T. Yang (2002). "Empirical correction to density functional theory for van der Waals interactions." Journal of Chemical Physics **116**(2): 515-524.

Xu, W., M. Dong, et al. (2007). "Cyanuric Acid and Melamine on Au(111): Structure and Energetics of Hydrogen-Bonded Networks13." Small **3**(5): 854-858.

Xu, W., M. D. Dong, et al. (2007). "Cyanuric acid and metamine on Au(111): Structure and energetics of hydrogen-bonded networks." Small **3**(5): 854-858.

Yaghi, O. M., M. O'Keeffe, et al. (2003). "Reticular synthesis and the design of new materials." Nature **423**(6941): 705-714.

Yang, X., X. Dou, et al. (2008). "Two-Dimensional Graphene Nanoribbons." J. Am. Chem. Soc. **130**(13): 4216-4217.

Yang, Y. and C. Wang (2009). "Hierarchical construction of self-assembled low-dimensional molecular architectures observed by using scanning tunneling microscopy." Chem. Soc. Rev. **38**(9): 2576-2589.

Yang, Y. C., C. H. Chang, et al. (2007). "Complexation of fullerenes on a pentacene-modified Au(111) surface." Chem. Mater. **19**(25): 6126-6130.

Yin, S., C. Wang, et al. (2001). "Theoretical study of the effects of intermolecular interactions in self-assembled long-chain alkanes adsorbed on graphite surface." Surf. Interface Anal. **32**(1): 248-252.

Zacharia, R., H. Ulbricht, et al. (2004). "Interlayer cohesive energy of graphite from thermal desorption of polyaromatic hydrocarbons." Phys. Rev. B **69**(15): 155406-155406.

Zallen, R. (1998). The Physics of Amorphous Solids, Wiley-VCH.

Zerkowski, J. A., C. T. Seto, et al. (1992). "Solid-State Structures of Rosette and Crinkled Tape Motifs Derived from the Cyanuric Acid Melamine Lattice." J. Am. Chem. Soc. **114**(13): 5473-5475.

Zhang, Y. K. and W. T. Yang (1998). "Comment on "Generalized gradient approximation made simple"." Phys. Rev. Letters **80**(4): 890-890.

Zhdanov, V. P. (1991). "Arrhenius parameters for rate processes on solid surfaces." Surf. Sci. Rep. **12**(5): 185-242.

Zwaneveld, N. A. A., R. Pawlak, et al. (2008). "Organized formation of 2D extended covalent organic frameworks at surfaces." J. Am. Chem. Soc. **130**(21): 6678-+.